Abstract

Title of Dissertation: THE RADIO-FREQUENCY SINGLE-ELECTRON TRANSISTOR DISPLACEMENT DETECTOR

Matthew D. LaHaye, Doctor of Philosophy, 2005

Dissertation directed by: Adjunct Professor Keith C. Schwab

Department of Physics

For more than two decades, the standard quantum limit (SQL) has served as a benchmark for researchers involved in ultra-sensitive force and displacement detection. In this thesis, I discuss a novel displacement detection technique which we have implemented that has allowed us to come within a factor of 4.3 from the limit, closer than any previous effort. Additionally, I show that we were able to use this nearly quantum-limited scheme to observe the thermal motion of a 19.7 MHz in-plane mode of a nanomechanical resonator down to a temperature of 56 mK. At this temperature, the corresponding thermal occupation number of the mode was $\langle n_{th} \rangle \approx 60$. This is the lowest thermal occupation number ever demonstrated for a nanomechanical (or larger) device. We believe that the combination of these two results has important and promising implications for the future study of nanoelectromechanical systems (NEMS) at the quantum limit.

The detection scheme that we used was based upon the single-electron transistor (SET). The SET has been demonstrated to be the world's most sensitive electrometer and is considered to be a near-ideal linear amplifier. We used stan-

dard lithographic techniques for the on-chip integration of the SET with both a microwave-matching network and nanomechanical resonator. The SET served as a transducer of the resonator's motion: fluctuations in the resonator's position modulated the SET impedance. The microwave-matching circuit allowed us to read-out the modulation of the SET's impedance with $\sim$ 75 MHz bandwidth. The combination of microwave-matching circuit and SET is known as the radio-frequency single-electron transistor (RFSET). Including the nanomechanical resonator, the configuration is called the radio-frequency single-electron transistor displacement detector.

In this thesis, I discuss the basics of quantum-limited measurement and some of the subtleties of observing mechanical quantum phenomena. I then discuss the basics of the RFSET displacement detector, its ultimate limits, its engineering and operation, the first generation results, and finally what improvements could be made to future generation devices.

THE RADIO-FREQUENCY SINGLE-ELECTRON TRANSISTOR DISPLACEMENT DETECTOR

by

Matthew D. LaHaye

Dissertation submitted to the Faculty of the Graduate School of the
University of Maryland, College Park in partial fulfillment
of the requirements of the degree of
Doctor of Philosophy
2005

Advisory Committee:

Professor Fredrick C. Wellstood, Chair
Professor Keith C. Schwab, Co-Chair
Professor Christopher J. Lobb
Professor James R. Anderson
Professor Donald L. DeVoe

Dedication

. . . to my lovely wife, Juhee, and her heart of gold.

Acknowledgements

This thesis is dedicated to my wife, Juhee Kothari LaHaye, for her enduring support and patience throughout these six years. She bore the brunt of the long hours, lost weekends, and endless uncertainty, yet still kept a smile on her face and on mine. Juhee is the binding that holds this book together.

I am forever grateful to my family, Mom, Dad, Mark, and Chris. They gave me the world, taught me the essentials, and then let me go on my way. With each success and blunder, they have stood behind me the same. I have had a great life, and they made that possible.

I am truly fortunate to have such wonderful in-laws. Mom, Dad, and Pooja have offered to me nothing but love and enlightenment since the day we met.

I am especially indebted to my advisor Professor Keith Schwab. Keith has been an inspiration, a mentor, and a friend. Along with the opportunity to travel and meet other leading researchers in the field, he provided a lab full of equipment and five years of ideas. From scratch, he built the LPS Nanomechanics group into a first-class research team. I am fortunate and proud to have been a part of this experience.

Also, thanks to Drs. Bruce Kane, Keith Miller, and Marc Manheimer for their support over the years and the hard work they put into the quantum computing group.

I owe many thanks to my labmates, fellow students, and staff in both the

physics department at the University of Maryland and at the Laboratory for Physical Sciences.

Thanks to the the nanomechanics group, a very unique collection of talented and friendly individuals: Emrah Altunkaya, Harish Bhaskaran, Dr. Olivier Buu, Benedetta Camarota, Jared Hertzberg, Akshay Naik, and Patrick Truitt.

Particularly, I would like to thank Dr. Olivier Buu. Olivier provided me with advice on everything from Matlab to cryogenics to life in general. He is a selfless and tireless individual who contributed greatly to my education as an experimental scientist. He played an integral role in these experiments, assembling the dilution refrigerator and SET-Gain feedback circuit, and sharing the measurement responsibilities with me.

Also, I would like to thank Benedetta Camarota for many, many insightful conversations, much sound advice, fabrication support, and half-a-million laughs. Benedetta also played an essential role in developing the device fabrication recipe.

Finally, thanks to Jared Hertzberg for reading drafts of this thesis and always offering his opinion or a helping hand.

I must also take the opportunity to thank Dan Sullivan, Carlos Sanchez, and Kenton Brown for their support, integrity, and friendship. Essentially, we all started the program together and have been through many years of ups and downs. Dan's humor, wit and insight into everything from physics to politics to sports will not be forgotten. Carlos was always willing to share his extensive knowledge, whether it was music, politics, electronics or fabrication. I must particularly recognize the advice he provided for SET fabrication. Kenton's intelligence and generosity will

also be greatly missed.

I would like to thank Josh Higgins, Ben Palmer, Jonghee Lee, and Nathan Siwak for both friendly and technical conversations over the years.

I am grateful for the technical support and machine work that Les Lorenz, J.B Dottellis, and Russell Frizzell provided. As well, I must thank them for many pleasant and informative conversations.

Thanks to Toby Olver for keeping the cleanroom running and being so patient with my requests.

Thanks to Butch Bilger for keeping the Helium flowing.

I would also like to thank Jane Hessing for her work over the years keeping me up-to-date on paperwork, informed of deadlines, and answering my questions.

As well I must thank Margaret Lukomska for her work expediting purchase orders, travel requests and various other questions.

I would like to thank Profs. Miles Blencowe and Aashish Clerk for their help clarifying the subtleties of SET back action and the quantum limit.

Finally, I would like to sincerely thank the members of my thesis committee, Profs. Keith Schwab, Fred Wellstood, Bob Anderson, Chris Lobb, and Don DeVoe for taking the time to read through 200 pages of technical information and run-on sentences, as well as to participate in my defense and provide very helpful feedback. I am especially grateful to Prof. Wellstood for accepting the responsibility of "Chairman" and meeting with me on multiple occasions to discuss corrections.

TABLE OF CONTENTS

LIST OF FIGURES

LIST OF TABLES

LIST OF SYMBOLS

Symbol	Definition
a_1	Relationship between resonator's mid-point motion and the average motion over the length of the SET island
$\hat{a}_{\alpha,\beta}$, $\hat{a}^{\dagger}_{\alpha,\beta}$	Lowering and raising operators of the input signal into ideal linear amplifier
A	Interaction strength between resonator and detector; also charge-to-voltage ratio for SET gate in electrons; total linear amplifier noise contribution in units of quanta; amplitude of resonator's thermal response; cross-sectional area of resonator
A_i	Linear amplifier noise contribution referred to input for each quadrature in units of quanta; also cross-sectional area of SET junctions
A_Q	Charge gain of RFSET electrometer based upon the 1 MHz calibration signal
A_r	Amplitude of reflected microwave signal
b	Geometric constant for the first derivative of C_{NR} with respect to y_{avg}
b	Geometric constant for the first derivative of C_{NR} with respect to y_{avg}
B	Bandwidth; magnetic field magnitude

Symbol	Definition
$\hat{b}_{\alpha,\beta}$, $\hat{b}^{\dagger}_{\alpha,\beta}$	Lowering and raising operators of the output signal from ideal linear amplifier
Δb	Total rms noise in the amplitude at the output of ideal linear amplifier
Δb_i	Total rms noise for each quadrature at the output of ideal linear amplifier
C_g	SET gate capacitance
C_{gnr}	Capacitance between SET gate and resonator
C_i	Individual SET junction capacitances
C_n	Effective electromechanical capacitance for magnetomotive detection, n^{th} mode
C_{NR}	Capacitance of resonator to SET island
C_T	Tank circuit capacitance
C_{Σ}	Total SET island capacitance
Δ	Quasiparticle gap energy of SET leads and islands (assumed to be equal)
d_{gnr}	Spatial separation between SET gate and resonator
d_{NR}	Spatial separation between SET island and resonator
$DJQP$	Double Josephson Quasiparticle Resonance
$\delta\epsilon$	Energy sensitivity of RFSET plus measurement circuit
$\delta\epsilon_{SET}$	Energy sensitivity of SET

Symbol	Definition
e	magnitude of electron charge
η_1	Projection of force on resonator's fundamental mode
E	Young's Modulus of resonator
E_C	Charging energy of SET
E_J	Josephson energy of SET junctions
Δf	Half-width of tank circuit resonance, bandwidth of RF-SET detection scheme; also used as noise equivalent bandwidth of the resonator
F_i	Noise contribution to each quadrature of input signal from ideal linear amplifier
ΔF_i	RMS noise contribution to each quadrature of input signal from ideal linear amplifier
$\Delta F_i^{\pm}$	Change in free-energy of SET circuit when an electron tunnels on or off of the SET island
γ_b	Damping of the resonator's fundamental mode due to dissipation in the thermal bath T_{bath}
γ_d	Damping of the resonator's fundamental mode due to dissipation in the effetive thermal bath T_{det}
γ_e	Total effective damping including both damping from environment and SET

Symbol	Definition
Γ	Reflection coefficient; also decoherence time of superposition of coherent states
Γ_{max}	Reflection coefficient at maximum SET conductance
$\Gamma_i^{\pm}$	Tunneling rates onto and off of SET island through SET junctions
G	Gain of measurement circuit including pre-amplifiers and loss
$\hbar$	Planck's constant divided by 2π
I	Moment of inertia for transverse, in-plane vibration of rectangular bar
IR	Integrated resonator response
I_{SD}	SET source-drain current
JQP	Josephson Quasiparticle Resonance
K_m	Spring constant of resonator defined with respect to average motion over the length of the SET island for the fundamental mode
k_B	Boltzman's constant
k_n	Roots of the characteristic equation for the transverse vibration of a doubly-clamped rectangular bar
K_1	Spring constant of resonator defined with respect to midpoint motion for the fundamental mode

Symbol	Definition
λ	Admittance or response of detector current to resonator displacement; also wavelength of microwave applied to RFSET; also roots for characteristic equation for the transverse vibration of a doubly-clamped rectangular bar under tension
L	Length of resonator; also, gain of linear amplifier in number quanta
L_n	Effective electromechanical inductance for magnetomotive detection, n^{th} mode
L_T	Tank circuit inductance
m	Geometric mass of the resonator
M	Depth of modulation of reflection coefficient
M_m	Effective mass of resonator with respect to average displacement over the length of the SET island for the fundamental mode
m_{eff}	Effective mass of resonator with respect to mid-point motion for the fundamental mode
m_i	Slopes of JQP resonance; and slope of the onset of tunneling in the normal state
n	Number of electrons on SET island; also mode number of transverse, in-plane resonator motion

Symbol	Definition
N_a	Number of quanta in the input signal to ideal linear amplifier
N_b	Number of quanta in the output signal from ideal linear amplifier
$\langle n_{th} \rangle$	Thermal occupation number of resonator's fundamental mode
Ω	Volume of SET island
ω_1	Resonator's fundamental mode frequency multiplied by 2π
ω_T	Resonant frequency of tank circuit multiplied by 2π
P	Resonator's thermal response
P_o	Background or noise-floor of detection scheme
P_{1MHz}	Power in 1 MHz sideband gain calibration
ϕ	Potential of SET island
Q	Total effective quality factor of tank circuit
$\dot{Q}$	Heat transfer down Nb microwave coax and dissipation in SET
$\dot{Q}_1$	Power conducted to bath through SiN membrane
$\dot{Q}_2$	Power conducted through SiN membrane from SET to region near nanoresonator

Symbol	Definition
$\dot{Q}_3$	Power conducted through SiN membrane from region near nanoresonator to bath
$\dot{Q}_4$	Power conducted through electron-phonon coupling to electrons in Au film on top of the nanoresonator
Q_b	Quality factor of the resonator's fundamental mode, accounting only for γ_b
Q_d	Quality factor of the resonator's fundamental mode, accounting only for γ_d
Q_e	Total effective resonator quality factor
Q_g	Polarization charge on SET gate electrode
ΔQ_g	Charge modulation on SET gate
Q_{NR}	Polarization charge on resonator electrode
Q_S	Quality factor of tank circuit due to loading from SET
Q_T	Quality factor of tank circuit due to loading from transmission line
$RFSET$	Radio Frequency Single-Electron Transistor
ρ	Mass density of resonator
R_i	Individual SET junction resistances
R_n	Real-component of electromechanical impedance for magnetomotive detection, n^{th} mode
R_Q	Resistance quantum

Symbol	Definition
R_Σ	Total resistance of SET junctions at large V_{SD}
R_S	Total resistance of SET junctions
SET	Single-Electron Transistor
$\bar{S}_F$	Symmetrized back action noise spectral density of linear detector
$\bar{S}_{F_b}$, S_f	Symmetrized thermal noise spectral density
S_F^y	Back action contribution to the spectral displacement sensitivity
$\bar{S}_I$	Symmetrized forward coupling noise spectral density of linear detector
Σ	Electron-phonon coupling
σ_{int}	Intrinsic axial stress in SiN film
S_{II}	SET shot noise spectral density
$S_{I\phi}$	Correlations between SET shot noise and island-potential fluctuations
S_I^y	Shot noise contribution to the spectral displacement sensitivity
SNR	Signal-to-noise ratio of 1 MHz sideband gain calibration
$S_{\phi\phi}$	SET island-potential fluctuations spectral density
S_Q, $S_{Q_{NR}}$	Spectral density of charge sensitivity in units of e^2/Hz
S_y	Total spectral displacement sensitivity

Symbol	Definition
τ	Effective resonator damping time; also used as measurement time
T	Intrinsic tension on SiN resonator
t_{Au}	Thickness of resonator's Au layer
T_b	Temperature of the thermal bath, the"environment" or "external bath"
T_d	Effective temperature of the SET noise environment
T_e	Total effective temperature of the resonator due to contact to T_{bath} and T_{det}
T_{island}	SET island electron temperature
T_N	Noise temperature of displacement detection scheme
T_n^{det}	Noise temperature contribution of measurement circuit including pre-amplifier and circuit loss
T_o	Noise temperature of measurement circuit plus the SET shot noise contribution
T_{QL}	Quantum limit of noise temperature for continuous linear detection
T_S	Temperature of the dilution refrigerator's sample stage
T_{SET}	Noise temperature contribution of the SET shot noise
t_{SiN}	Thickness of resonator's SiN layer
v_c	Incident microwave signal, or carrier

Symbol	Definition
V_D	Capacitive excitation voltage
V_g	SET gate bias
ΔV_g	Voltage modulation on SET gate
v_n	Average transverse, in-plane velocity of doubly-clamped rectangular bar over the bar's length, n^{th} mode
V_{NR}	Resonator bias, also referred to as coupling voltage
v_r	Reflected microwave signal
V_{SD}	SET source-drain bias
$V_t^{\pm,i}$	Threshold voltage for tunneling of electrons onto (off of) the SET island through junctions i, normal state SET
w	Width of resonator
ω	frequency in rad/s
ω_1	fundamental mode frequency in rad/s
X_i	Signal quadratures at the input of ideal linear amplifier
Y_n	Eigenfunctions of the wave-equation for in-plane displacement of the resonator
Δy_{QL}	Quantum limit for continuous linear position detection
Δy_{ZP}	Zero-point fluctuations of mechanical resonator for in-plane, fundamental mode
y_1	In-plane displacement of the resonator's mid-point for the fundamental mode

Symbol	Definition
$y_{1,m}$, y_m	Average, in-plane displacement of resonator over the length of the SET island for the fundamental mode
δy, δy_m	Total displacement sensitivity in resonator's noise-equivalent bandwidth
Z_o	50 Ω Transmission line impedance
Z_{LC}	Characteristic impedance of tank circuit
Z_{LCR}	Impedance of tank circuit and SET at the resonant frequency of the tank circuit
Z_m	Electromechanical impedance for magnetomotive detection

Chapter 1

Overview

1.1 Context and Motivation

The Heisenberg uncertainty principle [1] places a limit on the precision with which one can measure an object's position [2]. For the case of two successive measurements of a mass M undergoing simple harmonic motion, this limit, known as the "standard quantum limit", is neatly expressed as [2]

$$\Delta y_{SQL} = \sqrt{\frac{\hbar}{2M\omega}}, \tag{1.1}$$

where $\omega/2\pi$ is the frequency with which the mass oscillates, and $\hbar$ is Planck's constant.

Since the 1970's, researchers have been engaged in both theoretical and experimental efforts to understand and implement mechanical detectors and measurement strategies for displacement detection at (or even below) the standard quantum limit [2-17].

Inititally, the impetus for quantum-limited displacement detection arose out of the hunt for gravitational waves [2]. Through nearly three decades of effort, the gravitational-wave community has moved quantum-limited detectors from mere thought-experiments to nearly practicable measurement devices. For example, the 4 km L1 interferometer of the LIGO I project has demonstrated a sensitivity, at 200 Hz, of $\Delta \mathrm{y} \sim 150 \Delta \mathrm{y}_{SQL}$ [11] for the displacement detection of its 10 kg test-

masses. Researchers at Laboratoire Kastler Brossel, employing a tabletop Fabry-Perot interferometer, recently achieved a displacement sensitivity of $\Delta y \sim 25\ \Delta y_{SQL}$ for the read-out of the 2 MHz surface modes of a silica mirror [7]. The SQUID-based amplifiers developed for the Auriga project have demonstrated noise temperatures of $\sim$ 10's μK, corresponding to sensitivities of $\Delta y \sim$ 100 - 200 Δy_{SQL} for the read-out of the vibrational modes of $\sim$ 2000 kg acoustic bar resonators [9]. As well, researchers in the Supeconductivity Center at the University of Maryland used a scheme based on a Paik-style transducer [19] to achieve a noise temperature of $\sim$ 1 mK at 900 Hz, yielding $\Delta y \sim 200\ \Delta y_{SQL}$ [8].

In the last decade, the development of nanoelectromechanical systems (NEMS) has generated a second wave of interest in the standard quantum limit. Driven by potential applications to ultra-sensitive imaging [20] [21], mass detection [22], and quantum computing [23] [24], as well as, ultimately, the possibility to study mechanical quantum systems in the macroscopic limit [23-33], the NEMS community has rapidly pushed mechanical transduction to the quantum frontier. In the last year alone, several important results have been generated. For example, researchers at IBM used magnetic resonance force microscopy (MRFM) [20] to detect the spin of a single electron [21]. Using a magnetomotive technique [22], researchers at the California Institute of Technology demonstrated mass sensivity on the order of zeptograms, sufficient for the detection of a single molecule [34]. Finally, our group in the Laboratory for Physical Sciences at the University of Maryland used the radio-frequency single-electron transistor displacement detector [12] [13] to demonstrate both displacement sensitivity approaching closer to the standard quantum limit

than any previous measurement scheme ($\Delta y \sim 5.8\ \Delta y_{SQL}$[1]) [15] and an approach to low thermal occupation numbers ($\langle n_{th} \rangle \sim 60$) for a 20 MHz nanomechanical resonator[15].

It is important to note that the achievement of low thermal occupation numbers is a general and significant point of distinction between NEMS devices and the resonators used in gravitational-wave detection. We can see why this is by first looking at the definition of the thermal occupation number. For a resonant mode with frequency ω in thermal equilibrium with a bath of temperature T, the mode's thermal occupation number is given by [35]

$$\langle n_{th} \rangle = \frac{1}{2} + (e^{\hbar\omega/k_B T} - 1)^{-1}, \tag{1.2}$$

where k_B is Boltzman's constant and "$\frac{1}{2}$" accounts for the mode's zero-point fluctuations. This quantity provides a simple "rule-of-thumb" for gauging whether one should be able to observe a mode's quantum properties:

$$\frac{k_B T}{\hbar\omega} \leq 1, \tag{1.3}$$

If Eq. 1.3 is satisfied, the mode is said to be "frozen out". That is, the mode is in it's ground state and the contribution of the thermal energy to the mode's total energy is comparable to or less than the zero-point contribution. As $k_B T/\hbar\omega$ grows, so too does the contribution from thermal fluctuations, making it more difficult to observe the mode's quantum attributes. There is no general prescription for how small the ratio $k_B T/\hbar\omega$ must be before quantum behavior becomes observable (see Chapter

[1] In Chapter 2, I make the distinction between Δy_{SQL} and Δy_{QL}. In terms of Δy_{QL}, a more appropriate gauge for continuous position detection, we achieved $\Delta y \sim 4.3 \Delta y_{QL}$

2). For the purpose of observing the resonator in a pure quantum state such as a Fock state or superposition state, or for detection of the resonator's zero-point fluctuations, the smaller the ratio the better (see Chapter 2).

For the above-mentioned gravitational-wave detectors, the operating temperatures were sufficiently high (> 1 K) and resonators' frequencies were sufficiently low ($< 5MHz$), that, at a minimum, $\langle n_{th} \rangle \sim 3$ x 10^6 (the Auriga project at 1.5 K and the Fabry-Perot scheme at 300 K). In contrast, because NEMS devices have demonstrated resonant frequencies as high as ~ 1 GHz [36] [23] and are routinely installed on cryogenic probes for measurement at mK temperatures, it should be possible for researchers to observe $\langle n_{th} \rangle \leq 1$.

The demonstration of nearly quantum-limited position detection and low thermal occupation numbers promises NEMS researchers the opportunity to push the study of quantum mechanics to a significantly larger realm. For example, one recent proposal to prepare and measure a nanomechanical resonator mode in a superposition of position states could be implemented if one could cool the mode to $\langle n_{th} \rangle \sim 50$ [25] (please see Refs. [23-33] for other recent proposals). This is signficant because, while NEMS devices are, by definition, nanoscopic, they are typically composed of $\sim 10^{10}$ atoms. With a few exceptions, such as the measurement of the quantum of thermal conductance [37], previous demonstrations of mechanical quantum phenomena have been limited to the scale of molecules and atoms (for exmaple Refs. [38] [39] [40]).

In this thesis, I discuss the details of the first generation of radio-frequency single-electron transistor (RFSET) displacement detectors. The technique was first

proposed by Miles Blencowe and Martin Wybourne [12] and utilizes the RFSET's large bandwidth (demonstrated to be $>$ 100 MHz) [41] and near-ideal noise characteristics [42] to perform displacement detection near the quantum limit. Figure 2.3(a) shows an SEM image of an RFSET displacement detector, and Fig. 2.3(b) shows a generic circuit schematic for the transduction process. Here, a metallized SiN nanoresonator is positioned within 1 μm of an SET island, resulting in a coupling capacitance C_{NR} on the order of 10's aF. Displacement of the nanoresonator from its equilibrium position linearly modulates the coupling capacitance through

$$\Delta C_{NR} \approx \frac{C_{NR}}{d_{NR}} \Delta y, \tag{1.4}$$

where d_{NR} is the separation between the nanoresonator and the SET island, and $\Delta y \ll d_{NR}$ is the displacement of the resonator from equilibrium. Establishing a voltage V_{NR} between the resonator and the SET converts the capacitance fluctuations into charge fluctuations:

$$\Delta Q_{NR} \approx \frac{C_{NR} V_{NR}}{d_{NR}} \Delta y. \tag{1.5}$$

The charge fluctuations modulate the SET impedance which is then monitored by performing microwave reflectometry [41]. The use of an on-chip tank circuit (L_T and C_T in Fig. 2.3(b)) allows for matching between the large SET impedance (typically 10's kΩ) and 50 Ω transmission line.

Ultimately, the sensitivity of the RFSET displacement detector is limited by the intrinsic noise of the SET [12] [13]. This is composed of two sources [43] (1) the SET shot noise and (2) the potential fluctuations of the SET island. The SET shot noise is forward coupling. That is, it simply adds to the signal, resulting in

(a)

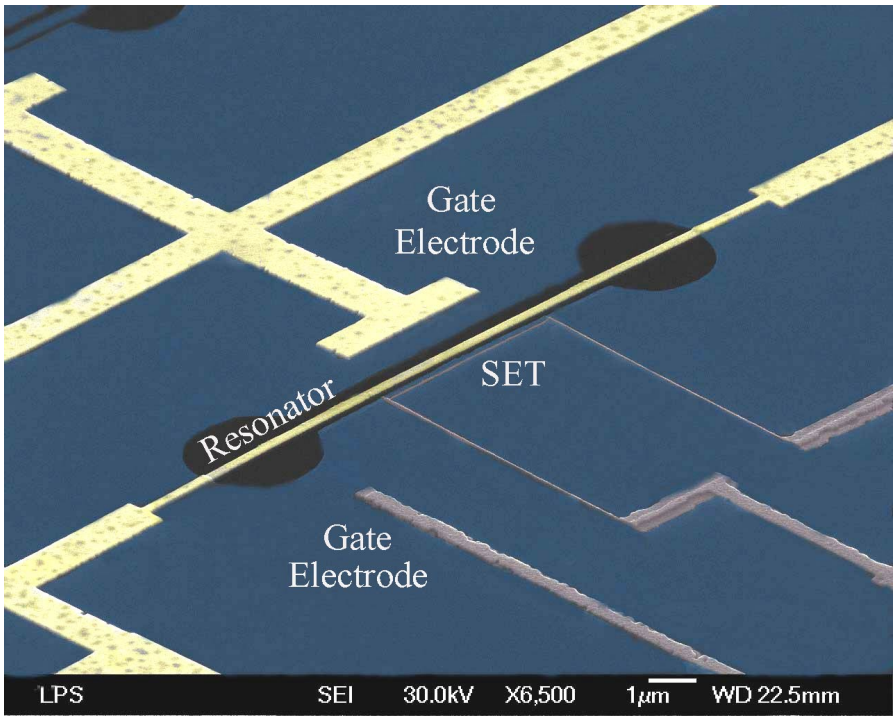

(b)

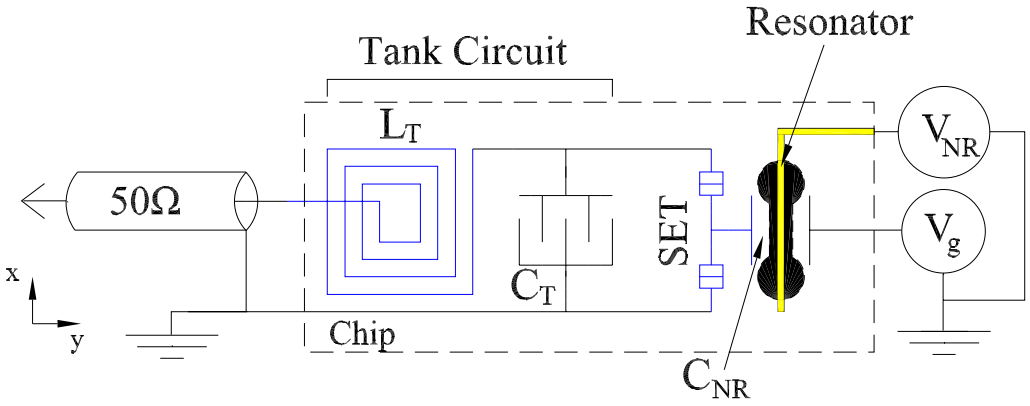

Figure 1.1: (a) SEM image of the RFSET displacement detector and (b) Circuit schematic

a contribution to the total displacement noise that is inversely proportional to the coupling $C_{NR}V_{NR}/d_{NR}$. The island-potential noise is back-acting. That is, the island-potential fluctuations couple to the resonator through C_{NR} and drive it, resulting in a contribution to the total displacement noise that is linearly proportional to the coupling. A minimum in the total displacement noise is found at a coupling strength where the two sources contribute equally. For such optimal coupling, and typcial device parameters (see Chapter 2), the total displacement noise has been predicted to be $\Delta y \sim 2\Delta y_{QL}$ [13].

In the measurement of the first generation of RFSET displacement detectors (LPS), we were not limited by the intrinsic noise of the SET. Instead, we were limited by the 80 pV/$\sqrt{Hz}$ noise (referred to the input) of our cryogenic pre-amplifier (see Chapter 4 and Chapter 7), which set our charge sensitivity at approximately a factor of 4 - 6 from the SET's intrinsic shot noise limit. Consequently, the lowest displacement sensitivity which we observed was on the on the order of a factor of 4 from the quantum limit [15]. Nevertheless, this is the closest approach to the quantum limit of displacement detection that anyone before or since has demonstrated, and marks a factor of 30 improvement over the SET-mixer technique previously demonstrated by Robert Knobel and Andrew Cleland at the University of California, Santa Barbara [14].

An additional improvement of the LPS detectors over the Santa Barbara SET-mixer technique was the $\sim$ 75 MHz bandwidth provided by the rf-matching network. In contrast, at best, the maximum bandwidth of the Santa Barbara technique would have been on the order of kHz, either limited by the DCSET or the dc electronics

at room temperature. Either way, as the quality factor and resonant frequency of the resonator were $\sim$ 1.5 x 10^3 and 116 MHz respectively [14], the half-width of the resonator's spectral response was $\sim 10^5$ and thus much larger than the detection bandwidth.

The large bandwidth of the RFSET technique allowed us to observe the resonator's full spectral response, facilitating the detection of the resonator's thermal motion. In the end, we were able observe the thermal motion of the nanoresonator down to a temperature as low as $\sim$ 56 mK, corresponding to a thermal occupation number of $\langle n_{th} \rangle \approx 60$, and demonstrating, that, indeed, NEMS is on the verge of the quantum regime.

1.2 Structure of the Thesis

The structure of this thesis is as follows.

Chapter 2 provides the basic definitions and theoretical concepts upon which the rest of the text is based. First, the quantum limits of a mechanical resonator are defined, and the criteria for reaching these limits are presented. This is followed by the introduction of the RFSET displacement detector and a discussion of its basic operating principles. In the final section, the intrinsic noise properties of the SET are reviewed and used to demonstrate that, in principle, the RFSET is capable of performing as a nearly quantum-limited displacement detector.

Chapter 3 presents a detailed account of the fabrication steps we developed and followed to produce our first generation of RFSET displacement detectors.

Chapter 4 discusses the details of the apparatus which we constructed for the measurement of our samples.

Chapter 5 presents and explains the RFSET reflectometry technique, the backbone of the detection scheme.

Chapter 6 describes the implementation of the RFSET displacement detection technique and presents our main research results. Relying heavily on the results of Chapter 5, it begins with a treatment of the basic methodology. This is followed by a discussion of the RFSET detection of capacitively driven nanoresonators. Next, the topic of nanomechanical noise thermometry is introduced. It is in this section that the central results of the thesis are put forth. Finally, the chapter finishes by addressing the issue of SET back action.

Chapter 7 concludes the main body of the thesis with a discussion of the technical improvements and future prospects.

The remaining chapters I label as Appendix A and Appendix B. They contain information that I think is either essential for understanding the basic concepts and limitations of the RFSET displacement detector or is useful for the actual implementation. Included in these chapters are tables of the various parameters for the devices around which this thesis is built.

Two of the devices, Device 3 and Device 4, are included even though they are not discussed in the main body of the dissertation. Initially, my intent was to produce a work that fully addresses the noise characteristics of the RFSET displacement detector, including the SET back action. Devices 1 and 2 were to be used for treating the forward-coupling limit. Devices 3 and 4 were to be used for discussing the

back action limit. However, the physics involved with SET back action, particularly the superconducting SET, are more complicated and interesting than I originally imagined, and their investigation would constitute an entire thesis. Furthermore, we do not understand all the observations that we have made of Devices 3 and 4.

I have left Devices 3 and 4 in the thesis mainly for illustrative purposes and for technical explanations of useful information (*ie.* RFSET gain calibration and RF tank-circuit characterization). Additionally, I would like to have the parameters and characteristics of all four devices and accompanying measurement circuits cataloged in one place.

Finally, Device X and Device Y, devices which are not in any of tables, I have also used for illustrative purposes in Chapter 5. The nanoresonator in Device X met an early demise, however, the data taken for the gain-feedback circuit and sideband amplitude versus V_g is the best data I have to illustrate these techniques. Device Y is actually from the latest generation of devices (courtesy of Akshay Naik). I used this data to illustrate the equivalence of the reflection map and the numerical derivative of the IV map. In the earlier devices, either this data is incomplete (for Devices 1 and 2 I have no simultaneous measurements of reflection map and numerical derivative) or the IV maps were less "photogenic" (for Devices 3 and 4 the DJQP and JQP resonances are either smeared or faint). I also used data from Device Y to help illustrate the principle of amplitude modulation.

Chapter 2

Introduction

At first glance, it might not be obvious why one can treat a nanomechanical device, such as a doubly-clamped resonator, as a simple harmonic oscillator. After all, a typical structure might have dimensions ranging from nanometers to microns, and be comprised of tens of billions of atoms and three times as many normal vibrational modes.

The situation is simplified, though, if one is only interested in the lowest-frequency transverse modes. In this case, the ratio of the wavelength-to-lattice spacing is sufficiently large, $\sim 10^4$, that deformation of the lattice occurs slowly over the length of the device, allowing for the use of continuum elasticity theory to model the mode's behavior [44] [45]. For deformations smaller than a critical amplitude [46], non-linear effects are negligible. Below the critical amplitude, the system can be reduced to a simple harmonic oscillator with an effective mass and spring constant determined by the mode shape and the portion of the oscillating structure that one considers (see Appendix A). The critical amplitude for the resonators measured in this research can be calculated to be $\sim$ nm's [46]. The typical displacements we measure are $\sim$ pm's.

Peering at such a structure, for example, through an optical microscope, if our eyes and brains had the temporal resolution, we would expect to see it jumping

about, its motion driven by thermal fluctuations and other classical interactions. We might not expect to observe any deviations from the classical behavior we are so familiar with from our daily experiences. However, the question arises: what would it take to observe one of these structures exhibiting quantum behavior?

In this chapter, I present some basic criteria which, when met, could allow for the observation of quantum phenomena in macroscopic mechanical resonators [4]. The first criteria, which I call Quantum Limit I, establishes an approximate level to which classical interactions must be reduced in order to observe the resonator's quantum dynamics. It is implicit in my discussion that thermal fluctuations are the biggest problem and that all other classical forces are negligible. The second criteria, which I call Quantum Limit II, establishes the characteristics that a linear amplifier must possess in order that it minimally disturb the resonator during the process of measurement. It is seen that quantum mechanics requires such an amplifier to add a minimum of one-half quanta of noise power in the bandwidth of the signal. In the final section, I present and discuss the basics of the radio-frequency single-electron transistor (RFSET) displacement detector, a detection scheme which we have implemented and which has allowed us to come closer than any previous scheme to satisfying both criteria.

2.1 The Quantum Limit I: Thermal Noise

The question of how cold a mechanical mode must be before thermal fluctuations are reduced to a level that does not obscure the mode's quantum dynamics is

rather subtle. To thoroughly treat the topic is beyond the scope of this section and thesis. However, here, I present some basic, case-specific constraints on temperature with which I can later guage our experimental results (Chapter 5 and Chapter 6). I first discuss the freeze-out of a mechanical mode to its ground state. This is the simplest case to treat and provides a back-of-the-envelope estimate of how "quantum" a particular mode at a given temperature is (*ie.* whether or not the mode's dynamics can be described by classical equations of motion). Second, I briefly examine the issue of decoherence. In particular, I discuss the decoherence of a pure harmonic oscillator state due to linear coupling to a thermal bath, and present an expression for the decoherence rate of a superposition of position states in terms of the mode's temperature. Finally, I consider the detection of a mechanical mode's zero-point motion in the presence of thermal noise. I show that, even if $\mathrm{k}_B\mathrm{T}_b \gg \hbar\omega_1$, depending on the duration of the measurement and the coupling of the resonator to the thermal bath T_b, it is possible to reduce the change in amplitude due to thermal fluctuations below that due to zero-point fluctuations.

Freeze-Out

The simplest constraint to consider is a resonator's "freeze-out" to the ground state. This is equivalent to determining the temperature at which a mode's thermal occupation number is reduced signifcantly below 1. The average thermal occupation of an oscillator mode with frequency $\omega_1/2\pi$ is given by [35]

$$\langle n_{th} \rangle = (e^{\hbar\omega_1/k_B T_b} - 1)^{-1}, \tag{2.1}$$

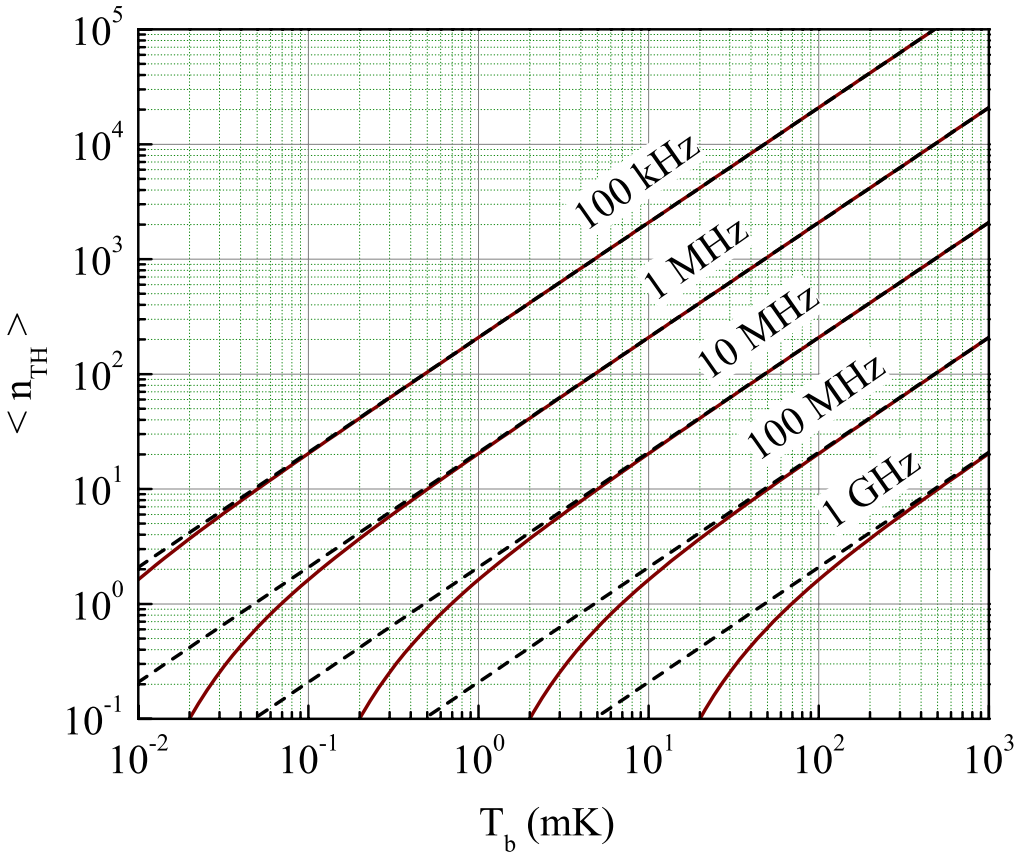

Figure 2.1: Thermal occupation number $\langle n_{th} \rangle$ plotted as a function of temperature for a range of nanomechanical resonant frequencies. The dashed lines represent the large-T_b limit given of Eq. 2.1. Note that the zero-point contribution of $\frac{1}{2}$ has not been included.

where $\hbar$ is Planck's constant, k_B is the Boltzman constant, T_b is the temperature of the mode, and the criteria for freeze-out is just

$$\frac{k_B T_b}{\hbar \omega_1} \leq 1. \tag{2.2}$$

Note that I have neglected the zero-point contribution of $\frac{1}{2}$.

Figure 2.1 shows the thermal occupation number for mode frequencies ranging from 100 KHz to 1 GHz. This range roughly represents the realm of demonstrated doubly-clamped, nanomechanical mode frequencies. Examination of the plot reveals that achieving freeze-out with passive refrigeration techniques (eg. dilution refrigeration) requires working with resonant frequencies in excess of 100 MHz. Of course with adiabatic demagnetization, the limit could be pulled down toward 10 MHz. Note, though, that I have not taken into account the issue of thermalization of the mechanical mode of interest. Whether a mechanical mode at 100 MHz can be tightly coupled to, say, the mixing chamber of a dilution refrigerator is a complicated problem that depends on both the experimental apparatus (*eg.* connections, "heat leaks", etc.) as well as the resonator's geometry and material (essentially the parameters that determine the resonator's quality factor), and one that I address in Section 7.2.

Decoherence of a Mechanical Superposition

The temperature constraint for the observation of a mechanical superposition state depends on the quality factor of the resonator under measurement and the desired duration of the superposition. A theoretical treatment of the harmonic

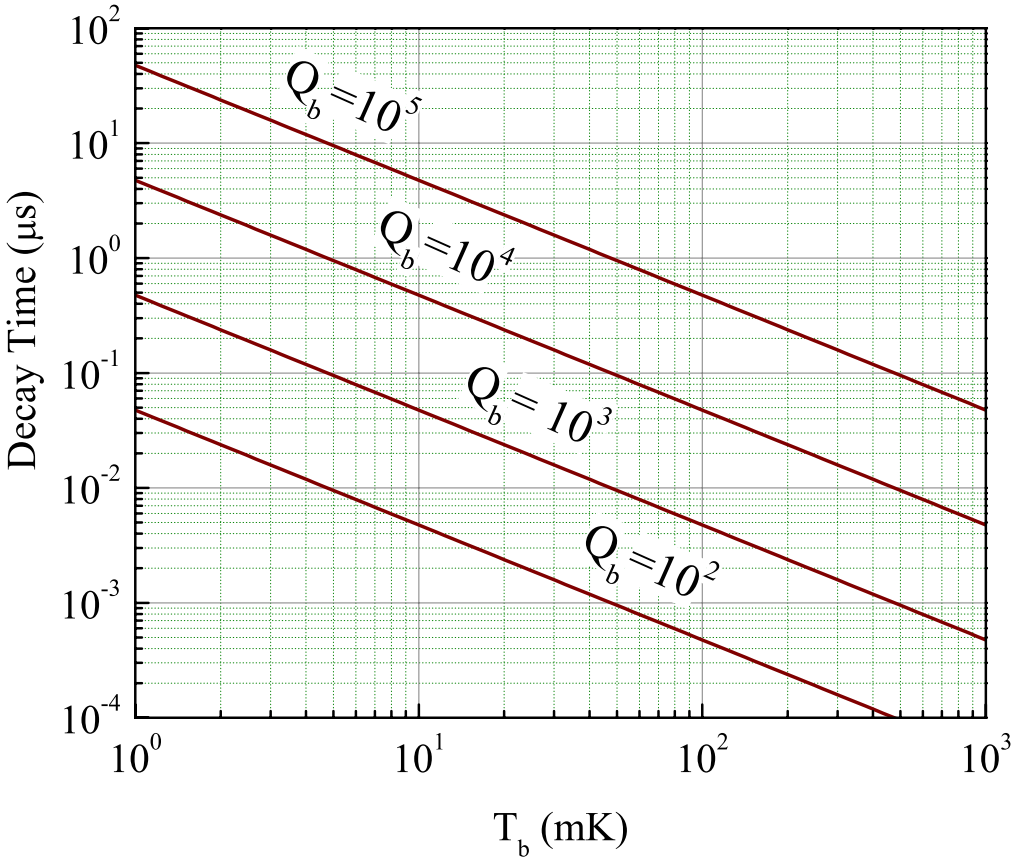

Figure 2.2: Decay time of a superposition of coherent states versus temperature for a range of nanomechanical resonant frequencies and quality factors. It is assumed that Gaussian peaks of the coherent states are separated by $2\Delta y_{zp}$.

oscillator states suggests that a mechanical superposition of two coherent states with spatial separation Δy between the Gaussian peaks will preferentially decay to a single coherent state at a rate given by [47]

$$\Gamma = \frac{4k_B T_b}{\hbar Q_b}\left(\frac{\Delta y}{\Delta y_{zp}}\right)^2, \tag{2.3}$$

where $Q_b = \omega_1 \tau$ is the resonator's quality factor, assumed to be determined strictly from coupling to the thermal bath, $\Delta y_{zp} = \sqrt{\hbar/2M_m\omega_1}$ is the resonator's zero-point deviation, and M_m is the resonator's effective mass.

Figure 2.2 displays a plot of the inverse of the decay rate versus temperature for resonators with quality factors in the range of 10^2 to 10^5. Here I assume that the superposition has been prepared so that $\Delta y = 2\Delta y_{zp}$ for each case. Thus the resonant frequency does not factor into Eq. 2.3. However, the quality factor for each of the resonators has been chosen to roughly reflect what has been demonstrated experimentally with real nanomechanical resonators. Ideally, one would want to engineer a nanoresonator with both large Q_b and high frequency, say $Q_b \sim 10^5$ and $f_1 \sim 1$ GHz, so that the decay would occur over many cycles at 50 - 100 mK. From Fig. 2.2, for such a device at 50 mK, the decay time would be on the order of 10^3 cycles. In practice, achieving such a large quality factor and high resonant frequency might prove difficult. To date, the only published, doubly-clamped 1 GHz resonator demonstrated a quality factor of approximately 10^2 [36], which would yield one cycle over the decay time at 50 mK. On the other hand, a 10 MHz resonator with quality factor in excess of 10^5 has recently been demonstrated [48], which would yield ~ 10 coherent cycles at 50 mK.

Thermal Amplitude Flutuations

In this subsection I estimate the temperature below which thermal fluctuations in a resonator's amplitude become negligible with respect to the resonator's zero-point motion.

The amplitude of a resonator in contact with a thermal bath T_b is seen to undergo a "random-walk" with a variance approximated by [49]

$$\langle y_m^2 \rangle \approx \frac{k_B T_b}{M_m \omega_1^2} \left(1 - e^{-t/\tau}\right), \tag{2.4}$$

where $\tau = Q_b/\omega_1$ is the resonator's thermal-relaxation time and I have assumed that at time $t = 0$ that the amplitude is known precisely, *ie.* that $\langle y_m^2 \rangle = 0$. I note that the subscript 'm' is used for consistency with later portions of the thesis. It denotes the mean displacement of the neutral surface over the segment of the nanoresonator that couples to the SET detector, essentially the length of the SET island.

For times $t \gg \tau$, Eq. 2.4 reduces to the standard equipartition relationship. In this case, I expect thermal fluctuations of the amplitude to become small with respect to the resonator's zero-point fluctuations when [4]

$$\frac{k_B T_b}{M_m {\omega_1}^2} \leq (\Delta y_{zp})^2 \tag{2.5}$$

or

$$k_B T_b \leq \frac{\hbar \omega_1}{2}. \tag{2.6}$$

This is a rather strict condition, and nearly identical to the criteria for freeze-out.

On the other hand, for $t \ll \tau$, the fluctuations in the resonator's amplitude

are seen to increase linearly with t:

$$\langle y_m^2 \rangle \approx \frac{k_B T_b}{M_m {\omega_1}^2} \frac{t}{\tau}. \tag{2.7}$$

The condition for thermal fluctuations to be small with respect to ground-state uncertainty in position is then [4]

$$\frac{k_B T_b}{M_m \omega_1^2} \frac{t}{\tau} \leq \frac{\hbar}{2 M_m \omega_1} \tag{2.8}$$

or

$$T_b \leq \frac{\hbar Q_b}{2 k_B} \frac{1}{t}. \tag{2.9}$$

Clearly this is a less stringent requirement; and it implies that, if one could prepare an high-Q resonator in a well known position at time $t = 0$ and then make a measurement in a time t $\ll 1/\tau$, the exchange of energy between the resonator and the thermal bath would be a fraction t/τ smaller than $k_B T_b$. Strictly speaking, then, the temperature to which one would have to cool a particular resonator for thermal fluctuations to become negligible would be inversely proportional to how quickly one could make a measurement of the resonator's position and linearly proportional to the quality factor.

This is just an order-of-magnitude analysis, and it begs a couple of questions: can one specify the position of the resonator with $\langle {y_m}^2 \rangle = 0$? And, what is the effect of the detector on the resonator during the measurement process? These are questions that I address in the following section.

2.2 The Quantum Limit II: Ideal Detection

In this section I consider a second aspect of the quantum limit dealing with optimizing measurement precision. Ultimately, quantum mechanics places a limit on the precision with which certain information (*ie.* conjugate coordinates) can be extracted from the measurement of an object[1] ignore here, and throughout the thesis. This fundamental measurement limit is a direct result of the Heisenberg uncertainty relations for both the measured object's coordinates of interest (*eg.* $\hat{y}$ and $\hat{p}_y$ of an oscillator) and the measurement device's detection coordinates (*eg.* $\hat{I}$ and $\hat{V}$ of transistor). The purpose of this section, then, is to develop an understanding of such constraints in the context of the measurement of the displacement of a mechanical mode, and determine the conditions necessary to perform detection at this fundamental limit.

Initially, I consider the simple case of "quick", repeated measurements of an harmonic oscillator's position coordinate $\hat{y}$, and derive the so-called Standard Quantum Limit for position detection. I then discuss the case of continuous linear detection of a generic narrow band signal, and derive the corresponding quantum constraints on amplifier noise temperature. Finally, I use linear response theory to phrase the quantum constraints on position detection in terms of an amplifier's intrinsic noise characteristics. The result is thus a prescription which an amplifier must fulfill in order to operate as a quantum-limited position detector; and fur-

[1]Techniques (*eg.* squeezed states, QND measurement, and contractive states) have been proposed for beating the quantum limit (for example, see Refs. [2] [4] [5] [6] [17]). However, these advanced measurement strategies are beyond the scope of the research presented here.

thermore, a guage by which I can assess our experimental results (Chapter 6 and Chapter 7).

The Standard Quantum Limit

Following reference [2], I start with a crude derivation of the Standard Quantum Limit. Consider a mechanical mode undergoing simple harmonic motion with frequency ω_1. The hamiltonian for such a system is given by

$$H = \frac{p_y^2}{2M_m} + \frac{1}{2}M_m\omega_1^2 y_m^2, \tag{2.10}$$

where p_y and y_m are the conjugate momentum and displacement of the resonator and M_m is the effective mass for the motion of interest (See Appendix A). I note that, as in the previous section, y_m is used for consistency with later sections in which it denotes the average displacement of the neutral surface over the length of the SET detector.

The task at hand is to determine how precisely one can measure y_m by making two measurements such that the measurement time $\tau \ll 1/\omega_1$. For a classical resonator, in principle, there is no limit on how precisely one can measure y_m or p_y. However, for a quantum resonator, the resonator's position and momentum are described by the operators $\hat{y}_m$ and $\hat{p}_y$, which are constrained through the commutation relation [50]

$$[\hat{y}_m, \hat{p}_y] = i\hbar$$

to obey the Heisenberg uncertainty principle

$$\Delta y_m \Delta p_y \geq \frac{\hbar}{2}. \tag{2.11}$$

Simply put, the more precisely one specifies $\langle \hat{y}_m \rangle$, the less precisely one can know $\langle \hat{p}_y \rangle$. This is not really a concern for one quick measurement of $\langle \hat{y}_m \rangle$; in principle, it can be done with arbitrary precision. However, if one intends to make two or more measurements of $\langle \hat{y}_m \rangle$ with the highest precision possible, the effect of the measurement on $\hat{p}_y$, or the quantum mechanical back action, must be taken into account.

From Eq. 2.10, in the Heisenberg representation, the equations of motion for $\hat{y}_m$ and $\hat{p}_y$ are given by [51]

$$\hat{y}_m(t) = \hat{y}_m(0) \cos \omega_1 t + \frac{\hat{p}_y(0)}{M_m \omega_1} \sin \omega_1 t \tag{2.12}$$

and

$$\hat{p}_y(t) = -M_m \omega_1 \hat{y}_m(0) \sin \omega_1 t + \hat{p}_y(0) \cos \omega_1 t. \tag{2.13}$$

If the resonator is *not* in an energy eigenstate, then the expectation values $\langle \hat{y}_m(t) \rangle$ and $\langle \hat{p}_y(t) \rangle$ will be oscillatory functions of time with the respective variances given by [2]

$$(\Delta y_m(t))^2 = (\Delta y_m(0))^2 \cos^2 \omega_1 t + \left(\frac{\Delta p_y(0)}{M_m \omega_1} \right)^2 \sin^2 \omega_1 t \tag{2.14}$$

and

$$(\Delta p_y(t))^2 = (\Delta y_m(0) M_m \omega_1)^2 \sin^2 \omega_1 t + \Delta p_y(0)^2 \cos^2 \omega_1 t. \tag{2.15}$$

I see that if, at time t = 0, I make an initial measurement $\langle \hat{y}_m(0) \rangle$ with precision $\Delta y_m(0)$, the uncertainty in the resonator's position due to the initial measurement

at a time t later is

$$(\Delta y_m(t))^2 \geq (\Delta y_m(0))^2 \cos^2 \omega_1 t + \left(\frac{\hbar}{2M_m\omega_1}\right)^2 \sin^2 \omega_1 t, \tag{2.16}$$

where I have assumed that there is no correlation between the uncertainties in $\langle \hat{y}_m \rangle$ and $\langle \hat{p}_y \rangle$, only that the rms amplitudes are related through the uncertainty principle, Equation 2.11.

To minimize the uncertainty in position due to the initial measurement, it is clear that I must have

$$\Delta y_m(0) = \frac{\hbar}{\Delta y_m(0) 2M_m\omega_1} \tag{2.17}$$

or

$$\Delta y_m(0) = \sqrt{\frac{\hbar}{2M_m\omega_1}}. \tag{2.18}$$

This is known as the Standard Quantum Limit (SQL) for position detection [4] [2]. From Equation 2.16, for such a measurement, $\Delta y_m(t)$ is constant in time, implying a resonator state with phase-insensitive noise. One set of phase-insensitive states, with the additional stipulation that the equality in Eq. 2.16 be satisfied, is the set of coherent states [52]. Thus I can conclude this section by stating that, to minimize the error in each of two consectutive quick measurements of $\langle \hat{y}_m(t) \rangle$, it is necessary that the first measurement projects the resonator into a minimum uncertainty state.

The Ideal Linear Amplifier

While the analysis of the preceding section provides us with an idea of the role of the Heisenberg uncertainty principle in measurement, it is unsatisfactory

for at least two reasons. First, one is not always interested in simply making two consecutive quick measurements of a system. For example, the results presented in this thesis were obtained in the continuous measurement limit (*ie.* the limit in which the time interval between measurements becomes small with respect to the time scale of the dynamics of the measured system). Second, the analysis makes no reference to a measuring device, relying only upon the uncertainty relation for the measured oscillator, or, essentially, its wave nature. Which begs the question: what is the role of the detector?

In this section, I paraphrase a work of Carleton Caves [3] and derive the quantum measurement limit for the case of a quantum signal continuously measured by a linear quantum amplifier. It is seen that such a detection scheme necessarily adds a minimum of one-half of a quanta of noise to the measured signal. As this minimum is imposed only by the assumptions of linearity and the appropriate commutation relations invoked by unitarity, the limit is known as the ideal linear amplifier limit, and such an amplifier is referred to as an ideal linear amplifier.

In Cave's model [3], the input signal and the amplifier are represented by Bosonic modes with noise power per unit bandwidth per mode given in terms of the number quanta $\hat{N}_a=\hat{a}_\beta\hat{a}^\dagger_\beta$ and $N_b=\hat{b}_\alpha\hat{b}^\dagger_\alpha$ respectively. Here $\hat{a}_\beta$, $\hat{a}^\dagger_\beta$ and $\hat{b}_\alpha$,$\hat{b}^\dagger_\alpha$ are annihilation and creation operators for the respective modes of the oscillator and detector, and obey the commuation relations

$$\left[\hat{a}_\alpha, \hat{a}^\dagger_\beta\right] = \delta^\beta_\alpha, \quad \left[\hat{b}_\alpha, \hat{b}^\dagger_\beta\right] = \delta^\beta_\alpha \tag{2.19}$$

and

$$[\hat{a}_\alpha, \hat{a}_\beta] = 0, \quad \left[\hat{b}_\alpha, \hat{b}_\beta\right] = 0. \tag{2.20}$$

The analysis proceeds in the Heisenberg representation where it is assumed that the evolution of the output (detector) operators can be expressed as a linear superposition of the input (oscillator) modes [3]:

$$\hat{b}_\alpha = \sum_\beta \left(M_{\alpha\beta}\hat{a}_\beta + L_{\alpha\beta}\hat{a}_\beta^\dagger \right) + \hat{F}_\alpha \tag{2.21}$$

and

$$\hat{b}_\alpha^\dagger = \sum_\beta \left(\hat{a}_\beta^\dagger M_{\alpha\beta}^\dagger + \hat{a}_\beta L_{\alpha\beta}^\dagger \right) + \hat{F}_\alpha^\dagger, \tag{2.22}$$

where $M_{\alpha\beta}$ and $L_{\alpha\beta}$ are matrices related to the amplifier's gain and $\hat{F}_\alpha$ is an operator representing the amplifier's noise contribution, which is assumed to be random in time with a Gaussian distribution.

It is further assumed that $\hat{F}$ depends only on the internal modes, or the internal state, of the amplifier and thus commutes with the input mode operators. It turns out that this assumption has rather important consequences, which I will discuss in the end. For a less ideal amplifier $M_{\alpha\beta}$ and $L_{\alpha\beta}$ would be replaced by operators to account for any time dependence in the gain (*ie.* gain fluctuations).

Next several assumptions are made. First, the analysis is restricted to the case of single mode detection[2] so that Eqs. 2.21 and 2.22 simplify to

$$\hat{b} = \left(M\hat{a} + L\hat{a}^\dagger \right) + \hat{F} \tag{2.23}$$

[2]I note that Caves also treats the more general multi-mode case. The purpose of this section, however, is to give a brief demonstration of how the quantum limit arises in the context of continous measurement. For this purpose, presentation of the single-mode analysis is sufficient.

and

$$\hat{b}^\dagger = \left(\hat{a}^\dagger M^\dagger + \hat{a} L^\dagger\right) + \hat{F}^\dagger. \tag{2.24}$$

Second, it is assumed that the amplifier is phase-conjugating, *ie.* that a phase-shift in the input signal generates the opposite sign phase-shift in the output signal. That is, if

$$\hat{a}' = \hat{a} e^{-i\phi},$$

then

$$\hat{b}' - \hat{F} = \hat{b} e^{i\phi} - \hat{F},$$

This requires that $M = 0$. Thus I am left with

$$\hat{b} = \hat{a}^\dagger L + \hat{F} \tag{2.25}$$

and

$$\hat{b}^\dagger = L^\dagger \hat{a} + \hat{F}^\dagger. \tag{2.26}$$

This assumption is made arbitrarily. I could have just as easily assumed phase-preseving. In the end, Caves demonstrates that for large gain amplifiers, the ultimate limit is the same.

Finally, it is assumed that the amplifier noise is phase-sensitive. That is, the amplifier's rms noise contribution is split unequally between the input signal's quadratures. Thus one must break up the input and output signals into their respective quadratures:

$$\hat{a} = \hat{X}_1 + i\hat{X}_2 \tag{2.27}$$

and

$$\hat{b} = \hat{b}_1 + i\hat{b}_2, \tag{2.28}$$

where

$$\hat{b}_1 = L\hat{X}_1 + \hat{F}_1 \quad \hat{b}_2 = L\hat{X}_2 + \hat{F}_2, \tag{2.29}$$

where $\hat{F}$=$\hat{F}_1$+i$\hat{F}_2$. To recover the phase-insensitive amplifier, simply set $F_1 = F_2$.

With these assumptions, one can now express the total output noise for each quadrature as [3]

$$(\Delta b_1)^2 = |L|^2(\Delta X_1)^2 + (\Delta F_1)^2, \tag{2.30}$$

$$(\Delta b_2)^2 = |L|^2(\Delta X_2)^2 + (\Delta F_2)^2, \tag{2.31}$$

where ΔX_1 (ΔX_2) and ΔF_1 (ΔF_2) are the signal and detector rms noise contributions to the quadratures respectively.

The amplifier contribution referred to the input for each quadrature is thus [3]

$$A_1 = \frac{(\Delta F_1)^2}{|L|^2}, \tag{2.32}$$

$$A_2 = \frac{(\Delta F_2)^2}{|L|^2}, \tag{2.33}$$

where $|L|^2$ plays the role of the amplifier's power gain in number of quanta.

Using the Schwartz inequality [3],

$$\Delta F_1 \Delta F_2 \geq \frac{1}{2}|\langle\left[\hat{F}_1, \hat{F}_2\right]\rangle|, \tag{2.34}$$

and the relation

$$\left[\hat{F}, \hat{F}^\dagger\right] = -2i\left[\hat{F}_1, \hat{F}_2\right], \tag{2.35}$$

one arrives at the uncertainty relation for a phase-sensitive linear amplifier [3]

$$A_1 A_2 \geq \frac{1}{16}|\langle[\hat{F}, \hat{F}^\dagger]\rangle|^2, \tag{2.36}$$

and the total amplifier noise contribution

$$A = A_1 + A_2 \geq \frac{1}{2}|\langle[\hat{F}, \hat{F}^\dagger]\rangle|. \tag{2.37}$$

As they stand, Eqs. 2.36 and 2.37 are not very illuminating. However, from the commutation relation for $\hat{b}$, Eq. 2.20, one finds [3]

$$[\hat{F}, \hat{F}^\dagger] = 1 + |L|^2. \tag{2.38}$$

Thus

$$\sqrt{A_1 A_2} \geq \frac{1}{4}(1 + |L|^{-2}), \tag{2.39}$$

and

$$A \geq \frac{1}{2}(1 + |L|^{-2}). \tag{2.40}$$

For large gain, $|L|^2 \gg 1$, Eqs. 2.39 and 2.40 tell us two things: noise in one quadrature can only be reduced at the expense of signal-to-noise degradation in the other quadrature [3]; and the absolute minimum total noise power per unit bandwidth that an amplifier can add to a narrow band signal is one-half quanta [3].

Using Eqs. 2.30, 2.31, 2.32, 2.33, and 2.37, one can re-express the total output noise as

$$\Delta b^2 = |L|^2 \left(\Delta X^2 + A \right). \tag{2.41}$$

If the signal contributes one-half quanta of noise, *ie.* $\Delta X^2 = \frac{1}{2}$, then

$$\Delta b^2 = |L|^2 \left(\frac{1}{2} + A \right). \tag{2.42}$$

From Eq. 2.40, this then yields

$$|\Delta b|^2 \geq \frac{1}{2}|L|^2 + \frac{1}{2}(1 + |L|^2) = |L|^2 + \frac{1}{2}, \tag{2.43}$$

which simply states that, for large gain, the minimum total noise at the output of an ideal amplifier is composed of two parts: one-half quanta contributed by the internal amplifier modes, and one-half quanta contributed by the input mode; both of which are amplified by $|L|^2$ [3]. The fact that the two noise sources add in quadrature is a consequence of the assumption that the internal states of the amplifier and the initial input signal state are independent. As a result, their fluctuations are uncorrelated.

Finally, Caves defines the noise temperature, T_{QL}, of the ideal linear amplifier by assuming that the total input noise is given by the Planck distribution (plus the zero-point energy),

$$|\Delta a|^2 = \frac{1}{2} \coth \left(\frac{\hbar \omega_1}{2 k_B T_b} \right), \tag{2.44}$$

and asking: by how much would one have to increase T_b to observe $|\Delta b|^2$ at the output of the amplifier? In the limit of large gain, after working through the algebra,

Caves finds:

$$T_{QL} = \frac{\hbar\omega_1}{k_B \ln(3)}, \tag{2.45}$$

if T_b =0; and

$$T_{QL} = \frac{\hbar\omega_1}{2k_B}, \tag{2.46}$$

if $k_B T_b \gg \hbar\omega_1$.

This minimum is imposed only by the assumptions of linearity and the appropriate commutation relations invoked by unitarity, and is known as the ideal linear amplifier limit. An amplifier that meets this condition is referred to as an ideal linear amplifier.

In the low-T_b limit, then, the resulting minimum position sensitivity is

$$\Delta y_{QL} = \sqrt{\frac{T_{QL} k_B}{K_m}} = \sqrt{\frac{\hbar}{ln(3) M_m \omega_1}}, \tag{2.47}$$

which is greater than the standard quantum limit, Equation 2.18:

$$\Delta y_{QL} = \sqrt{\frac{2}{\ln(3)}} \Delta y_{SQL}. \tag{2.48}$$

Quantum-Limited Position Detection

In the previous sections it was demonstrated that quantum mechanics places a limit on the minimum rms uncertainty in the knowledge of a resonator's position; it was also shown that quantum mechanics requires that there be an additional minimum noise contribution from the amplifier itself.[3] However, the discussion up until this point has been rather abstract; it is not obvious how to extend the formalism or the results to a solid-state position amplifier such as the SET.

[3]I implicitly mean an amplifier with linear, time-indepedent coupling to the resonator's position.

In this section, I present and discuss the results of Aashish Clerk's linear response approach to quantum-limited position detection [16]. This approach arrives at the same conclusion as Cave's Bosonic-mode model, with the advantage of phrasing the quantum constraints on continuous linear amplification in terms of an amplifier's intrinsic noise properties.

Clerk considers a resonator with conjugate momentum, $\hat{p}_y$, and displacement, $\hat{y}_m$, and an amplifier with input and output characterized by the hermitian operators $\hat{F}$ and $\hat{I}$ respectively.

He further assumes that the resonator is coupled to both an equilibrium bath with temperature T_b and to the amplifier via the interaction

$$H_{int} = -A\hat{F} \cdot \hat{y}_m, \tag{2.49}$$

where A sets the strength of the interaction and $\hat{F}$ can be thought of as the interaction force or equivalently the back action of the amplifier on the resonator.

The analysis is restricted to the case of weak coupling ($H_{int} \to 0$) the relevant parameter regime for our experiments (see Section 2.3). There are two consequences of this. First, the response of the output of the amplifier $\langle \hat{I} \rangle$ to a small change $\langle \hat{y}_m \rangle$ can be determined using linear response theory [53]. From Liouville's theorem, to first-order in H_{int}, Clerk finds that the amplifier's output response is given by

$$\langle \Delta \hat{I}(t) \rangle = Tr(\hat{I} \Delta\rho(t)) = A \int_{-\infty}^{\infty} dt' \lambda(t - t') \langle \hat{y}_m(t) \rangle, \tag{2.50}$$

where $\Delta\rho(t)$ is the first-order density matrix term in the iterative solution of the Liouville equation.

The admittance or amplifier gain, λ, is given by [16]

$$\lambda(t-t') = \frac{1}{i\hbar}\Theta(t-t')\langle\left[\hat{I}(t), \hat{F}(t')\right]\rangle; \tag{2.51}$$

and the expansion is done about the amplifier's zero-coupling configuration.

The second consequence of the weak-coupling assumption is that the equation of motion for $\langle\hat{y}_m(t)\rangle$ reduces to a "Langevin-like" expression. Specifically, Clerk finds that

$$M_m\frac{\partial^2\langle\hat{y}_m(t)\rangle}{\partial t^2} = -M_m{\omega_1}^2\langle\hat{y}_m(t)\rangle - \gamma_b\frac{\partial\langle\hat{y}_m(t)\rangle}{\partial t} - \tag{2.52}$$

$$- A^2\int dt'\gamma(t-t')\frac{\partial\langle\hat{y}_m(t')\rangle}{\partial t'} + F_b(t) + A\cdot F(t), \tag{2.53}$$

where γ_b and F_b describe the damping and fluctuating forces provided by the bath respectively and are related through the fluctuation-dissipation theorem:

$$\bar{S}_{F_b} = \gamma_{bath}\hbar\omega\coth\left(\frac{\hbar\omega}{k_bT_b}\right). \tag{2.54}$$

The detector's influence is manifest in the damping term $\gamma(t-t')$ and the back action force $F(t)$. In the limit where the resonator's frequency is small with respect to the intrinsic time-scale of the amplifier, Clerk demonstrates that the detector-induced damping and back action force are related in a manner simliar to the fluctuation-dissipation theorem:

$$2k_BT_d = \frac{\bar{S}_F}{\gamma}. \tag{2.55}$$

Here,

$$\bar{S}_F = \lim_{\omega \to 0} \frac{S_F(\omega) + S_F(-\omega)}{2} \tag{2.56}$$

and

$$\gamma = \lim_{\omega \to 0} \frac{S_F(\omega) - S_F(-\omega)}{2\hbar\omega}, \tag{2.57}$$

where,

$$S_F(\pm\omega) = \int_{-\infty}^{\infty} dt \langle \hat{F}(t)\hat{F}(0)\rangle e^{\pm i\omega t} \tag{2.58}$$

are the positive and negative frequency components of the amplifier's back action noise spectral density, with (+) referring to energy transfer from the resonator to the amplifier, and (-) referring to energy transfer from the amplifier to the resonator. See reference [54] for a nice explanation of positive and negative frequencies in quantum noise.

Classically, $\langle F(t)F(0)\rangle = \langle F(0)F(t)\rangle$, so that $S_F(\omega) = S_F(-\omega)$. However, this is not generally true for a quantum mechanical system, *ie.* $\left[\hat{F}(t), \hat{F}(0)\right] \neq 0$ [54] . It is convenient then to use the relation

$$\hat{F}(t)\hat{F}(0) = \frac{1}{2}\left(\left\{\hat{F}(t), \hat{F}(0)\right\} + \left[\hat{F}(t), \hat{F}(0)\right]\right)$$

to break-up Eq. 2.58 into two components: a real component representing the total force spectral density experienced by the resonator due to the amplifier's back action noise (Eq. 2.56); and an imaginary component representing the energy-loss rate of the resonator due to the interaction with the amplifier, or detector-induced damping (Eq. 2.57). With these definitions, the effective amplifier temperature T_d is thus interpreted as gauging the asymmetry between the amplifier's positive and negative frequency back action noise.

For the case of normal-state SET's and tunnel-junctions, it has been found that T_d is positive and propotional to the average energy lost by an electron as it traverses the device's junctions [55] [56] [57]. On the other hand, due to the myriad tunnelling processes, the case of the superconducting SET (SSET) is much more complicated [58] [59] [60]. For example, both positive and negative effective temperature and dissipation are possible when the SSET is biased near the single and double Cooper-pair resonances (see Appendix B for brief discussion of the SSET); the "direction" of the exchange of energy depending on whether energy needs to be removed or added for the resonant tunneling of Cooper-pairs to occur .

Regardless of whether T_d is positive or negative, the total effective temperature, T_e, of the resonator is given by the sum of T_d and T_b, weighted by the respective coupling to each reservoir [16] [55]:

$$T_e = \frac{1}{\gamma_e}\left(\gamma_b T_b + \gamma_d T_d\right), \tag{2.59}$$

where

$$\gamma_e = \gamma_b + \gamma_d = \frac{M_m \omega_1}{Q_e}, \tag{2.60}$$

$$\gamma_d = A^2 \gamma, \tag{2.61}$$

and Q_e is the effective quality factor of the resonator due to damping induced from both the detector and the environment.

From the above definitions, and Eqs. 2.54 and 2.55, Clerk expresses the spectral density of the resonator's motion as

$$\bar{S}_y(\omega) = \frac{\bar{S}_{F_b}(\omega) + A^2\bar{S}_F(\omega)}{\left|M_m\left(\omega^2 - {\omega_1}^2 + i\omega\omega_1/Q_e\right)\right|^2} =$$

$$= |g(\omega)|^2\left(\bar{S}_{F_b}(\omega) + A^2\bar{S}_F(\omega)\right). \tag{2.62}$$

Using Eqs. 2.51 and 2.62, the total noise-power density at the output of the detector is thus

$$\bar{S}_{I,tot}(\omega) = \bar{S}_I(\omega) + A^2|\lambda(\omega)|^2\bar{S}_y(\omega) - 2A^2\mathrm{Re}\left[\lambda(\omega)^* g^*(\omega)\bar{S}_{IF}\right], \tag{2.63}$$

where $\bar{S}_I(\omega)$ is the symmetrized spectral density of the amplifier's forward coupling noise, $\bar{S}_{IF}(\omega)$ is the symmetrized spectral density of the cross-correlations between forward and back-acting noise sources.

Finally, Clerk shows that Eq. 2.63 can be converted into an equivalent displacement noise density, referred to the input of the amplifier:

$$S_{y,tot}(\omega) = \frac{\bar{S}_I(\omega)}{|\lambda(\omega)|^2A^2} + A^2|g(\omega)|^2\bar{S}_F(\omega) - \frac{2\mathrm{Re}\left[\lambda^*(\omega)g^*(\omega)\bar{S}_{IF}(\omega)\right]}{|\lambda(\omega)|^2} +$$

$$+|g(\omega)|^2\bar{S}_{F,b}(\omega). \tag{2.64}$$

The first three terms represent the amplifier's contribution to the total displacement noise; whereas the last term represents resonator fluctuations due strictly to the equilibrium bath.

Minimization of Eq. 2.64 is a rather involved process, requiring the optimization of the noise sources $\bar{S}_I(\omega)$, $\bar{S}_F(\omega)$, and $\bar{S}_{IF}(\omega)$ and the coupling A. However,

Clerk imposes two important constraints that allow for the determination of a minimum on resonance, ω=ω_1.

First, $\bar{S}_I(\omega)$ and $\bar{S}_F(\omega)$ are constrained by the amplifier uncertainty principle:

$$\bar{S}_I(\omega)\bar{S}_F(\omega) \geq \frac{\hbar^2}{4}(\mathrm{Re}\left[\lambda(\omega)\right])^2 + \left(\mathrm{Re}\left[\bar{S}_{IF}(\omega)\right]\right)^2 \tag{2.65}$$

with the equality fulfilled for the case of a quantum-limited amplifier.

Strictly speaking, Eq. 2.65 states that in the presence of gain, even an ideal or quantum-limited amplifier must add a minimal amount of back-acting and forward-coupling gain. An alternative interpretation of the equality in Equation 2.65 is that no signal information is lost in the process of measurement [61]. One can see this by recognizing that the rate at which information is attained from the output of the detector, Γ_{meas}, is inversely proportional to $\bar{S}_I(\omega)$ (*ie.* the smaller $\bar{S}_I(\omega)$, the better the signal-to-noise, and the less time for which one needs to integrate); whereas, the rate at which information "enters" the detector, Γ_ϕ, is proportional to the interaction S_F. At the quantum-limit, Clerk et al. demonstrated that $\Gamma_{meas} = \Gamma_\phi$, implying a tight coupling between the amplifier input and output degrees of freedom. In a sub-ideal amplifier, $\Gamma_\phi > \Gamma_{meas}$, implying that some information about the input signal is lost to internal degrees of freedom which do not influence the amplifier's output.

Second, Clerk demands that the total power available at the output of the amplifier be much greater than the total power delivered from the amplifier to the resonator. He shows that, for a quantum-limited amplifier, this is equivalent to

requiring that

$$\frac{k_B T_d}{\hbar\omega_1} \gg 1. \tag{2.66}$$

With these two constraints, the requisite conditions for minimization can be stated. First, it is necessary that the amplifier noise terms satisfy the equality in Equation 2.65. That is, the amplifier must be quantum-limited.

Second, the symmetrized cross-correlation term $\bar{S}_{IF}(\omega)$ must vanish, minimizing the product $\bar{S}_I(\omega)\bar{S}_F(\omega)$.

Third, the back action and forward-coupling must contribute equally to the total displacement noise. This requirement falls out of the optimization of the coupling A,

$$A_{opt} = \sqrt{\frac{\bar{S}_I(\omega)}{|\lambda(\omega)g(\omega)|^2 \bar{S}_F(\omega)}}, \tag{2.67}$$

and can be thought of as being analagous to noise impedance matching for optimization of signal-to-noise.

A consequence of this third condition is that the detector-induced damping, γ_d, must be small with respect to γ_{bath} to ensure that the resonator is more tightly coupled to T_b than T_d (a consequence of the second constraint and Eq. 2.59). Explicitly, Clerk shows that the third condition implies

$$\frac{{A_{opt}}^2\gamma}{\gamma_b + {A_{opt}}^2\gamma} = \frac{\hbar\omega_1}{4k_B T_d}, \tag{2.68}$$

which is necessarily much less than one due to the assumptions I have made.

If all three conditions are satisfied, Clerk shows, then, that an amplifier must contribute at least the equivalent of the resonator's zero-point contribution to the measured signal. From Eqs. 2.68 and 2.59, it is evident that half of the contribution

is in the form of back action or heating of the resonator:

$$T_e = \frac{{A_{opt}}^2 \gamma T_d + \gamma_b T_b}{{A_{opt}}^2 \gamma + \gamma_b} = \frac{\hbar\omega_1}{4k_B} + T_b, \tag{2.69}$$

as one would expect, having optimized with respect to the coupling A. The other half of the amplifier contribution is necessarily forward-coupling noise. Thus, the noise temperature of a such an optimized detector is

$$T_{QL} = \frac{\hbar\omega_1}{2k_B}. \tag{2.70}$$

Essentially, this is the same result derived in the previous section: an amplifier must add at least one-half quanta of noise power per unit bandwidth to the measured signal. However, the advantage of the present approach is that it provides a prescription (*ie.* the three conditions listed above) which an amplifier must fulfill in order for quantum-limited displacement detection to be possible. Additionally, the effect of the amplifier's back action on the resonator is explicitly manifest as heating of the resonator by one-half its zero-point energy.

2.3 Nanomechanical RFSET Displacement Detection

With the development of the RFSET [41] [62] [63], came the suggestion that, it could be implemented as a nearly quantum-limited nanomechanical displacement transducer [12] [13]. The realization was spurred by a combination of factors. For one, theoretical treatments of the SET suggested that the electrometer could achieve near-ideal noise characteristics required for quantum measurement schemes [43] [42] [64]. Secondly, the RFSET had been demonstrated to be capable of operating with

over 100 MHz bandwidth [41], a pre-requisite for the read-out of the high frequency nanoresonators thought to be necessary to demonstrate freeze-out. And third, the similarities in size-scale and fabrication between SETs and nanoresonators suggested that sub-micron positioning of the devices and, hence, tight coupling should be possible.

In this section I first review the basic idea behind nanomechanical RFSET displacement detection. I then review the theoretical work on the noise characteristics of the SET and apply the results of the previous section to discuss the ultimate limits of the detection scheme.

The RFSET Displacement Detector

In essence, the RFSET displacement detector is a capacitive microphone: mechanical fluctuations are converted into an electrical signal via the capacitive modulation of an SET's differential resistance; the differential resistance of the SET is then read-out using microwave reflectometry. A generic circuit schematic for the transduction process and an SEM micrograph of an RFSET displacement detector are displayed in Fig. 2.3.

By application of a large DC bias, V_{NR}, between the nanoresonator and the SET island, mechanical displacement of the resonator, y_m, results in modulation of the polarization charge on the SET island through the relation

$$\Delta Q_{NR} = \frac{\partial C_{NR}}{\partial y_m} V_{NR} y_m \approx b \frac{C_{NR} V_{NR}}{d_{NR}} y_m, \tag{2.71}$$

where C_{NR} and d_{NR} are the capacitive-coupling and spatial separation between the

(a)

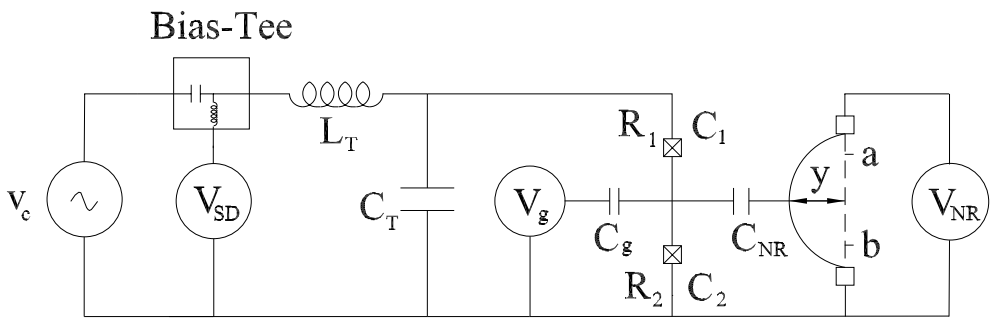

(b)

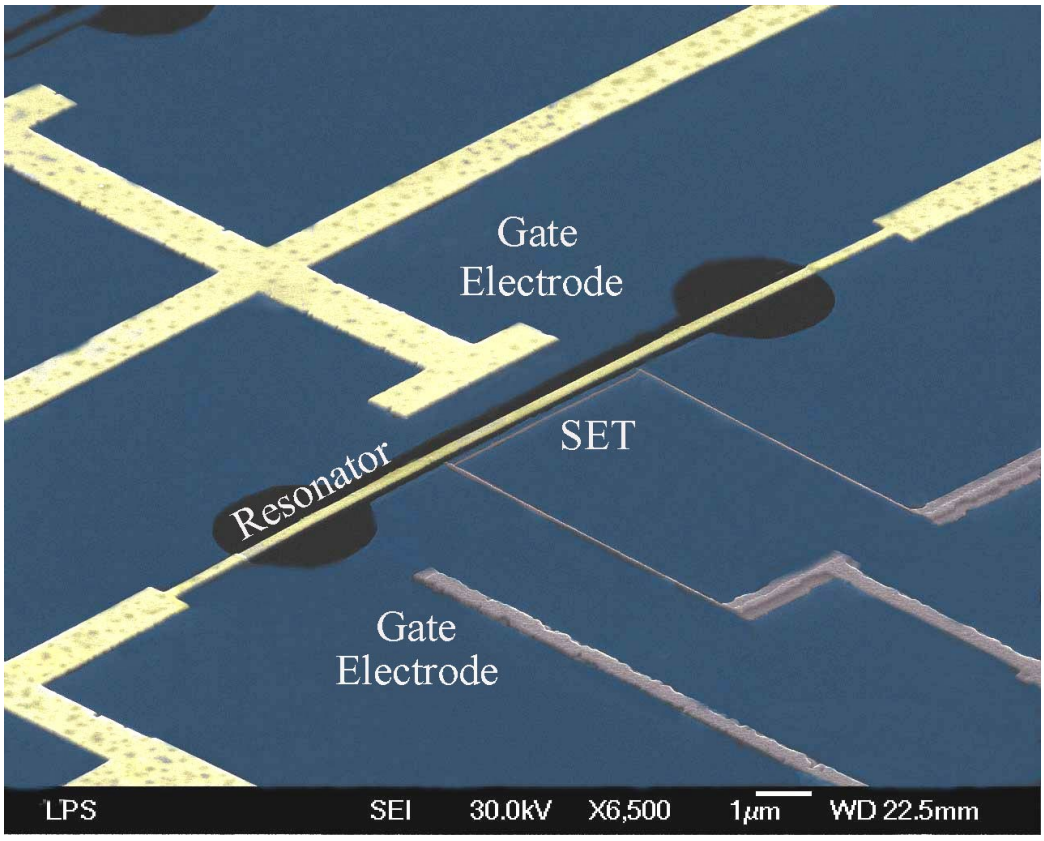

Figure 2.3: (a) Circuit schematic and (b) SEM image of the RFSET displacement detector

resonator and the SET island respectively. In principle, C_{NR} can be found to high precision from measurements of the SET conductance versus V_{NR} (see Appendix B). However, the derivative of C_{NR} with respect to y_m must be calculated numerically. Thus, in the last step in Eq. 2.71, I have used a capacitance extraction program [65] and found, for typical device parameters, that $\partial C_{NR}/\partial y_m \approx bC_{NR}/d_{NR}$ where b is of order unity.

In Fig. 2.3(a), y is the in-plane displacement of the mid-point of the neutral surface (solid line) from the equilibrium position (dashed line). The quantity y_m is defined as the average displacement of the neutral surface over the region a to b, the length of the SET island (the relationship between y_m and y is calculated in Appendix A). It is straight-forward to show that the resonator's fundamental mode couples most strongly to the SET island (*ie.* both $y_{n,m}$ and $\partial C_{NR}/\partial y_{n,m}$ decrease with increasing number, n, of resonator nodes). For the remainder of the thesis, I will assume that y_m represents the average displacement of resonator's fundamental in-plane mode over the length of the SET island.

It should also be noted that, in Fig. 2.3(b), the resonator's displacement, the lengths of the SET island and the resonator, and the separation between the resonator and SET are not drawn to scale. For our samples the resonator's displacement is about $10^{-6} \times d_{NR}$, the length of the SET island is about 0.33 - 0.5 times the length of the resonator, and d_{NR} is typically about 0.02 - 0.05 times the length of the resonator.

The modulation of the SET-island charge by ΔQ_{NR} results in the modulation of the SET's differential resistance, R_S. For a normal-state SET, biased at

the edge of the Coulomb blockade, the relationship between Q_{NR} and R_S can be approximated by (see Chapter 5 and Appendix B)[4]

$$R_S \approx \frac{V_{SD}}{I_{SD}} \approx \frac{2R_\Sigma}{\sin(\pi Q_{NR}/e)+1}, \tag{2.72}$$

where V_{SD} and I_{SD} are the source-drain voltage bias and current respectively.

For small displacement and, hence, small charge modulation, $\Delta Q_{NR} \ll e$, the maximum modulation of R_S is given by

$$\Delta R_S \approx -2\pi R_\Sigma \frac{\Delta Q_{NR}}{e} \approx -b\frac{2\pi R_\Sigma C_{NR} V_{NR}}{e d_{NR}} y_m, \tag{2.73}$$

where R_Σ is the SET's differential resistance at large source-drain bias V_{SD} and e is the magnitude of the electron charge.

The modulated differential resistance ΔR_S is measured by applying a microwave signal $v_c(t)$ to the SET drain and measuring the modulation in the reflected-signal (sideband microwave reflectometry is discussed in Chapter 5). Because $R_S \gg Z_o$, where Z_o is the characteristic transmission line impedance of 50 Ω, an LC circuit is inserted in series with the SET for impedance matching. Ideally, the values of L_T and C_T are chosen so that, at the carrier frequency $\omega_T = 1/\sqrt{L_T C_T}$, the impedance of the $L_T C_T R_S$ circuit is

$$Z_{LCR} = \frac{L_T}{R_S C_T} = Z_o. \tag{2.74}$$

[4] As is discussed in Chapter 5 for both normal-state and superconducting-state SET's no analytic expression for the differential resistance for an arbitray bias point is known. One must either solve the SET master equation numerically or use a measured IV curve and take the numerical derivative to find the relationship between ΔQ_{NR} and ΔR_S.

Equivalently, this can be seen as transforming the transmission line impedance so that $Q_T^2 Z_o = R_S$ where $Q_T = \omega_T L_T / Z_o$ is the external quality factor.

The resulting modulation of the reflected-signal $\Delta v_r(t)$ is well approximated by linearizing it with respect to $\Delta R_S(t)$ [66], so that, on resonance ω_T,

$$\Delta v_r(t) \approx v_c(t) \Delta\Gamma(t), \tag{2.75}$$

where

$$\Delta\Gamma(t) \approx -b \frac{Q_T^2 Z_o C_{NR} V_{NR}}{R_\Sigma} \frac{\pi}{\sqrt{2} e d_{NR}} y_m(t) \tag{2.76}$$

at a bias-point of maximum Q_{NR}-response (see Chapter 5 for details).

As stated, in Eq. 2.76, I have assumed that the reflected-signal frequency is at the tank-circuit resonance, ω_T, so that the $Z_{LRC} = L_T / R_S C_T$. Typically, the carrier frequency is tuned to ω_T. However, $y_m(t)$ might be modulated at, say, 5 MHz. The reflected signal will then have sidebands at $\omega_T \pm (2\pi * 5MHz)$. The magnitude of the sidebands will depend on the half-width of the $L_T C_T$ resonance. This is determined by loading from both Z_o and R_S:

$$\Delta f = \frac{\omega_T}{4\pi Q} \tag{2.77}$$

where

$$\frac{1}{Q} = \frac{1}{Q_T} + \frac{1}{Q_S} = \frac{Z_o}{\omega_T L_T} + \frac{\omega_T L_T}{R_S}. \tag{2.78}$$

Δf is essentially the bandwidth of the RFSET. For optimal matching, it reduces to

$$\Delta f = \frac{\omega_T}{2\pi Q_T}. \tag{2.79}$$

In practice, the desired bandwidth, along with the matching-condition, sets the choice of the tank-circuit inductor and capacitor values.

The role of the tank circuit is clear from Eq. 2.76: near resonance, it effectively serves to amplify the modulation of the reflected-signal by Q_T^2. Without the tank-circuit $\Delta\Gamma \propto Z_o/R_S \sim 10^{-3}$, and thus

$$\Delta v_r \approx -10^{-3}\frac{b\pi}{\sqrt{2}}\frac{C_{NR}V_{NR}}{e}\frac{y_m}{d_{NR}}v_c. \tag{2.80}$$

On the otherhand, with the tank circuit, and for optimal matching, $Q_T^2 Z_o = R_S$, I have

$$\Delta v_r \approx -\frac{b\pi}{\sqrt{2}}\frac{C_{NR}V_{NR}}{e}\frac{y_m}{d_{NR}}v_c. \tag{2.81}$$

Finally, I close this subsection with some remarks about optimizing the reflected-signal modulation response. First, it is obvious that maximizing the reflected-signal response requires optimizing the impedance matching. However, it also requires optimizing v_c and the coupling $C_{NR}V_{NR}/d_{NR}$. The optimal carrier amplitude depends on the bias-point, tank-circuit quality-factor Q [66] [67], as well as whether the SET is superconducting or normal. In practice, it is simplest to determine the optimal value by tuning the amplitude manually and looking for the maximum response. The optimization of the coupling is more subtle. This is because I am not simply interested in maximizing the SET reponse to fluctuations in position of a nearby resonator. I am primarily interested in optimizing the SET displacement sensitivity, which, because of the SET back action, is a separate issue. In the following section, then, I consider the intrinsic SET noise, address the issue of optimal coupling $C_{NR}V_{NR}/d_{NR}$, and present the predictions for the ultimate limit to RFSET position sensitivity.

The Ultimate Limit

For simplicity, I develop the ultimate limit of RFSET displacement detection by considering the intrinsic noise of a normal-state DCSET. At the end of the section, I briefly address the much more complex intrinsic noise limits of the superconducting SET (SSET). Also, I assume that the difference in position sensitivity between the dc and rf modes of operation can be accounted for by applying the predicted reduction factor of 1.4 - 1.9 for the RFSET's optimal intrinsic sensitivity [67]. The authors in Reference [67] state that the degradation of ultimate sensitivity in the rf mode compared to the dc mode is simply a result of the increased bandwidth of the rf mode.

I assume that the orthodox theory (see Reference [68] and Appendix B) is applicable, and thus neglect the effects of co-tunneling [69]. Additionally, I assume that $k_B T_b \ll E_c$, and neglect any thermal contributions to SET tunneling. Finally, I assume that the frequency range of interest is above the 1/f noise tail, $\sim$ 10 kHz, and below the intrinsic SET tunneling rate, $(R_\Sigma C_\Sigma)^{-1} \sim$ 1 - 100 GHz.

In the relevant limits, the intrinsic noise of the SET is due to two white sources [43] [42]: the shot noise in the source-drain current I_{SD}; and fluctuations in the SET-island potential, ϕ. The origins of both sources arise from the stochastic nature of electron tunneling events, of which I_{SD} is composed (see Appendix B).

First, consider the shot noise. From the Orthodox Model, if one could insert an ammeter at each of the SET junctions, the tunneling-events would appear as delta-function peaks, separated in time according to a correlated-Poisson distri-

bution. The correlations arise from the fact that the probabilities for successive tunneling events are not independent but related through the accompanying change in the SET's free-energy. To calculate the spectral density of the current fluctuations, one must solve the SET master equation and calculate the auto-correlation function, taking into account all the relevant tunneling processes. However, near the Coulomb-blockade threshold (the sequential tunneling regime), an approximate analytic expression for the shot noise spectral density exists[5], and is given by [43]

$$S_{II}(\omega) = \eta_I 2eI_{SD}, \tag{2.82}$$

where

$$\eta_I = \frac{\Gamma_1^2 + \Gamma_2^2}{(\Gamma_1 + \Gamma_2)^2}. \tag{2.83}$$

Here η_I accounts for the correlations between tunneling events, and Γ_1 and Γ_2 are the tunneling rates through junctions 1 and 2 respectively. It is $S_{II}(\omega)$ that ultimately sets the limit of the SET charge sensitivity,

$$S_{Q_{NR}}(\omega) = S_{II}(\omega)\left(\frac{\partial I_{SD}}{\partial Q_{NR}}\right)^{-2}. \tag{2.84}$$

In terms of the SET parameters, for symmetric junctions, this is expressed as [42]

$$S_{Q_{NR}}(\omega) \simeq \frac{(1-\alpha^2)(1+\alpha^2)}{8\alpha^2} eV_{SD}R_\Sigma C_\Sigma^2, \tag{2.85}$$

where

$$\alpha = \frac{(2C_{NR}V_{NR} - e)}{C_\Sigma V_{SD}}. \tag{2.86}$$

[5]From the initial assumptions, this is a classical analysis of the amplifier's noise sources, and, thus, it follows that there is no need to symmetrize the sources as in Section 2.2.

Here, the parameter α specifies I_{SD} and the set of (V_{NR}, V_{SD}) bias points which yield that particular value of current. The expresion above is valid provided that one restrict the bias-points to non-degeneracy points, $0 < \alpha < 1$ - $R_Q/\pi R_\Sigma$, where R_Q is the quantum of resistance. The expression requires that $V_{SD} < e/C_\Sigma$ so that only two charge states are involved in the tunneling process.

Next, I consider the SET-island potential fluctuations. If one could connect a voltmeter to the SET island, the potential, ϕ, would be seen to decrease (increase) by e/C_Σ for each electron tunneling-event onto (off of) the island. Calculation of the spectral density of the potential fluctuations requires solving the master equation for all contributing tunneling events. But, in the sequential tunneling regime, the potential noise spectral density takes the simple form [43]:

$$S_{\phi\phi}(\omega) \simeq \eta_\phi \frac{e^2}{C_\Sigma}, \tag{2.87}$$

where

$$\eta_\phi = \frac{4\Gamma_1\Gamma_2}{(\Gamma_1+\Gamma_2)^3}. \tag{2.88}$$

Similiar to η_I, η_ϕ accounts for the correlations between successive steps in the island potential. Essentially, these steps cause the SET back action. In terms of the SET parameters, the back action can be expressed as [42]

$$S_{\phi\phi}(\omega) \simeq \frac{(1-\alpha^2)}{4}\frac{e^3 R_\Sigma}{C_\Sigma^2 V_{SD}}, \tag{2.89}$$

where α has the same definition and restrictions as above.

From these results for the SET shot noise and back action, I can now gauge the overall noise performance of the SET, and determine if it meets the three conditions

necessary for quantum-limited linear position detection. It is straightforward to show that [42]

$$\sqrt{\omega^2 S_{Q_{NR}}(\omega) S_{\phi\phi}(\omega)} \approx 2.2\hbar\omega \tag{2.90}$$

for an "optimized" SET, where ω is the frequency of the mesured signal. Thus, while it is apparent that the "optimized" SET fails to meet condition (1) (Eq. 2.65), this result demonstrates that the SET, in principle, is a nearly quantum-limited detector. Note also that Eq. 2.90 does not include correlations between the shot noise and back action.

The correlations between the shot noise and back action are given by [42]

$$\frac{|S_{I\phi}(\omega)|}{\sqrt{S_{\phi\phi}(\omega) S_{II}(\omega)}} \approx \sqrt{\frac{2}{1+\alpha^2}} \frac{\alpha}{2}. \tag{2.91}$$

For the range of α allowed in this approximation, the relative magnitude of $S_{I\phi}(\omega)$ can range from ~ 0.0 to ~ 0.5. Depending on the bias-point and on the source impedance, the correlations could add to or reduce the total noise power added by the SET amplifier [16] [43] [42]. Regardless, it appears that, at least in some cases, the SET also fails to meet condition (2).

Lastly, I address the condition (3) (optimal coupling). I first assume that the SET is biased such that the correlation term is negligible. Next, I convert the SET's intrinsic noise sources into a total effective position sensitivity by assuming that the SET is coupled to a nanomechanical resonator as described in the previous subsection. The shot noise contribution is simply:

$$S_I^y(\omega) \approx S_Q(\omega) \left(\frac{d_{NR}}{b C_{NR} V_{NR}} \right)^2. \tag{2.92}$$

Equation 2.92 simply states that as I increase the coupling, $bC_{NR}V_{NR}/d_{NR}$, between the resonator and the SET island, the mechanically-induced charge signal increases linearly above the SET's shot noise background.

The contribution due to the back action is approximated by considering the force of the SET-island potential fluctuations on the resonator:

$$F(t) \approx b\frac{C_{NR}V_{NR}}{d_{NR}}\delta\phi(t), \tag{2.93}$$

where $\delta\phi(t)$ represents the step-wise potential fluctuations.

On resonance, the response of the resonator is given by the standard relation:

$$y_m(\omega) = \frac{Q_e f}{K_m}, \tag{2.94}$$

where f is the normalized force, accounting for the mode shape as discussed in Appendix A. Here, the quality factor Q_e (Eq. 2.60) is used to account for the detector induced damping[6] [16] [55]. For the case of the normal state SET, the effective quality factor is given by [16] [55]

$$\begin{aligned}\frac{1}{Q_e} &= \frac{1}{Q_b} + \frac{1}{Q_d} = \\ &= \frac{1}{Q_b} + \left(\frac{bC_{NR}V_{NR}}{C_\Sigma V_{SD}}\right)^2 \frac{e^2 R_\Sigma}{2M_m\omega_1 d_{NR}^2},\end{aligned} \tag{2.95}$$

where I have assumed symmetric junctions, and Q_b is the quality factor relating to damping due the equilibrium bath.

[6]The detector also induces a shift in the resonator's spring constant. I neglect this affect as the resulting frequency shift is small with respect to the shift induced by the electrostatic softening of the mode due to the coupling voltage V_{NR}.

From Eqs. 2.93 and 2.94, the resulting back action contribution to the displacement noise is thus

$$S_F^y(\omega) \approx \left(\frac{Q_e}{K_m}\right)^2 \left(\frac{bC_{NR}V_{NR}}{d_{NR}}\right)^2 S_{\phi\phi}(\omega). \tag{2.96}$$

The total effective mean square displacement noise for the SET displacement detector is now written simply as

$$(\delta y_m)^2 = (S_I^y(\omega) + S_F^y(\omega))\,\Delta f, \tag{2.97}$$

where $\Delta f = \omega_1/4Q_e$ is the noise equivalent bandwidth of the resonator.

It is clear from Eqs. 2.96 and 2.92 that Eq. 2.97 can be minimized with respect to the coupling. Thus condition (3) is satisfied. For a given sample, the only parameter in the coupling which can be tuned is V_{NR}. In the simple case where damping from the equilibrium bath dominates, the weak-coupling limit, I find the optimal coupling voltage to be

$$V_{NR,opt}^2 = \left(\frac{d_{NR}}{bC_{NR}}\right)^2 \frac{K_m}{Q_b} \sqrt{\frac{S_Q(\omega)}{S_{\phi\phi}(\omega)}}. \tag{2.98}$$

Figure 2.4 displays the total rms displacement noise of the SET displacement detector. The parameter values are chosen to roughly represent Device 2. The back action and shot noise are seen to contribute equally at a voltage of $V_{NR,opt}$ $\approx$ 13 Volts. This so-called "sweet-spot" yields an ultimate intrinsic displacement sensitivity $\sim 1.5\Delta y_{QL}$, where,

$$\Delta y_{QL} = \sqrt{\frac{\hbar}{\ln(3) M_m \omega_1}}, \tag{2.99}$$

as determined from the definition of T_{QL}, Eq. 2.45.[7]

[7]Choosing the low-temperature limit of T_{QL} rather than the high-temperature limit is simply a matter of convention.

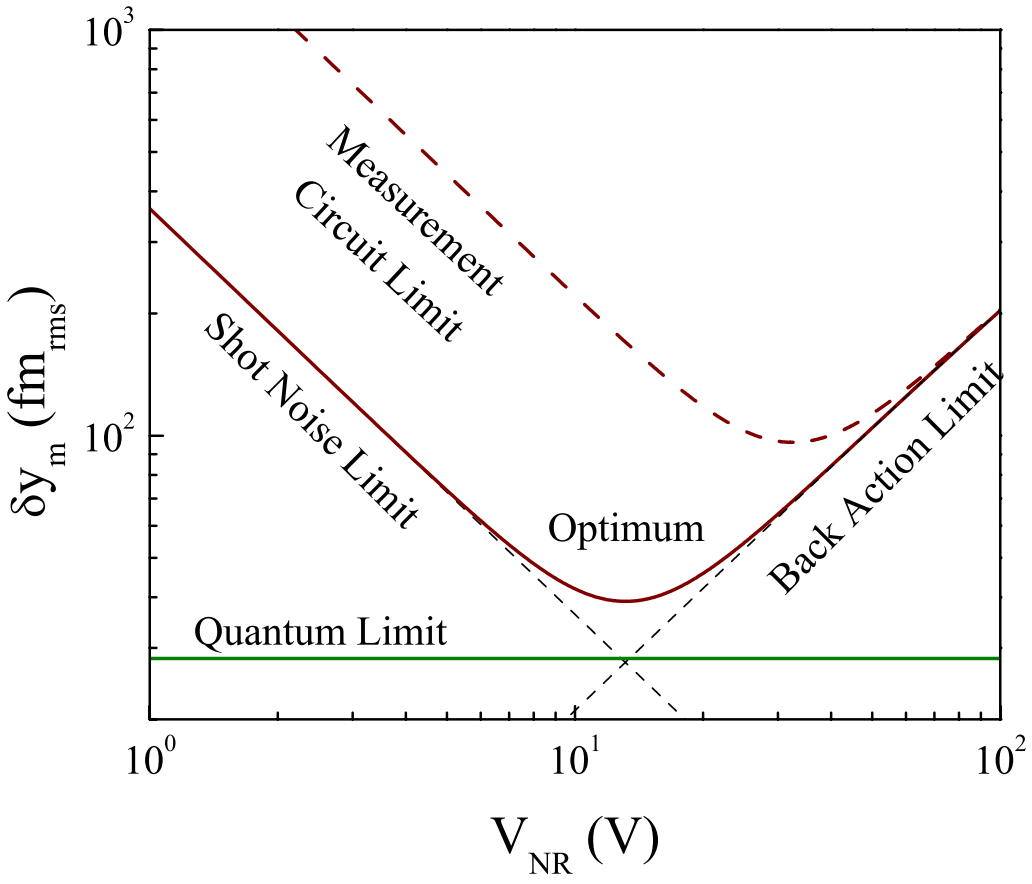

Figure 2.4: Log-log plot of displacement noise of the SET displacement detector in the weak coupling limit. Parameter values: $Q_b = 5.0 \times 10^4$, $C_\Sigma = 450$ aF, $C_{NR} = 26$ aF, $f_1 = 19.7$ MHz, d_{NR}= 600 nm, and $K_m \approx 15$ N/m. The line representing the measurement circuit limit is for $S_Q = 15\ \mu e/\sqrt{Hz}$.

For comparison, also included in Fig. 2.4 is the additive measurement circuit noise (labeled 'measurement circuit limit'). As discussed in Appendix B and in Chapter 5, this noise is due to the input voltage noise of the pre-amplifer. It is uncorrelated with the intrinsic sources, and simply adds to the forward coupling noise $S_Q(\omega)$ in Eq. 2.92.

Figure 2.5 demonstrates the limit where the damping crosses over from bath-limited to detector-limited. Optimal coupling is achieved at $\sim$ .5 Volts. The cross-over from the bath-limited regime to the detector-limited regime occurs at $\sim$ 15 Volts. In this regime, the effective resonator temperature T_e, Eq. 2.59, is determined primarily by the effective detector bath temperature T_d, Eq. 2.55. For the case of the normal-state SET [55],

$$T_d \propto \frac{eV_{SD}}{k_B} \tag{2.100}$$

where the proportionality constant is of order .5, and depends on the specific bias SET bias point. For typical parameters, this should be on the order of .5 - 1 K.

Before concluding, it is necessary to comment on how the preceding dicussion would have differed if I considered the case of a superconducting single-electron transistor (SSET). As discussed in Appendix B, the combination of Coulomb blockade and Josephson phenomena leads to a large variety of potential tunneling processes. Consequently, a general statement about the the differences between the noise characteristics and response of the SSET and the SET cannot be made; it depends on the particular bias point and the dominant tunneling processes at that point.

For example, at the onset of single quasiparticle tunneling (at 4 Δ), the re-

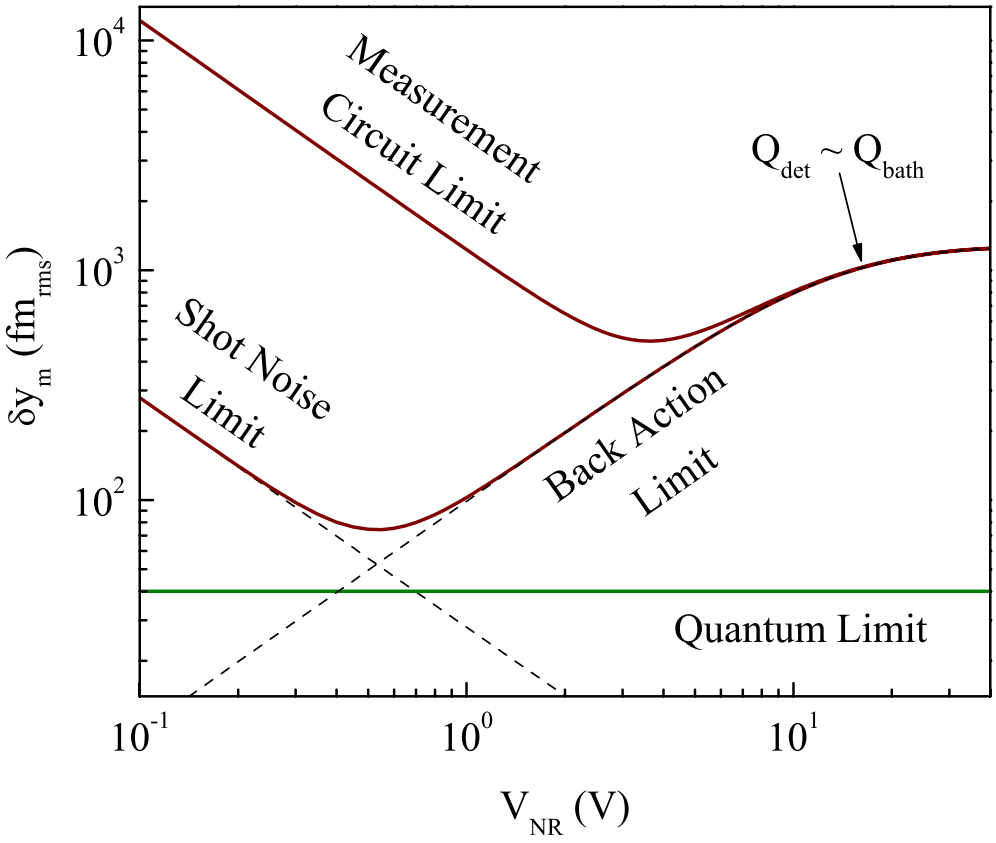

Figure 2.5: Log-log plot of displacement noise of the SET displacement detector, demonstrating the cross-over from bath-limited damping to detector-limited damping. Parameter values: $Q_b = 2.0 \times 10^5$, $C_\Sigma = 550$ aF, $C_{NR} = 65$ aF, $f_1 = 9.5$ MHz, d_{NR}= 300 nm, and $K_m \approx 2$ N/m. The line representing the measurement circuit limit is for $S_Q = 90\ \mu e/\sqrt{Hz}$.

sponse or $I_{SD}Q_{NR}$ transfer function of the SSET has been found to be greater than the SET response at the onset of tunneling by a factor of $\sim 1.6\Delta/E_C$ [70]. Predictions for the optimized ultimate charge sensitivity of the SSET for this particular bias regime also show improvement over the normal-state [71].

As well, around the JQP resonance, it is expected that, because of the suppression of the shot noise from resonant tunneling, the charge sensitivity should improve over what is achievable in the normal-state [72].

Finally, recent theoretical investigations of the measurement effects of the noise characterisics near the DJQP and JQP resonances have shown that, just as in the normal-state, the SSET back action should appear as an effective thermal bath, driving, damping and shifting the frequency of the measured resonator [59] [60]. It is still seen that

$$Q_d^{-1} \propto V_{NR}^2 \tag{2.101}$$

and

$$T_{d/} \propto V_{SD}. \tag{2.102}$$

However, unlike in the normal state, assymmetry in the quantum noise can yield both negative and positive T_d and Q_d [59] [60]. Additionally, it has been predicted that the SSET biased near the DJQP should be able to approach more closely to the quantum measurement limit than a normal-state device [58]. Preliminary experimental results appear to verify the predictions of negative and positive T_d and Q_d near both the JQP and DJQP resonances [73].

I conclude the section and the chapter by noting that, while the normal-state

SET is not an ideal linear detector, it comes within a factor of 2. It is expected that the SSET should perform even better. Configured as a displacement detector, the SET or SSET can be optimally coupled to a nanomechanical resonator, and perform detection near the quantum limit of position detection (Quantum Limit II). Furthermore, implementation of the RFSET, which will result in the loss of at most a factor ~ 2 in detection sensitivity, should be capable of providing the bandwidth necessary for the read-out of the high frequency nanoresonators required to observe freeze-out (Quantum Limit I).

Chapter 3

Design and Fabrication

The following sections describe the design considerations and the sequence of steps involved in the fabrication of our RF-SET displacement detectors.

3.1 The Wafers

Each sample was fabricated from 500 μm thick, (100)-oriented, silicon wafers (doped p-type with resistivity quoted to be 1 - 10 Ω-cm at room temperature). The wafers were purchased from *The MEMS Exchange* [74], and provided to us with a 100 nm low-stress, amorphous silicon nitride (SiN) coating on each side (Fig. 3.1(a)). The SiN was deposited using low pressure chemical vapor deposition (LPCVD). Each side of each wafer was polished.

3.2 Silicon Nitride Membrane Fabrication

The first step in the process was to fabricate the SiN membrane from which the nanomechanical resonators would eventually be cut. Using silicon nitride membranes provided two advantages: (1) a relatively large Young's modulus (200 - 300 GPa) [75] [76], yielding, for a given geometry, larger nanoresonator frequencies than any alternative processing material other than diamond; and (2) convenience in the processing of the nanoresonator (see the final section in the chapter on etching the

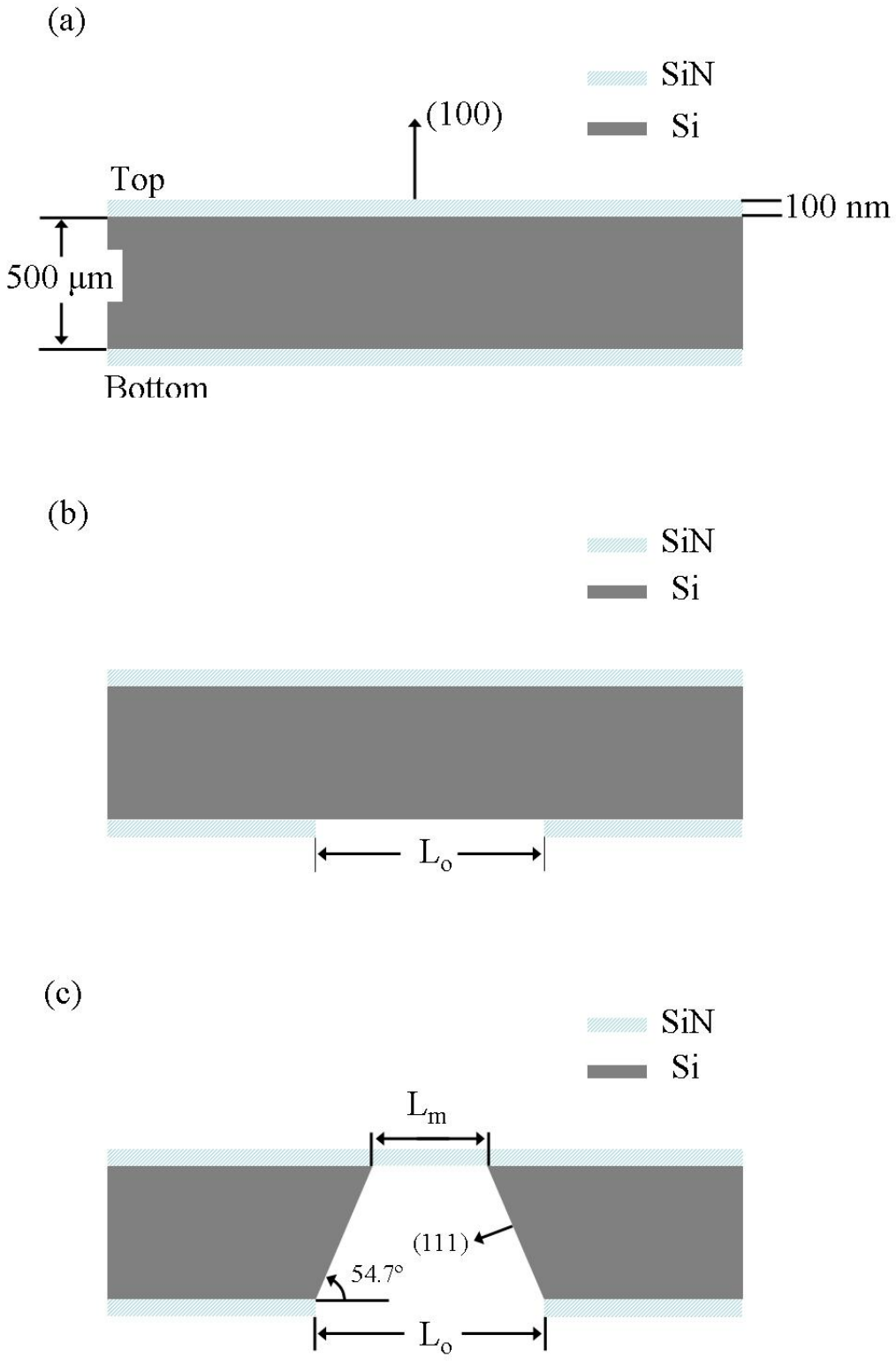

Figure 3.1: (a) SiN-coated Si wafer. (b) After RIE etch. (c) After KOH etch.

nanoresonator).

Initially, a protective layer of photoresist was spun on the top of each wafer:

1. Spin protective layer of photoresist on top side of wafer at 2000 rpm.

2. Let dry in air at room temperature.

Next, square openings in each wafer's bottom SiN layer were defined by means of contact optical lithography and reactive ion etching (RIE). The etch was timed so that all the SiN was etched away, leaving the underlying silicon substrate exposed (Fig. 3.1(b)):

1. Spin negative photoresist NR7-1500py [77] on bottom of wafer at 3000 rpm for 1 minute; bake at 150°C for 1 minute on vacuum hot-plate.

2. Expose with $\sim$ 400 nm wavelength light, for 20 seconds with an intensity of 12 mW/cm^2

3. Post-bake at 120°C for 1 minute on vacuum hot-plate

4. Develop in RD6 [77] for 15 seconds, and a rinse in deionized (DI) water.

5. RIE etch for 10 minutes in SF_6 with SF_6 flow rate and chamber pressure 20 sccm and 20 mTorr respectively; and RF power of 170 Watts.

Finally, an anisotropic wet etch was used to etch the Si substrate. Aqueous potassium hydroxide was used, providing an etch rate of $\sim$ 70 μm/hr on the [100] Si-planes:

1. Place wafer in aqueous potassium hydroxide (KOH) solution of concentration 425 grams of K [78] per liter of DI H_2O, at 80°C, stirred at 120 rpm, for $\sim$ 8 hours

2. Remove from the KOH bath, rinse wafer with DI water, clean with acetone, methanol, and isopropanol (IPA), and then blow dry with compressed N_2.

After $\sim$ 8 hours in the KOH solution, the result was a v-groove through the silicon, stopping at the SiN top layer, and yielding a square SiN membrane on the top of the wafer (Fig. 3.1(c)). The size of the membrane depended on the size of the opening on the bottom of the wafer through the relationship

$$L_m = L_o - \frac{2t}{\tan\theta}, \tag{3.1}$$

where L_m was the length of each side of the membrane, L_o was the length of each side of the opening on the wafer's bottom, t = 500 μm was the silicon wafer thickness, and $\theta = 54.7°$ was the angle between the (100) and (111) silicon planes. Typically, we chose $L_o \simeq 765$ μm so that $L_m \simeq 55$ μm. This size was large enough to allow for two complete resonator/SET devices on each membrane.

After this step, the wafers were diced into units containing four membranes each.

3.3 Fabrication of the Bond Pads and Tank Circuit

The main design considerations for the fabrication of the bond pads and tank circuits were as follows: (1) safegaurd the SET junctions and nanoresonator from

electrostatic discharge by implementing on-chip room-temperature electrical shorts; (2) reduce dissipation in the rf circuit by constructing the entire circuit out of superconducting materials; and (3) choose the appropriate values of tank circuit capacitance and inductance in order to achieve both large bandwidth (50 - 100 MHz) and matching between 50 Ω and the SET dynamic resistance R_S.

It was equally important to choose the tank-circuit parameters so that the resonant frequency would be large enough to employ an rf amplifier, but small enough to "look" like a lumped element to the incident radiation. Thus, for the first generation of devices, we chose an rf amplifier with a band-pass between approximately 1.2 and 1.7 GHz (see Chapter 4), and we engineered the tank circuits to be resonant at approximately 1.5 GHz. For a silicon substrate, the wavelength of 1.5 GHz radiation is on the order of centimeters and is much larger than any of the components in the microwave circuit (see the subsections below).

Through the relation

$$f_T = \frac{1}{2\pi}\frac{1}{\sqrt{L_T C_T}}, \tag{3.2}$$

the choice of 1.5 GHz operating frequency set the product of the tank circuit inductance and capacitance to be $L_T C_T \approx 1 \text{ x } 10^{-20}$. The individual inductance and capacitance values would then have been set by the bandwidth condition $\Delta f = 50$ - 100 MHz and the optimal matching condition (Eq. 2.79). The optimal inductance would have been given by

$$L_T = \frac{Z_o}{\Delta f \pi}. \tag{3.3}$$

However, mistakes were made in the design phase, and the inductor value

we chose (50 nH) was approximately a factor of 3.2 less than the optimal value. Through Eq. 3.2, this increased the value of capacitance by approximately a factor of 3.2 (300 fF). As a result, the SET/tank-circuit impedance on resonance (Z_{LCR}, see Eq. 2.74) was approximately a factor of 10.3 smaller than 50 Ω for $R_S = 50$ kΩ. Additionally, for Devices 1 - 3, R_S was closer to 100 kΩ (see Section 3.4), making the impedance mismatch nearly a factor of 2 worse. Finally, the tank-circuit quality factor (Eq. 2.78) was dominated by loading from the 50 Ω transmission line, resulting in measurement bandwidth of approximately 70 MHz.

Fabrication of the Bonds Pads and Tank Circuit Capacitor

The first step in the process was to define the bond pads and the tank circuit capacitor. This was done using optical lithography and metal lift-off on the top-side of the wafer:

1. Spin negative photoresist NR7-1500 at 4000 rpm for 1 minute; baked at 150°C for 1 minute on vacuum hot-plate.
2. Expose with ∼ 400 nm wavelength light, for 20 seconds with an intensity of 12 mW/cm^2.
3. Bake at 120°C for 1 minute.
4. Develop in RD6 for 20 seconds.
5. Rinse in deionized (DI) water.

Before the deposition of the metal layers, the SiN within the regions defined by the optical lithography step was removed by an RIE etch:

1. RIE etch with CHF_3 and O_2 at respective flow rates of 18 sccm and 2 sccm and a pressure and RF power of 40 mTorr and 175W.

2. O_2 plasma etch for 30 seconds at 1.75 Torr and 100 W.

This step served to provide electrical contact between the bond pads and the silicon substrate, and was implemented in order to reduce electrostatic buildup across the SET junctions and resonator before the device was installed on the dilution refrigerator. At room-temperature, the "short" between leads was measured to be on the order of kΩ,

Next, a tri-layer of metals [80] was deposited using electron-beam evaporation. The evaporation was done in a vacuum chamber at a pressure of less than 1 μTorr. The following layers were evaporated sequentially, without breaking vacuum:

1. Evaporate 190-200 nm of Al.

2. Evaporate 20 nm of Ti.

3. Evaporate 200 nm of Au.

4. Lift-off in RR2 [77] at 80°C for 10 minutes.

5. Rinse in IPA and blow dry with compressed N_2.

The purpose of the tri-layer was to reduce dissipation in the circuit components and at the same time ensure oxide-free overlaps between the components. We found that the tri-layer superconducted below 700 mK.

Fabrication of the Tank Circuit Inductor

The planar-coil inductors for the LC resonator were defined by electron-beam lithography and electron-beam evaporation. Resist exposure was performed with a Jeol 6500 scanning electron-beam field emission microscope (SEM) [81]. The pattern for the exposure was generated using Design Cad LT 2000 [82]. The exposure was controlled using the Nanometer Pattern Generation System version 8.001.77 [83].

1. Spin electron-beam resist PMMA 495K [84] on top of wafer at 5000 rpm for 60 sec; baked at 180°C for 5 minutes on vacuum hot-plate.

2. Spin electron-beam resist PMMA 950K [84] on top of wafer at 5000 rpm for 60 sec; baked at 180°C for 5 minutes on vacuum hot-plate.

3. Expose resist at an acceleration voltage of 30 KV, with beam current of 2 nA, and magnification of 150x.

4. Develop for 25 seconds in MIBK [84], diluted in IPA to one-part-in-three by volume.

5. Rinse in IPA for 25 seconds and blow dry with with compressed N_2.

6. O_2 plasma etch for 15 seconds to remove any residual resist in defined regions.

The metal deposition was performed using an electron-beam evaporator at a pressure of less than 1 μTorr.

1. Deposit 100 nm Al at .5 nm/s.

2. Lift-off in acetone at 80°C for 10 minutes.

3. Rinse with IPA and blow dry with compressed N_2.

Contact between the inner coil of the inductor and the appropriate bond pad was achieved using an Al cross-over bridge (Fig. 3.3). The cross-over and the inner coil made contact via a tri-layer connector[1] (Fig. 3.3). The cross-over was insulated from the coils of the inductor by a layer of SiO_2. The bridges were defined in two steps: (1) electron-beam exposure followed by deposition of SiO_2; (2) electron-beam exposure followed by deposition of Al.

Deposition of SiO_2 layer:

1. Spin electron-beam resist MMA EL 11 [84] diluted in anisole to one-part-in-one by volume at 2500-3000 rpm for 60 seconds; bake at 200°C for 5 minutes.

2. Spin PMMA 950k at 4000 rpm for 60 seconds; and bake at 180°C for 5 minutes.

3. Expose at accelerating voltage of 30 kV with 1 nA current and magnification of 150x.

4. Develop for 30 seconds in MIBK/IPA (1:3).

5. Rinse for 30 seconds in IPA.

6. O_2 plasma etch for 15 seconds.

[1]The tri-layer connector was deposited in the same step as the bond pads, leads, and tank-circuit capacitor.

7. Evaporate 220 nm of SiO_2 at a rate of 0.5 nm/s using electron-beam evaporator.

8. Lift-off in acetone at 80°C for 10 minutes.

9. Rinse in IPA and blow dry with compressed N_2.

Deposition of Al layer:

1. Spin electron-beam resist MMA EL 11 [84] diluted in anisole to one-part-in-one by volume at 2500-3000 rpm for 60 seconds; bake at 200 °C for 5 minutes.

2. Spin PMMA 950k at 4000 rpm for 60 seconds; and bake at 180°C for 5 minutes.

3. Expose at accelerating voltage of 30 kV with 1 nA current and magnification of 150x.

4. Develop for 30 seconds in MIBK/IPA (1:3).

5. Rinse for 30 seconds in IPA.

6. O_2 plasma etch for 15 seconds.

7. Evaporate 330 nm of SiO_2 at a rate of 0.5 nm/s using electron-beam evaporator.

8. Lift-off in acetone at 80°C for 10 minutes.

9. Rinse in IPA and blow dry with compressed N_2.

Figures 3.2 and 3.3 are scanning electron micrographs of Device 2, displaying the completed bond pads and tank circuits. For Devices 1 - 4 , the inductor coils consisted of 13 - 14 turns and were 130 x 130 μm^2 at their outer edge. Each turn of a coil was 1 μm wide, and the separation between turns was 1 μm. The corresponding inductance was found to be approximately 50 nH. The capacitor was made up of 7 inter-digitated fingers, each 300 μm long and 25 wide. The resulting capacitance was found to be approximately 300 fF.

Table 3.1 lists the values of inductance L_T, capacitance C_T, the resonant frequency f_T, bandwidth ΔF, the tank circuit characteristic impedance Z_{LC}, and the impedance of the SET and tank circuit on resonance Z_{LCR}. In Appendix B, I discuss how these parameters were determined.

For Devices 3 and 4, we found that the values of L_t agree to within 5% of values calculated using microwave circuit simulation software. For Device 2, the quality of the tank resonance was very poor due to additional "sub-resonances" in the peak. Hence it was difficult to fit with precision better than $\sim$ 20%, and thus the Q fell somewhere between 8 and 10, putting bounds on L_T of 46 nH and 58 nH respectively.

The capacitance values C_T for Devices 3 and 4 were greater than the simulations by 25 - 40%. This was probably a result of not including in the simulation the contribution to C_T from the lead connecting C_T to L_T and the parasitic capacitance of L_T.

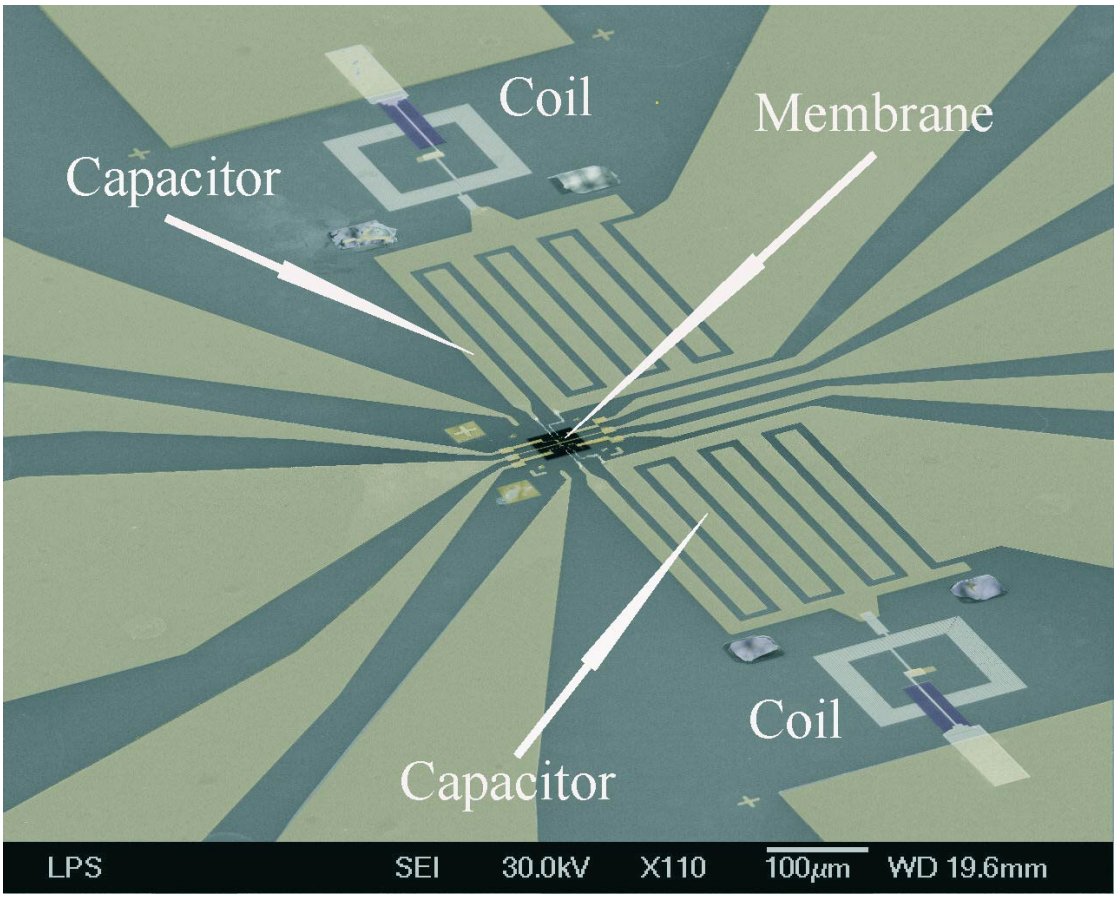

Figure 3.2: Scanning electron micrograph of the tank circuit and bond pads, Device 2. The SiN membrane is seen as the black square at the center of the sample.

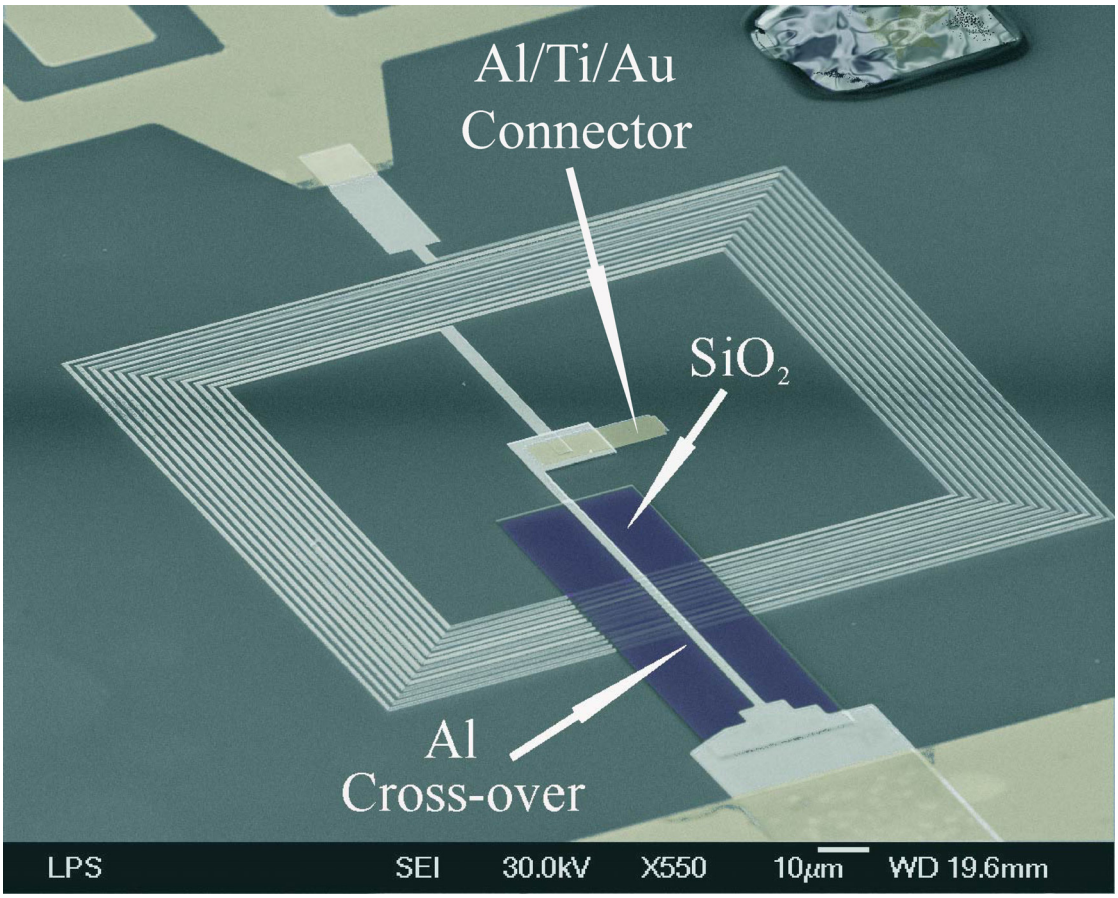

Figure 3.3: Scanning electron micrograph of tank circuit inductor, Device 2.

Table 3.1: Tank circuit parameters Devices 1 - 4.

Device	turns	L_T(nH)	C_T(fF)	f_T(GHz)	ΔF(MHz)	$Z_{LC}(\Omega)$	$Z_{LCR}(\Omega)$
1	13	-	-	1.43	-	-	-
2	13	46	290	1.37	68	357	2.2
3	14	52	287	1.30	76	425	2.5
4	14	51	320	1.23	79	400	5.6

The tank capacitance for Device 2, depending on Q, could have ranged from 230 - 290 fF. As the capacitor design and fabrication were identical for all three samples, it is more likely that $C_t \sim 290$ fF. This would imply, then, that $L_T \sim 46$ nH.

For the Devices 2 - 4, $Z_{LCR} \approx 0.04$ - $0.12Z_o$. As a result, the reflection coefficients at maximum conductance Γ_{max} ranged from ~ 0.8 - 0.92, yielding maximum depths of modulation, $M = 20\log(\Gamma_{max})$ of ~ 0.7 - 2.0 dB. Additionally, the SETs were "over-coupled" to the transmission line, and, hence, the Q's were dominated by Z_o, setting the measurement bandwidth to $\Delta F \sim 70$ - 80 MHz.

3.4 Fabrication of the Nanomechanical Resonator and SET

The main design considerations for the fabrication of the nanoresonators and the SETs were as follows: (1) produce resonators with in-plane fundamental-mode resonant frequencies large enough to approach low thermal occupation numbers on the dilution refrigerator, yet small enough so that the response could be easily detected using both magnetomotive (Appendix A) and SET techniques; (2) produce SETs with as large of a charging energy as possible to minimize the intrinsic SET charge sensitivity (Eq. 2.85); and (3) engineer as small a separation as possible between the nanoresonator and the SET to maximize the coupling C_{NR} and the displacement-induced charge modulation (Eq. 2.71).

Fabrication of Nanoresonator and SET Gate

The nanomechanical resonators and the central coupling gate were defined on the SiN membrane using electron-beam lithography and Au deposition. Defining the nanoresonator from gold served two purposes: (1) the gold layer acted as a gate electrode with which we could establish a voltage bias between the resonator and SET island (*ie.* couple the resonator's motion to the SET's conductance); and (2) the gold layer acted as an etch mask for the freeing of the nanomechanical resonator from the SiN membrane in the final step (see Fig. 3.5).

The geometry of the nanoresonators was determined by the desired nanoresonator frequency. We assumed that the in-plane fundamental-mode frequency of

each of the nanoresonators was described by

$$f_1 = \frac{k_n^2 w}{2\pi L^2}\sqrt{\frac{E_{Au}t_{Au} + E_{SiN}t_{SiN}}{12(\rho_{Au}t_{Au} + \rho_{SiN}t_{SiN})}}, \tag{3.4}$$

where $k_1 = 4.73$ from the clamped-clamped boundary conditions, E_{Au} and E_{SiN} were the Young's moduli of Au and SiN respectively, t_{Au} and t_{SiN} were the thickness of the Au and SiN layers respectively, ρ_{Au} and ρ_{SiN} were the densities of the respective layers, w was the width of the nanoresonator, and L was the nanoresonator's length. In Appendix A, I list the values of the Young's moduli and density for each layer; as well, there, I discuss the calculation of the resonator's effective mass and spring constant k_m for SET detection.

The sequence of steps used to define the nanoresonators and gates were as follows:

1. Spin electron-beam resist PMMA 495K [84] on top of wafer at 5000 rpm for 60sec; baked at 180°C for 5 minutes on vacuum hot-plate.

2. Spin electron-beam resist PMMA 950K [84] on top of wafer at 5000 rpm for 60sec; baked at 180°C for 5 minutes on vacuum hot-plate.

3. Expose resist at accelerating voltage of 30 kV, with 50 pA beam current, and a charge dose of 400 μC/cm^2 at a magnification of 500x.

4. Develop in MIBK/IPA (1:3) for 40 seconds.

5. Rinse in IPA for 40 seconds.

6. O_2 plasma etch for 15 seconds.

7. Electron-beam evaporate 10 nm of Ti at a pressure of less than 1 μTorr.

8. Electron-beam evaporate 700 nm of Au at a pressure of less than 1 μTorr.

9. Lift-off in acetone at 80° C for 10 minutes.

For Devices 1 - 4, Table 3.2 lists the geometrical parameters and raw mass, m_r. Table 3.3 lists the corresponding calculated and measured resonant frequencies and effective spring constants.

Fabrication of the SET

Each SET was fabricated on the SiN membrane, with the SET island parallel to a nearby nanoresonator (see Fig. 3.7). The separation between the SET and the nanoresonator d_{NR}, as well as the length of the SET island L_i, were chosen to maximize the capacitive coupling C_{NR}. Due to limitations in the alignment of successive layers of electron-beam lithography, the minimum separation d_{NR} that we were able to achieve was on the order of 300 nm.[2] Because we wanted to ensure that the SET island self-capacitance did not become comparable to the SET junction capacitances [85], we chose $L_i = 5$ μm.

The widths of the SET island and leads varied between 50 - 100 nm. Ideally, to minimize junction capacitances C_i and, hence, the charge sensitivity of the SETs (see Eq. 2.85), we would have liked to have made these narrower. However, we were not able to develop a consistent recipe for such on the SiN membrane.

[2]More recently other members of our group have been able to engineer the nanoresonator and SET in the same lithography step and decrease d_{NR} to less than 100 nm.

Table 3.2: Geometry and raw mass, m_r, of Devices 1-4. The error in the length and width of the resonator comes from 10% quoted error in the SEM calibration. The error of 30% in the thickness of the Au layer on the resonator comes from the spread in etch rates over time, and is a very rough estimate.

Device	$w(nm)$	$L(\mu m)$	$t_{Au}(nm)$	$t_{SiN}(nm)$	m_r (pg)
1	300 ±30	10 ±1	30 ±20	100 ±2	2.6 ±1.2
2	200 ±20	8 ±.8	30 ±20	100 ±2	1.4 ±.7
3	200 ±20	15 ±1.5	30 ±20	100 ±2	2.6 ±1.2
4	225 ±23	18 ±1.8	30 ±20	100 ±2	3.2 ±1.5

Table 3.3: Effective masses, M_m, and spring constants of Devices 1-4. "a" corresponds to frequency calculated using either Eqs. A.15 and A.16 or Eq. A.17. "b" corresponds to the frequency measured using SET detection at a temperature of 100mK and coupling voltage V_{NR}.

Device	$M_m(pg)$	$\omega_1/2\pi(MHz)^a$	$K_m^a(N/m)$	$\omega_1/2\pi^b$	K_m^b
1	1.5 ±.7	17 ±5	17 ±8	17.976648(3)	19 ±9
2	.96 ±.45	18 ±6	12 ±6	19.654505(7)	15 ±7
3	1.2 ±.54	6 ±1.8	1.5 ±.7	9.37163340(2)	4 ±2
4	1.4 ±.66	4 ±1	.9 ±.4	4.8976624(2)	1.4 ±.6

The oxidation time and pressure for the fabrication of oxide junctions was determined by trial and error. We sought to make the total SET resistance $R_\Sigma = R_1 + R_2 = 50$ kΩ. For this value of resistance, tank-circuit matching could be performed with on-chip components; at the same time, co-tunneling processes would not be a dominant effect (see Appendix B).

We fabricated the SETs using electron-beam lithography and the bi-layer/double-angle evaporation technique [86] (Fig. 3.4):

1. Spin MMA EL (8.5) 11 at 5000 rpm for 60 seconds; bake at 140°C in an oven.

2. Expose membrane to 60 μC/cm^2 electron-beam dose (30 pA beam current, 30 kV accelerating voltage, and magnification of 500x)to insure quick development of the MMA layer.

3. Spin PMMA 950K A4 at 5000 rpm for 60 seconds; bake for 30 minutes at 140°C in an oven.

4. Evaporate 100 nm layer of Al in thermal evaporator to serve as both an anti-charging layer and a focusing standard for the electron-beam exposure.

5. Expose SET leads and island each with an area charge dose and line charge dose of 50 μC/cm^2 and 1.0 nC/cm respectively; 30 kV accelerating voltage, beam current of 30 pA, and magnification 1000x.

6. Remove Al layer with OPD4262 [87], 40 seconds.

7. Rinse in DI water and blow dry with compressed N_2 gas.

8. Develop in MIBK/IPA (1:3) for 1 minute.

9. Rinse in IPA for 1 minute.

10. O_2 plasma etch for 10 seconds to remove residuals.

Figure 3.4(a) displays a schematic of the result of the exposure and development process.

The double-angle depositions were done in a thermal evaporator. The system was connected to building ground through a copper-braided strap to prevent sample damage due to electrostatic discharge. Both evaporations were performed at a chamber pressure less than 1 μTorr. Three-nines Al [88] was evaporated from a tungsten boat [89] at a rate of .2 - .4 nm/s:

1. Evaporate 30 nm Al at $\phi_1 = 12$ - 15° with respect to the sample surface normal (Fig. 3.4(b)).

2. Oxidize Al by introducing oxygen into chamber for 2-3 minutes. For Device 1 and 2, the pressure in the chamber during oxidation was 10 mTorr. For Devices 3 and 4, a different chamber was used and the requisite pressure was 90-100 mTorr (Fig. 3.4(c)).

3. Evaporate 60 nm Al at $\phi_2 = 12$ - 15° (Fig. 3.4(d)).

4. Lift-off in acetone for 30 minutes at 90°C .

Tables 3.4 and 3.5 lists the values of C_i, R_i, C_g, C_{NR}, d_{NR}, and the charging energy for Devices 1 - 4. In Appendix B, I discuss how we determined these parameters.

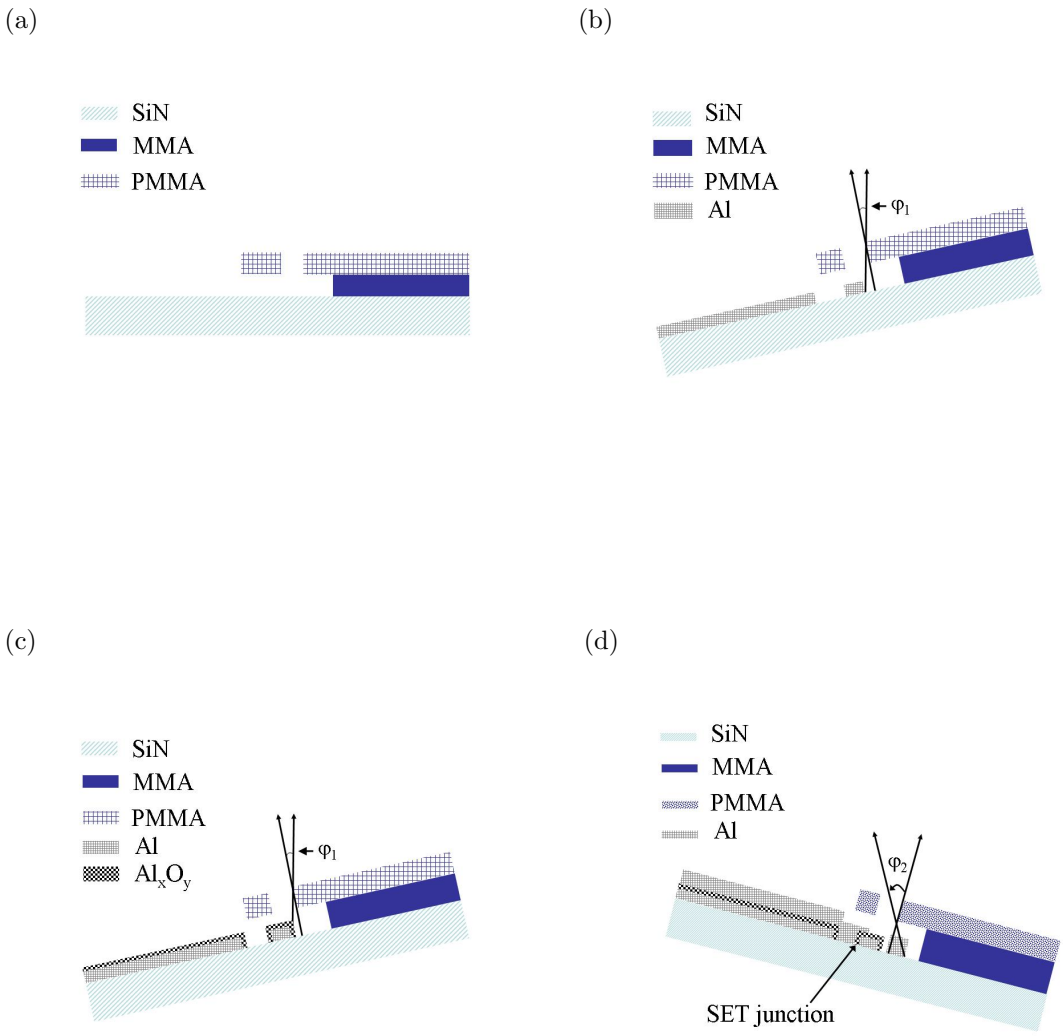

Figure 3.4: Cross-section schematic of the double-angle evaporation of an SET junction. (a) Developed bi-layer of resist. (b) First deposition of Al. (c) Oxidation of Al. (d) Second deposition of Al.

Table 3.4: Junction capacitances and resistances of Devices 1-4.

Device	$C_1(aF)$	$R_1(k\Omega)$	$C_2(aF)$	$R_2(k\Omega)$	$C_g(aF)$	$C_{NR}(aF)$	$d_{NR}(nm)$
1	81	61	84	59	14	61	600
2	250	21	100	53	10	26	600
3	173	47	341	24	14	64	300
4	~ 600	~ 15	~ 600	~ 15	19	63	300

Table 3.5: Total capacitance, charging energy, gap energy and Josephson energies Devices 1 - 4. (a) Total capacitance found by summing C_i, C_g , C_{NR}. (b) Total capacitance found from position of JQP peak. (c) Total capacitance found from position of DJQP peak.

Device	$C_\Sigma^a(aF)$	$C_\Sigma^b(aF)$	$C_\Sigma^c(aF)$	$\frac{E_c}{e}(\mu V)$	$\frac{\Delta}{e}(\mu V)$	$\frac{E_{j,i}}{e}(\mu V)$
1	241	-	279	287	220	12, 12
2	386	410	435	184	220	37, 14
3	592	577	540	148	200	15, 21
4	-	1310	-	61	180	~ 40, 40

Etching the Nanoresonator

The last step in the fabrication of the samples was the etching of the nanomechanical resonator from the silicon nitride membrane (Fig. 3.5):

1. Spin PMMA 950K A4 [84] at 4000 rpm for 60 seconds; bake for 5 minutes at 180°C on a hot-plate, no vacuum.

2. Spin PMMA 950K A4 [84] at 4000 rpm for 60 seconds; bake for 5 minutes at 180°C on a hot-plate, no vacuum (Fig. 3.5(a)).

3. Expose resist with charge dose of 350 - 400 μC/cm^2 (30 pA beam current, accelerating voltage of 30 kV, and magnification of 1000x).

4. Develop resist in MIBK/IPA (1:3) for 1 minute and rinse in IPA for 1 minute.

This defined a 400 nm wide window along the length of the beam (Fig. 3.5(b)). The remaining resist served to mask the SET and accompanying circuit while the resonator was etched (Fig. 3.5(c)):

1. RIE etch in CHF_3/O_2 (18 sccm/2 sccm, 40 mTorr, and 175 Watts) for 6 minutes to etch through SiN membrane (Fig. 3.5(c)).

2. O_2 plasma etch for 1 minute to remove remaining resist (Fig. 3.5(d)).

The selectivity of the etch between SiN and the PMMA was approximately 1:1 at about 20 nm/min. The etch rate on gold was about 10 nm/min.

The final result (Device 2) is displayed in Fig. 3.6 and Fig. 3.7.

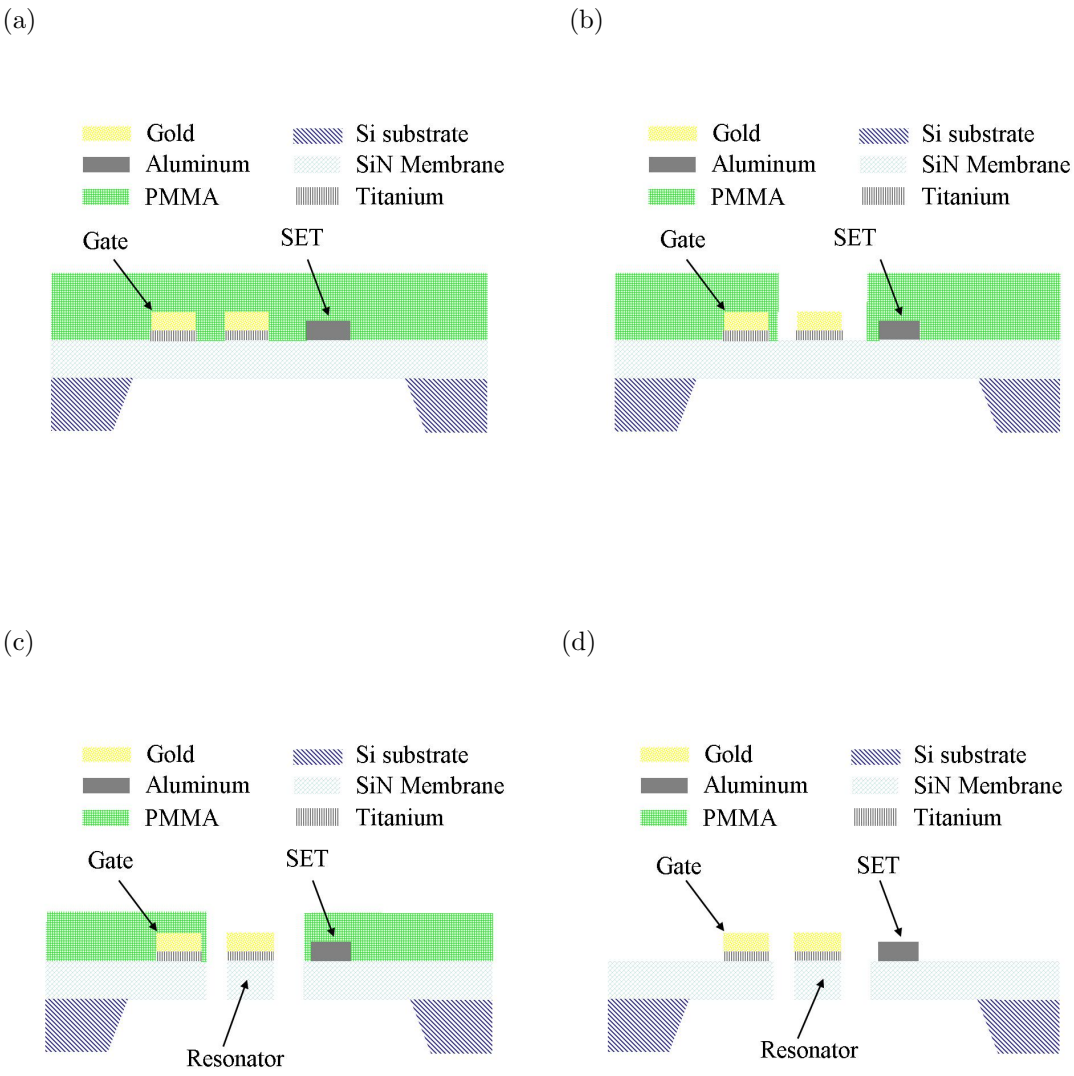

Figure 3.5: Etching of the nanomechanical resonator. (a) Sample coated with resist (PMMA). (b)Etch mask defined. (c) Resonator suspended after RIE etch. (d) Resist removed with O_2 etch.

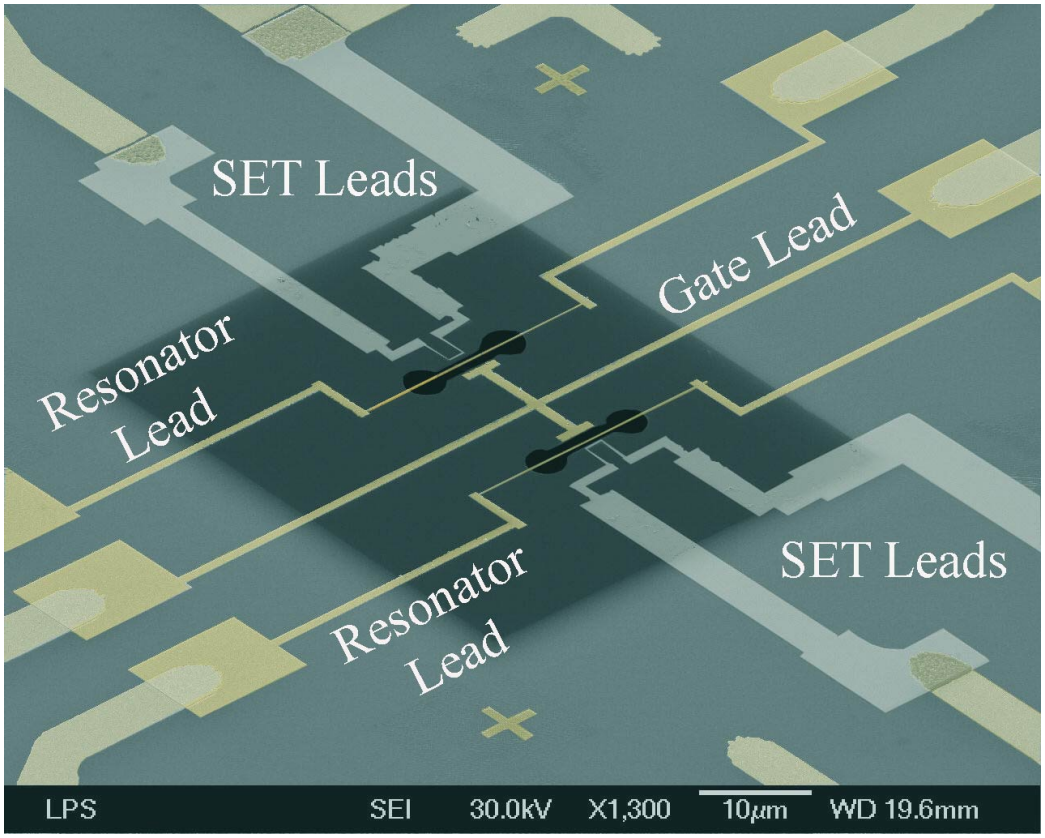

Figure 3.6: Two detectors were fabricated on each sample.

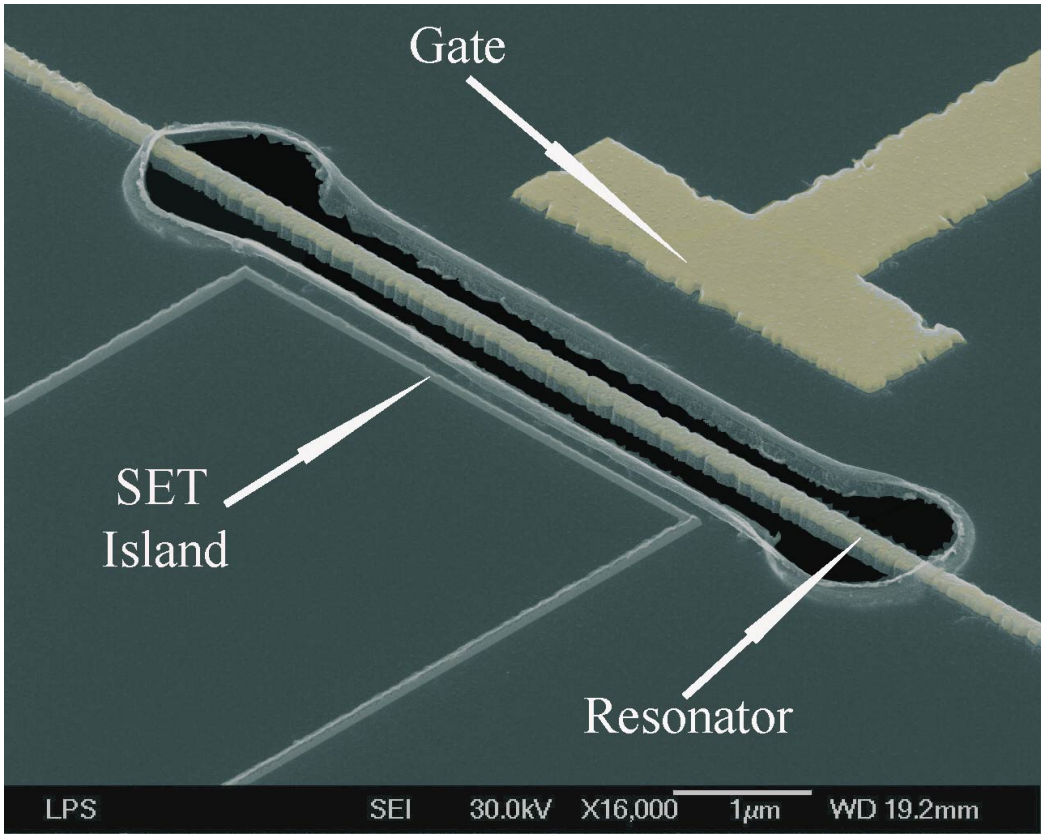

Figure 3.7: SEM image of an RFSET displacement detector: Device 2.

Chapter 4

Apparatus

In the following sections I discuss the measurement equipment which we used for the implementation of our RF-SET displacement detectors. The chapter is divided into three main sections. The first section is a brief description of the packages in which the samples were mounted for measurement. The second section describes the dilution refrigerator and shielded room. In the final section, I discuss the refrigerator wiring, including the dc and microwave circuitry and thermometry.

4.1 The Sample Package

Each sample was placed in a homemade, gold-plated silver sample package and held in place atop a gold-plated circuit board with copper clips (Fig. 4.1). Connections from the sample to the circuit boards were made using 0.025 mm diameter Au wire and a commerical wedge bonder. The circuit boards [90] were designed to provide four 50 Ω microstrip transmission lines; each microstrip was soldered to an SMA connector for external connections.

Gold-plating of the circuit boards and sample packages was done in a fume hood with a standard electroplating technique: 20 grams of $KAu(Cn)_2$ [91] and 50 grams of $(NH_4)_2HC_6H_5O_7$ [92] per liter of DI H_2O, at 65°C, constantly stirred, with a current density of 2-10 mA per square-cm of the surface area to be coated.

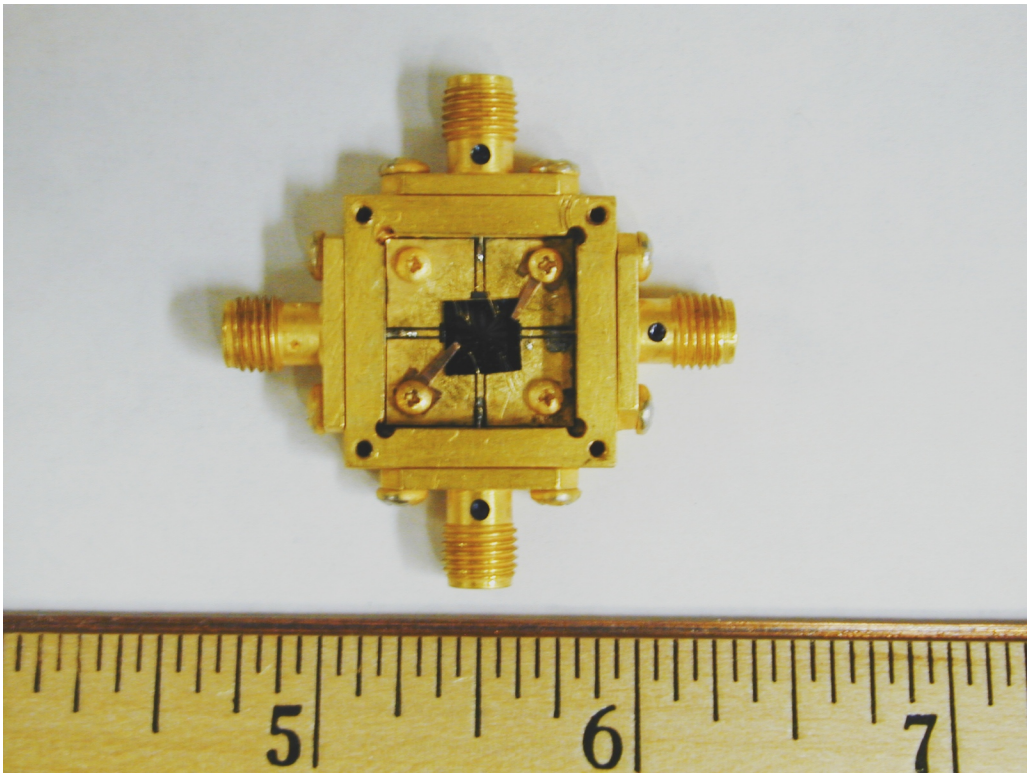

Figure 4.1: Homemade sample package (without the cover). Scale in inches.

4.2 The Dilution Refrigerator and Shielded Room

The sample packages were thermally anchored to the mixing chamber stage of an Oxford Kelvinox 400 dilution refrigerator (Figs. 4.2 and 4.3). The base temperature of the refrigerator was measured to be 9 mK. For operation, the refrigerator was inserted into an Oxford 175 liter helium storage dewar, equipped with a 9 T superconducting magnet. The entire cryostat was suspended from a 750 Kg optical table supported by air dampers on four pillars, each of which was loaded with 750 Kg of lead and sand (Fig. 4.4).

The set-up was enclosed in a shielded room with its own ground connection (Fig. 4.4), providing 100 dB isolation between 10 KHz and 5GHz. All control and measurement electronics was located outside the shielded room, except for home-made battery-powered voltage sources. Low-frequency signals were applied from outside the shielded room through opto-isolators [94]; microwave signals were transmitted into the shielded room through DC blocks [95].

At the input to the cryostat, low-frequency signals and DC biases were divided by a factor of 100 to 1000 and filtered (Fig. 4.5). Commercial RF filters [96] with cut-off frequency in the MHz range were used in conjunction with two home-made powder filters [97] connected in series. Each filter consisted of a box containing a π-filter [98], which connected two RF-tight compartments (Fig. 4.6(a)). The compartments were filled with a mix of epoxy resin [99] and 10 μm grain copper powder [78] in equal weight proportions. The π-powder filters provided more than 90 dB attenuation above 1 GHz (Fig. 4.6(b)). Commercial high-pass filters [100]

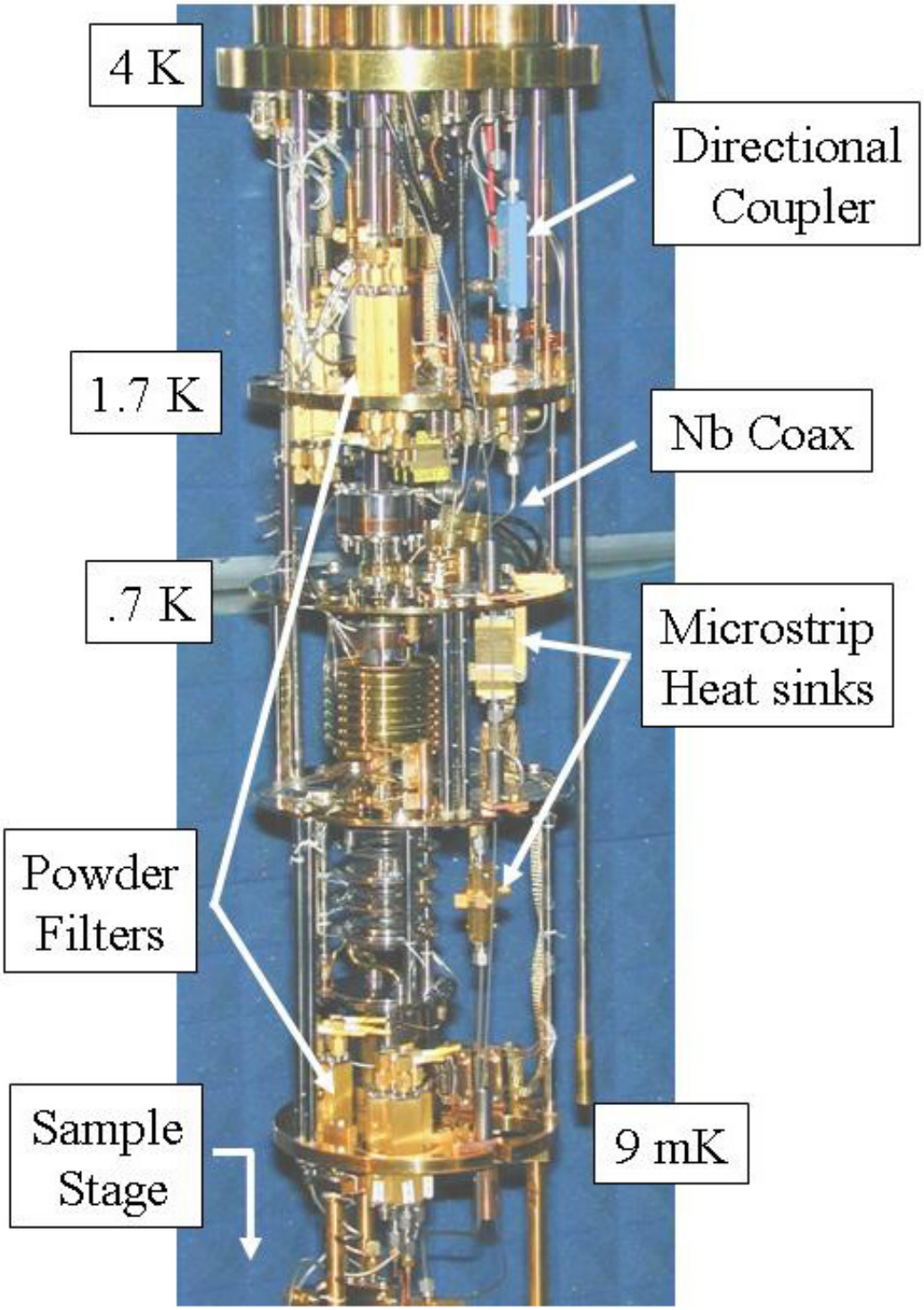

Figure 4.2: Image of dilution refrigerator: 4 K flange to mixing chamber.

(a)

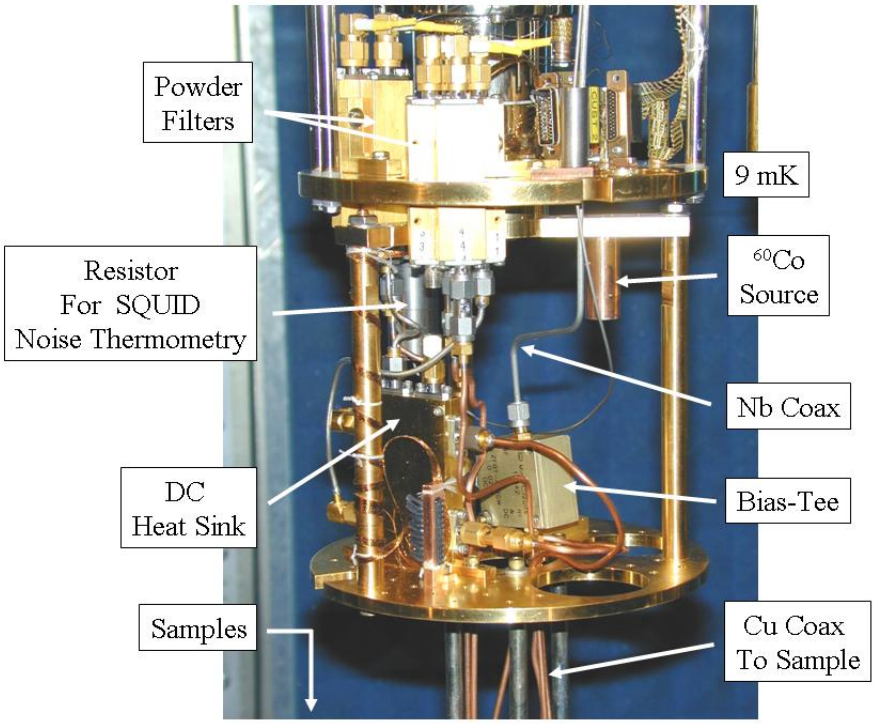

(b)

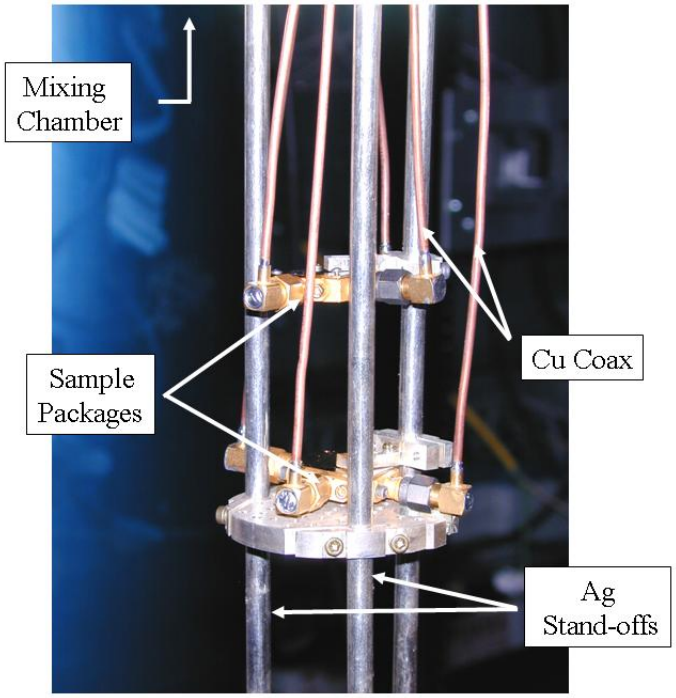

Figure 4.3: Dilution refrigerator. (a) Mixing chamber. (b) Sample stage.

Figure 4.4: Picture of shielded room and optical table. The ^{4}He dewar is visible behind the front pillar. A winch is used to raise the dewar over the refrigerator.

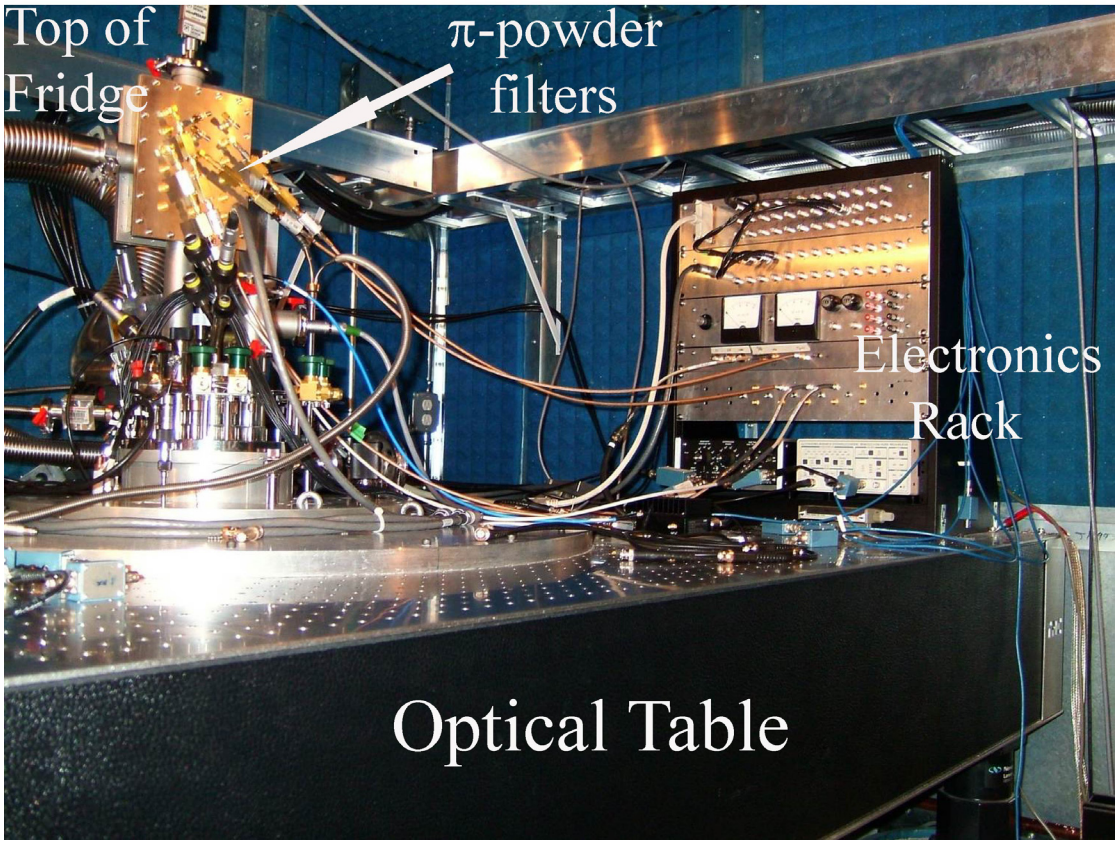

Figure 4.5: Picture of the top of the optical table. DC connections at the top of the fridge are made through π-powder filters. Battery-powered pre-amps and voltage sources as well as break-out boxes are shelved on the electronics rack.

(a)

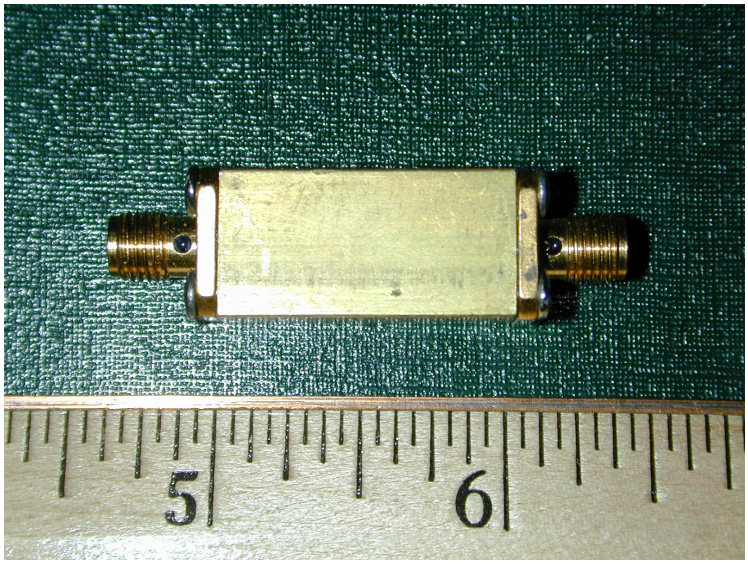

(b)

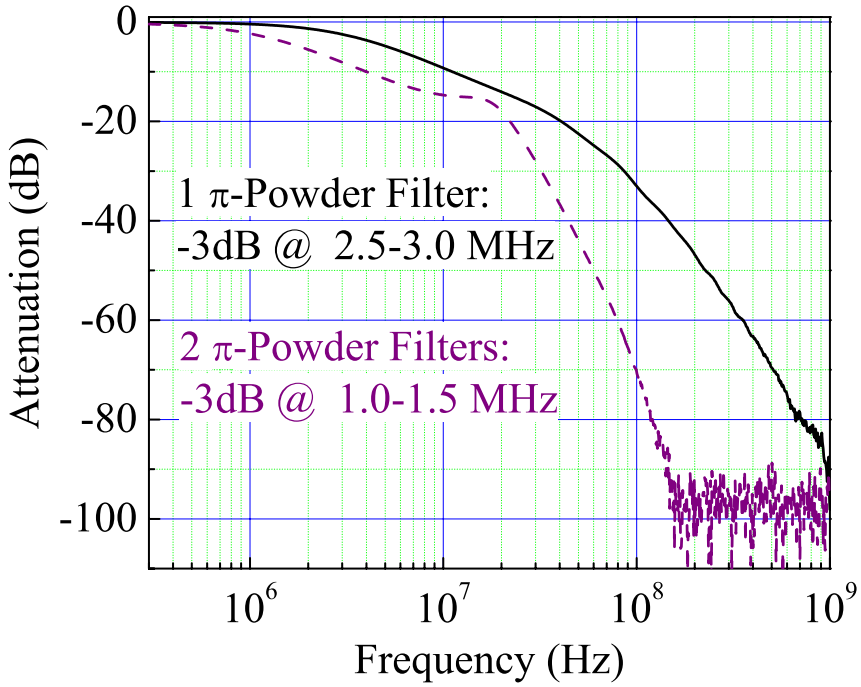

Figure 4.6: (a) Homemade π-powder filter (scale in inches). (b) The 3 dB point is 2.5 - 3.0 MHz for one filter (solid curve) and 1.0 - 1.5 MHz for two filters in series (dashed curve).

and attenuators [101] were used on the input microwave lines.

4.3 Refrigerator Wiring

A generalized schematic of the wiring inside the refrigerator is shown in Fig. 4.7.

Low-Frequency Circuitry

Between room temperature and the 1K pot stage, low-frequency signals were transmitted through 1 meter of lossy, flexible, stainless steel, coaxial cables [102]. These lines were heat sunk at 4K and connected to a bank of microwave filters at the 1K pot flange (Figs. 4.2 and 4.3). The filters were built in banks of four and were based on the same principle as the room temperature microwave pi-powder filters, but they did not include any pi-filters. The room temperature transfer characteristics of one microwave powder filter bank are displayed in Fig. 4.8(a). I do not have the transfer characteristics for the filters at low temperature.

Below the 1K pot flange, the lines consisted of 1 meter of lossy CuNi coaxial cables [103], and another bank of microwave filters at the mixing chamber flange. The transfer characteristics of the lossy coax are displayed in Fig. 4.8(b). For Devices 1 and 2, from the filters to the sample package, the connections were made via semi-rigid Cu coaxial cables. The total attenuation through each of these lines was ~ 90 dB above 800 MHz (Fig. 4.9). At 1 MHz and 10 MHz, the loss through the gate line, including the pi-powder filters at the top of the fridge, was ~ 2 dB and ~ 11

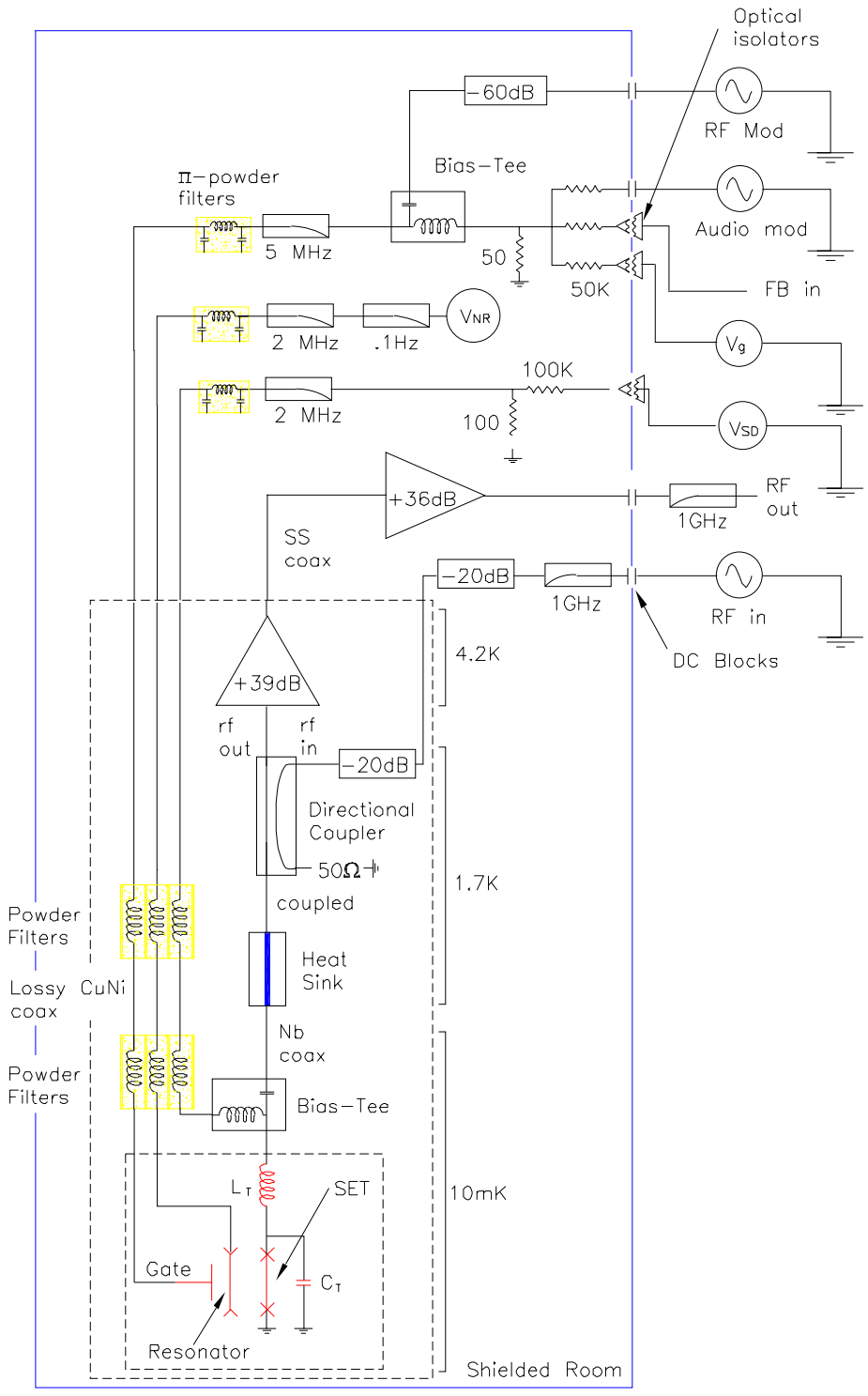

Figure 4.7: General schematic of circuitry inside the shielded room and the refrigerator.

(a)

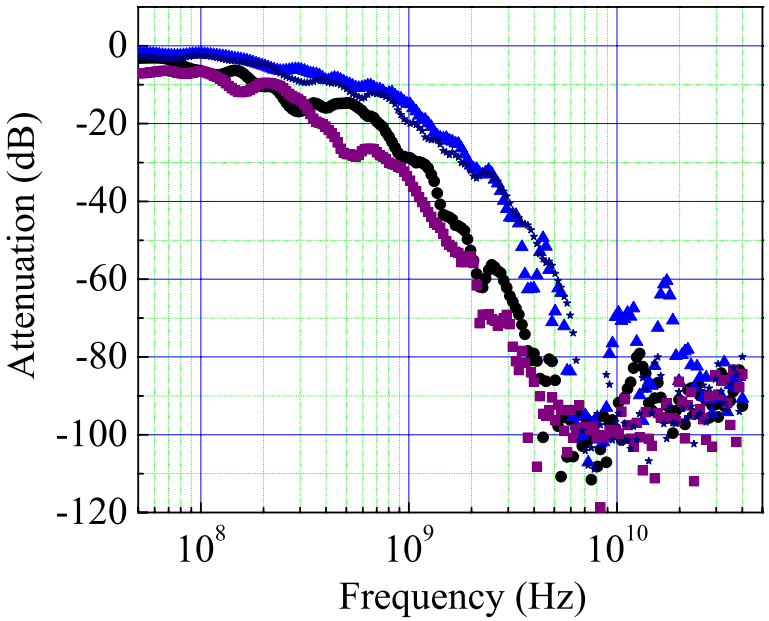

(b)

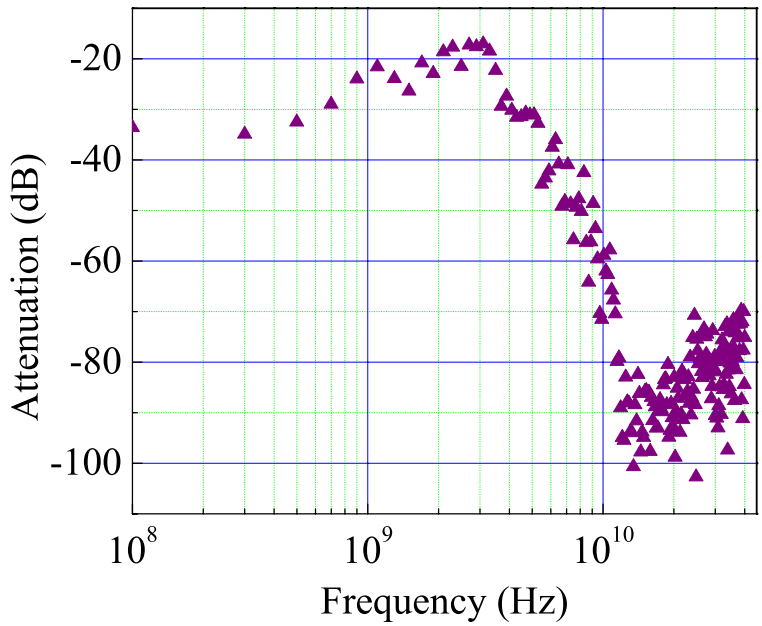

Figure 4.8: (a) S21 measurement of powder filters. (b) S21 measurement of 1 meter of lossy CuNi coax. Measurements made at room temperature.

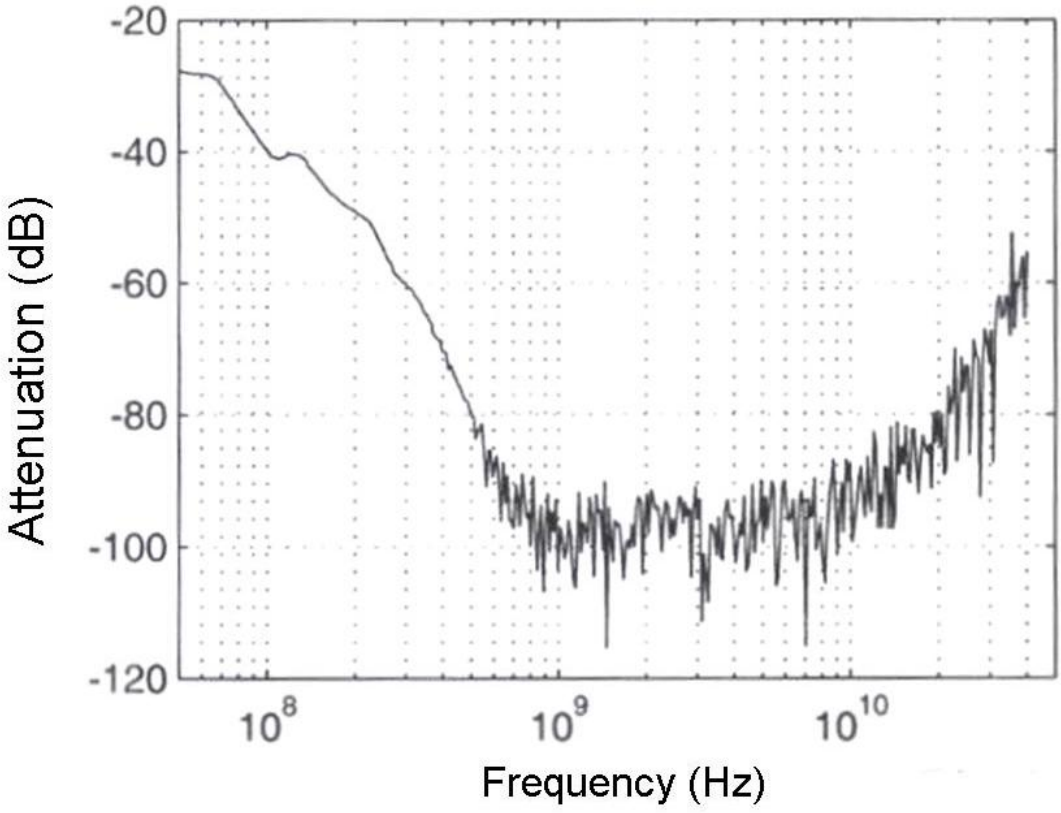

Figure 4.9: S21 measurement of gate line, including CuNi coax and two banks of powder filters. Measurement made at room temperature.

dB respectively.

Additionally, a dc heat sink was added at the mixing chamber after the powder filters (Fig. 4.3). The heat sink consisted of a center conductor of alternating Au and Al sections (see the microstrip heat sinks below) on top of a .4 mm thick quartz substrate inside a Au-plated RF-tight Cu package. We found 5 - 6 dB attenuation from 1 MHz to 1 GHz. For Devices 3 and 4, the total loss through the gate line at 1 MHz was found to be $\sim$ 7 dB.

Microwave Circuitry

For clarity, the discussion of the microwave circuit below is broken up into three regions defined by the ports of the directional coupler: "rf in", "coupled", and "rf out". Please refer to the general schematic in Fig. 4.7. However, note that the configuration of the refrigerator microwave circuit in Fig. 4.7 is for the measurement of Devices 2, 3 and 4. The configuration of the microwave circuit for the measurement of Device 1 is not shown but can be recovered by changing the position of the bias tee and heat sink as explained below.

At the input to the microwave circuit, at room temperature, the signal was attenuated through a 20 dB attenuator. From the room temperature attenuator to 4.2 K, the input microwave signal was transmitted through a semi-rigid stainless steel coaxial cable. The attenuation through the stainless steel coax was measured at room temperature to be $\sim$ 6 dB. The signal was attenuated by 20 dB in the cryostat before being fed into a directional coupler [104] at the 1K pot flange (Fig.

4.2). Between the input port of the directional coupler and the coupled port, the signal was attenuated by an additional 20 dB at 1.5 GHz at a temperature of 1 K.

The coupled region of the circuit was modified several times during the course of the measurements of Devices 1 - 4. For Device 1, the coupled port of the directional coupler was directed to a bias tee [105] at 1.7 K where the input rf signal was added to the dc bias V_{SD}. The output of the bias tee was directed to the mixing chamber plate via a niobium semi-rigid coaxial cable [106], clamped at various stages of the refrigerator for thermalization purposes. At the mixing chamber, the Nb coaxial cable was clapmed and connected to a Cu semi-rigid coaxial cable, which ran to the sample holder at the sample stage.

For the measurement of Devices 2, 3 and 4, the coupled port of the directional coupler was connected to a microstrip heat sink through a Nb semi-rigid coaxial cable. The heat sink was clamped at the 1K pot on the dilution refrigerator. The output of the heat sink was connected to the bias tee via a section of Nb semi-rigid coaxial cable. The bias tee was clamped at the mixing chamber. The output of the bias tee was connected to the sample package through a Cu semi-rigid coaxial cable.

The purpose of the microstrip heat sink was to thermalized the inner conductor of the coax while providing 50 Ω transmission. For the measurement of Device 2, the heat sink consisted of a 1.5 inch long, Au, 50 Ω microstip transmission line on a 0.4 mm thick quartz wafer housed in an RF-tight, Au-plated Cu package (similiar to the microstrip shown in Fig. 4.10(a)). At 1.5 GHz and a temperature of 77 k, the attenuation through the microstrip was less than 1 dB. For Devices 3 and 4 the center conductor of the microstrip was made of alternating sections of Au and Al

(a)

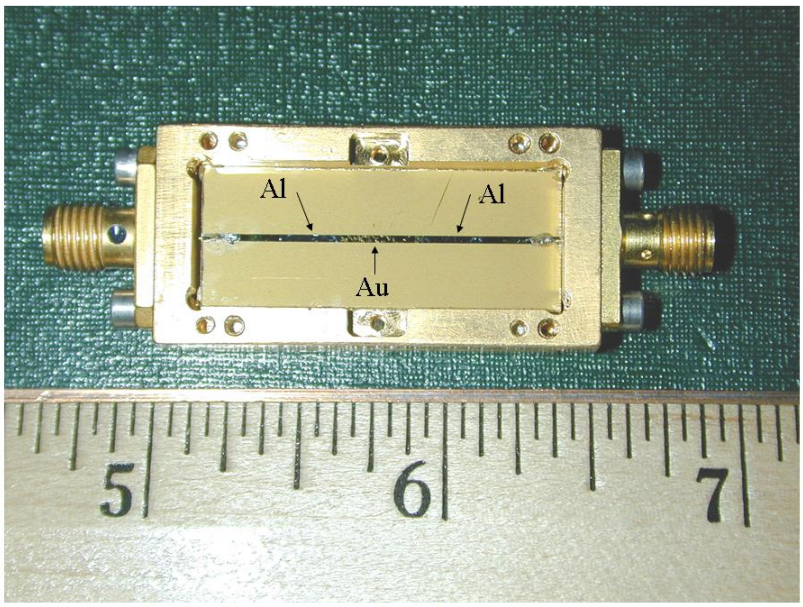

(b)

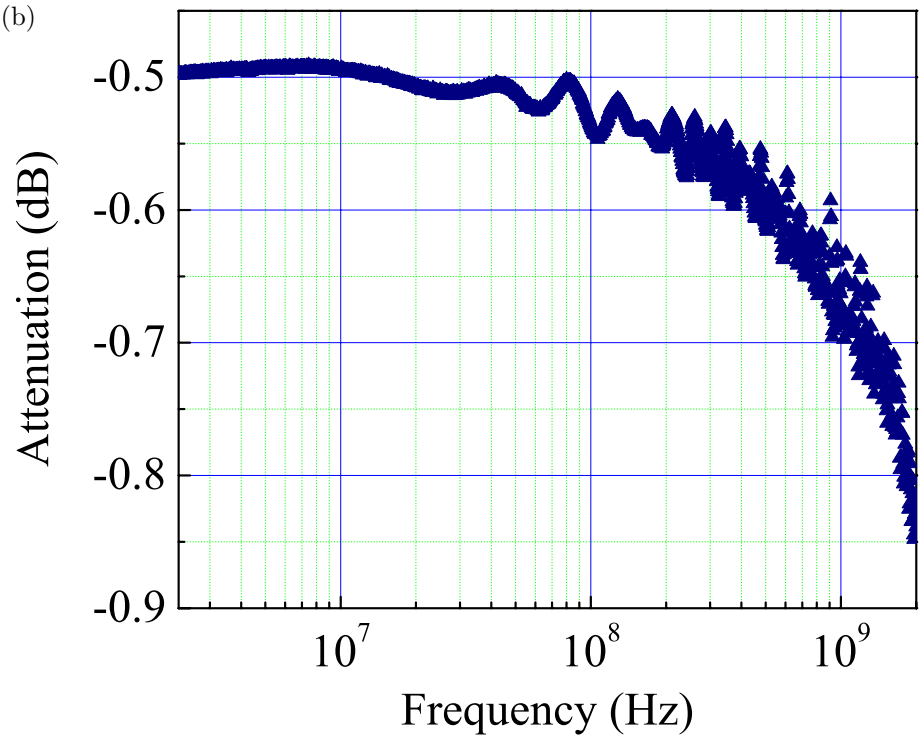

Figure 4.10: (a) Au/Al RF microstrip. Scale is in inches. (b) S21 measurement of Au/Al RF microstrip. Measurement made at 77 K.

(Fig. 4.10(a)). At 1.5 GHz and a temperature of 77 k, the attenuation through the Au/Al microstrip was also less than 1 dB (Fig. 4.10(b)).

The transfer characteristics from the input of the fridge, through the directional coupler, to the bias tee, for the wiring of Devices 3 and 4 are displayed in Fig. 4.11. At 1.5 GHz, including the losses in the attenuator (20 dB), the directional coupler (20 dB) and the SS semi-rigid coax (6 dB), 4 dB of attenuation is unaccounted for in this section of the circuit.

On the return path from the directional coupler (rf out) the signal was sent through another section of niobium semi-rigid coaxial cable to an ultra-low noise cryogenic HEMT-amplifier [107], sitting in the helium bath at 4.2 K. The HEMT-amplifier had a gain of 39 dB between 1 and 1.8 GHz (Fig. 4.12(a)), and noise temperature of 2 K. A semi-rigid stainless steel coaxial cable connected the HEMT-amplifier output to a Mini-Circuits room-temperature amplifier [108] with a gain of 36 dB. The attenuation in the stainless steel coax was found to be 6 dB at 1.5 GHz at room temperature. The transfer characteristics of the room-temperature amplifier are shown in Fig. 4.12(b).

From Fig. 4.12, at 1.5 GHz, we see that the total gain of the amplifiers plus the stainless steel coaxial cable was approximately 72 dB. From Fig. 4.11, we see that approximately 4 dB was lost in the coupled portion of the microwave circuit for the measurement of Devices 3 and 4. There was an additional loss of $\sim$ 4 dB in the coax leading out of the shielded room. We would thus expect a measurement circuit gain of $\sim$ 64 dB. For Devices 3 and 4, this agrees to within 3 dB of the gain determined using the shot noise calibration (see Appendix B). Unfortunately, we

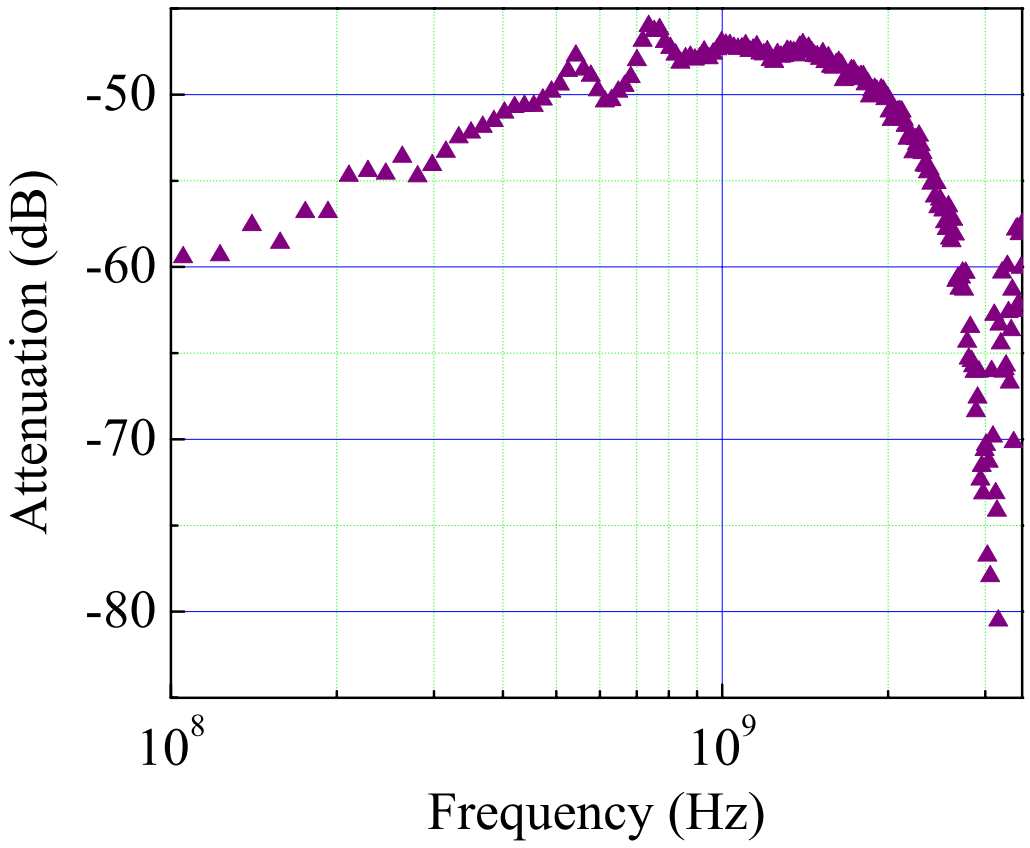

Figure 4.11: S21 measurements of the microwave circuit from the input of the fridge to the bias tee, for the measurement of devices 3 and 4. Measurements done at room-temperature. Including the 20 dB lost through the attenuator at the input of the directional coupler, the 6 dB lost through the stainless steel semi-rigid coaxial cable, and the 20 dB lost between the input port and coupled port of the directional coupler, $\sim$ 4 dB attenuation was unaccounted for at 1.5 GHz. This was probably due to connections, the bias tee, and the RF microstrip.

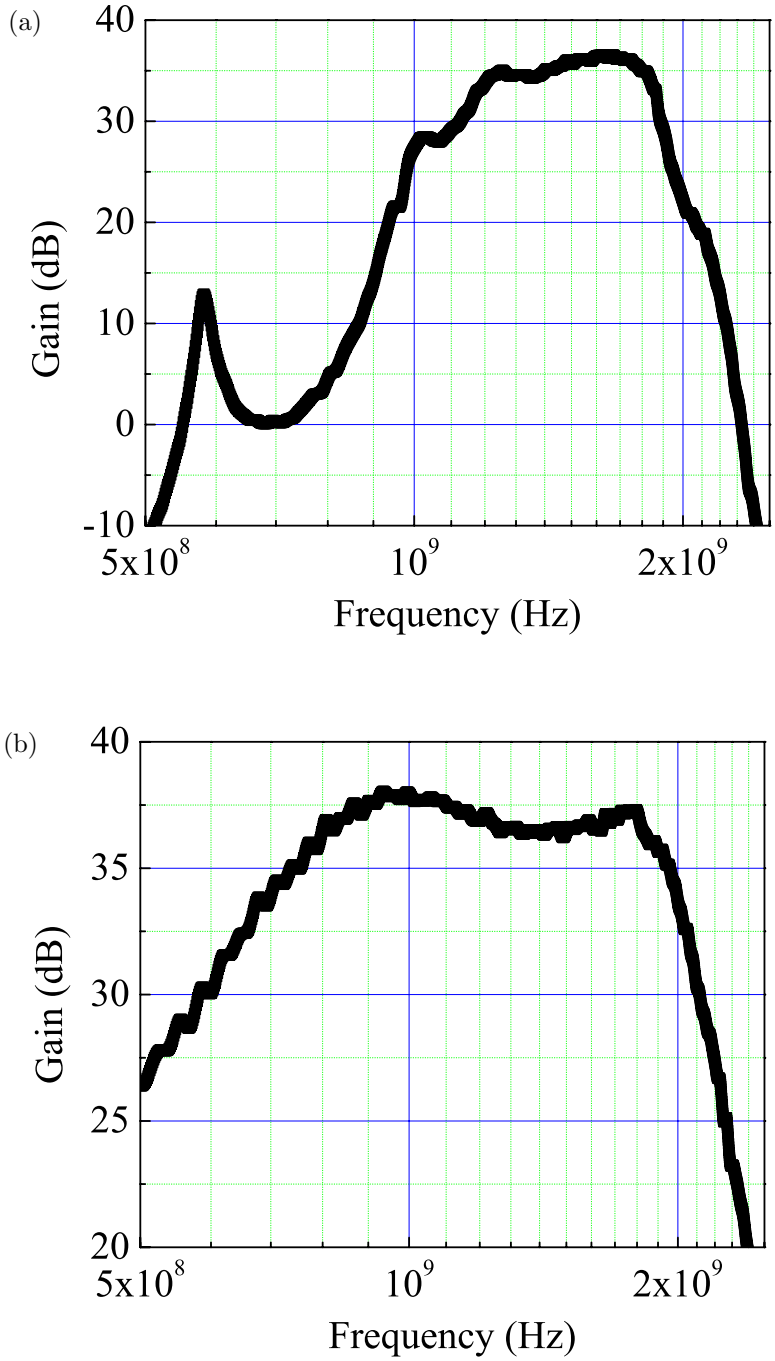

Figure 4.12: Gain of microwave amplifiers. (a) S21 measurement of cryogenic HEMT amplifier plus 4 ft of stainless steel semi-rigid coaxial cable. Measurement made at 4 K. (b) S21 measurement of Mini-Circuits room-temperature amplifier.

Table 4.1: Measurement circuit gain and noise temperature Devices 1 - 4.

Device	T_n^{det} (K)	G (dB)
1	-	-
2	20	64
3	12.6	67
4	13.4	66.5

do not have the data for the transfer characteristics of the coupled portion of the microwave circuit for the measurement of Devices 1 and 2. Table 4.1 lists the noise temperature and gain of the measurement circuit for Devices 1 - 4.

Thermometry

The temperature of the sample package was monitored using a RuO chip resistor [109]. The chip resistor was glued to the sample package using GE varnish [93]. The resistance of the chip was monitored using four-terminal measurements and a battery-powered resistance bridge [110]. Twisted pairs connected the bridge to the resistor. From room temperature to 1 K, the pairs were made of Constanan. From 1 K to the mixing chamber, CuNi-clad NbTi pairs were used.

The calibration of the RuO resistance was checked below 20 mK using nuclear orientation thermometry [111] [112]. At a mixing chamber temperature of 10 mk, the uncertainty in the calibration was approximately $\pm$ 1.5 % for 300 seconds of

counting. Above 20 mK, the calibration of the RuO resistance was checked with dc SQUID thermometry [113]. The dc SQUID [114] was installed on the 1 K stage, with the input connected to a 10 mΩ Cu film resistor at the mixing chamber via homemade NbTi twisted pair. The SQUID, twisted pairs, and film resistor were all shielded using various diameter Nb tubing. At 100 mK, the uncertainty in the sample-stage temperature was dominated by the uncertainty in the measurement of the RuO resistance and was approximately ± 1.0 mK.

Chapter 5

The RFSET

In this chapter I discuss our RFSET reflectometry measurement scheme. The chapter is broken into two sections. In the first section I discuss the basics of the reflectometry measurement and circuitry. In the second section I discuss the feedback technique with which we used to stabilize the RF-SET gain in the presence of low-frequency charge noise.

5.1 RFSET Reflectometry

RF-SET reflectrometry was performed using the measurement circuit shown in Fig. 5.1. The basic process was first described by Schoelkopf et al. [41] and can be summarized in three steps: a microwave carrier resonant with the microfabricated L_TC_T circuit is applied to the port "rf in" and directed to the sample via the directional coupler; a fraction of the incident signal is reflected from the $\mathrm{L}_T\mathrm{C}_T\mathrm{R}_{SET}$ circuit and directed back through the directional coupler and the two amplifier stages to the port "rf out"; from rf out, the signal is fed into a microwave mixer [115] for homodyne detection.

In essence, the measurement of the reflected signal provides a measurement of the SET impedance R_S via $R_S = \partial \mathrm{I}_{SD}(\mathrm{V}_{SD},\mathrm{Q}_g)/\partial \mathrm{V}_{SD}$. This is to be distinguished from the quantity R_Σ defined in Appendix B which is R_S in the limit of large SET

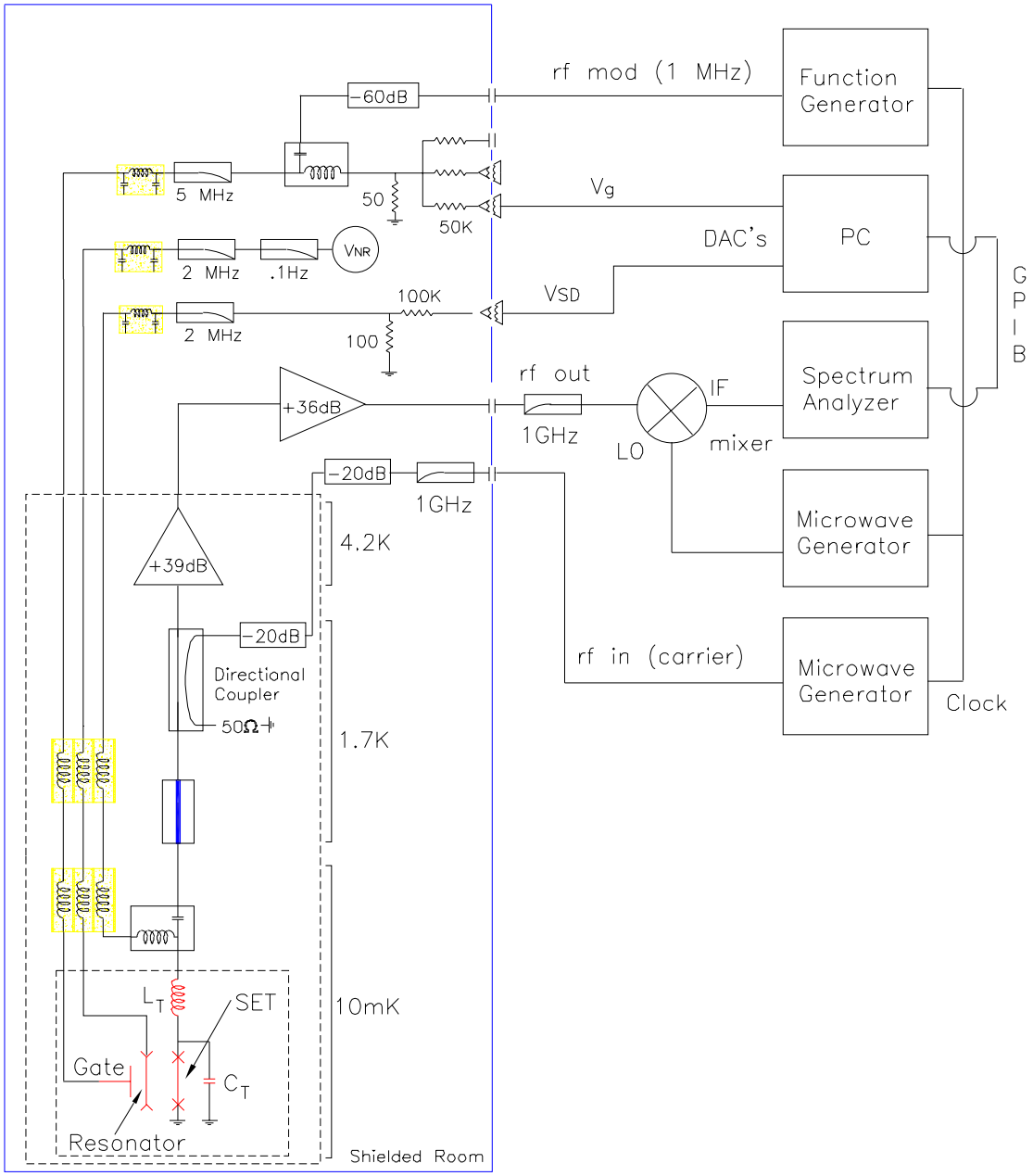

Figure 5.1: Circuit schematic for RFSET reflectometry. Components left unlabeled here are labeled in Figure 4.7.

source-drain bias, V_{SD}. As I_{SD} is a sensitive function of the gate charge Q_g (see Appendix B), both R_S and the reflected signal are as well. As a result, modulation of Q_g is detected as modulation of the amplitude of the reflected microwave signal, and can be recovered by mixing the reflected signal with the original carrier signal (homodyne detection). It is the sensitive dependence of the reflected signal on Q_g which we exploit to perform our displacement detection. The remainder of the section is dedicated to developing a quantitative understanding of this dependence and discussing how, experimentally, we maximize it.

The Relationship Between Γ and Q_g

The dependence of the reflected signal on Q_g can be made explicit by first writing the reflected voltage signal as

$$v_r = \Gamma v_c \cos \omega_T t \tag{5.1}$$

and the reflection coefficient as

$$\Gamma = \frac{Z_{LCR} - Z_o}{Z_{LCR} + Z_o}, \tag{5.2}$$

where v_c is the amplitude of the incident microwave carrier, $\omega_T = \sqrt{1/L_T C_T}$ is the tank circuit resonant frequency, $Z_{LCR} = L_T/R_S C_T$ is the transformed SET impedance at the tank-circuit resonance, and $Z_o = 50\ \Omega$ is the characteristic transmission line impedance.

For the measurement of Devices 1 - 4, $Z_{LCR} \ll Z_o$ (see Appendix B), so I can expand Eq. 5.2 as

$$\Gamma \approx 1 - \frac{2Q_T^2 Z_o}{R_S} \tag{5.3}$$

where $\mathrm{Q}_T \approx \sqrt{L_T/C_T}1Z_o$. Using Eq. 5.1 I find then that

$$v_r \approx \left(1 - \frac{2Q_T^2 Z_o}{R_{SET}}\right) v_c \cos\omega_T t. \tag{5.4}$$

In general, there is no closed-form expression for R_S in terms of Q_g. However, from the considerations of Appendix B, I know we can approximate I_{SD} near the onset of tunneling as a sinusoidal function of Q_g with period-e:

$$I_{SD} \approx \frac{e}{2R_\Sigma C_\Sigma} \left(\sin(\pi Q_g/e) + 1\right). \tag{5.5}$$

I can write R_S as

$$R_S = \frac{\partial V_{SD}}{\partial I_{SD}} \simeq \frac{V_{SD}}{I_{SD}} \approx \frac{2R_\Sigma}{\sin(\pi Q_g/e) + 1}, \tag{5.6}$$

where I have assumed that $\mathrm{V}_{SD} \approx e/C_\Sigma$.

From Eq. 5.4, I expect v_r also to be sinusoidal in Q_g but with a phase shift of π-radians from I_{SD}:

$$v_r = \left(1 - \frac{Q_T^2 Z_o}{R_\Sigma} \left(\sin(\pi Q_g/e) + 1\right)\right) v_c \cos\omega_T t. \tag{5.7}$$

Figure 5.2 shows a plot of v_r vs. Q_g for Device X. While not exactly sinusoidal, the reflection coefficient is seen to be e-periodic in Q_g, with maxima occuring at minima in I_{SD}. For this particular sample $R_\Sigma \sim 50$ kΩ and $Q_T \sim 10$. Plugging these values into Eq. 5.7, I see that the depth of modulation, $M = 20\log(\Gamma_{max}/\Gamma_{min})$, is on the order of 2 dB, consistent with the ~ 2.5 dB seen in the plot, and of the same order of magnitude as the values calculated for the Devices 1 - 4.

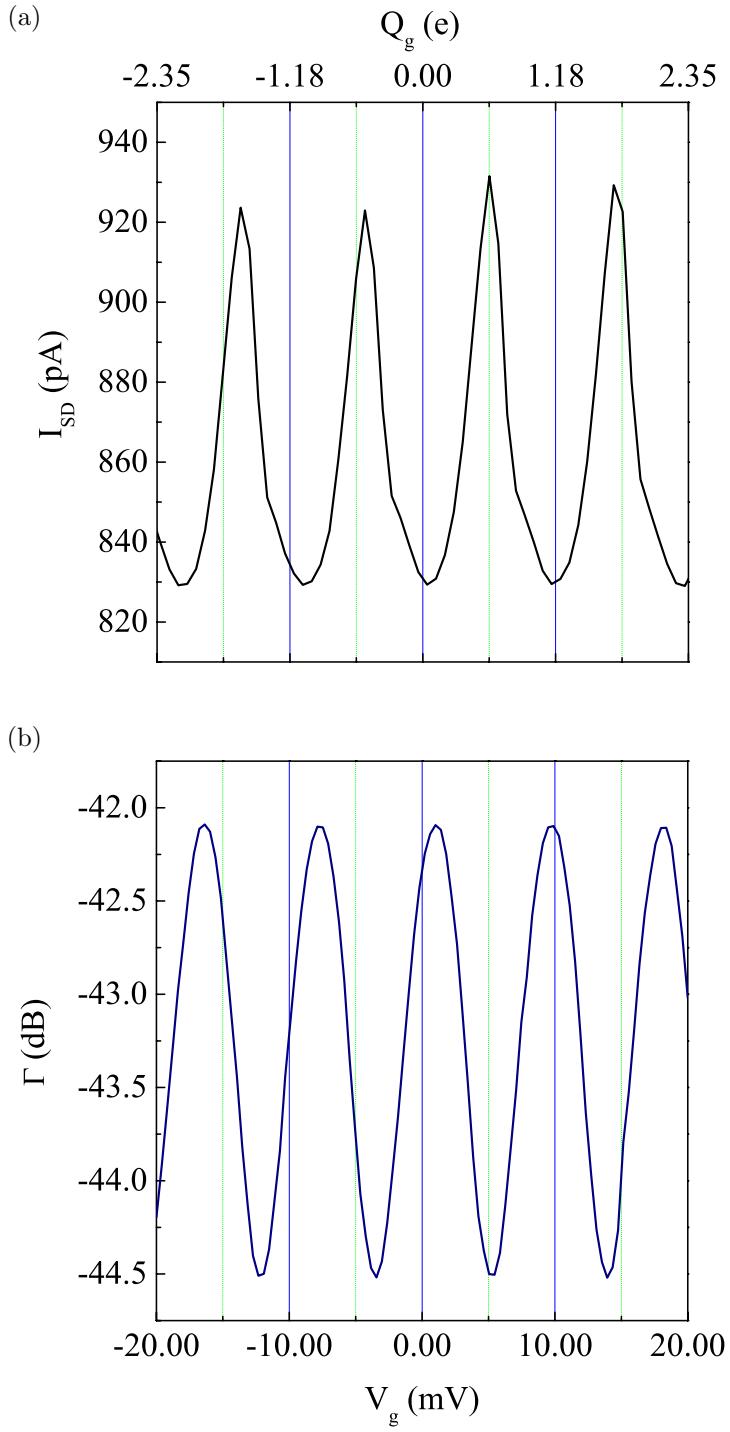

Figure 5.2: (a) Plot of I_{SD} vs. Q_g at $V_{SD} \approx \frac{e}{C_\Sigma}$ and (b) the corresponding reflection coefficient Γ. Due to an offset in Q_g, the maxima in I_{SD} do not occur exactly at Q_g = .5 e. Device X.

Charge Sensitivity

The utility of the transfer function Γ-Q_g in Fig. 5.2 is that it specifies, for a given V_{SD} bias, the Q_g bias points at which one can expect Γ and hence v_r to be maximally responsive to small changes in the SET-gate charge. Because the noise floor of our charge-detection scheme is dominated by measurement circuit noise (see Appendix B), the bias points which yield maximum charge responsivity also yield the maximum charge sensitivity [66].

For the small-signal analysis, I set $Q_g = Q_{g,o}+Q_g(t)$, where $Q_{g,o}$ is the bias point set by the external source V_g, and $Q_g(t) \ll Q_{g,o}$ is the time-dependent charge signal we wish to measure. From Fig. 5.2, I see that the maximum response occurs for $Q_g \approx$ n+e/4. Plugging Q_g into Eq. 5.7 and expanding about $Q_{g,o}$ =e/4, I find

$$v_r \approx (\Gamma_o + \Delta\Gamma)\, v_c \cos \omega_T t, \tag{5.8}$$

where

$$\Gamma_o = \left(1 - \frac{Q_T^2 Z_o}{R_\Sigma \sqrt{2}} \left(1 + \sqrt{2}\right)\right) \tag{5.9}$$

and

$$\Delta\Gamma = -\frac{Q_T^2 Z_o}{R_\Sigma} \frac{\pi}{\sqrt{2}e} Q_g(t). \tag{5.10}$$

From Eq. 5.8, I see that this measurement technique is equivalent to amplitude-modulation: the signal, a time-dependent charge on the SET gate, modulates the amplitude of an externally applied carrier. In most of our measurements, $Q_g(t)$ was a sinusoidal signal. So I set $Q_g(t) = Q_1 \cos(\omega_1 t)$, where Q_1 and ω_1 are the charge

modulation amplitude and frequency respectively. Thus Eq. 5.8 becomes

$$\begin{aligned} v_r &\approx v_c\Big[\Gamma_o \cos\omega_T t + \\ &\quad - \frac{Q_T^2 Z_o \pi}{2\sqrt{2} R_\Sigma e} Q_1 \Big(\cos\left(\omega_T - \omega_1\right) t + \cos\left(\omega_T + \omega_1\right) t \Big) \Big] \end{aligned} \tag{5.11}$$

After homodyne mixing, the reflected signal takes the form:

$$v_r \approx -v_c \frac{Q_T^2 Z_o}{R_\Sigma} \frac{\pi}{2\sqrt{2} e} Q_1 \cos\omega_1 t, \tag{5.12}$$

where I have just retained the terms with frequency ω_1, which, in practice, can be achieved with simple filtering.

It is perhaps helpful to stop here and comment briefly on the importance of the tank circuit in the RFSET measurement. Without the tank circuit and the impedance matching between the transmission-line impedance Z_o and SET impedance R_S, v_r would be reduced by a factor of $Q_T^2 \sim 100$. If you consider the RFSET electrometer to be a charge amplifier, then this can be thought of as losing a factor of 100 or 40 dB in the amplifier gain.

Eq. 5.12 specifies what signal to expect for a given gate charge modulation. I can estimate the signal-to-noise ratio of the charge-detection scheme using the measurement circuit noise temperature $\mathrm{T_n^{det}}$, discussed in Appendix B. The rms voltage noise per frequency band referred to the input of the detector is given by [116]

$$\sqrt{S_V} = \sqrt{\frac{k_B \mathrm{T_n^{det}} Z_o}{2}}. \tag{5.13}$$

Using Eq. 5.13 and the rms amplitude of Eq. 5.12, the signal-to-noise ratio

can be defined roughly as

$$\frac{S}{N} \approx \left| \sqrt{\frac{Z_o}{4k_B T_n^{det} \Delta B}} \frac{Q_T^2}{R_\Sigma} \frac{\pi Q_1 v_{carrier}}{\sqrt{2}e} \right|^2, \tag{5.14}$$

where ΔB is the measurement bandwidth.

The charge sensitivity, in units of $e_{rms}/\sqrt{Hz}$, is then defined by calculating the charge modulation that yields $\frac{S}{N}$=1:

$$\sqrt{S_Q} = \frac{\Delta Q}{e\sqrt{\Delta B}} \approx \sqrt{\frac{8k_B T_n^{det}}{Z_o}} \frac{R_\Sigma}{\pi Q_T^2 v_{carrier}}. \tag{5.15}$$

This result can be compared with what we have found experimentally. For example, Fig. 5.3 shows the sinusoidal modulation of v_r of Device X. Here, a carrier signal with frequency $\omega_T/2\pi$ = 1.17 GHz and power

$$P_{carrier} = 10\log(\frac{v_{carrier,rms}^2}{50\Omega * mW}) \approx -29\ dBm$$

is applied to rf in. Additionally, a modulation signal of ω_1= 1 MHz and Q_1 = 0.13 e_{rms} is applied through rf mod (Fig. 5.1) to the SET gate.

Fig. 5.3(a) displays $P_r = 10\log(v_{r,rms}^2/50\Omega * mW)$ before homodyne detection. Evident are the sidebands at ± 1 MHz from the carrier signal. Fig. 5.3(b) shows the reflected signal, P_r after mixing, and demonstrates the recovery of the 1 MHz modulation. From the ratio of the power in the 1 MHz band P_{1MHz} to the power level of the background P_o, I can find the charge sensitivity at 1 MHz:

$$\sqrt{S_Q} = \frac{Q_1}{\sqrt{\Delta B}} 10^{-\frac{\mathrm{SNR}}{10}}, \tag{5.16}$$

where SNR(dBm) = $P_{1MHz} - P_o$ is the signal-to-noise ratio, and ΔB is the resolution bandwidth of the spectrum analyzer. For the values in Fig. 5.3, I find $\sqrt{S_Q} \approx 65$

(a)

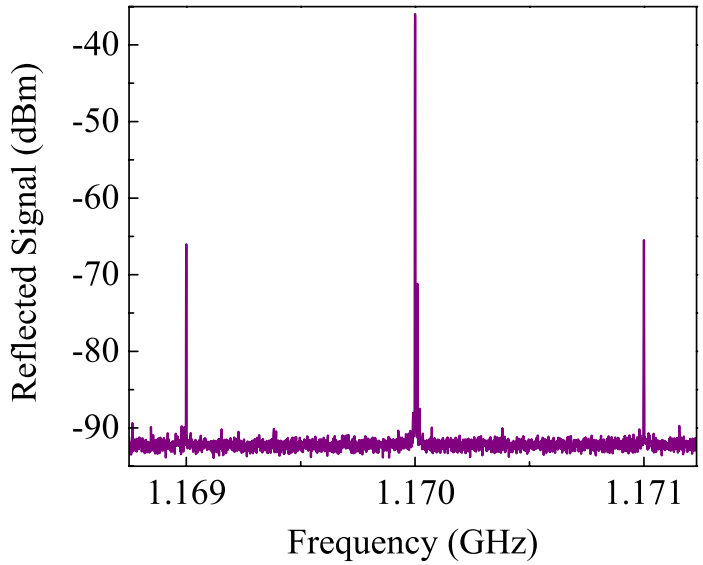

(b)

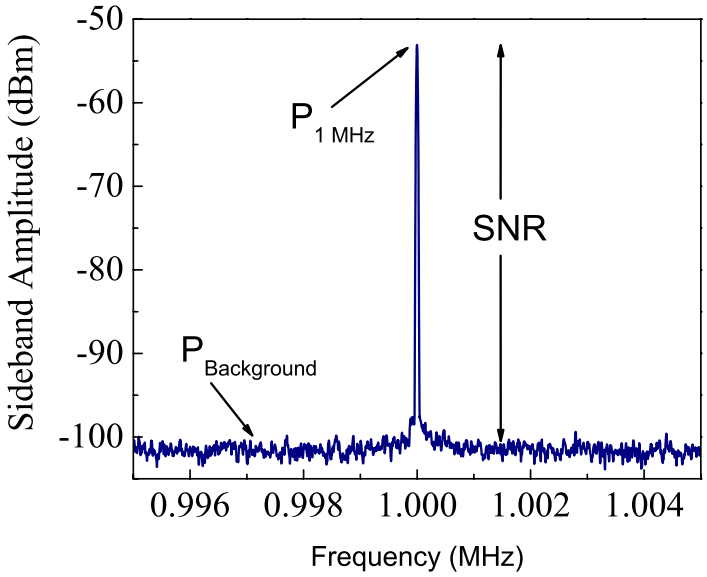

Figure 5.3: (a) Power spectrum of rf out, before mixing. (b) Power spectrum of rf out after mixing, demonstrating the recovery of the 1 MHz gate modulation. The difference in background level between (a) and (b) is due to mixing (-8 dB), an extra amplification stage before mixing (+16 dB), insertion loss in power-splitters (-8 dB), and a change in resolution bandwidth from 1 kHz to 100 Hz. Device Y.

$\mu e_{rms}/\sqrt{Hz}$. In comparison, using Eq. 5.15 and the parameters for this device ($v_c \sim$ 3 $\mu \mathrm{V}_{peak}$ after $\sim$ 72 dB attenuation, R_Σ=80 k Ω, $\mathrm{T_n^{det}} \sim$ 22 K, $Q_T \sim$ 8), I calculate $\sqrt{S_Q} \approx 10^{-3} e_{rms}\sqrt{Hz}$.

The Derivative Map

There are two main factors contributing to the discrepancy between the theoretical estimate of the charge sensitivity and what we determined experimentally. The first is the sinusoidal approximation of I_{SD} (Q_g). This approximation simply assumes that the SET is in the normal state and biased at the onset of tunneling. In fact, for the data displayed in Fig. 5.3, the SET was in the superconducting state and biased around a DJQP resonance (see Appendix B). Second, the estimate does not take into account the self heating of the SET, which, while not a problem at that DJQP resonance, could certainly be a factor for bias points near the onset of tunneling. Therefore, to obtain an accurate estimate of the charge sensitivity as a function of the bias-points V_{SD} and Q_g (V_g), I would need to model both superconducting processes and self heating on top of the Coulomb-blockade effects. This would be an involved numerical task.

For an existing device, the same information can be obtained more efficiently by simply taking an $I_{SD}V_{SD}V_g$ map and numerically calculating the curvature. Going back to Eq. 5.3, it is simple to see that measuring the modulation of the reflection coefficient, Γ, is equivalent to measuring the second-order derivative of I_{SD}

with repsect to V_{SD} and V_g:

$$\Gamma \approx 1 - \frac{2Q_T^2 Z_o}{R_{SET}} \approx 1 - 2Q_T^2 Z_o \frac{\partial I_{SD}}{\partial V_{SD}}. \tag{5.17}$$

The small V_g or Q_g response of is thus

$$\Delta\Gamma(t) = \frac{\partial \Gamma}{\partial Q_g}\Delta Q_g(t) = -2Q_T^2 Z_o \frac{\partial^2 I_{SD}}{\partial V_{SD}\partial Q_g}\Delta Q_g(t). \tag{5.18}$$

The charge sensitivity is then

$$\sqrt{S_Q} = \sqrt{\frac{k_B \mathrm{T_n^{det}}}{Z_o}} \left(\frac{\partial^2 I_{SD}}{\partial V_{SD}\partial Q_g}\right)^{-1} \frac{1}{Q_T^2 v_c}, \tag{5.19}$$

where Q_g is in units of e and v_c should be in units of V_{peak}. Additionally, the response has been divided by a factor of 2 to account for mixing.

Figures 5.4 and 5.5 display plots of $I_{SD}V_{SD}V_g$, the numerical second-derivative, and the modulated reflected signal for Device X. The $I_{SD}V_{SD}V_g$ map was taken in the superconducting state (see Appendix B for a description of how this is done). The numerical derivatives of the IV-map (Fig. 5.5(a)) were then taken using Savitzky-Golay filtering [117]. Finally, the reflected-signal modulation was measured (Fig. 5.5(b)) by applying a charge modulation of amplitude 0.02 e_{rms} and frequency 1 MHz to the SET gate and a carrier signal of P_c = -26 dBm to rf in. A computer was used to increment V_{SD} and V_g. For each bias point, the modulated reflected-signal amplitude was measured with an RF lock-in and recorded using GPIB (see Fig. 5.1).

Comparing Fig. 5.5(a) and Fig. 5.5(b), I find agreement to within a factor of two between the numerically calculated derivative and the measured reflection modulation. Using Eq. 5.19, I calculate the sensitivity at the bias point $V_{SD} \approx$ 0.4 mV and $V_g \approx$ - 9.8 mV (the DJQP resonance) to be $\sim$ 70 $\mu e_{rms}/\sqrt{Hz}$, which

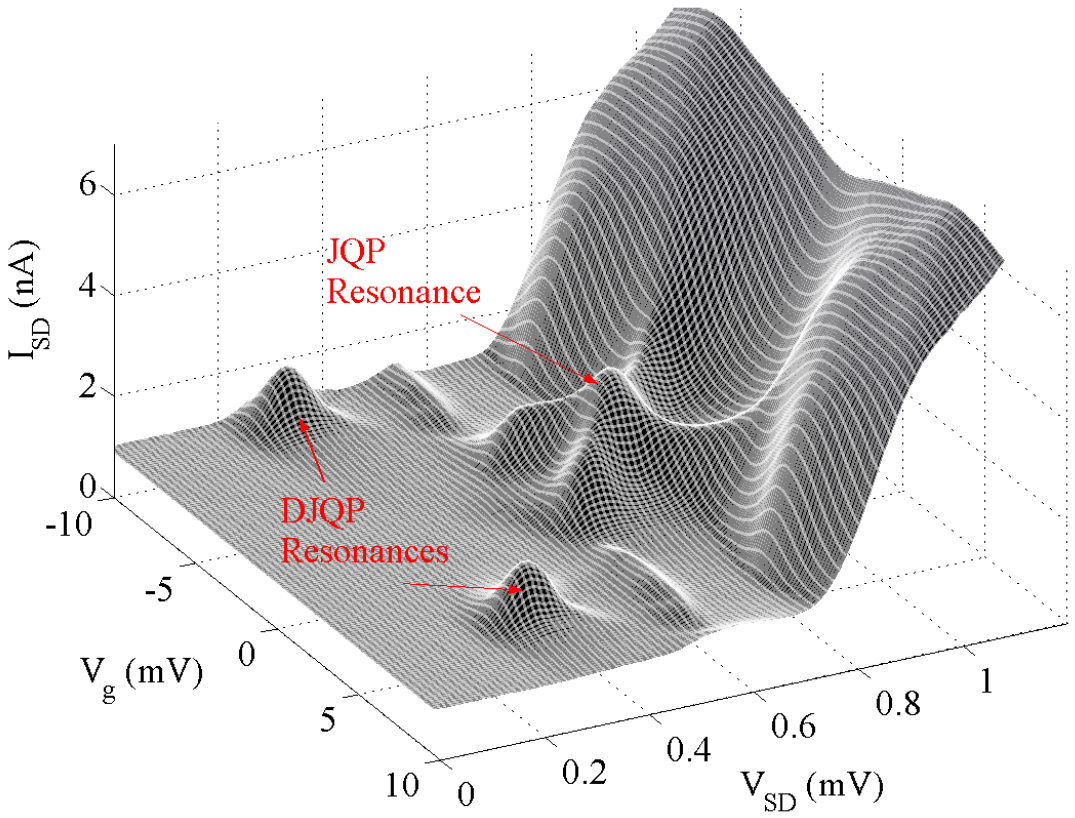

Figure 5.4: $I_{SD}V_{SD}V_g$ map in the superconducting state.

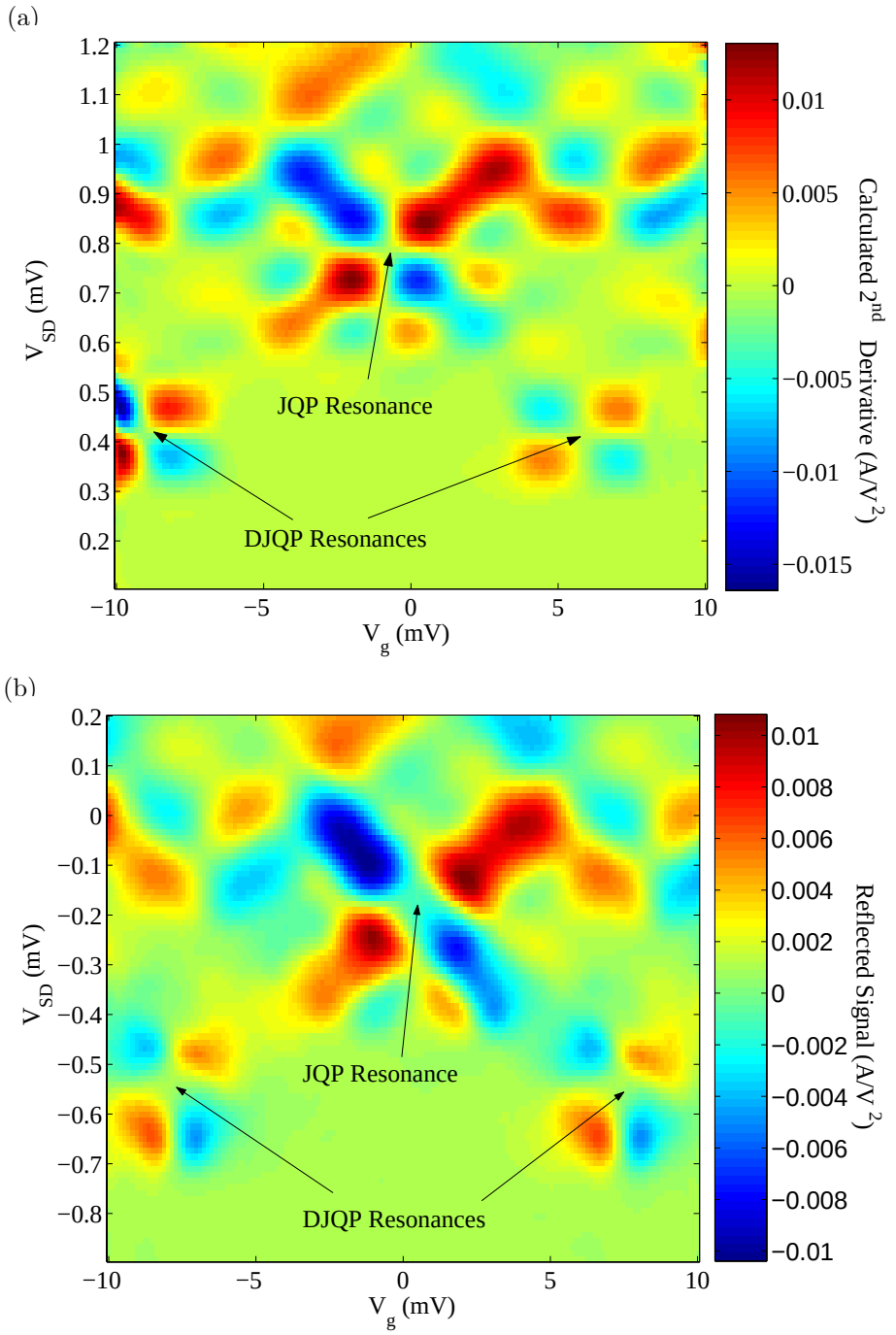

Figure 5.5: (a) Plot of the numerical derivative $\frac{\partial^2 I_{SD}}{\partial V_{SD} \partial V_g}$ of the superconducting IV map in Figure 5.4. (b) Plot of the measured reflected signal modulation $\Delta\Gamma$ for the same range of V_g and V_{SD} as in (a). Here $\Delta\Gamma$ has been scaled so that $\frac{\Delta\Gamma}{2Q_T^2 Z_o \Delta V_g}$ is the quantity plotted. Device Y.

is in good agreement with the 65 $\mu e_{rms}/\sqrt{Hz}$ calculated from the signal-to-noise ratio measured in Fig. 5.3. Here, a carrier amplitude of 4 μV_{peak} (-26 dBm applied, -72 dB attenuatation in the circuit) was used to construct the reflection map. To perform the conversion from V_g to Q_g, it is necessary to know that $C_g = 11$ aF for this device. I also used $T_n^{det} \sim 22$ K and $Q_T \sim 8$ for the calculation.

The value of the derivative map is that it allowed us to quickly and accurately determine which points in the V_{SD}-V_g plane yielded maximum gain and hence maximum charge sensitivity (the dark red and blue regions of Fig. 5.4(a). We then biased the SET at one of these points, turned on the 1 MHz rf mod and the carrier signal, and adjusted v_c until we maximized the 1 MHz sideband, which we measured with the rf lock-in or spectrum analyzer.

Close comparison of Fig. 5.5(a) and Fig. 5.5(b) reveals a problem. While the calculated curvature and measured reflection amplitude are in close ageement, it is clear that the reflection amplitude map is shifted by ~ 3 mV along the V_g axis. This is a result of the slow SET background charge drift and the fact that the $I_{SD}V_{SD}V_g$ map and the reflection map were taken several minutes apart. Especially in the presence of large electric fields, which were necessary for RFSET displacement detection, the SET background charge was so unstable that retuning of the V_g bias point was necessary every few seconds. Clearly this is not ideal if one needs to average for times longer periods of time. In the next section, we discuss the engineering that allowed us to overcome this problem.

5.2 Gain Stabilization

In our SET's, charge-drift and telegraph noise tended to destabilize the SET gain, and limit the detection time to several minutes or less before retuning of V_g was required. To overcome this, we implemented a feedback scheme to keep the amplitude of the 1 MHz reflection sideband maximized.

The basic idea of the feedback technique can be understood by refering to Fig. 5.6. The plot shows the amplitude of the 1 MHz sideband as a function of V_g (Q_g). As one would expect from the discussion in the previous section, the sideband amplitude is a maximum with respect to V_g (Q_g) when $\partial \mathrm{I}_{SD}/\partial \mathrm{V}_g$ is a maximum. This occurs twice for each e-period, with the difference in height of the two peaks directly related to the difference in the magnitude of the positive and negative $\mathrm{I}_{SD}\mathrm{V}_g$ slopes. Obviously, for maximum gain, I would like to set V_g to bias position A (or an integer multiple of e from position A).

To keep the SET biased at point 'A', I consider the curvature of the sideband response. For small displacement from point 'A', the sideband response is approximately quadratic. Therefore, if I apply a small $Q_g(t)$ modulation, with amplitude $C_g\Delta \mathrm{V}_g \ll$ e and frequency ω_A, on top of the initial V_g=A bias, I expect to amplitude-modulate the 1 MHz sideband at $2\omega_A$ (Fig. 5.7(a)):

$$v_r \propto Q_g(t)^2 \cos\omega_1 t \propto \frac{(C_g \Delta V_g)^2}{4} \left[2\cos\omega_1 t + \cos(\omega_1 + 2\omega_A)t + \cos(\omega_1 - 2\omega_A)t\right].$$

Alternatively, if I bias the SET at points such as those labeled 'B' and 'C' in Fig. 5.6, the small $\mathrm{Q}_g(t)$ modulation response is approximately linear, resulting in

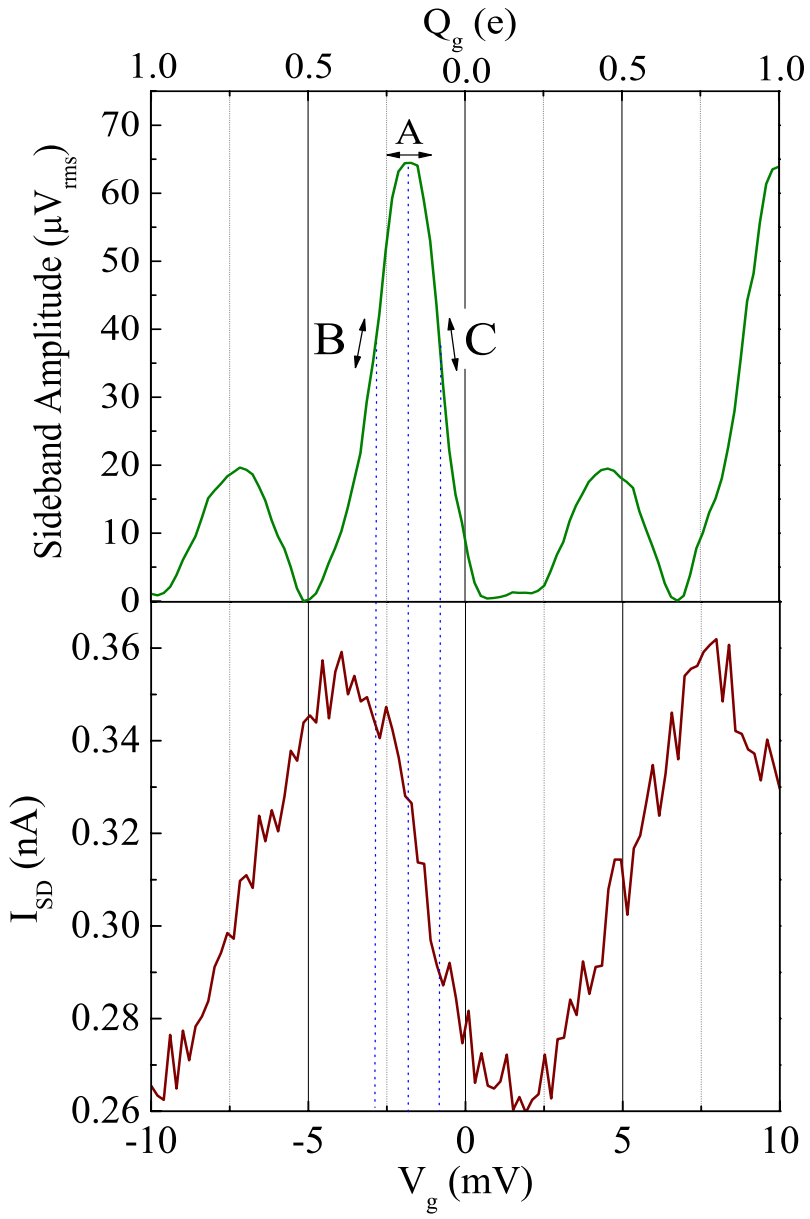

Figure 5.6: Dependence of the 1 MHz sideband amplitude on V_g (1 MHz sideband response) in Device 1 at a mixing chamber temperature of 35 mK. As expected there are two maxima in the sideband amplitude per period. The arrows about bias points A, B, and C indicate audio modulation of the sideband.

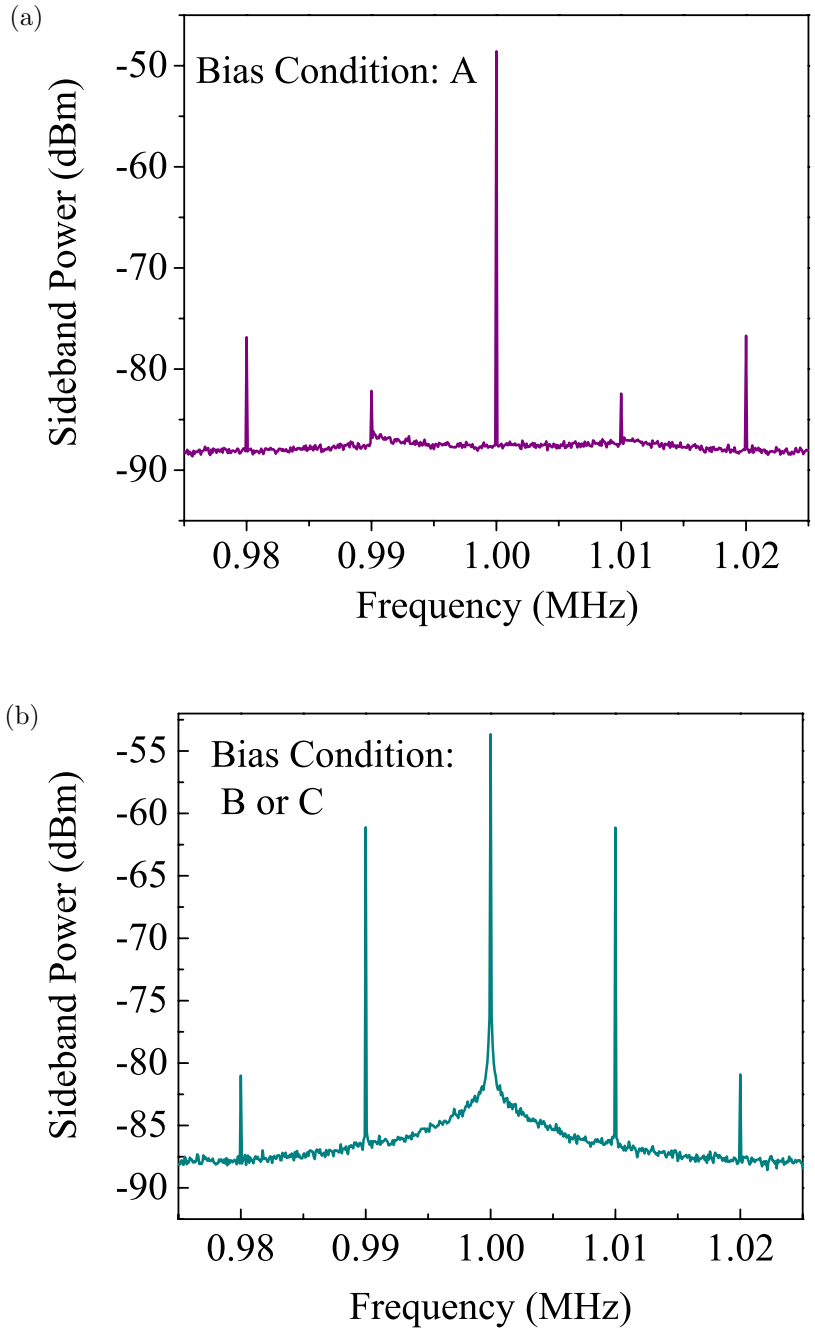

Figure 5.7: Power spectrum of the audio modulation of the 1 MHz sideband response. (a) Bias condition A. Sidebands at ± 20 KHz from 1 MHz sideband are prominent. (b) Bias condition B or C. Sidebands at ± 10 KHz from 1 MHz sideband are prominent. Device X.

the amplitude moudlation of the 1 MHz sideband at ω_A (Fig. 5.7(b)):

$$v_r \propto Q_g(t)\cos\omega_1 t \propto \frac{(C_g\Delta V_g)}{2}\left[\cos\omega_1 t + \cos(\omega_1+\omega_A)t + \cos(\omega_1-\omega_A)t\right].$$

In addition, if the bias point is off maximum, at positions such as 'B' or 'C', the phase of the resulting audio sidebands depends on the sign of the slope of the transfer function; this tells me whether to increase or decrease Q_g to return to the maximum, 'A'.

Thus by modulating the 1 MHz sideband with an audio signal, and monitoring the harmonic content and phase of the resulting product frequencies, I can determine the bias point Q_g of the SET and whether Q_g should be increased, decreased or left alone to maximize the SET gain. I then apply the appropriate correction to Q_g.

Obviously, we did not make the corrections to Q_g by hand. A schematic of the circuit we used is presented in Fig. 5.8 and Fig. 5.9. A charge modulation of amplitude 0.02 e_{rms} and frequency $\omega_A = 10$ kHz was applied to the SET gate through the port labeled "audio mod" for the modulation of the 1 MHz sideband.

The reflected signal v_r was monitored at port "rf out", and directed to the audio feedback circuit. In the audio feedback circuit (Fig. 5.9), v_r was amplified and then mixed with the orignial carrier signal to recover the sideband modulation.

The signal was then filtered and mixed with the original 1 MHz modulation to recover the audio sidebands of the 1 MHz modulation. The resulting audio signal was amplified and mixed with the original 10 kHz modulation.

The product of the audio mixing, or the error signal, was sent into a PID controller with the reference set to 0.0 Volts (*ie.* it was set to minimize the 10 kHz

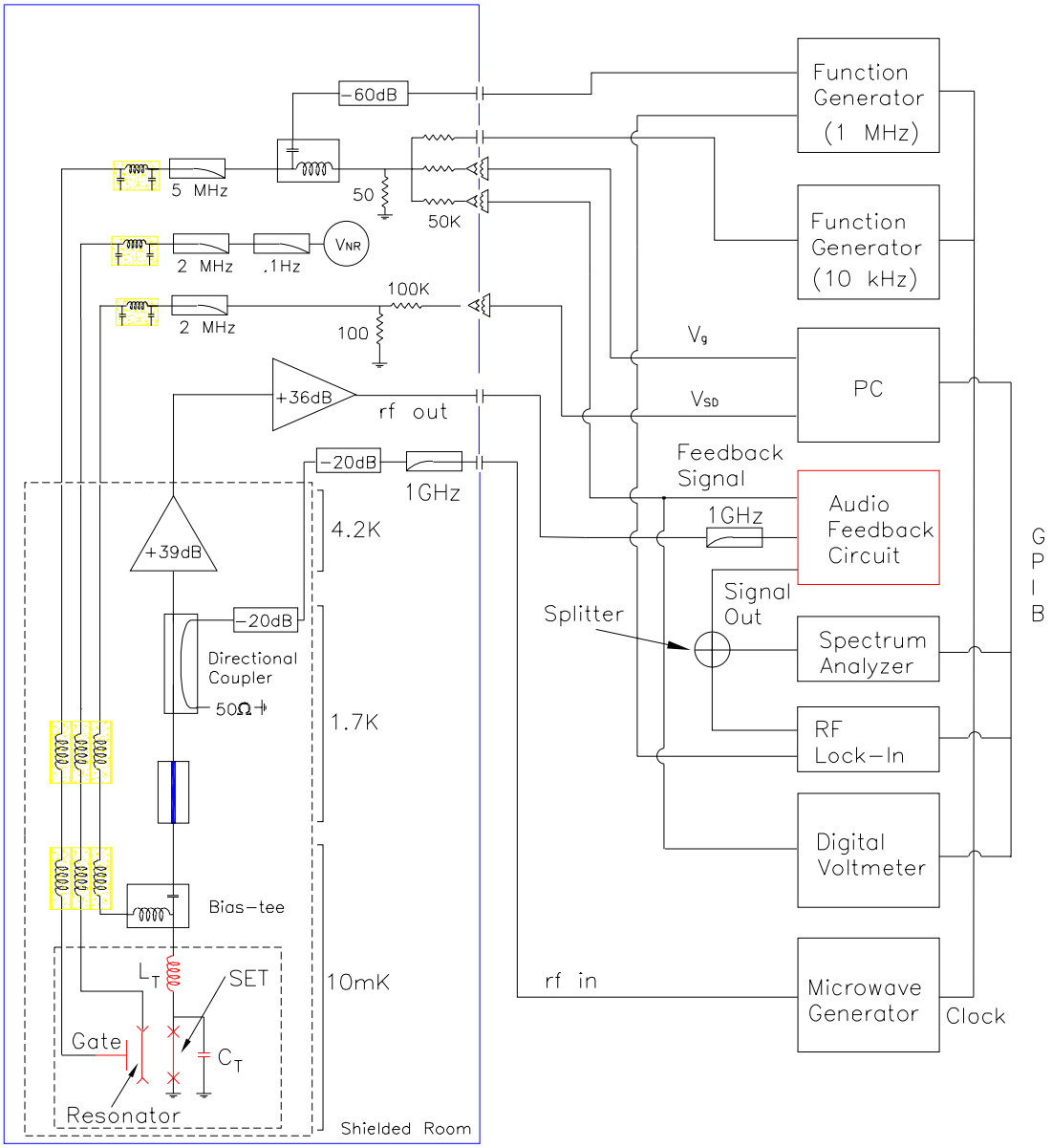

Figure 5.8: Circuit schematic for RFSET gain stabilization.

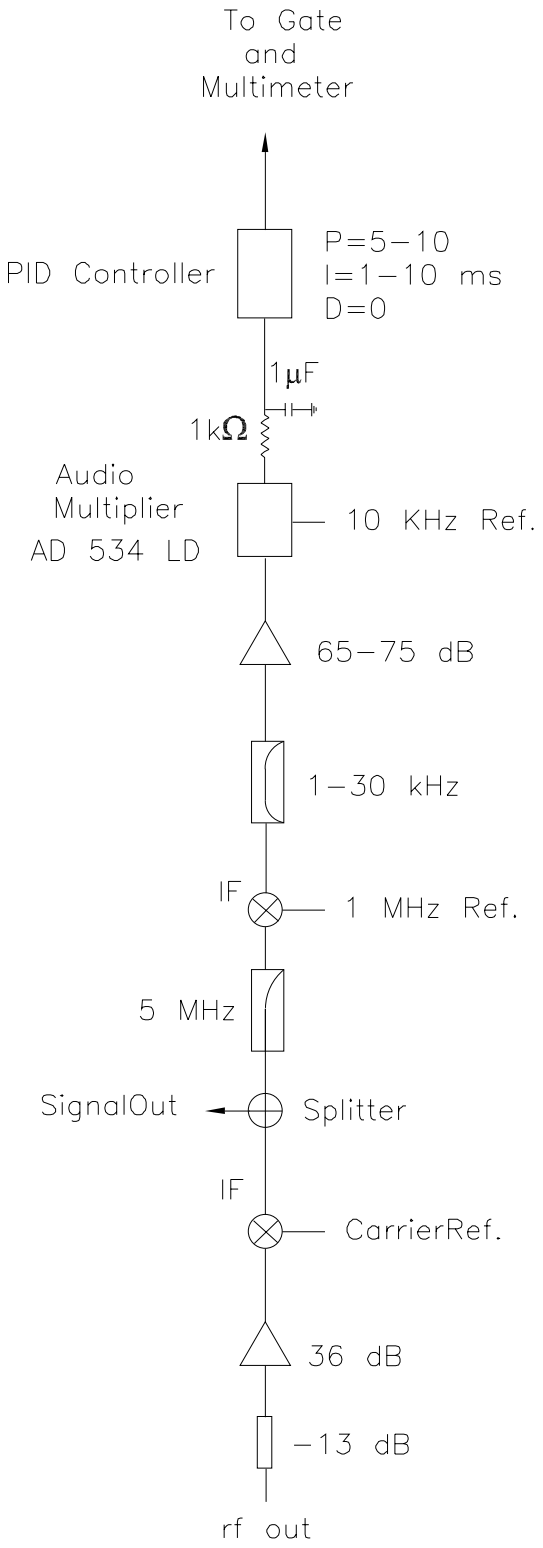

Figure 5.9: Feedback scheme for gain stabilization.

sidebands). The output of the PID was split: one branch directed the signal to the SET gate to adjust the bias position; the other branch fed the signal into a digital voltmeter that was monitored by the PC using GPIB. Using LabVIEW software, the PC monitored the feedback signal. By adjusting the DAC output V_g, it kept the output of the PID below a predefined threshold voltage.

Finally, for the rapid charge drift which occured when a large electric field was used to couple the nanoresonator and SET, the DAC output V_g saturated within minutes. To compensate for this, the same LabVIEW program reset the DAC output by 1 electron (*ie.* one period in the I_{SD} vs. Q_g curve) at the SET gate.

The effectiveness of the feedback scheme is demonstrated in Fig. 5.10. With feedback on (Fig. 5.10(a)), the 1 MHz sideband amplitude was stabilized to within 1% over minutes to hours, depending on the coupling voltage between the resonator and the SET. In the frequency domain (Fig. 5.10(b)) the effect of the feedback was seen as a reduction by nearly a factor of 100 in the spectral noise density of the 1 MHz sideband amplitude. The bandwidth of the feedback circuit was set by the time constant of the integrator in the PID controller, which was typically on the order of 1 - 10 ms.

(a)

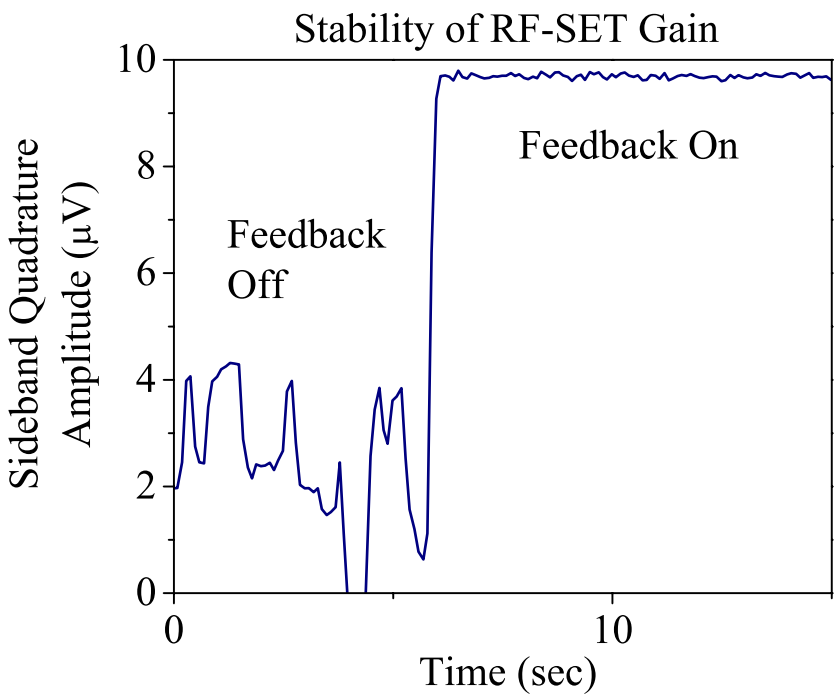

(b)

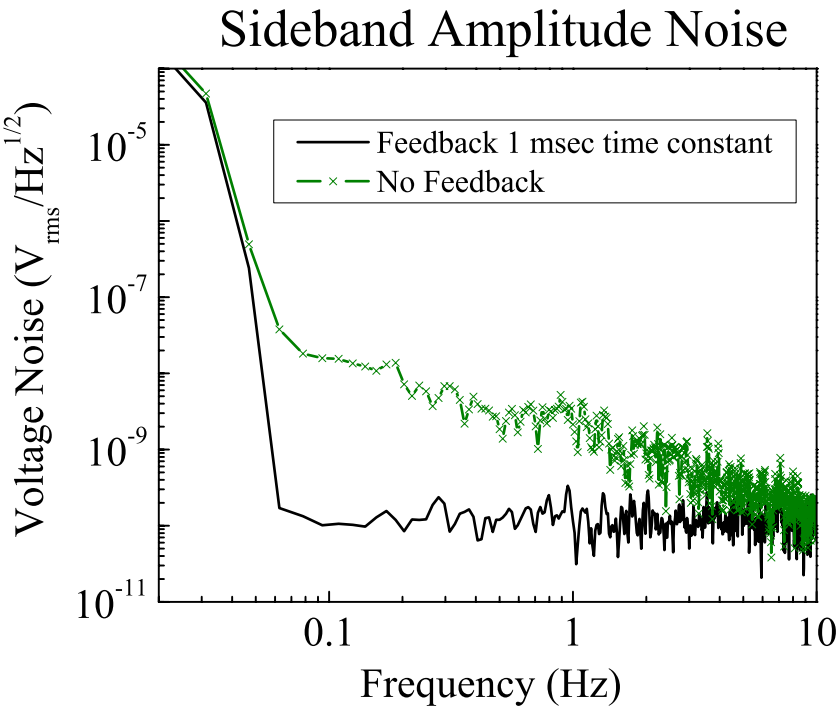

Figure 5.10: (a) Sideband amplitude stability in time domain and (b) sideband amplitude spectral noise density. Device X.

Chapter 6

RFSET Displacement Detection

In this chapter I discuss the implementation of the RFSET as a displacement detector and present the main results of my thesis. The chapter is divided into three sections. In the first section I draw on the results of the previous chapter to discuss the basic principles of the detection scheme and the measurement methodology. Some of our results for the RFSET detection of capacitively driven nanoresonators is presented and discussed. In the second section I discuss the RFSET displacement detector as a mechanical noise thermometer and use the results to characterize the performance of our devices. In particular, I show a minimum resonator mode temperature of approximately 56 mK for Device 2. Further, I demonstrate our RFSET displacement detection scheme to be nearly an ideal one, approaching within a factor of 5 from the quantum limit. In the final section I address the issue of SET back action.

RFSET Displacement Response and Sensitivity

Having developed the small charge-signal response for the RFSET in the previous chapter, I discuss how we implemented the RFSET electrometer as a displacement transducer. In principle, the main idea [12] [13] is straightforward (Fig. 6.1): a static SET gate is replaced with a metallized nanoresonator and a large dc bias

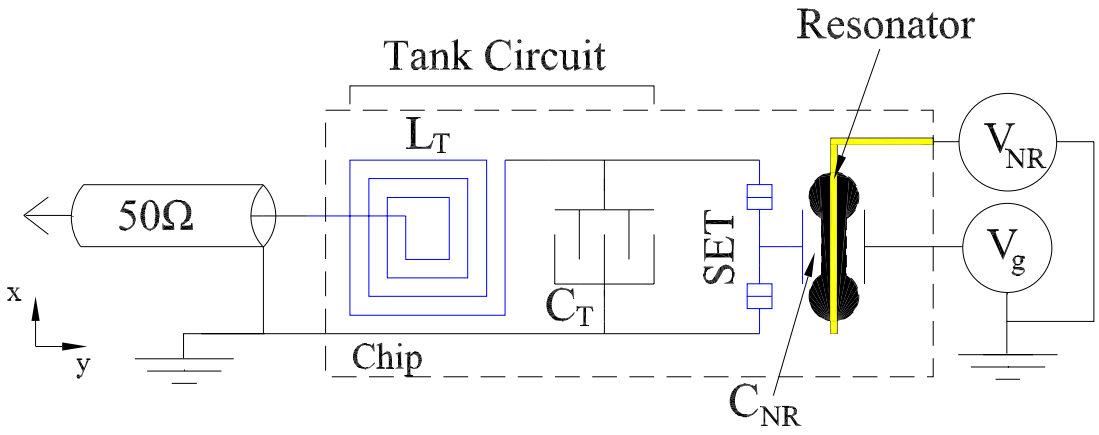

Figure 6.1: A circuit schematic of the RFSET displacement detector. A metallized nanoresonator serves as an SET gate to modulate the induced SET-island charge and, consequently, the SET's impedance. The impedance fluctuations are measured using microwave reflectometry at the frequency of the L_TC_T tank circuit resonance.

V_{NR} is applied between the suspended gate and the SET island; displacement of the resonator from its equilibrium position modulates the induced SET-island charge; the resulting modulation of the SET impdedance is then monitored by microwave reflectometry.

6.1 Methodology

Using Eq. 5.18, I can express the amplitude modulation of the reflected microwave signal in terms of the mechanically-induced SET-island charge ΔQ_{NR}:

$$v_r(t) = \Delta\Gamma(t)v_c(t) \approx -2Q_T^2 Z_o \frac{\partial^2 I_{SD}}{\partial V_{SD}\partial Q_{NR}} \Delta Q_{NR}(t)v_c(t), \tag{6.1}$$

where $Q_{NR} = C_{NR}V_{NR}$. For small displacment $y_m(t)$ of the resonator, I can approximate the corresponding charge modulation as

$$\Delta Q_{NR} \approx \frac{\partial C_{NR}}{\partial y_m} V_{NR} y_m \approx b\frac{C_{NR}V_{NR}}{d_{NR}} y_m(t) \tag{6.2}$$

where d_{NR} is the separation between the nanoresonator and the SET island, and b is a geometrical constant of order unity and calculated using the capacitance extraction software FastCap [65]. I consider $y_m(t)$ to be the in-plane fundamental mode displacement of the resonator averaged over the length of the SET island.

I can rewrite Eq. 6.1 as

$$v_r(t) \approx -2Q_T^2 Z_o \frac{\partial^2 I_{SD}}{\partial V_{SD}\partial y_m} y_m(t)v_c(t). \tag{6.3}$$

Here I have simply replaced ΔQ_{NR} with y_m as the differential quantity. It is important, though, to clarify a simple, yet, potentially confusing point. As discussed

in Appendix B, the SET current I_{SD} is dependent on the change in free energy ΔF of the SET circuit for the respective electron tunneling events. This in turn is a function of the SET-island potential,

$$\phi_{island}C_{\Sigma} = -ne + C_1V_{SD} + C_{NR}V_{NR} + C_gV_g, \tag{6.4}$$

where I have assumed an asymmetrical source-drain bias as in Appendix B.

In the previous chapter, as V_g was the modulated quantity, I discussed the RFSET response in terms of V_g or Q_g; in other words, $\Delta\phi_{island}\mathrm{C}_{\Sigma}= \Delta Q_g$. In this chapter, the modulated quantity is C_{NR}, so that $\Delta\phi_{island}C_{\Sigma} \approx \Delta Q_{NR}$ - assuming that $C_{\Sigma} \gg \Delta C_{NR}$. The important point is that, for $\Delta Q_g = \Delta Q_{NR}$, the modulation of $\Delta\phi_{island}$ and the RFSET response are the same:

$$\frac{\partial^2 I_{SD}}{\partial V_{SD}\partial Q_g} = \frac{\partial^2 I_{SD}}{\partial V_{SD}\partial Q_{NR}} \approx \frac{d_{NR}}{bC_{NR}V_{NR}}\frac{\partial^2 I_{SD}}{\partial V_{SD}\partial y_m},$$

Thus, I use the curvature $\partial^2\mathrm{I}_{SD}/\partial\mathrm{V}_{SD}\partial\mathrm{Q}_g$, which I numerically calculate from the $I_{SD}V_{SD}Q_g$ map, to determine the RFSET displacement response:

$$v_r(t) \approx -2Q_T^2Z_o\frac{bC_{NR}V_{NR}}{d_{NR}}\frac{\partial^2 I_{SD}}{\partial V_{SD}\partial Q_g}y_m(t)v_c(t). \tag{6.5}$$

Assuming that the noise floor of our detection scheme is limited by the measurement circuit noise, I estimate the displacement sensitivity to be

$$\delta y \equiv \sqrt{S_y} \approx \frac{d_{NR}}{bC_{NR}V_{NR}}\frac{1}{Q_T^2v_c}\sqrt{\frac{k_B\mathrm{T}_{\mathrm{N}}^{\mathrm{det}}}{Z_o}}\left(\frac{\partial^2 I_{SD}}{\partial V_{SD}\partial Q_g}\right)^{-1}. \tag{6.6}$$

As in the previous chapter, I divide the response by a factor of two to account for the homodyne detection; and v_c is the carrier amplitude given in peak units to calculate the sensitivity.

Equation 6.6 can be expressed in terms of the charge sensitivity using Eq. 5.19

$$\delta y \equiv \sqrt{S_y} \approx \frac{d_{NR}}{bC_{NR}V_{NR}}\sqrt{S_Q}. \tag{6.7}$$

Equation 6.7 simply states that, for a given resonator displacement, as I increase V_{NR}, I increase the charge signal detected by the SET. Of course, there are obvious limitations that will affect how far I can turn the knob for V_{NR} before Eq. 6.7 breaks down.

For one, I have not taken into account the SET back action, the contribution of which to the spectral displacement noise density increases linearly with V_{NR}. In Chapter 2, I discussed how the coupling voltage at which back action becomes a factor depends on many parameters, and can range from milli-volts to 10's of volts.

A second limitation arises from the electrostatic force between the resonator and the gate electrode and the resonator and the SET island. Increasing V_{NR} will eventually result in the resonator "snapping" to either the gate or SET island. A crude approximation of the voltage at which this will occur can be made by finding V_{NR}, for a given d_{NR}, which yields an inflection point in the resonators potential energy, $U(y) \approx \frac{1}{2}ky^2$-$1C_{NR}V_{NR}^2/2$. The result, $V_{snap} = \sqrt{4kd_{NR}^2/9C_{NR}}$, yields 100's Volts for the devices presented here, and is not relevant. However, it could easily be reduced to the order of Volts and be a greater concern for much more tightly coupled devices.

A final limitation occurs if the resonator's motion is so large that the swing in the induced SET-island charge approaches one electron. For 1 pm of motion, a typical thermal amplitude at 100 mK for the resonators we study, the corresponding

voltage at which this "shuttling" should occur is $V_{NR} \approx .5ed_{NR}/y_m C_{NR} \approx$ 100's Volts. Again, this is much larger than any voltage which we used. However, this estimate does suggest, and experiments seem to confirm, that shuttling is a concern for the SET measurement of resonators driven into the non-linear regime, where amplitudes are $\sim$ nm's.

RFSET Detection of Capacitively Excited Nanoresonators

In practice, we maximized v_r by first applying V_{NR} to the resonator and then measuring the $I_{SD}V_{SD}V_g$ characteristics. After numerically calculating the curvature, we then adjusted V_g and V_{SD} to the positions yielding maximum curvature. Finally, we adjusted v_c, and then implemented the feedback stabilization as described in the previous chapter. There was a good deal of tuning involved, but these were the general steps.

With the SET gain stabilized at maximum, we then tried to detect the resonator's motion. Typically, before we cooled down a new sample with the dilution refrigerator, we used the magnetomotive technique (Appendix A) to identify the resonator's fundamental in-plane mode frequency in a test probe at 4 Kelvin. The resonant frequency measured at 4 K, thus, served as the starting point at which to "look" for the resonance once we have cooled the sample down to mK.

Figure 6.2 shows a schematic of the circuit we used to probe the resonator's response with the RFSET. Essentially, we used the same circuit as the stabilized-RFSET reflectometry circuit described in the previous chapter. However, we applied

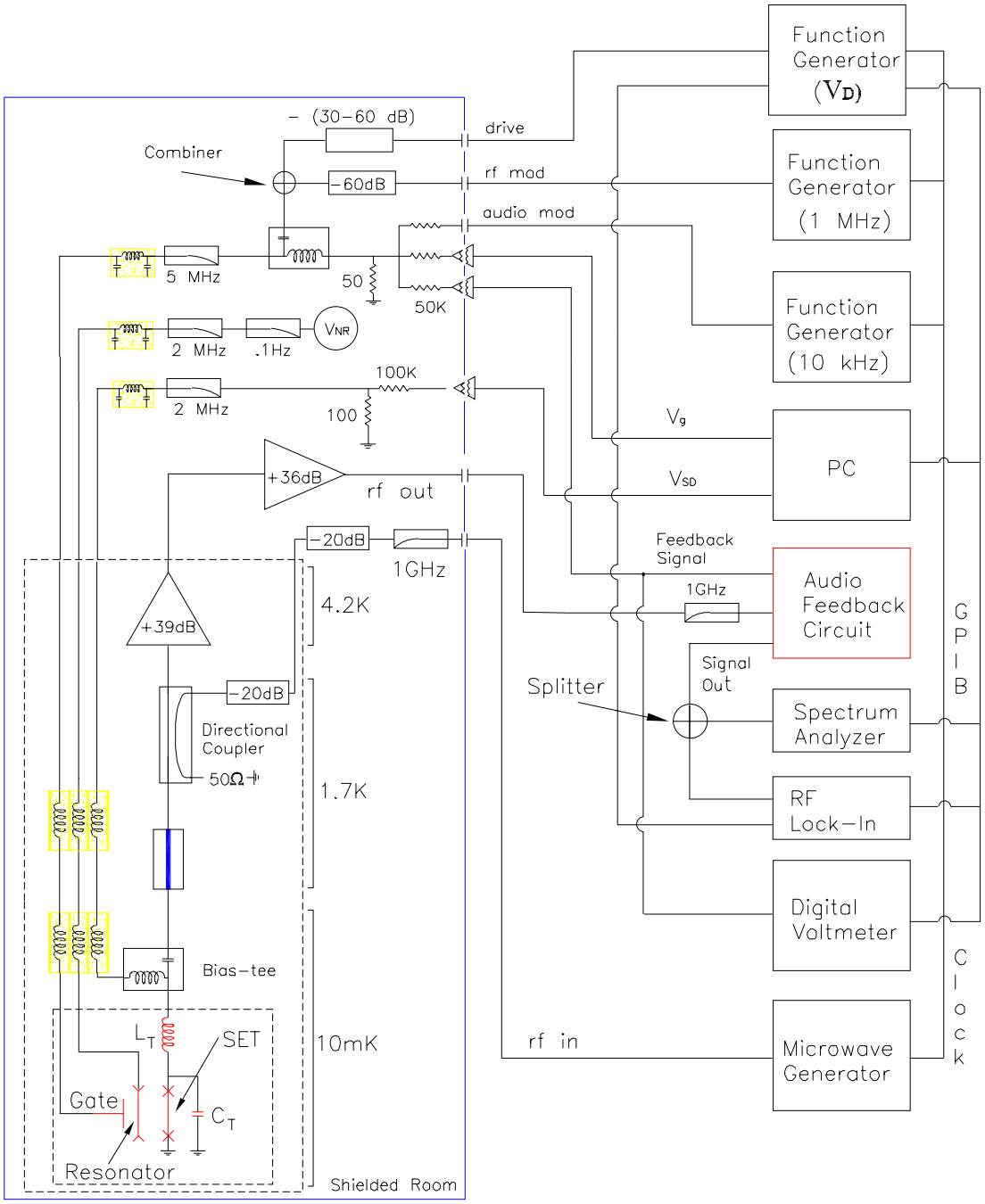

Figure 6.2: Circuit schematic for RFSET detection of capacitively excited nanoresonators.

an additional swept-sine signal $V_D \cos \omega t$, to the SET gate to capacitively excite the nanoresonator's motion. The nature of the excitation can be understood by writing the potential energy of the capacitor C_{gnr}formed by the metallized nanoresonator and the gate electrode,

$$U = -\frac{1}{2} C_{gnr} (V_{NR} + V_D \cos \omega t)^2, \tag{6.8}$$

and the force from the potential energy gradient,

$$F = -1 \frac{1}{2} \frac{\partial C_{gnr}}{\partial y} (V_{NR} + V_D \cos \omega t)^2 \approx \frac{b}{2} \frac{C_{gnr}}{d_{gnr}} (V_{NR} + V_D \cos \omega t)^2, \tag{6.9}$$

where d_{gnr} is the separation between the nanoresonator and the gate electrode.

There is a dc component of the force as well as terms at both ω and 2ω. Keeping just the ω term, I find

$$F \approx b \frac{C_{gnr} V_{NR} V_D}{d_{gnr}} \cos \omega t. \tag{6.10}$$

From Eqs. A.19, A.25, and A.26, the fundamental mode response of the resonator is described by

$$y(x,t) = b \frac{C_{gnr} V_{NR} V_D}{d_{gnr} m_{eff}} \frac{\eta_1 Y_1(x)}{((\omega_1{}^2 - \omega^2) + j\,(\omega_1 \omega / Q_e))} \cos \omega t, \tag{6.11}$$

where $Y_1(x)$ is the fundamental eigenmode for a clamped-clamped rectangular bar. For the calculation of η_1, I have assumed that the force is uniform over the section of the resonator defined by the ends of the gate electrode, and that it is zero outside of this section. The function $Y_1(x)$ has been normalized so that it is dimensionless and the mid-point displacement, Y(L/2), is equal to 1.

From Eqs. A.11 and 6.11, the average displacement over the length of the SET island is given by

$$y_m(t) \approx \frac{b}{a_1}\frac{C_{gnr}V_{NR}V_D}{d_{gnr}M_m}\frac{a_1\eta_1}{((\omega_1{}^2-\omega^2)+j\,(\omega_1\omega/Q_e))}\cos\omega t, \tag{6.12}$$

where a_1 is the geometrical factor accounting for the averaging of $Y_1(x)$ over the length of the SET island.

Using Eqs. 6.5 and 6.12, the modulation of the reflected signal due to the motion of the capacitively driven resonator is given by

$$\begin{aligned} v_r(t) \;&\approx\; 2Q_T^2Z_o\left(\frac{\partial^2 I_{SD}}{\partial V_{SD}\partial Q_{NR}}\right)\frac{b^2C_{gnr}C_{NR}V_{NR}^2V_D}{a_1d_{NR}d_{gnr}M_m}\times \\ &\quad\times\frac{a_1\eta_1}{((\omega_1-\omega^2)+j(\omega_1\omega/Q_e)}v_c(t)\cos\omega t. \end{aligned} \tag{6.13}$$

On resonance, and using the definition of the K_m from Appendix A, I find the amplitude of the modulated reflected signal:

$$A_r \approx 2Q_T^2Z_o\left(\frac{\partial^2 I_{SD}}{\partial V_{SD}\partial Q_{NR}}\right)\frac{\eta_1b^2Q_eC_{gnr}C_{NR}V_{NR}^2V_D}{a_1d_{NR}d_{gnr}K_m}v_c. \tag{6.14}$$

In practice, the real and imaginary components of the response were measured by directing the output of the homodyne detection to an RF lock-in (Fig. 6.2) and sweeping the drive $V_D\cos\omega t$ through resonance ω_1. A computer program incremented the frequency of the sinusoidal drive step-wise and recorded the two quadratures of the output of the amplifier at each step.

Figure 6.3 shows the response of the nanoresonator in Device 2 to continuous swept-sine capacitive excitation as measured with an RFSET. The data was taken at a sample-stage temperature of 30 mK, and the RFSET was biased near the JQP resonance as illustrated in Fig. 6.4. A coupling voltage of V_{NR}= 4 V was applied.

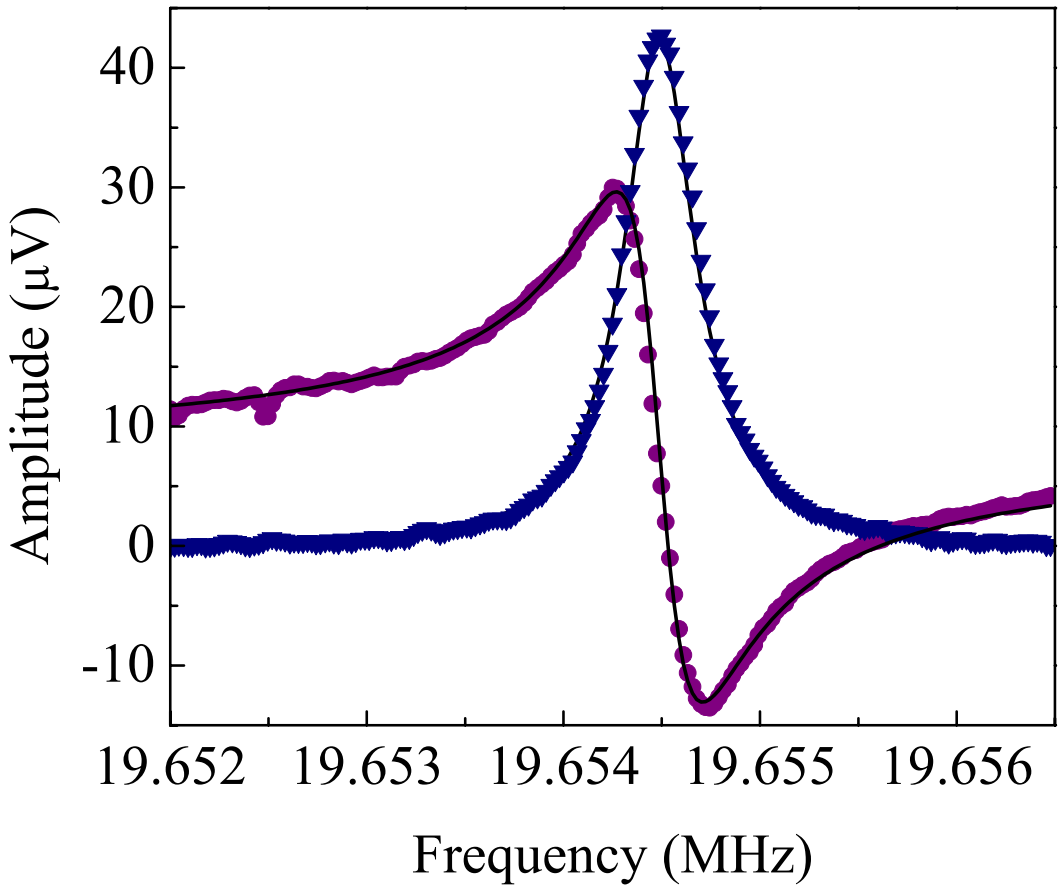

Figure 6.3: Response of the capacitively excited resonator as measured with an RFSET, Device 2.

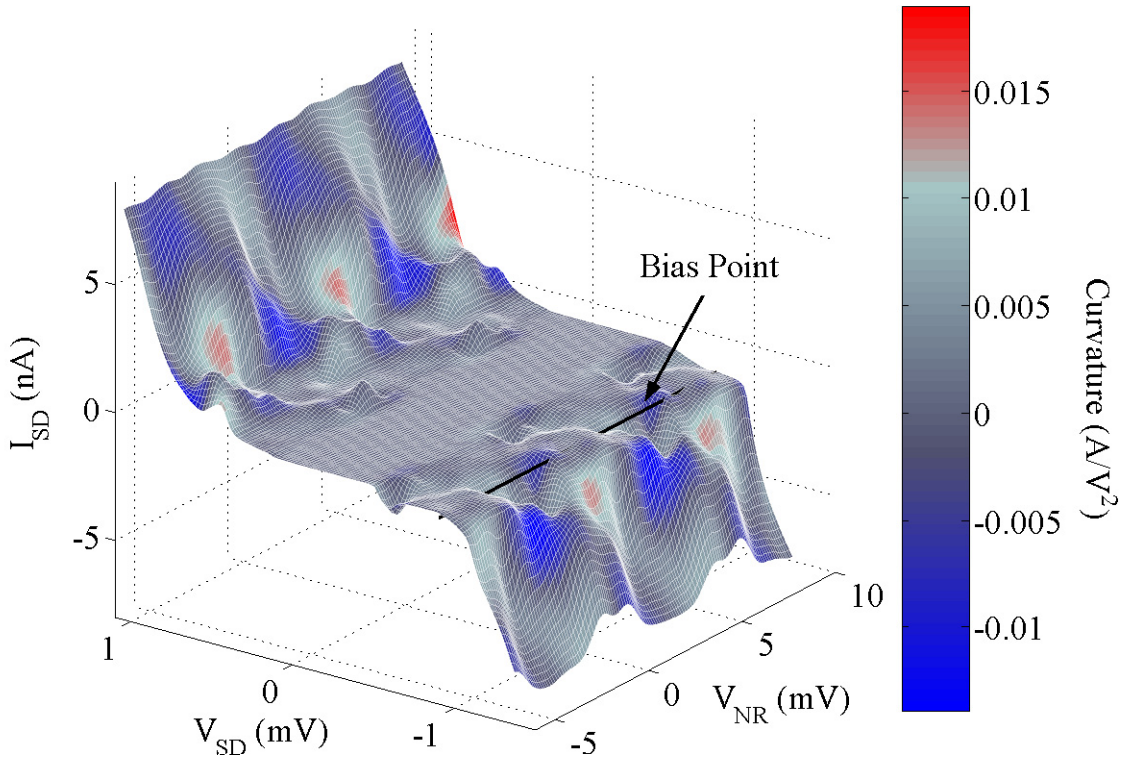

Figure 6.4: $I_{SD}V_{SD}V_{NR}$ map of Device 2 with color surface depicting numerically calculated curvature. Bias point is near the JQP resonance ridge.

Fitting the quadratures to a harmonic oscillator response, the resonant frequency, quality factor and peak amplitude were determined to be f_1 = 19.654486(3) MHz, Q_e = 44.85(6) x 10^3 , and A_r = 75.95(6) μV_{rms} respectively.

I can compare the measured amplitude A_r with what is expected from Eq. 6.14. For Device 2, d_{NR}= 600 nm, d_{gnr} = 1.2 μm, v_c = 7.9 μV_{peak}, η_1 = .838, C_{gnr} $\approx$ 15 aF, $V_D \approx$ 350 μV_{peak}, and b $\approx$ .47 - the other parameters are listed in Tables A.3, B.1, and 3.1. From Fig. 6.4, I estimate that $\partial^2 I_{SD}/\partial V_{SD}\partial Q_{NR} \approx 0.01/C_{NR}$ = 3.8 x 10^{14}. The gain of the detection circuit at the output of the shielded room is +64 dB. The gain of the audio feedback circuit is -1 dB (attenuator -13 dB, amplifier +36 dB, 2 power splitters -8 dB, and mixer -8 dB). Thus, using the rms value of Eq. 6.14, I estimate the amplitude at the input of the lock-in to be 110 $\pm$ 60 μV_{rms}. The uncertainty in the estimate is due mainly to the $\sim$ 50% error in K_m. It does not include the uncertainty the attenuation and gain in the measurement circuit. These can be estimated from the discrepancy between measured and calculated charge sensitivity at the measurement bias point V_{SD}= -.9 mV. The values are 60 and 30 $\mu e/\sqrt{Hz}$ respectively.

I can also determine the amplitude of the resonator's displacement from the measured reflected signal and Eq. 6.5. I calculate that the amplitude A_r = 76 μV_{rms} roughly corresponds to 50 pm_{rms} of motion. From Eq. 6.12, I expect approximately 20 pm_{rms} of motion. Again, the uncertainty is at least 50 % due to uncertainties in the spring constant and measurement circuit gain.

Given the uncertainty in the estimate of the amplitude of the reflected signal and in the conversion of the reflected signal to resonator displacement, order-of-

magnitude agreement between the estimates and measurements is about the best I can expect. The total uncertainty could be reduced by determining more precisely the resonator's spring constant and the measurement circuit's transfer characteristics. However, as I will discuss in the next section, it is not necessary to go to such efforts in order to assess the performance of the detection scheme in terms of the quantum limit.

Before concluding this section, I want to discuss the measurement of the nanoresonator's response in the time domain. In addition to applying a swept-sine to the gate and measuring the nanoresonator's frequency response with a lock-in, we also applied a pulse to the gate and measured the nanoresonator's amplitude decay with a digital oscilloscope. We used the same measurement circuit as in Fig. 6.2 except we replaced the lock-in with a digital oscilloscope - the same function generator was used to apply the drive signal except we switched it from "swept-sine" mode to "burst" mode. Also, an additional amplifier with gain of 36 dB and an high-pass filter with a 10 MHz cut-off were inserted between the mixer and the oscilloscope.

Typically, the pulse we applied was a 60 kilo-cycle sinusoid at the nanoresonator's fundamental mode frequency ω_1. At the falling edge of the pulse, the digital oscilloscope was triggered, and the resonator's decay was recorded for 20 ms at a sampling rate of 50 - 100 MS/s. The process was repeated 50 - 100 times and the waveforms were averaged.

Figure 6.5 shows the "ring-down" of the nanoresonator in Device 2. The signal has been digitally filtered in three steps. First, in the time domain, I multiplied the waveform by an exponential decay with time constant $\tau = Q_e/\omega_1$ [118]. Second,

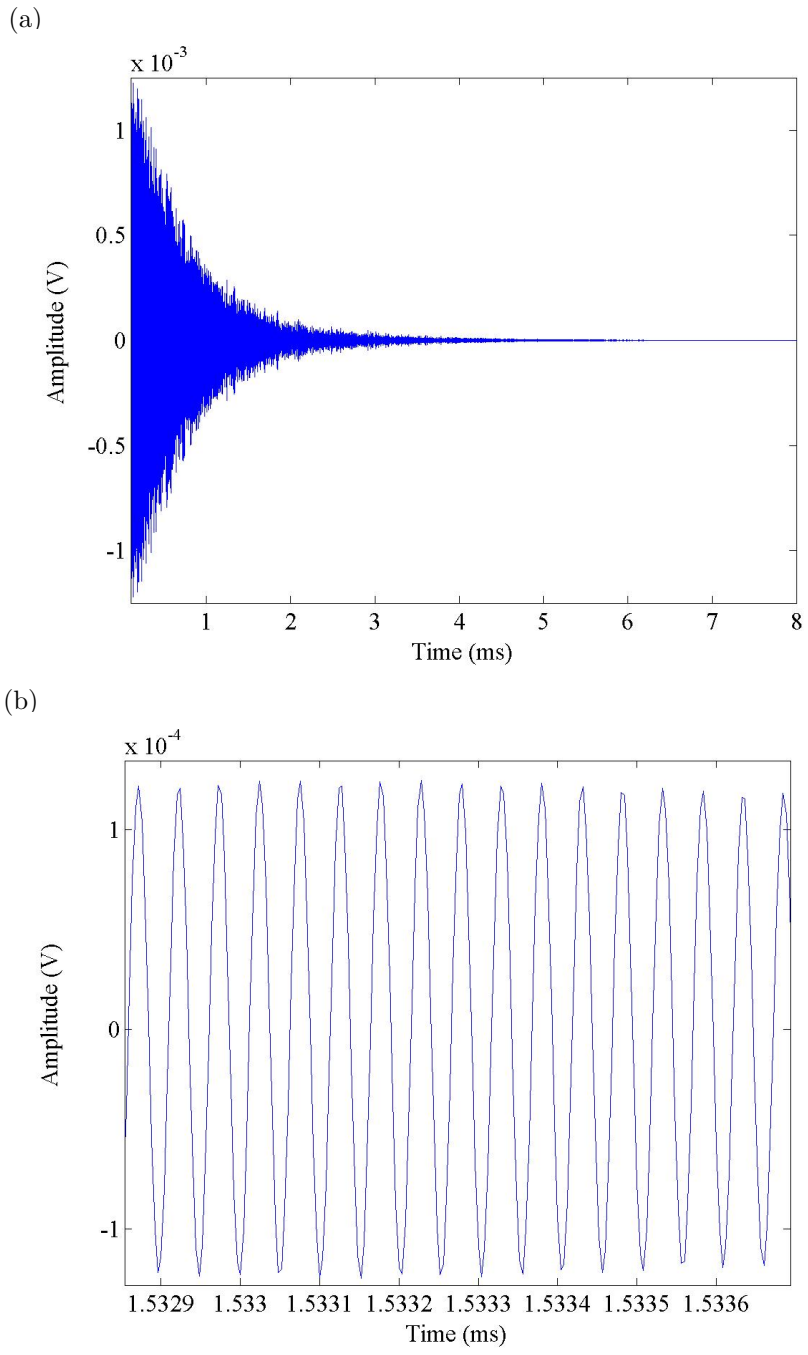

Figure 6.5: (a) Filtered time-domain response of a nanoresonator to capacitive-pulse at the fundamental mode frequency, captured using a digital oscilloscope. (b) Blow-up of (a) to demonstrate time-resolved oscillations at 19.65 MHz. Device 2, T_S = 30 mK, V_{NR} =6 V.

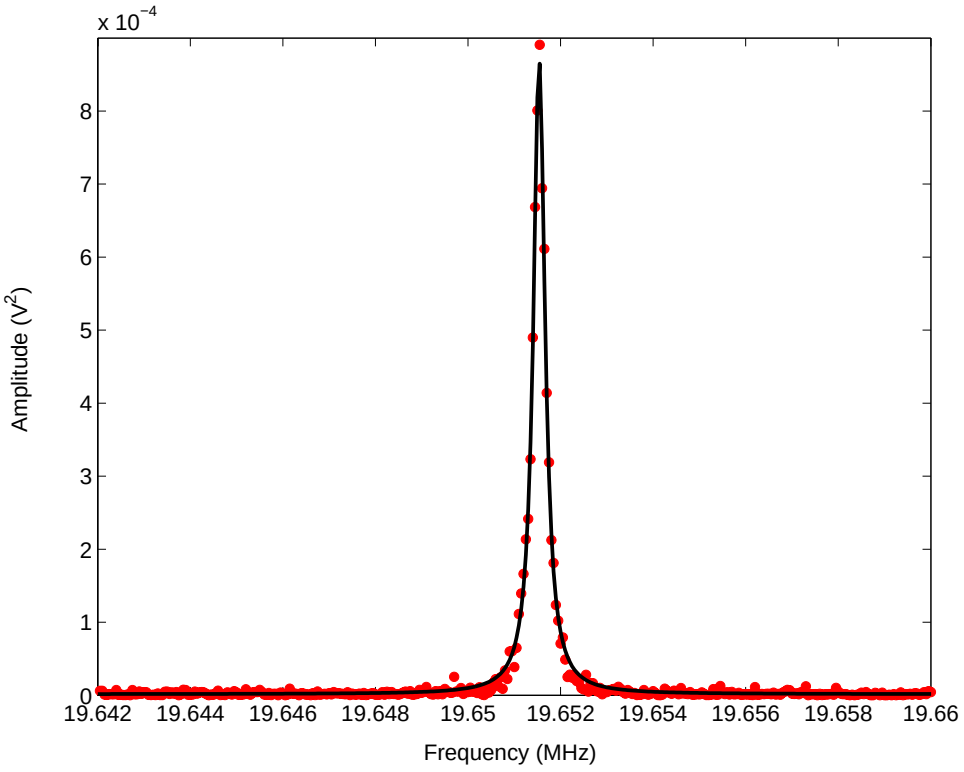

Figure 6.6: FFT of the raw time-domain response of a nanoresonator to a capacitive-pulse, Device 2.

I numerically calculated the FFT of the waveform and multiplied the result by a Gaussian with a width of $\sigma = 10$ MHz. Third, I transformed the data back into the time domain by numerically calculating the inverse FFT. The decay time for the exponential in the first step was determined by taking the FFT of the raw time-domain data and fitting it to an harmonic oscillator response (Fig. 6.6). From the fit, the frequency and quality factor were determined to be $f_1 = 19.6515382(4)$ MHz and $Q_e = 64300 \pm 250$ respectively.

Finally, I note that the difference in resonant frequency of ~ 2.9 kHz between Figs. 6.3 and 6.6 was due to the electrostatic softening of the resonator's mode. Expanding the electrostatic energy of the resonator to second order about the equilibrium position of the resonator,

$$\Delta^2 U_e \approx -\frac{C_{NR}}{d_{NR}^2} V_{NR}^2 y^2, \tag{6.15}$$

I find the correction to the fundamental mode frequency to be

$$\frac{\Delta\omega}{\omega_1} \approx -\frac{C_{NR} V_{NR}^2}{K_{avg} d_{NR}^2}. \tag{6.16}$$

Thus, if I increase V_{NR} from 4 V to 6 V, I expect a shift in resonant frequency of $\sim$ - 2 kHz , which is comparable to what we measured. For a more precise determination it would be necessary to include the capacitive coupling between the resonator and the gate, and, as well, determine the geometrical coefficient for the second derivative of C_{NR}.

6.2 Mechanical Noise Thermometry

The Equipartition of Energy

I now turn to discuss the measurement of the resonators' random thermal motion. I assume that the resonator and RFSET detector are sufficiently weakly coupled so that the back action effects of the detector are negligible with respect to the thermal fluctuations. From Eq. 2.59 and Eq. 2.60, then, $T_e = T_b$ and $Q_e = Q_b$. In this case, then, the classical equation of motion for a resonator in thermal contact with a heat bath is given by the Langevin equation [49],

$$M_m \frac{\partial^2 y_m(t)}{\partial t^2} + \mu \frac{\partial y_m}{\partial t} + K_m y_m = f_N(t), \tag{6.17}$$

where

$$f_N(t) = \frac{F_N(t)}{a_1} \int_0^L dx Y_1(x) \tag{6.18}$$

and

$$\mu = \frac{\gamma_1}{a_1} \tag{6.19}$$

Here, the equation of motion is written in terms of the average displacement of the resonator over the length of the SET island, which is the measured quantity. For each of the devices I discuss, M_m, K_m and a_1 are defined in Appendix A.

Simply put, the Langevin equation states that a resonator in thermal contact with a heat bath is subject to two external forces: a frictional force proportional to μ and a random driving force represented by $f_N(t)$. Generally, it is assumed that $f_N(t)$ is both Gaussian and Markovian, meaning it has a white power spectrum,

$S_f(\omega)$, and its auto-correlation function is given by

$$\langle f_N(t_1) f_N(t_2)\rangle = S_f(\omega)\delta(t_1 - t_2). \tag{6.20}$$

Here $S_f(\omega) = S_{f_b}$ (see Chapter 2) in the limit that $\hbar\omega/k_B T_b \to 0$.

From these assumptions, and the fact that the resonator is considered to be in thermal contact with the heat bath, it can be shown that the dissipative force and the random driving force are related through [53]

$$\mu = \frac{1}{k_B T_{eff}} \int_0^\infty dt \langle f_N(t_1) f_N(t_2)\rangle = \frac{S_f(\omega)}{2k_B T_e}, \tag{6.21}$$

or

$$S_f(\omega) = 2\mu k_B T_e = \frac{2M_m \omega_1 k_B T_e}{Q_e}, \tag{6.22}$$

where I have used the relationship $\mu = M_m\omega_1/Q_e$; T_e=T_b is the bath temperature; and $Q_e = Q_b$ is the quality factor due to coupling to the thermal bath.

Equation 6.21 is generally known as the fluctuation-dissipation theorem [53], and is a fundmantal classical statement equating the random forces which define a state of equilibrium to the dissipative forces which tend to bring a driven or nonequlibrium state back toward equilibrium. Practically speaking, then, knowing the resonator's response, one can determine the thermal forces driving the resonator, and, thus, determine the resonator's temperature.

The resonator's response is found by solving Eq. 6.17 for the time-averaged, mean-square displacement, [31]:

$$\langle y_m(t)^2\rangle = \frac{1}{2\pi} \int_{-\infty}^{\infty} d\omega S_y(\omega), \tag{6.23}$$

where

$$S_y(\omega) = \frac{S_f(\omega)}{{M_m}^2\left(\left(\omega_1^2 - \omega^2\right)^2 + \left(\omega_1\omega/Q_e\right)^2\right)} \tag{6.24}$$

is the mechanical displacement noise spectral density.

Separating into positive and negative frequencies and integrating Eq. 6.23, I find

$$\langle y_m(t)^2\rangle = \frac{S_f(\omega)Q_e^2}{K_m^2}\Delta f + \frac{S_f(\omega)Q_e^2}{K_m^2}\Delta f, \tag{6.25}$$

where $\Delta f = \omega_1/4Q_e$ is defined as the resonator's noise-equivalent bandwidth and I have assumed that $Q_e \gg 1$.

Using Eqs. 6.22 and 6.25, I recover the equipartition theorem:

$$\langle y_m(t)^2\rangle = \frac{1}{2}\frac{k_B T_e}{K_m} + \frac{1}{2}\frac{k_B T_e}{K_m} = \frac{k_B T_e}{K_m}. \tag{6.26}$$

Of course, Eq. 6.26 is a classical expression and ceases to be valid when $k_B T_e/\hbar\omega_1 \simeq 1$. However, for the temperature and frequency ranges in which we conducted our experiments, the resonators were still more than an order of magnitude above this limit. Consequently, we were able to use Eq. 6.26 and measurements of $\langle y_m(t)^2\rangle$ to determine T_e.

Power Spectra

Equation 6.26 is the basis of mechanical noise thermometry. Of course, as I discussed earlier in the chapter, the RFSET is sensitive to $y_m(t)$ rather than $\langle y_m(t)^2\rangle$. To recover $\langle y_m(t)^2\rangle$, we used a spectrum analyzer with FFT capability to record and average the power density spectrum of the output of the mixer ("signal out" in Fig. 6.2).

From Eqs. 6.5, 6.22, and 6.24, the power spectral density at the input to the spectrum analyzer takes the form:

$$P_s \approx 4G\frac{Q_T^4 Z_o v_c^2 (\partial^2 I_{SD}/\partial V_{SD}\partial Q_{NR})^2 (bC_{NR}V_{NR}/d_{NR})^2 \omega_1}{\left((\omega^2-\omega_1^2)^2+(\omega_1\omega/Q_e)^2\right)M_m Q_e}k_B T_e, \tag{6.27}$$

where G represents the total gain of the measurement circuit up to the spectrum analyzer.

In practice to compare each averaged power spectrum, we simultaneously recorded the charge gain of the circuit by measuring the magnitude of the 1 MHz reflection modulation with a lock-in ("rf lock-in" in Fig. 6.2). We then divided the power spectrum by the average gain A_Q (in units of W/e_{rms}^2) recorded during the measurement of the power spectrum. This converted the measured thermal response of the resonator into units of e_{rms}^2/Hz. I thus rewrite Eq. 6.27 as

$$P = \frac{A}{\left((\omega^2-\omega_1^2)^2+(\omega_1\omega/Q_e)^2\right)}\frac{\omega_1^4}{Q_e^2}, \tag{6.28}$$

where "A" is in units of $\frac{e_{rms}^2}{Hz}$ and is given by

$$A = GQ_T^4 Z_o v_c^2 \left(\frac{\partial^2 I_{SD}}{\partial V_{SD}\partial Q_{NR}}\right)^2 \left(\frac{bC_{NR}V_{NR}}{d_{NR}}\right)^2 \frac{k_B T_e}{K_m}\frac{1}{A_Q \Delta f}. \tag{6.29}$$

Figure 6.7 displays the power spectra of a nanoresonator's thermal response at sample-stage temperatures T_S = 75 mK, 150 mK, 300 mK, and 500 mK and a coupling voltage of V_{NR}=10 V. The data was taken using Device 2. For each temperature, 500 to 1500 traces were taken, averaged, and fit (lines) to Eq. 6.28 plus a background. From the fit we extracted the resonant frequency ω_1, quality factor Q_e, peak amplitude A, and background P_o, for each temperature. The error

bars for each of these quantities was determined using standard error propagation with a uniform variance assigned to each point in the power spectrum plot. The variance was taken from the variance in the background level far from resonance. The background is Gaussian and due the 80 $pV/\sqrt{Hz}$ input voltage noise of the cryogenic microwave pre-amplifier.

Effective Resonator Temperature

Knowing the resonator's amplitude A, quality factor Q_e and fundamental mode frequency $\omega_1/2\pi$, I can calculate the effective temperature of the resonator's fundamental mode. There are two ways that I can do this: (1) use Eq. 6.29 and the known device parameters (*eg.* K_m, G, etc.); or (2) use a a primary thermometer (*eg.* nuclear orientation thermometer) or calibrated secondary thermometer (*eg.* RuO resistor) to calibrate the temperature dependence of one of the resonator's extracted parameters (*eg.* A, Q_e, etc.). The total uncertainty in the device parameters is greater than 50 % (due mainly to uncertainties in K_m and G), whereas the uncertainty in the extracted parameters is typcially 1 - 10 % (see Fig. 6.7). Provided I choose a suitable parameter, it is clear that the second method is much more precise.

While not necessary, it is preferable that I choose a parameter that varies linearly with T_e. Neither the resonator's amplitude A, quality factor Q_e or fundamental mode frequency $\omega_1/2\pi$ demonstrate this behavior. However, if I integrate Eq. 6.28, for $Q_e \gg 1$, I find

$$\mathrm{IR} = \int_0^\infty P d\omega = \frac{\omega_1}{4Q_e} A = G Q_T^4 Z_o v_c^2 \left(\frac{\partial^2 I_{SD}}{\partial V_{SD} \partial Q_{NR}} \right)^2 \left(\frac{b C_{NR} V_{NR}}{d_{NR}} \right)^2 \frac{k_B T_e}{A_Q K_m}, \quad (6.30)$$

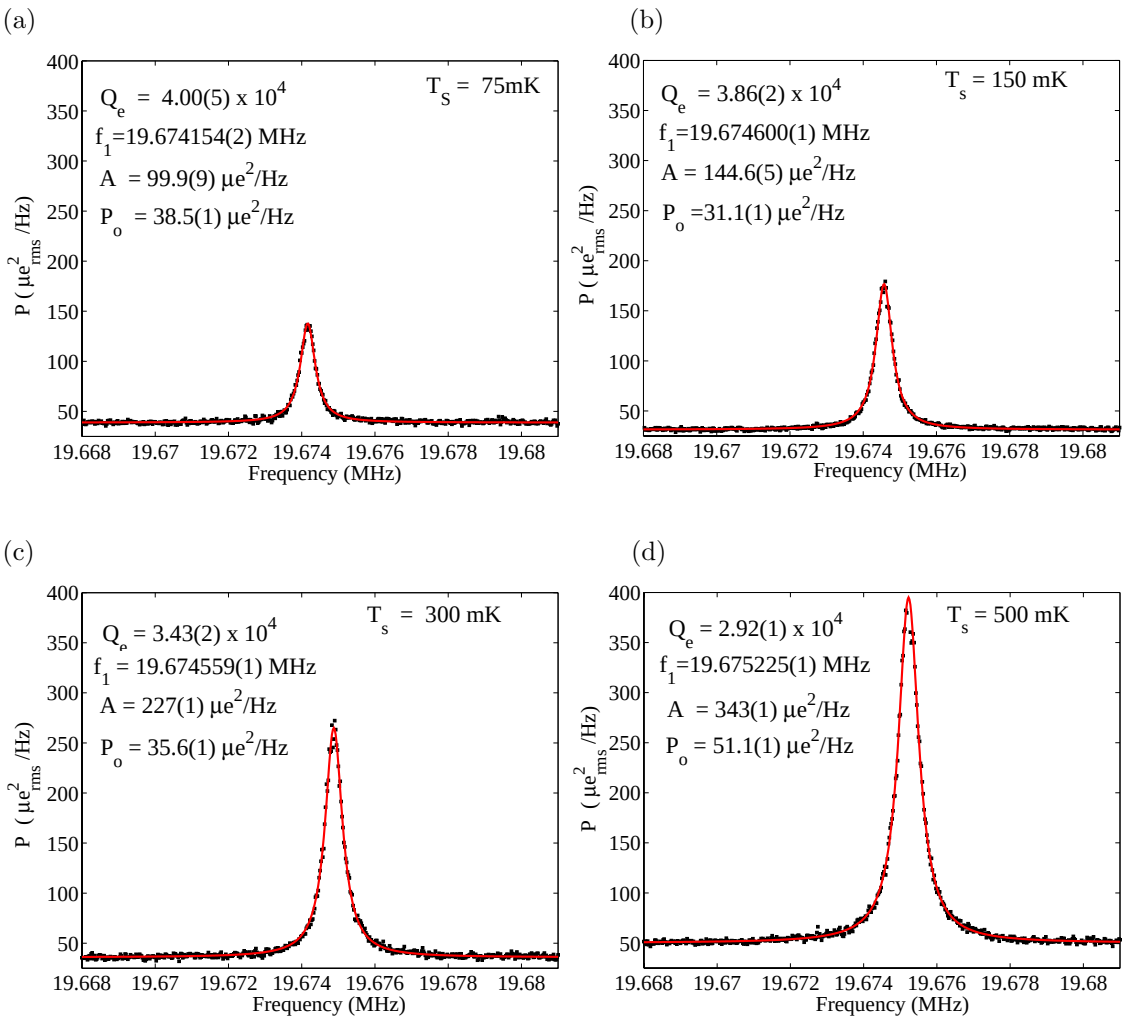

Figure 6.7: Power spectrum measurements of a nanoresonator's thermal response, P, (squares) fit to harmonic oscillator response (lines). Data taken with coupling voltage $V_{NR} = 10$ V. Device 2.

where IR stands for integrated response. Below 500 mK, the temperature dependence of the parameters in Eq. 6.30 is negligible and, hence, IR is linear in T_e. Above 500 mK, the temperature dependence of $\partial^2 I_{SD}/\partial V_{SD}\partial Q_{NR}$ becomes significant, and IR is no longer linearly proportional to T_e.

In practice, to calibrate IR, we first measured the resonator's frequency response P as a function of sample-stage temperature T_S (see the Thermometry section in Chatper 4 to see how we measured T_S)and extracted the parameters A, Q_e, and $\omega_1/2\pi$ from an harmonic oscillator fit to the data at each temperature. We then calculated IR via

$$\mathrm{IR} = \frac{\omega_1}{4Q_e}A. \tag{6.31}$$

From the scatter in the power spectra data, the error in the calculation of this quantity was typically 1 - 15%. Finally, we plotted IR versus T_S (Fig. 6.8).

For $T_S > 100$ mK, we found IR exhibited a linear dependence on T_S. The y-intercept was within measurement error of the origin (Fig. 6.8). Furthermore, the data scaled with V_{NR}^2, Figs. 6.9 and 6.10. That is, when divided by the square of the coupling voltage, for a given T_e, IR exhibited no dependence on V_{NR}^2. These observations were sufficient evidence to conclude that IR was an accurate measurement of the temperature of the fundamental mode of the resonator, and that the mode was in thermal equilibrium with the sample holder and RuO_2 thermometer (*ie.* $T_e = T_S$). Accordingly, in this temperature regime, the slope of IR versus T_S could be used as a calibration for performing noise thermometry. It is evident in both Fig. 6.9 and Fig. 6.10 that there was scatter of 10 - 20% in some of the data

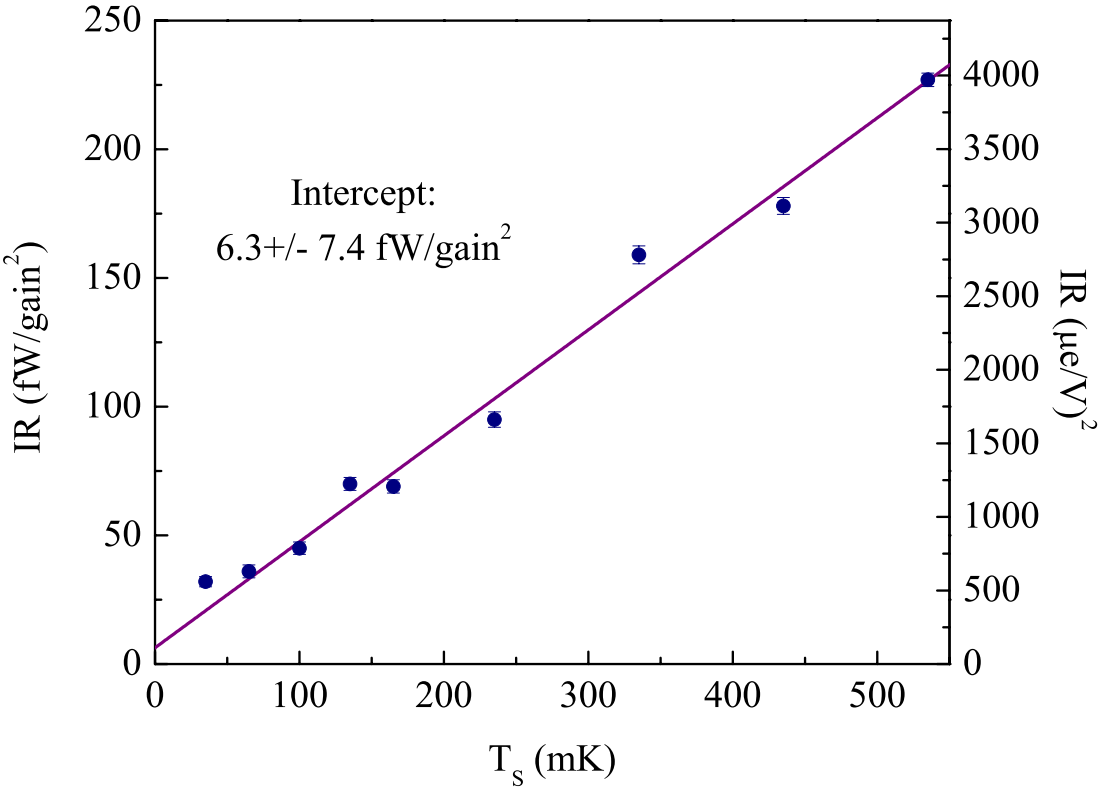

Figure 6.8: Plot demonstrating the integrated resonator response, IR, versus T_S at a coupling voltage of $V_{NR} = 4$ V. Data is for device 2.

points. I address this issue at the end of the section when I discuss evidence for back action.

From Fig. 6.9 and Fig. 6.10, it is clear that, for $T_S < 100$ mk, the data did not exhibit a linear dependence on sample-stage temperature. From Eq. 6.12, several microvolts at the SET gate could have driven the resonators to an rms amplitude of $\sim$ 200 fm - approximately the thermal amplitude of device 2 at 50 mK. However, this can be ruled out based on several facts. First, the data for 100 mK and above fit to a straight line through the origin. Second, the integrated power data, both above and below 100 mK, exhibited no obvious dependence on V_{NR}^4, as one would expect if the resonator was driven by a capacitively coupled signal. And third, we knew from transmission measurements that the attenuation down the gate lead was around -20 dB at 20 MHz, and, thus, the noise at the input to the fridge would have to have been $\sim$ 10's μV_{rms}, which was much greater than the expected Johnson noise from the resistors in the voltage dividers (10's nV/$\sqrt{Hz}$ at most) or the output noise of the optical isolators (also 10's nV/$\sqrt{Hz}$ at 20 MHz). It was more likely the result of either power from the RFSET line or dissipation in the SET heating the resonator - in Chapter 7, I address these possible reasons and solutions for the hang-up.

Regardless of the source of the heating, we could use the calibration of IR at and above 100 mK to determine the effective temperature T_e below 100 mK. For example, T_e, at a sample-stage temperature of $T_S = 35$ mK was determined by dividing the integrated response at 35 mK by the integrated response at 100 mK, Fig. 6.11. For the left peak, $IR_{35mK} = 423 \pm 43\ \mu e^2/V^2$, and for the right peak,

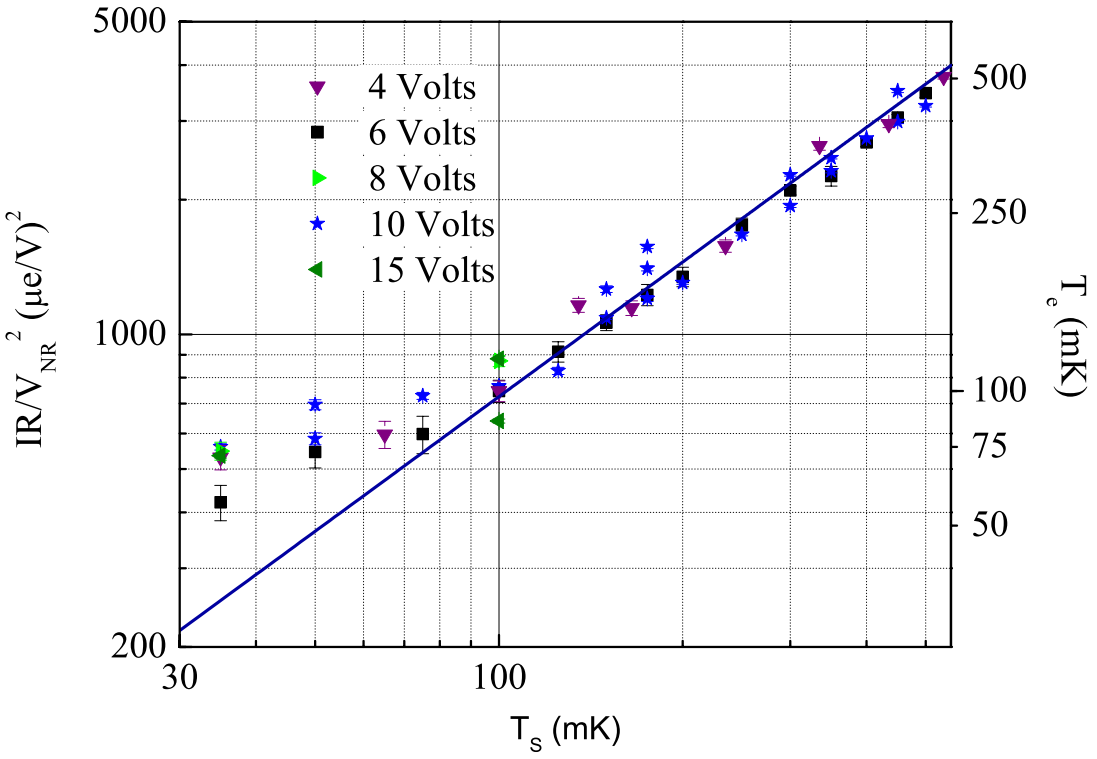

Figure 6.9: A log-log plot demonstrating the integrated resonator response, IR, versus T_S temperature scaled by V_{NR}^2 for Device 2. Using the data from 100 mK and above as a calibration, the minimum temperature of the resonator's fundamental mode is found to be 56 ± 7 mK.

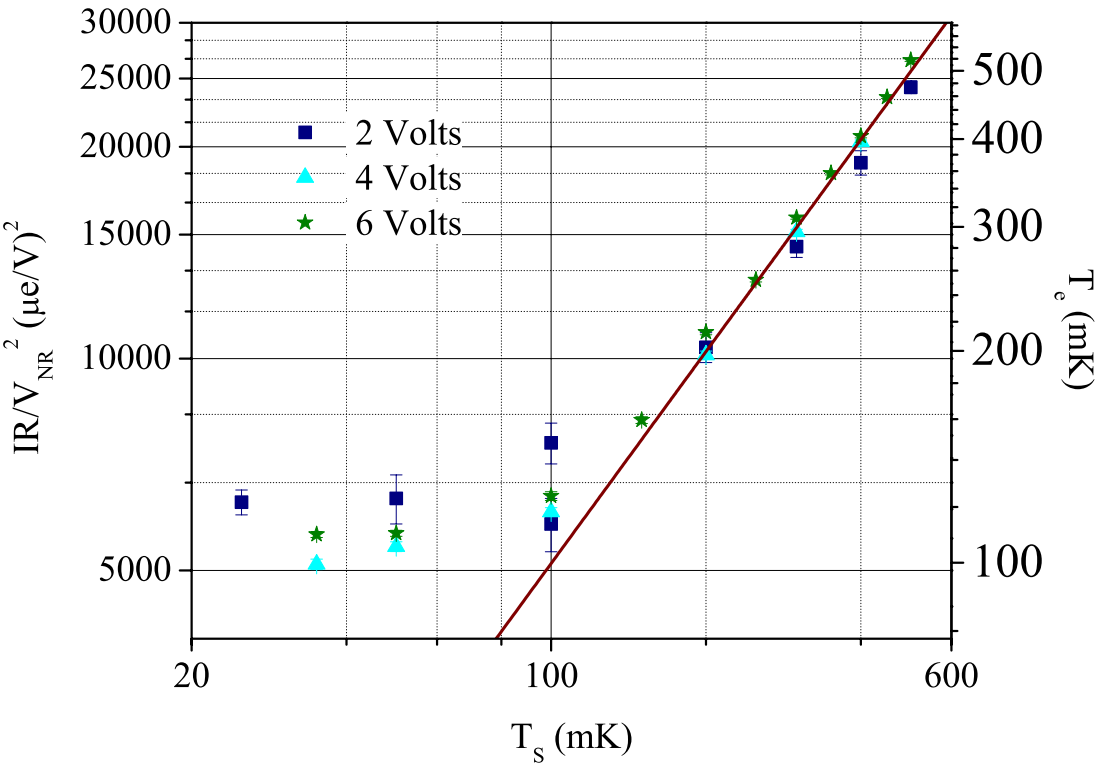

Figure 6.10: A log-log plot demonstrating the integrated resonator response, IR, versus T_S scaled by V_{NR}^2 for Device 1. Using the data from 100 mk and above as a calibration, the minimum temperature of the resonator's fundamental mode is found to be 99 $\pm$ 4 mK.

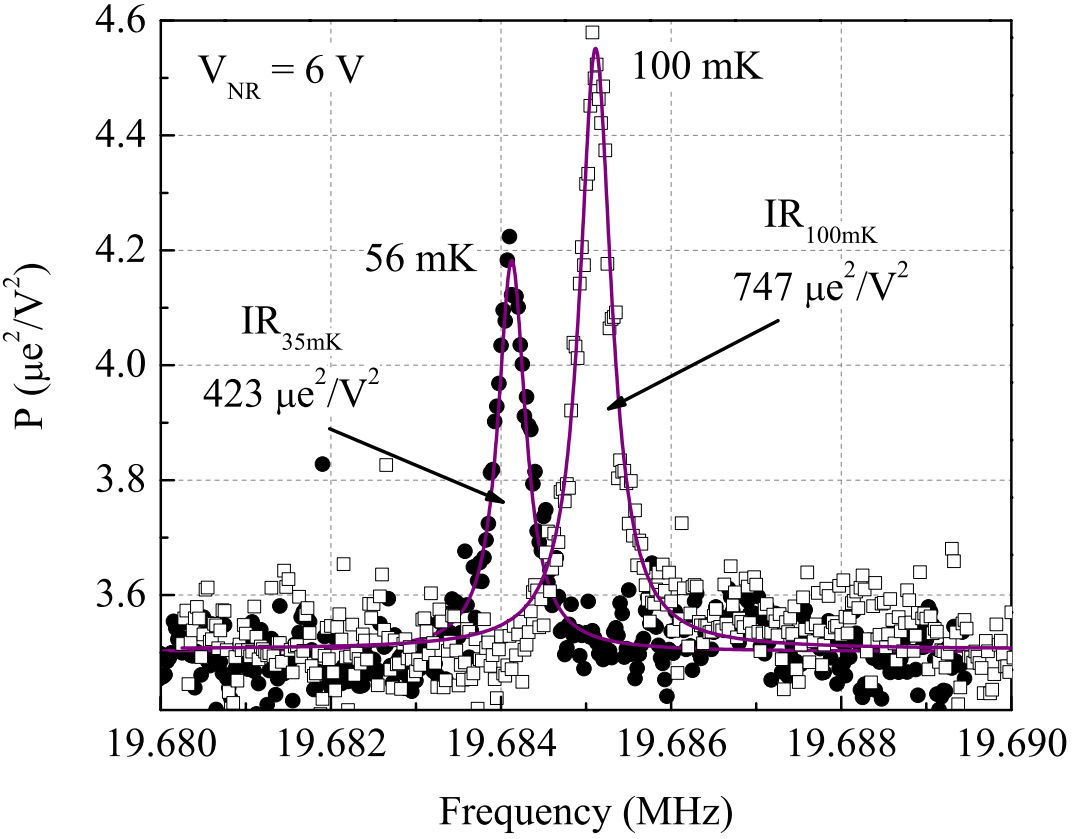

Figure 6.11: Using the data from the 100 mK peak as a calibration, the integrated response at 35 mK is found to correspond to $T_e = 56$ mK. The data is for Device 2. Please note that the 100 mK peak has been shifted by 1.0 kHz for clarity.

$\mathrm{IR}_{100\mathrm{mK}} = 747 \pm 47\ \mu e^2/V^2$. Thus we obtained

$$T_e = \frac{\mathrm{IR}_{35\mathrm{mK}}}{\mathrm{IR}_{100\mathrm{mK}}} = 56 \pm 7\ \mathrm{mK.}, \tag{6.32}$$

Incidentally, $T_e = 56$ mK was the lowest mode temperature that we measured. Using the the Planck distribution function,

$$\langle n_{th} \rangle = (e^{\hbar\omega_1/k_B T_{eff}} - 1)^{-1} \tag{6.33}$$

we calculate that this corresponds to a thermal occupation number of 59 ± 7. This is the lowest thermal occupation number ever measured for a collective mechanical mode [15].

Finally, I note that the slope of the IR/V_{NR}^2 versus T_S for Devices 1 and 2 differ by approximately a factor of 7 (see Figs. 6.9 and 6.10). This is a result of several factors: (1) the increased coupling capacitance of Device 1 compared to Device 2 (61 aF compared to 27 aF); (2) the increased bandwidth of the spectrum analyzer for the measurement of Device 1 (a factor of 1.7); and (3) different spring constants for the two devices (19 N/m for Device 1 compared with 15 N/m for Device 2).

Figure 6.12 shows a plot of the integrated resonator response versus sample-stage temperature for both Devices 1 and 2. The data has been scaled with respect to the derivative of the capacitive coupling, $\partial \mathrm{C}_{NR}/\partial \mathrm{y}_m$ and the effective spring constant K_m for each device. That is, I have plotted $\mathrm{IR}/(\mathrm{K}_m \partial \mathrm{C}_{NR} \mathrm{V}_{NR}^2/\partial \mathrm{y}_m)$. Note that the data for the two devices fall on the same line, confirming that we understand the basic principles of the detection scheme, and have taken into account the dominant parameters - eg. C_{NR}, K_m. However, the fact that the slope of the scaled response deviates from k_B by a factor of ~ 3 tells us that there is systematic uncertainty in

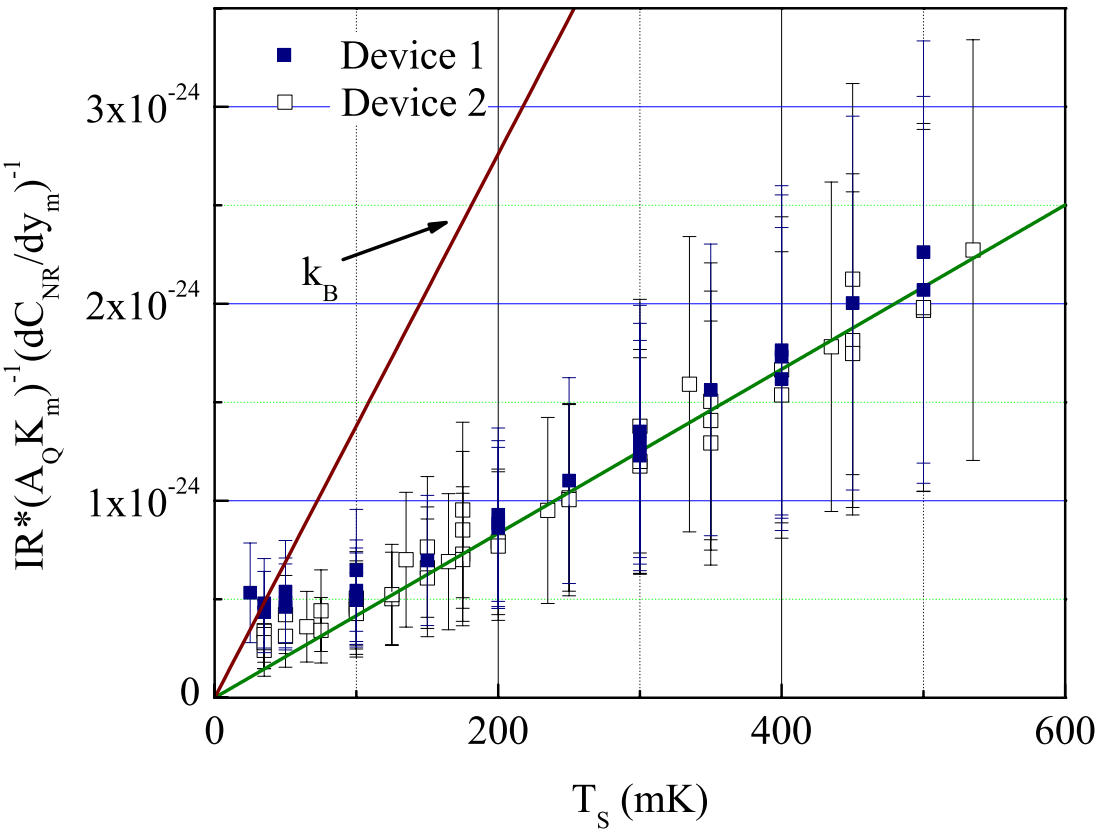

Figure 6.12: A plot demonstrating that the integrated resonator response, IR, for Devices 1 and 2 collapse onto the same line when the data for each device is scaled by the corresponding A_Q, V_{NR}, C_{NR}, and K_m.

our estimate of the measurement circuit gain. This discrepancy is consistent with the deviation in the calculation of the capacitively driven resonator response from the measured response, Section 6.1, and the deviation between the measured and calculated charge sensitivity. Also note that the errors bars on the data points in Fig. 6.12 are considerably larger then the error bars in the previous integrated power plots. The main source of the error is from uncertainty in the spring constant, $\sim$ 50%. I have not included uncertainty in the gain of the measurement circuit.

Noise Temperature

The noise performance of the displacement detection scheme can be evaluated by defining the noise temperature T_N. This quantity correponds to the effective resonator mode temperature, T_e, at which the resulting thermal displacement can be transduced and detected with a signal-to-noise ratio of 1. In other words, it is the temperature at which the rms amplitude of the resonator response A is equal to the rms background level P_o.

Figure 6.13 displays a plot of the resonator response (Device 2) for sample-stage temperature $T_S = 35$ mK and coupling voltage $V_{NR} = 15$ V. The data was fit to an harmonic oscillator response, and the frequency, quality factor, amplitude, background, and integrated response (IR), were extracted. Using the integrated resonator response versus T_S ($7.3 \pm .1$ $\mu e^2/V^2$) as the calibration (Fig. 6.9), the integrated response of the peak (535 ± 24 $\mu e^2/V^2$) was found to correspond to a resonator mode temperature of $T_e = 73 \pm 2$ mK. From the ratio of the amplitude

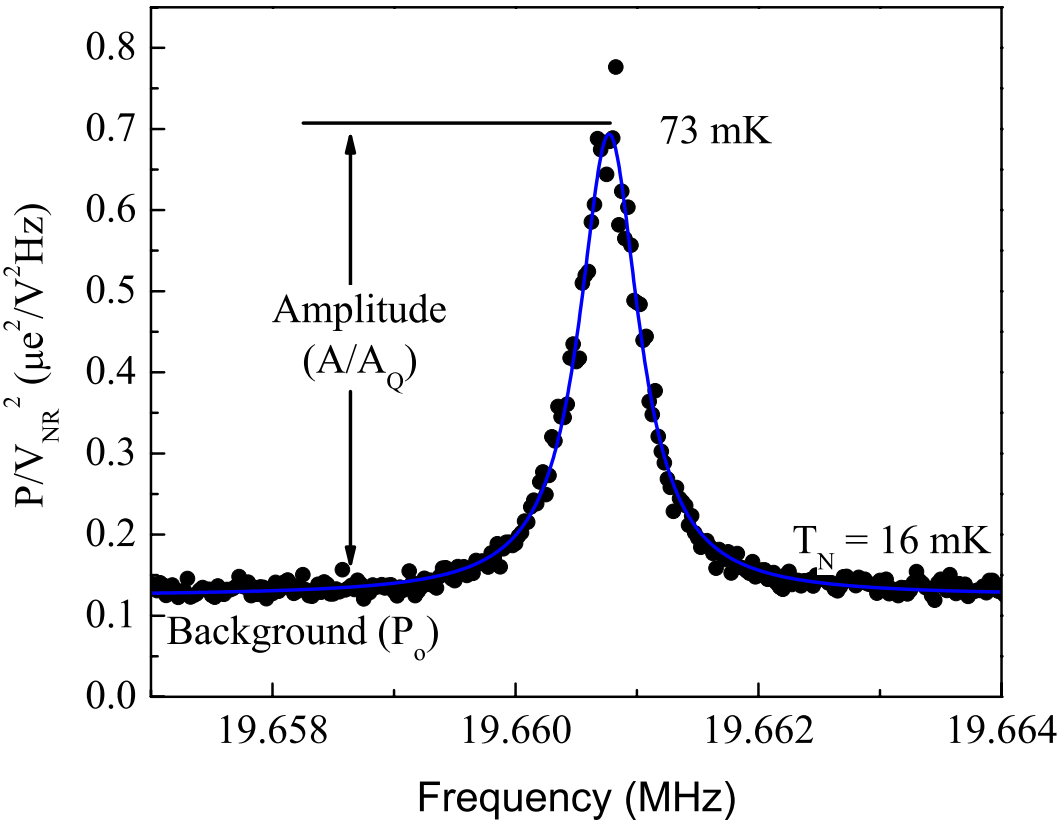

Figure 6.13: A plot demonstrating the lowest noise temperature, T_N achieved by RFSET displacement detection. From the slope of the integrated response versus sample-stage temperature, T_e = 73 mK . The ratio of the amplitude to the background yields a noise temperature of 15.5 ± .4 mK. Data is taken at V_{NR}= 15 V, and is for device 2.

to the background (4.71 ± .01) the noise temperature for the measurement of the peak was found to be

$$T_N = \frac{T_e}{4.71} = 15.5 \pm .4 \text{ mK}. \tag{6.34}$$

Similiarly, we found, for Device 1, that the minimum noise temperature achieved was 43 ± 2 mK.

From T_N and the equipartition relation, a rough estimate of the corresponding displacement noise spectral density within the resonator's noise equivalent bandwidth can be made:

$$S_y = \frac{k_B T_N}{K_m} \frac{4Q_e}{\omega_1}. \tag{6.35}$$

Thus, a noise temperature of T_N=15.5 ± .4 mK corresponded to a displacement sensitivity of 3.8 ± .9 fm/$\sqrt{Hz}$, for $Q_e \sim$ 3.5 x 10^4. For Device 1, the minimum T_N corresponded to a displacment sensitivity of 7.5 ± 2 fm/$\sqrt{Hz}$. Notice, though, that because the calculation of the displacement sensitivity requires knowledge of the spring constant, K_m, the error in the estimate was roughly 25 % for both devices.

To find out how close our detection scheme was to the ideal, we expressed the displacement sensitivity in terms of the quantum limit for each device, Chapter 2:

$$\left(\frac{\delta y_m}{\Delta y_{QL}}\right)^2 = \frac{T_N}{T_{QL}} = \frac{\ln 3 k_B}{\hbar \omega_1} T_N. \tag{6.36}$$

Notice that the dependence on K_m has dropped out. For Device 1 then,

$$\frac{\delta y_m}{\Delta y_{QL}} = 7.4 \pm .2, \tag{6.37}$$

For Device 2,

$$\frac{\delta y_m}{\Delta y_{QL}} = 4.3 \pm .3. \tag{6.38}$$

These numbers represented the closest approach to the quantum limit, to date, achieved in the read-out of the displacement of a mechanical system [15].

Finally, Figs. 6.14 and 6.15 show the noise temperature, T_N (left axis) and mean-square displacement noise (right axis) of Devices 1 and 2 as a function of V_{NR}^2. The displacement noise was normalized with respect to the quantum limit for each device, $\delta \mathrm{y}_m/\Delta \mathrm{y}_{QL}$. Also plotted in the figure are lines (dashed) representing the expected displacment sensitivity for a measurement circuit charge sensitivity of 10 and 20 $\mu e_{rms}/\sqrt{Hz}$. Thus as we increased the coupling voltage, the noise temperature improved linearly with V_{NR}^2, as expected from Eq. 6.7.

6.3 Discussion of SET Back Action

From the discussion in Chapter 2, SET back action produces three effects in the measurement of a nanomechanical resonator's displacement: a frequency shift, damping, and displacement fluctuations. In this section, I argue that there is no clear evidence of any of these effects in the measurement of Device 1 or Device 2.

First, I note that the SET-induced frequency shift and damping arise as a result of the dependence of the SET-island potential ϕ on resonator position. A change in the resonator's position alters the island potential, which changes the electrostatic force between the SET island and the resonator.

The in-phase component of the response shifts the resonator's frequency ac-

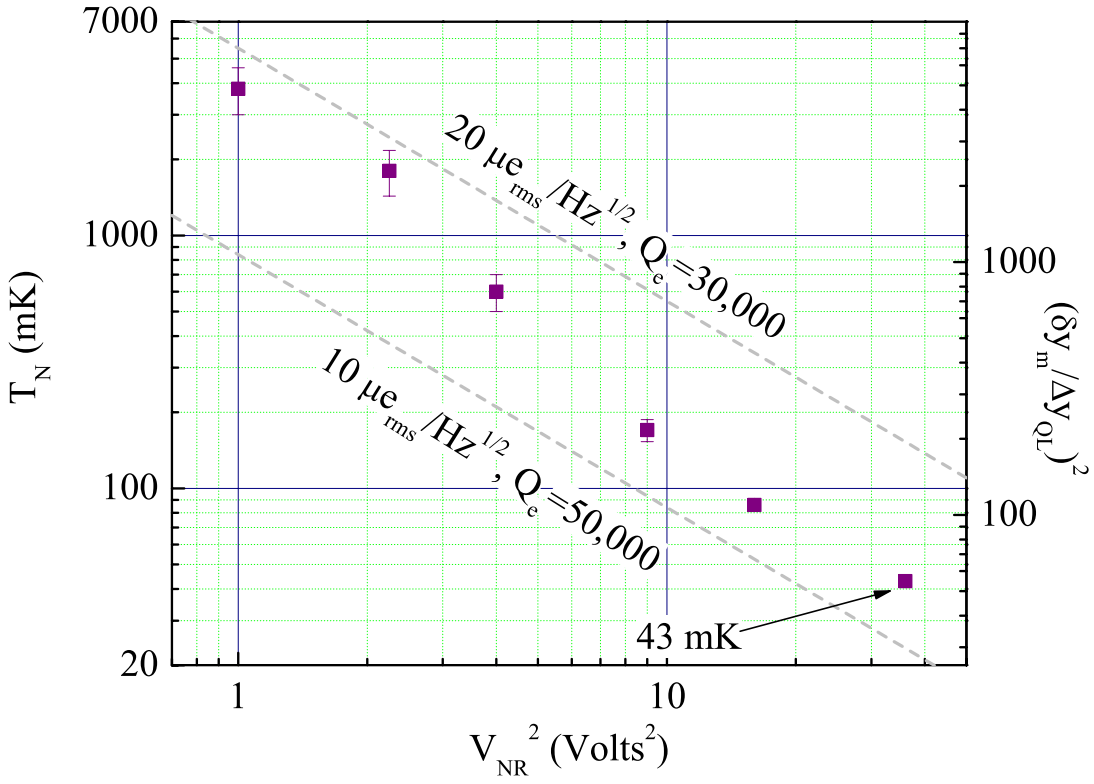

Figure 6.14: A plot demonstrating the noise temperature, T_N, of the RFSET displacement detection scheme as a function of V_{NR}^2 for device 1. The right axis is the corresponding square of the position sensitivity normalized with respect to the quantum limit. A minimum noise temperature of 43 $\pm$ 2 mK was achieved. This corresponds to a displacement sensivity of a factor of 7.4 $\pm$ .2 from the quantum limit, or 7.5 $\pm$ 2 fm/$\sqrt{Hz}$.

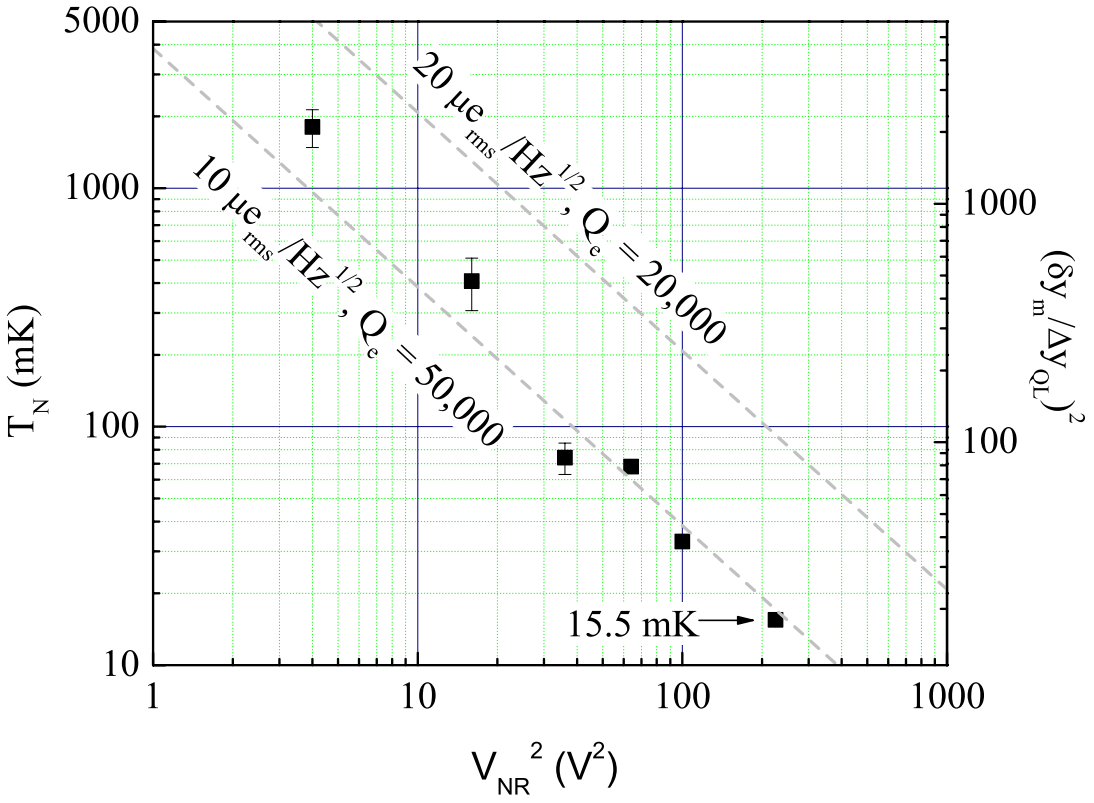

Figure 6.15: A plot demonstrating the noise temperature of the RFSET displacement detection scheme as a function of V_{NR}^2 for device 2. The right axis is the corresponding square of the position sensitivity normalized with respect to the quantum limit. A minimum noise temperature of 15.5 ± .4 mK was achieved. This corresponds to a displacement sensivity a factor of 4.3 ± .3 from the quantum limit, or 3.8 ± .9 fm/$\sqrt{Hz}$.

cording to

$$\frac{\Delta\omega_1}{\omega_1} \approx -\frac{C_{NR}V_{NR}^2}{K_m d_{NR}^2}\frac{C_{NR}}{2C_\Sigma}. \tag{6.39}$$

Comparison with Eq. 6.16 shows that this shift in the resonator's frequency should be $\sim \frac{C_{NR}}{C_\Sigma}$ smaller than the frequency shift due strictly to the electrostatic softening from V_{NR}. For Devices 1 and 2, the ratio is $\sim$ 0.1 - 0.2, so the effect should provide a small correction.

Figure 6.16 shows the frequency shift of the nanoresonators from Device 1 and Device 2 versus V_{NR}^2.[1] From a linear fit to the data, a slope of 72 and 124 Hz/V^2 were obtained respectively. These values are to be compared with the estimates of 140 and 100 Hz/V^2 provided by Eq. 6.16.

From Eq. 6.39, I expect that the effect of the back action should have been about 10 - 20% of these values or $\sim$ 10 Hz/V^2, which was approximately the magnitude of the scatter in the data points. Little more can be said as we lacked the data to make a more precise determination of the slope. Furthermore, for this small of an effect, I would need to develop a more detailed model of both the frequency shift due strictly to V_{NR}^2 (ie. calculate numerically $\partial^2 C_{NR}/\partial y_m^2$) and the frequency shift due to the back action (ie. calculate correlations between tunneling and position fluctuations). Thus, the frequency shift of the resonator cannot be used as a gauge of the level of SET back action in the measurement.

Second, I note that the out-of-phase component of the SET response produces

[1]The data for Device 1 excludes the 6 V coupling data as it was taken on a separate cool-down, and exhibited a shift of 15 kHz.

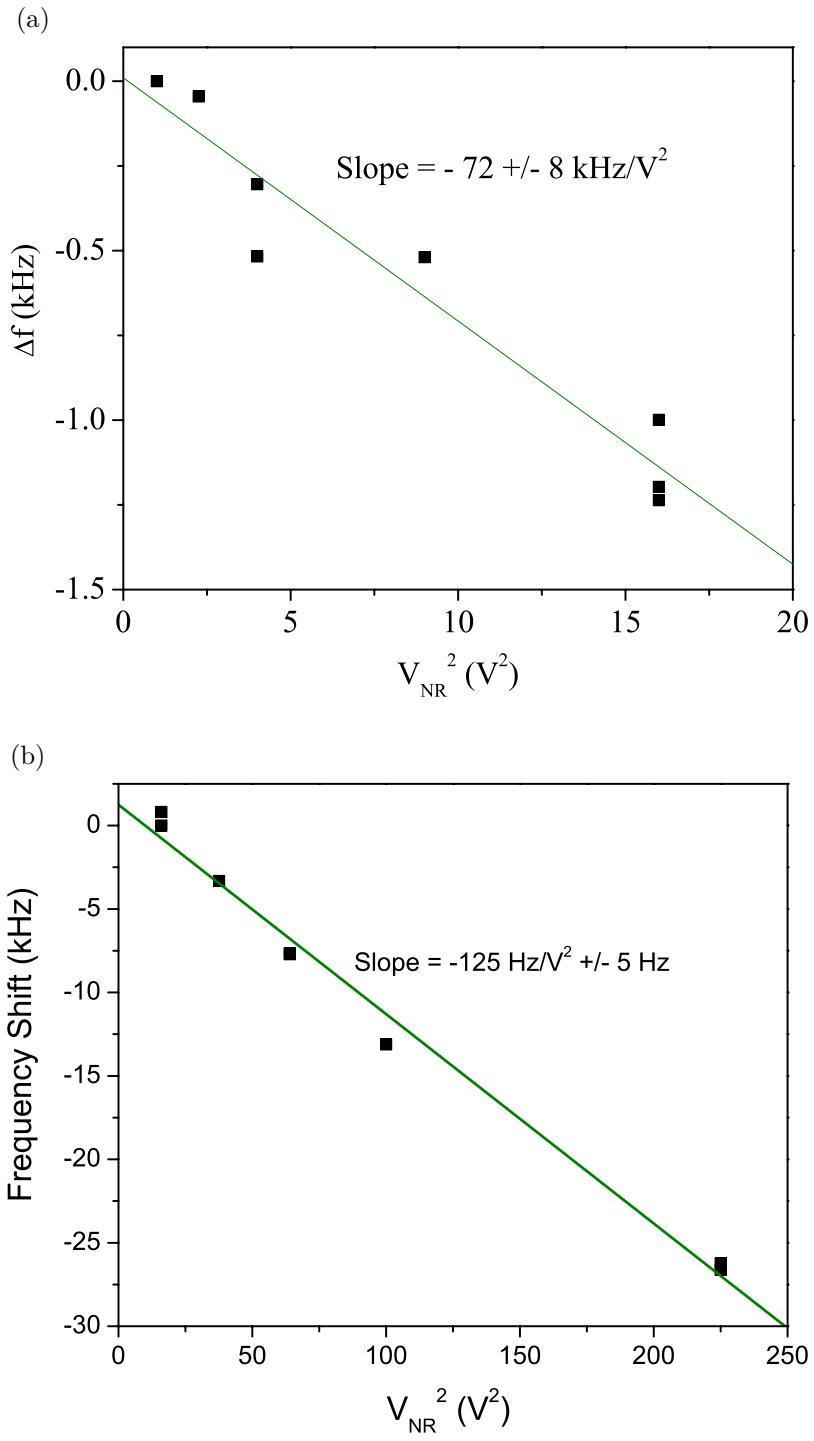

Figure 6.16: Plot of the frequency shift versus V_{NR}^2 for (a) Device 1 at 35 mK and (b) Device 2 at 100 mK. The shift is measured with respect to the lowest voltage data point.

damping:

$$\gamma_{det} \equiv \frac{\omega_1}{Q_d} = \left(\frac{bC_{NR}V_{NR}}{C_\Sigma V_{SD}}\right)^2 \frac{e^2 R_\Sigma}{2M_m d_{NR}^2} = A_{NR}V_{NR}^2, \tag{6.40}$$

where $A_{NR}/2\pi \sim 0.02$ and $0.003\ Hz/V^2$ for Devices 1 and 2 respectively. The total effective resonator damping is thus

$$\gamma_{eff} = \frac{\omega_1}{Q_{eff}} = \gamma_{bath} + AV_{NR}^2. \tag{6.41}$$

It is assumed that A_{NR} is independent of the bath temperature, T_b. I expect, then, that the temperature dependence of γ_e should follow the temperature dependence of γ_b. While the sources responsible for γ_b in nanoresonators are not well understood, γ_b has generally been observed to obey a power-law dependence of T_b^a in several different materials, with $a \sim 0.2$ [121]. Assuming that the power-law holds down to mK temperatures, if γ_d is comparable to or greater than γ_b, then its effect should be evident in the deviation of γ_e from the $T_b^{1/5}$ dependence; the deviation becoming more pronounced at lower T_b as γ_b decreases and γ_d remains constant.

Figure 6.17 shows plots of $\gamma_e/2\pi$ versus T_S for $V_{NR} = 6$ V (Device 1) and 10 V (Device 2). The data sets each represent the largest bias voltage for each device for which complete data sets (35 mK to 500 mK) were taken. If back action is a factor, it should be most pronounced here. The solid line in each plot denotes $T_S^{1/5}$dependence, and was generated by forcing a fit of the data to

$$\gamma_{eff} = C + DT_S^{.2}, \tag{6.42}$$

where A and B are off-set and slope parameters. It is clear from the plots that the effective damping does not saturate as T_S decreases to 35 mK.[2]

[2]The other complete data sets for both Device 1 and Device 2 exhibit similiar behavior.

(a)

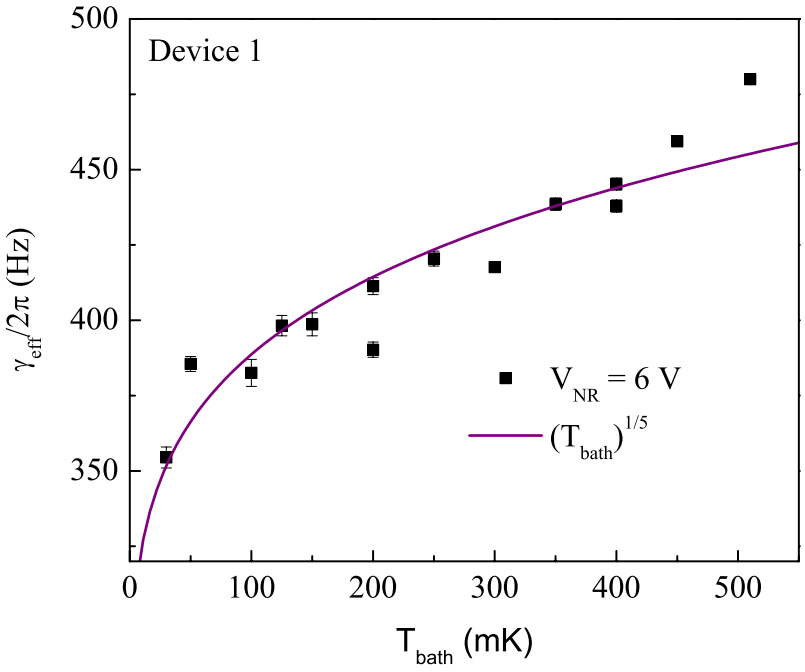

(b)

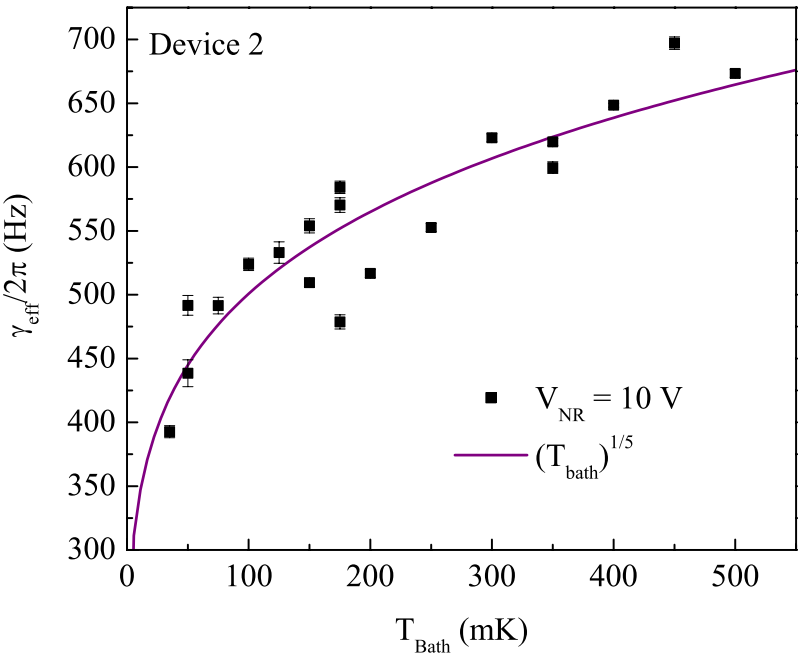

Figure 6.17: Plots of $\gamma_e/2\pi$ Vs. T_S for (a) Device 1 at $V_{NR} = 6$ V and (b) Device 2 at $V_{NR} = 10$ V.

Furthermore, at the lowest T_S, it is seen that there was no obvious dependence of damping on V_{NR} (Fig. 6.18). For both devices, $\gamma_e/2\pi$ was scattered about 500 Hz, ranging from 400 to 900 Hz. Using the estimate of γ_d from Eq. 6.40 and the parameters for Devices 1 and 2, I find that $\gamma_d/2\pi$ should have become comparable to this range of values when $V_{NR} > 100$ V, which is well above the parameter range explored.

Finally I turn to the third back action effect: position-fluctuations. In Chapter 2, I showed that, in the absence of coupling to any other environment, the SET will drive the measured resonator, resulting in fluctuations in the resonator's position with a variance given by

$$\langle y_m^2 \rangle = \frac{k_{\mathrm{B}} T_{\mathrm{d}}}{K_m}, \tag{6.43}$$

where T_d is considered to be a measure of the asymmetry in the SET's quantum noise.

If, in addition, the resonator is coupled to a thermal bath, then the resonator's variance will be given by

$$\langle y_m^2 \rangle = \frac{k_B}{K_m} T_e, \tag{6.44}$$

where

$$T_e = \frac{(\gamma_b T_b + \gamma_d T_d)}{\gamma_e}. \tag{6.45}$$

For small V_{NR}, one expects $T_e = T_b$. However, as one increases V_{NR}, it is expected that the dependence of T_e on T_b will become weaker until $\gamma_d T_d \gg \gamma_b T_b$, at which point the resonator will hang-up at $T_e = T_d$.

Turning back to Figs. 6.10 and 6.9, there is no discernible evidence for this

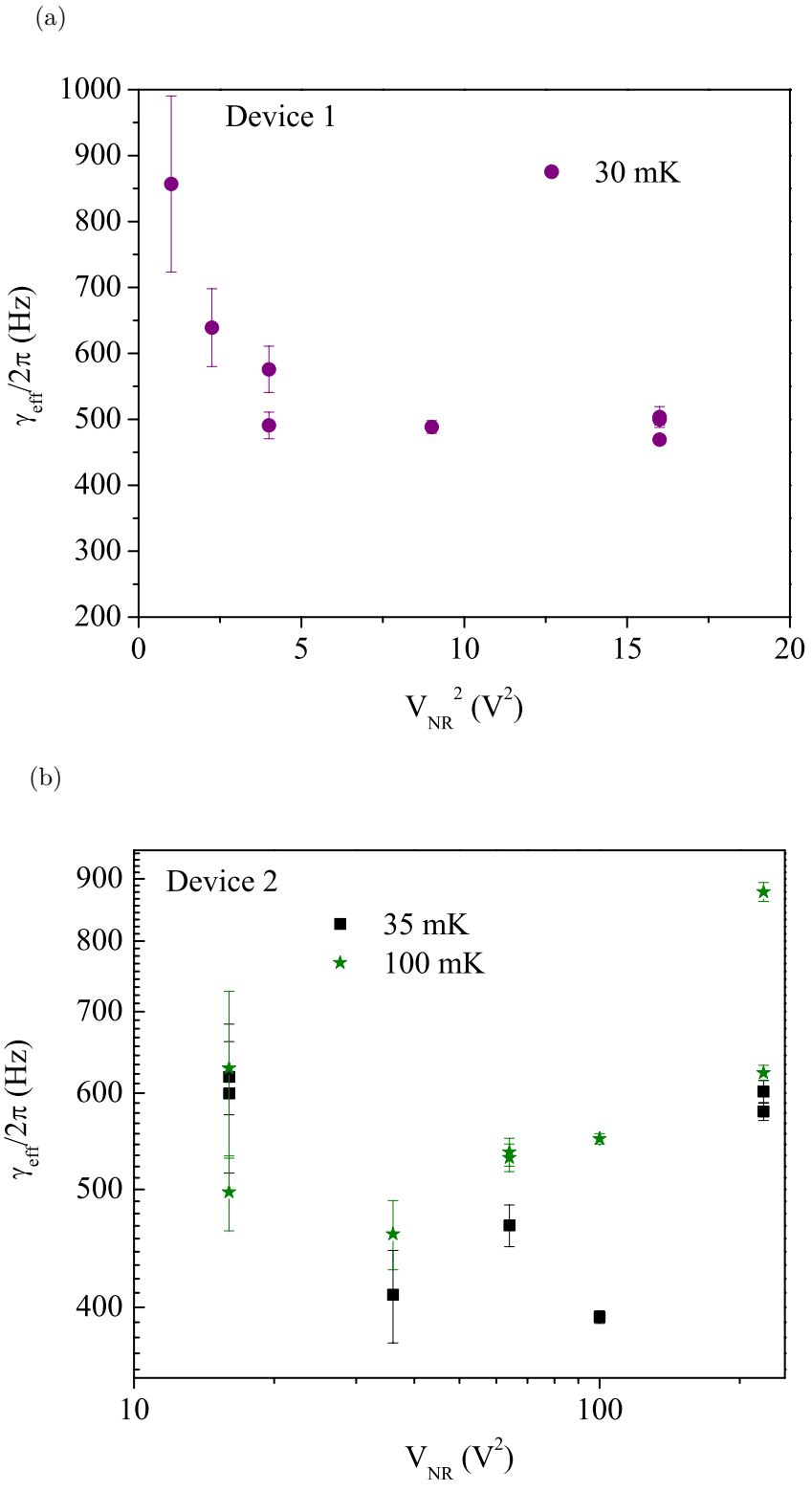

Figure 6.18: A plot of damping versus coupling for (a) Device 1 and (b) Device 2.

effect in either Device 1 or Device 2. As V_{NR} was increased, the dependence of T_e on T_S (or T_b above 100 mK) remained constant.

From Eq. 2.96 and the parameters for Device 2, it is stright-forward to estimate the expected contribution of the SET back action to T_e at 15 V coupling. An order of magnitude estimate of the SET potential fluctuations yields $S_{\phi\phi}^{1/2}(\omega) \sim 1$ nV/$\sqrt{Hz}$. The SET-island potential fluctuations should have then driven the resonator to an rms amplitude of 30 fm_{rms}. This would have corresponded to an effective heating of ~ 100 μK, and, at $T_b = T_S = 100$ mK, would have been a 0.1 % effect.

I close this chapter with a few comments. First, it is clear that, for each of the three quantities (Δf_1, γ_e, and T_e), there is scatter beyond the statistical uncertainty determined from the least-squares fit of the power spectrum data and error propagation. For example, in Fig. 6.9, at 175 mK, the three data points for 10 V coupling each have error bars representing $\pm$ 2% relative uncertainty. However, the scatter about the mean of the three points is $\sim$ 10 - 15 %.

While it is not shown, there may have been a correlation between the scatter in T_e and the scatter in γ_e; that is, for a set of data points at a particular coupling voltage and temperature, the data points which exhibited larger T_e - as compared to the other data points in the set - also exhibited larger γ_e, and vice versa.

Additionally, for Device 2, the scatter in the data at 10 V and 15 V coupling was accompanied by fluctuations in the RFSET gain. These fluctuations were substantial, and resulted in the RFSET gain-feedback unlocking. The frequency and magnitude of the fluctuations appeared to increase with V_{NR}.

Two-level charge fluctuators and back action are both possible explanations for

the observed scatter in the Δ f_1, γ_e, and T_e. The possibility of charge fluctuations is bolstered by the observation that the magnitude of scatter appeared to increase with increasing coupling, and that it was accompanied by RFSET gain fluctuations. The possibility of back action being the culprit is weakened by the estimates above which demonstrate that all three back action manifestations should be small with respect to thermal noise and other factors. Of course, until the back action is measured, limited confidence can be placed in these estimates.

Finally, in all of the back action estimates, we used normal-state SET approximations. Recent theoretical [59] [60] and experimental [73] investigations of the SSET back action near the JQP resonances demonstrate significantly different behavior than what is predicted for a simple normal-state SET. For instance, both the magnitude and the sign of T_d and γ_d are very sensitive functions of the SET's detuning from the JQP (DJQP) resonance ridges. Furthermore, it has been found that the SET must be biased off of the center of the JQP ridge and the RFSET carrier amplitude (v_c) must be reduced to a fraction of the JQP resonance-width in order to avoid sampling both the stable (negative γ_d, negative detuning) and unstable (positive γ_d, positive detuning) regimes.

At the time the measurements of Device 1 and Device 2 were made, we were not aware of these details. We were also not particularly careful with maintaining a consistent SET bias point. Typically, the intent was to choose whichever bias point maximized the RFSET gain. The records we have for the bias points (Fig. 6.3 for example) demonstrate that at least some of the time we were biased near the top of the JQP ridge. As well, the peak-peak amplitude of v_c at the SET corresponded to

$\sim 2Q_T$ 8 μV $\sim$ 140 μV, which is on the order of the half-width of the JQP resonance.

There are significant differences though between the present work (Devices 3,4,Y) and the work I report in this Chapter (Devices 1 and 2). The level of coupling is much greater. For the present generations devices, d_{NR}, the resonator/SET spacing, has been decreased to $\sim$ 100 nm. This is to be compared with the 600 nm spacing of Devices 1 and Devices 2. Additionally, the spring constants of the present generations devices have been reduced by as much as a factor of 2 - 3, making the resonator more "susceptible" to the SET's back action forces.

Finally, the evidence for back action in the more recent samples, while not yet fully understood, is much greater. For example, in Device 3, the effective quality factor has been observed to decrease with V_{NR}^2 dependence from above 1 x 10^5 at 1 V coupling to 2 x 10^4 at 12 V coupling. For the same span in coupling voltage, the relationship between T_e and T_S is shown to go from directly proportional at 1 V to independent at 12 V. Finally, in an even more recent sample (Device Y), both positive and negative damping have been observed in the vicinity of the both the JQP and DJQP resonances.

In the light of these facts, while we cannot completely rule out the influence of SET back action in Devices 1 and 2, it is clearly not a significant effect.

Chapter 7

Conclusions

So far, I have demonstrated that we are capable of approaching the quantum limit on two fronts: we have implemented a near-ideal displacement detection scheme with sensitivity $\delta y_m = 4.3\Delta y_{QL}$; and we have cooled a mode of a nanomechanical oscillator to $\langle n_{th} \rangle \approx 60$. These observations are the closest approach to the quantum limit for a nanomechanical or macroscopic object to date. In this final chapter, I discuss possible reasons why our observations were limited to these values and suggest several technical improvements to push even closer to the quantum limit in future work.

7.1 Shot Noise Limited Detection

Figure 7.1 demonstrates the deviations from ideality of the displacement detection scheme for the measurement of Device 2. We found that as we increased V_{NR}^2, the noise temperature T_N decreased linearly with a slope (dashed line) determined by $S_Q \sim 10\mu e\sqrt{Hz}$. This is at odds with the charge sensitivity of $30\mu e/\sqrt{Hz}$ we measured from the 1 MHz gain calibration (Chapter 5 and Appendix II). The discrepancy could be a result of the improper calibration of charge sensitivity during the measurement of Device 2. At that time we were not aware of the Bessel function calibration method. It could also be the case that the charge sensitivity was

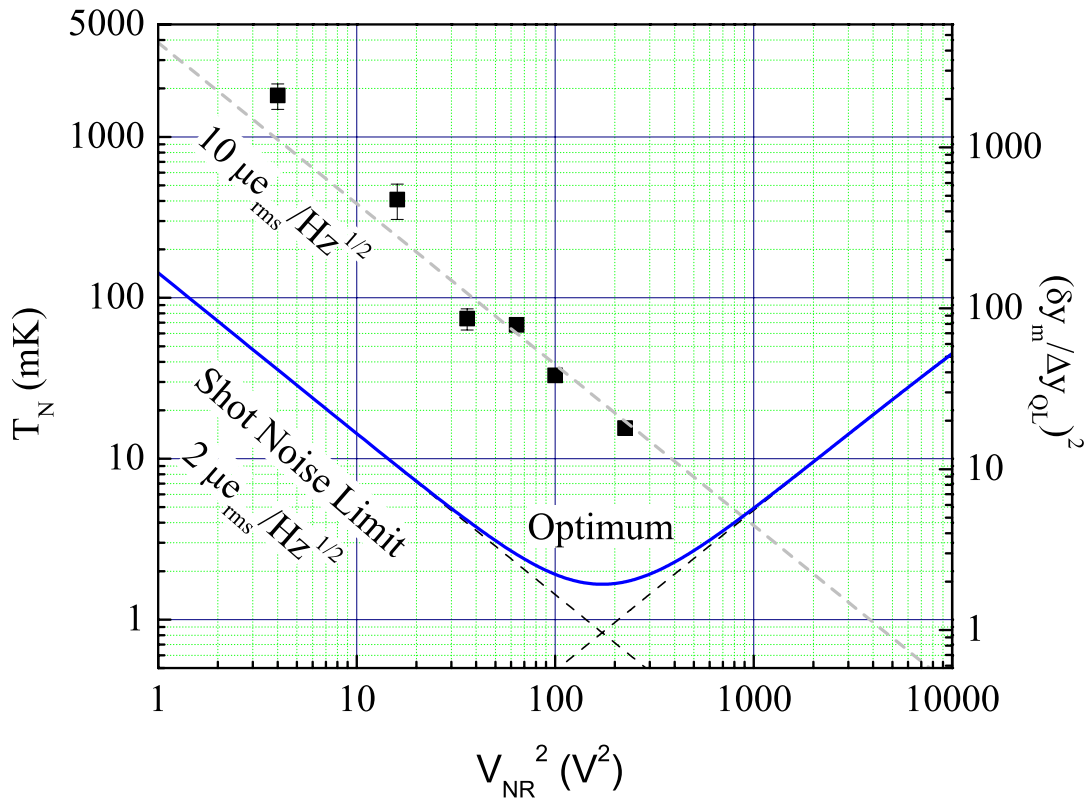

Figure 7.1: A plot of T_N Vs. V_{NR}^2 for Device 2. The solid line is the total noise temperature including both SET shot noise and back action.

better at 20 MHz than at 1 MHz. Nevertheless, the solid lines denote the estimated SET shot noise and back action contribution to the noise temperature, assuming a normal-state SET.

It is clear that there is room for a factor of 5 reduction in the forward-coupling measurement circuit contribution before the detection scheme becomes limited by the SET shot noise. To achieve this, there are at least three improvements that we could make.

First, we could account for and reduce the 4 - 5 dB attenuation in the portion of the microwave circuit between the sample and the HEMT pre-amplifier.[1] From a simple consideration of the measurement circuit noise performance, one can see that a loss of 4 - 5 dB between the RFSET and the HEMT pre-amplifier is a significant contribution to the mesasurement circuit noise temperature

$$T_n^{det} \approx T_L + \frac{T_{HEMT}}{10^{-L/10}} \approx 11 - 15 \text{ K}, \tag{7.1}$$

where $T_L = 4(10^{L/10} - 1)$ is the equivalent noise temperature for the section of the circuit where the 4 - 5 dB is lost, L = 4 - 5 dB is the loss, and $T_{HEMT} \approx 2$ K is the equivalent noise temperature of the pre-amplifier. Thus, while it is still a significant factor, the ultra-low noise HEMT accounts for less than 20% of the measurement circuit noise temperature.

Second, we could replace the HEMT with a better cryogenic amplifier and use the HEMT as a follower. One possibile replacement would be the nearly-quantum limited microstrip SQUID amplifier [119], which has been demonstrated with an

[1]For Devices 1 and 2, we do not have a record of the loss in this portion of the circuit. Considering that $T_n^{det} \approx 20$ K for Device 2, the attenuation was probably closer to 6 dB.

equivalent noise temperature a factor of 2 from the quantum limit at 500 MHz [119]. It has been used routinely with a noise temperature of 100 mK and gain of 20 dB up to 500 MHz. These amplifiers can operate below 100 mK, which would allow for placement very close to the sample, and thus reduce the possibility of signal-loss in the coupled-portion of the microwave circuit (See Chapter 5 and Appendix II).

I can calculate the overall improvement in the noise temperature of the measurment circuit for the case that the RFSET is read-out with a microstrip SQUID. Assuming a gain of 20 dB and noise temperature of 100 mK for the SQUID, and using the 2K HEMT[2] as a follower, I calculate

$$T_n^{det} \approx 120 \text{ mK}, \tag{7.2}$$

without loss in the circuit.

With 5 dB of loss following the SQUID, I calculate

$$T_n^{det} \approx 250 \text{ mK}. \tag{7.3}$$

This is a factor of at least 40 improvement in the noise temperature of the measurement circuit. Assuming, an SET with the identical parameters as Device 1 or Device 2, this should result in the reduction of the charge sensitivity to the SET shot noise limit.

There are several concerns with using the microstrip SQUID amplifier. One is that it might require the use of a lower carrier frequency for the RFSET, and hence lower bandwidth. This problem could probably be circumvented by detuning

[2]There is a HEMT amplifier available from Reference[107] with a quoted noise temperature of .9 K at 650 MHz which could be used as a follower for the SQUID.

the carrier frequency from the tank circuit resonance by the expected mechanical resonator frequency. The second concern deals with dynamic range. It isn't clear whether the reflected signal from the RFSET would swamp the SQUID amplifier. For example, in Reference[120], the author calculates that the maximum output power a typical SQUID in open-loop configuration could supply to a 50 Ωload is approximately 3 nW. Based on this calculation, if the SQUID amplifier has a gain of 20 dB, then the maximum input power is limited to approximately 30 pW. For RFSET operation, depending on the bias point, the reflected power could be as large as several 100 pW. This requires further invsetigation.

Finally, the third improvement that we could make would be to the matching characteristics of the RFSET LC circuit. For Devices 1 - 4, the transformed SET impedance on resonance, Z_{LRC}, was approximately 0.04 - 0.12 Z_o. As a result, the reflection coefficients at maximum conductance, $\Gamma_{\max}$, ranged from $\sim$ 0.8 - 0.92, and yielded maximum depths of modulation M = 20log($\Gamma_{\max}$) of $\sim$ 0.7 - 2.0 dB. The obvious solution to this is to begin using larger inductance coils. Keeping C_T fixed at $\sim$ 250 fF would require increasing the inductance up to 100's nH for optimal matching. This would also have the desired affect of reducing the tank-circuit frequency down to an acceptable range for the microstrip SQUID amplifier. Again, though, we would pay the price in bandwidth. For $C_T \sim$ 250 fF, optimal matching at 400 MHz, would require $L_T \approx$ 600 nH. This fixes the tank-circuit quality factor and bandwidth to be $\sim$ 15 and 27 MHz respectively. Obviously, the optimization is tricky. One might not need to implement perfect matching. For example, increasing L_T so that $Z_{LRC} \sim 0.5\ Z_o$ would increase M by 6 - 8 dB, and

hence improve the charge sensitivity by approximately a factor of 2.

7.2 Sample Thermalization

Ultimately, the base temperature of the dilution refrigerator is ~ 9 mK. This has been confirmed using nuclear orientation thermometry. In the previous chapter, I showed that the minimum resonator mode temperature that we measured was around 60 mK. Thus, it is clear that considerable improvement could be made to bring the mixing chamber and the nanoresonator's fundamental mode into thermal equilibrium. There are at least three components to this problem: (1) minimizing the thermal impedance between the mixing chamber and the sample stage; (2) minimizing the thermal impedance between the nanoresonator's mode and the sample stage; and (3) reducing heat to the device. I assume that the first component, while not trivial, can be made negligible using the proper materials and connections. The second component is also not trivial and should depend on both the material out of which the samples are made and the geometry and mode of the nanoresonator. While, for a given nanoresonator mode, the thermal coupling between the mode and the substrate "bath" can be inferred from measurements of the resonator's quality factory, the nature of the coupling is not well understood [121] and is deserving of an entire thesis. Thus, in the section, I focus on the third component. In particular, I discuss two possible sources of heating: the Nb-Nb microwave coax and the SET.

Heat Transfer Through Nb-Nb Coax

It is possible that heat was conducted via the microwave coaxial cable to the sample stage. From 1 K down to the mixing-chamber, we used Nb-Nb UT-85 coax (see Chapter 4) [106]. Gold-plated copper clamps were used to thermalize the outer-shield of the coax at the still-stage and cold-plate. At the mixing-chamber, the coax connected to a bias tee. The connection from the bias tee to the sample holder was made via a Cu UT-85 semi-rigid coax. From the clamps and the low thermal conductivity of the superconducting Nb [111], it seems unlikely, then, that heat flow through the outer-shield of the coax was responsible for heating of the sample. However, because of the Teflon insulation between the outer shield and inner conductor, it is possible that heat transfer through the coax's center conductor could have resulted in the center conductor being out of equilibrium with the shield and the mixing chamber.

To estimate the temperature difference between the inner and outer conductor of the coax at the mixing chamber, I consider the coax to be a cylinder of length L and composed of three concentric regions (Fig. 7.2): (1) an inner Nb conductor with thermal conductivity κ_1 and radius r_1; (2) a Teflon insulator with thermal conductivity κ_o; and (3) an outer Nb shield with thermal conductivity $\kappa_2 = \kappa_1$, inner diameter $2\pi r_2$, and thickness t. I assume that the inner and outer conductors are in thermal equilibrium at the 1 K pot ($z = 0$). On our dilution fridge, a typical 1 K pot temperature was 1.7 K. Thus $\mathrm{T}_1(0) = \mathrm{T}_2(0) = 1.7$ K. I further assume that, at the mixing chamber ($z = L$), the shield and the mixing chamber are in thermal

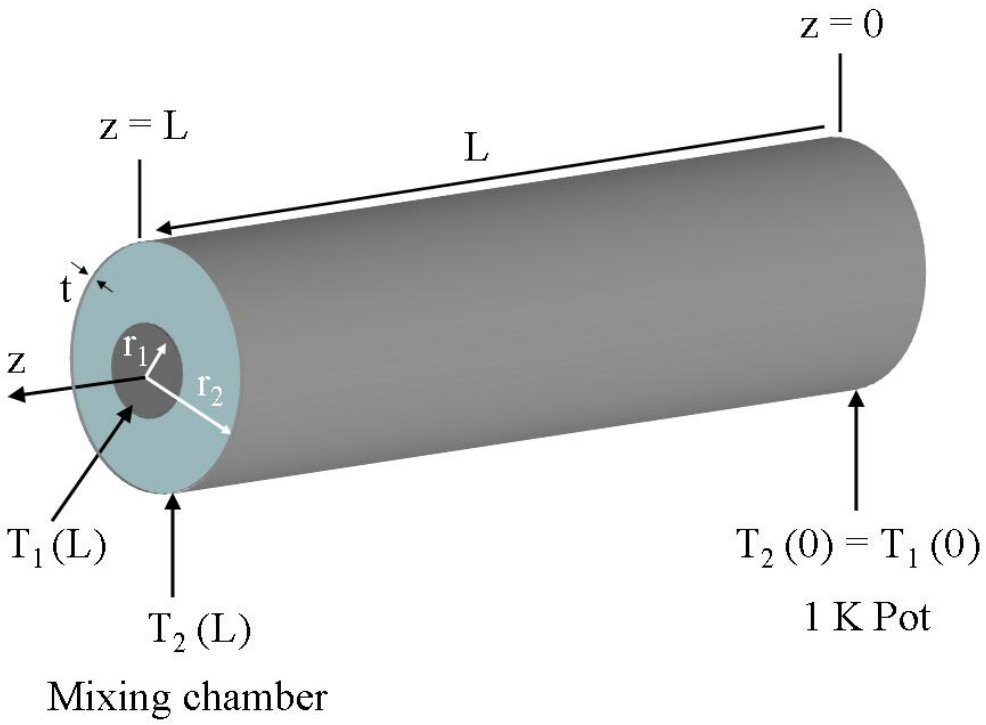

Figure 7.2: An illustration of the Nb-Nb coax semi-rigid coax for heat-flow calculation. It is assumed that the center conductor and shield are in thermal equilibrium at 1 K (T_{1K}) and that the mixing-chamber end of the shield is in thermal equilbrium with the mixing chamber.

equilbrium. The problem is to find the temperature $T_1(L)$ of the inner conductor at the mixing chamber.

As a first approximation, I assume that the heat transfer in the Teflon is purely radial (*ie.* the heat transfer along the length of the coax between 1.7 K and the mixing chamber is dominated by the Nb conductors, which have a much larger thermal conductance due to $\kappa_{1,2}/\kappa_o \gg 1$ below 1 K [111]). Thus, I write the heat transfer per unit length between the inner conductor and the shield at a position z along the length of the coax as [122]

$$\dot{Q} = \frac{2\pi\kappa_o}{\ln(r_2/r_1)}(T_1(z) - T_2(z)). \tag{7.4}$$

I also assume that the heat transfer is purely axial (along z) *within* the inner conductor and *within* the shield. Fourier's law [122] for a segment dz of each conductor thus yields

$$\kappa_1\pi r_1^2\frac{\partial T_1}{\partial z}\bigg|_z - \dot{Q}dz = \kappa_1\pi r_1^2\frac{\partial T_1}{\partial z}\bigg|_{z+dz} \tag{7.5}$$

and

$$2\pi r_2 t\kappa_2\frac{\partial T_2}{\partial z}\bigg|_z + \dot{Q}dz = 2\pi r_2 t\kappa_2\frac{\partial T_2}{\partial z}\bigg|_{z+dz}, \tag{7.6}$$

where I have assumed that $r_2 \gg t$.

Expanding about z, the steady-state temperature profile of the inner conductor is found from

$$\pi r_1^2\kappa_1\frac{\partial^2 T_1(z)}{\partial z^2} + \frac{2\pi\kappa_o}{\ln(r_2/r_1)}\left(T_2(z) - T_1(z)\right) = 0. \tag{7.7}$$

As well, the steady-state temperature profile of the shield is found from

$$2\pi r_2 t\kappa_2 \frac{\partial^2 T_2(z)}{\partial z^2} + \frac{2\pi\kappa_o}{\ln(r_2/r_1)}\left(T_1(z) - T_2(z)\right) = 0. \tag{7.8}$$

If I assume that the thermal conductivities κ_1, κ_2, and κ_o are temperature independent and that $\kappa_1 = \kappa_2 = \kappa$, then the temperature difference between the inner conductor and shield is given by

$$T_1(z) - T_2(z) = (T_{1K} - T_{m/c})\frac{r_1^2 + 2r_2 t}{r_1^2 \sinh(L/\lambda) + (2r_2 tL/\lambda)\cosh(L/\lambda)}\sinh(z/\lambda), \tag{7.9}$$

where

$$\lambda = \sqrt{\left(\frac{\kappa \ln(r_2/r_1)}{\kappa_o}\right)\frac{r_1^2 r_2 t}{r_1^2 + 2r_2 t}}. \tag{7.10}$$

Using the ratio $\kappa/\kappa_o \sim 1$ x 10^3 at 100 mK [111], and measuring $r_1 \sim 0.25$ mm, $r_2 \sim 3.5 r_1$ and $t \sim 0.75 r_1$, I calculate that, for $T_{m/c} = .01$ K and $T_{1K} = 1.7$ K,

$$T_1(L) \approx 30 \text{ mK}, \tag{7.11}$$

where I have assumed that L = 0.5 m.

This analysis suggests that the inner-conductor of the microwave coax is heated by approximately 20 mK above the mixing chamber. However, the assumption that the thermal conductivities of Teflon and Nb are independent of temperature between 1 K and 10 mK (and that their ratio is given by their values at 100 mK) is not accurate. In fact, both materials exhibit a strong temperature dependence below 1 K. Specifically, $\kappa \propto T^3$ and $\kappa_o \propto T^2$ [111]. Thus, the ratio κ/κ_o is a function of position along the length of the cable, decreasing from $\sim 10^4$ at 1.7 K to $\sim 10^2$ at the mixing-chamber. It is likely, then, that $T_1(L)$ could be heated less than

indicated by the above considerations. To estimate a lower bound, I assume that the ratio of the thermal conductivities is given by their values at 10 mK (~ 100). I calculate, then, that $T_1(L) \approx 17$ mK. To conclude, I note that, at a minimum, the center conductor should have been heated by approximately 10 mK above the mixing chamber. However, a more detailed analysis taking into account the temperature dependence of the thermal conductivity of each component of the coax must be done.

Dissipation in the SET

It is also possible that the heating of the resonator mode was due to the dissipation of power in the SET. I can estimate the phonon temperature in the vicinity of the resonator using a steady-state thermal circuit model (Fig. 7.3). I make several assumptions. First, I assume that the power dissipated in the SET was determined by the dc current I_{SD} and the SET resistance R_Σ:

$$\dot{Q} \approx I_{SD}^2 R_\Sigma = 400 \text{ fW} \tag{7.12}$$

for $I_{SD} = 2$ nA and $R_\Sigma = 100$ kΩ.

Second, I assume that the power dissipated in the SET must have been conducted from the electrons in the SET island to the phonons in the SiN membrane beneath the SET via the electron-phonon coupling for normal metals [123] [124]

$$\dot{Q} = \Sigma_1 V_1 \left(T_1^5 - T_2^5 \right), \tag{7.13}$$

where $\Sigma_1 \simeq 2 \text{ x } 10^9$ nW/m^{3}K, $V_1 \simeq 5 \text{ x } 10^{-21}$ m^3 is the volume of the SET island, T_1 is the temperature of the electrons in the SET island, and T_2 is the temperature

of the phonons in the membrane in the vicinity of the SET. It is not known how accurate this assumption is for superconducting metals.

Next, I assume that the phonon transport in the SiN membrane was diffusive [125] and that the power delivered through the SiN membrane (beneath the SET) to the Si substrate can be written as [125]

$$\dot{Q}_1 = .0145\frac{A}{3L}\left(T_2^3 - T_0^3\right), \tag{7.14}$$

where $A \simeq 5$ x 10^{-12} m^2 is the cross-sectional area of the SiN membrane between the SET and the edge of the mebrane, $L = 25$ μm is the distance between the SET and the edge of the membrane, and $T_0 = 30$ mK is the bath temperature, assumed to be the temperature of the Si substrate and sample stage.

Similarly, I write the power delivered through the SiN membrane, from the SET island to the phonons in the vicinity of the resonator, as [125]

$$\dot{Q}_2 = .0145\frac{A'}{3L'}\left(T_2^3 - T_3^3\right), \tag{7.15}$$

where $L' = 600$ nm is the distance between the SET island and the resonator, $A' \simeq$ 1 x 10^{-12} m^2 is the cross-sectional area of the SiN membrane between the SET and the resonator, and T_3 is the phonon temperature near the resonator.

Finally, I assume that there were two "paths" between the region around the resonator and the sample-stage bath: (1) diffusive transport through the SiN membrane [125]

$$\dot{Q}_3 = .0145\frac{A}{3L}\left(T_3^3 - T_0^3\right); \tag{7.16}$$

and (2) electron-phonon coupling [123] [124] between the phonons in the SiN membrane near the resonator and the electrons in the Au film, which are thermally

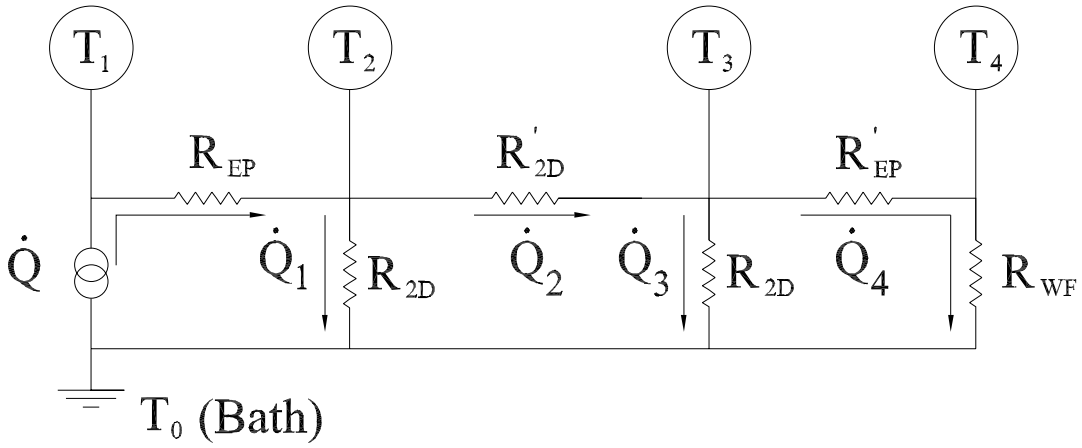

Figure 7.3: Thermal circuit for the SET and resonator on the SiN membrane. Dissipation in the SET ($\dot{Q}$) results in the heating of the phonon temperature around the resonator to T_3. The thermal resistances in the circuit are: (R_{EP}) electron-phonon resistance for the Al SET island; (R_{2D}) 2D thermal resistance of the SiN membrane from the SET to the bath; (R'$_{2D}$) 2D thermal resistance of SiN membrane between the SET and resonator; (R'$_{EP}$) electron-phonon coupling for the Au layer of the resonator; and (R_{WF}) Weidemann-Franz resistance of the Au layer of the resonator to the bath.

connected to the bath through electron scattering (Weidemann-Franz) [111],

$$\dot{Q}_4 = \Sigma_2 V_2 \left(T_3^5 - T_4^5\right) = \frac{A''}{L''}\sigma L_o \left(T_4^2 - T_0^2\right), \tag{7.17}$$

where, for simplicity, I set $\Sigma_2 = \Sigma_1$ Here, $V_2 \simeq 1$ x 10^{-18} m^3 is the volume of the Au on the membrane (this does not include the Au film on top of the resonator, just the Au film leading to the resonator), $A'' = 2$ x 10^{-14} m^2 is the area of the interface between the Au layer and the SiN membrane, $L'' = 2{\times}25$ μm is the length of the Au film (essentially from the ends of the resonator to the edges of the membrane), T_4 is the temperature of the electrons in the Au film layer, $\sigma \simeq 1$ x 10^8 $1/\Omega$m is the conductivity of Au, and $L_o = 2.4$ x 10^{-8} $W\Omega/K^2$ is the Lorenz number [111].

With the additional assumption that Kirchoff's law applies (*ie.* $\dot{Q} = \dot{Q}_1 + \dot{Q}_2$ and $\dot{Q}_2 = \dot{Q}_3 + \dot{Q}_4$), I use Matlab to solve Eqs. 7.13, 7.14, 7.15, 7.16, and 7.17 for T_3. I find that, for $T_0 = 30$ mK and $\dot{Q} = 400$ fW , approximately 200 fW is delivered to the SiN membrane near the resonator. This results in the heating of the resonator region to

$$T_3 \approx 60 \text{ mK}. \tag{7.18}$$

Figure 7.4 shows a numerical calculation of the local resonator temperature T_3 as a function of both the bath temperature T_0 and the power dissipated in the SET $\dot{Q}$. For the calculation of the plot in Fig. 7.4(a), I assumed that the total power dissipated in the SET is $\dot{Q} = 400$ fW. It is seen that T_3 saturates at approximately 60 mK. Above 100 mK, T_3 is linear with T_0. It appears that this behavior results from the increase in electron-phonon conductance above 100 mK. For example, at 10 mK, $\dot{Q}_4$ (the power delivered from the phonons in the vicinity of the resonator through

(a)

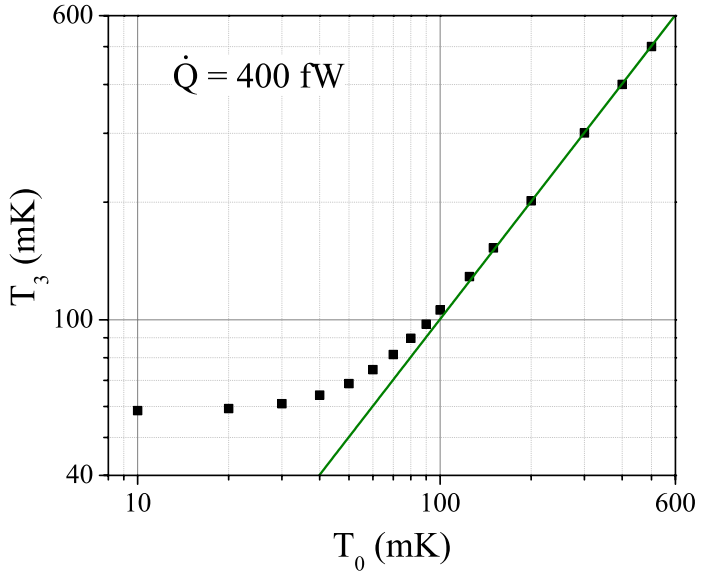

(b)

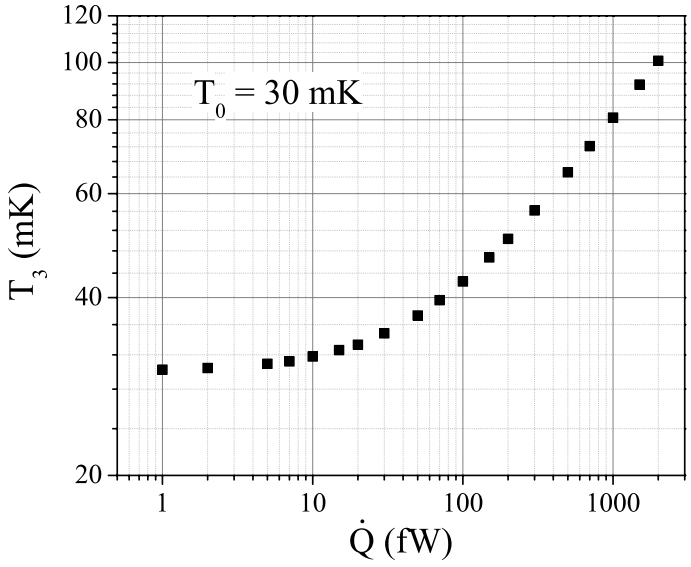

Figure 7.4: Numerical calculation of temperature T_3 of phonons near the nanoresonator as a function of (a) bath temperature T_0 for $\dot{Q}$ = 400 fW and (b) power dissipated in the SET $\dot{Q}$ for T_0 = 30 mK.

the electron-phonon coupling to the electrons in the Au film) is approximately 1.4 fW. On the other, at $T_0 = 500$ mK, $\dot{Q}_4 \approx 80$ fW. The electron-phonon coupling throughout this temperature range ($T_0 = 10$ - 500 mK) is still weak enough, though, that the electrons in the Au layer stay thermalized with the bath T_0. I note that the SET electron temperature T_1 saturates at 380 mK below $T_0 = 200$ mK, rising to approximately 520 mK at $T_0 = 500$ mK.

For the calculation of the plot in Fig. 7.4(b), I assumed that the bath temperature $T_0 = 30$ mK. It is seen that for $\dot{Q} < 10$ fW, the local phonon temperature T_3 is heated by less than 2 mK. For $\dot{Q} = 1$ pW, $T_3 \approx 80$ mK.

The actual power dissipated in the SETs during measurement is not known with high precision. Typically, the SET was biased near IV features like the JQP and DJQP peak (see Appendix B). However, for Devices 1 and 2, we did not keep a record of both the IV characteristics and the bias point for each measurement. For most of the measurements, we simply recorded the value of V_{SD} and adjusted V_g to maximize the gain. I can estimate the order-of-magnitude of the dissipated rf and dc power from the existing $I_{SD}V_{SD}V_g$ maps (see Figs. 5.4 and 5.5). The half-width (in V_{SD}) and height of the JQP peaks were $\sim$ 50 - 100 μV and $I_{SD} \sim$ 1 - 2 nA respectively. Thus, the dissipated dc power should have been $\dot{Q_{dc}} \sim$ 100s fW. Typically, the incident rf signal was on the order of 10s μV. Thus, the dissipated rf power should have been comparable to the dissipated dc power.

To conclude this section I make several remarks. First, the temperature T_3 calculated in the above analysis is not necessarily the effective temperature of the resonator's fundamental flexural mode T_e. To calculate T_e, it would be necessary

to determine the thermal conductance between the flexural mode and the phonons in the SiN membrane near the resonator. In general, the thermal conductance of a suspended nano-bar is a complicated problem (see references [37] [126] [127]) and is beyond the scope of this thesis. Future work could involve incorporating the existing nanoresonator thermal models into the above circuit analysis and fitting the data for Devices 1 and 2 to the theroetical predictions. This work could be important for understanding the nature of dissipation in nanoresonators. For instance, from such an analysis, I could extract the thermal conductance between the nanoresonator and the bath and compare this with the measured quality factor Q_e of the fundamental flexural mode. If I assume that the heat capacity of the flexural mode is given by [35]

$$C_v = \frac{\partial E}{\partial T_0} = k_B, \tag{7.19}$$

and that the thermal time constant for the mode is given by

$$\tau = \frac{Q_e}{\omega_1} = R_1 C_v, \tag{7.20}$$

where R_1 is the thermal resistance between the fundamental flexural mode and some dissipative environment, then I expect that the thermal conductance should be related to Q_e through the relationship

$$g_1 = \frac{1}{R_1} = \frac{\omega_1 k_B}{Q_e}. \tag{7.21}$$

Of course, other sources of dissipation, such as the SET detector (see Chapters 2 and 6) or charge noise in the substrate (see Chapter 6), might contribute to Q_e. From the considerations of Chapter 6, I expect that the back action was a negligible

factor in the resonator's dynamics. However, a comparison of the agreement between Q_e predicted from thermal conductance models and Q_e measured over a range of coupling voltages V_{NR} might allow for a more precise determination of how small the effect was.

Second, I note that it is also possible that the heating of the resonator mode could have been a result of dissipation in the Au film on top of the resonator. However, from an analysis similiar to the analysis for heating due to SET dissipation, I have found that this would require the electron temperature in the Au film to be approximately 200 mK, far out of equilibrium with the sample stage. Based upon the thermalization of the wiring for the resonator connection (see Chapter 4), it seems unlikely that the resonator lead on-chip would have been at such a temperature. Future work is necessary, though, to rule out black body radiation from the copper grains in the powder filters at the mixing chamber.

Finally, I note that several experimental implementations could be made to determine the nature of the sample's heating. First, heat sinks (see Chapter 4) could be added to the microwave circuit below the 1 K pot to see if better thermalization of the Nb coax's center conductor reduces the sample temperature. Second, the SiN membrane geometry could be eliminated or the SETs could be fabricated off of the membrane to allow for the dissipation from the SET to radiate ballistically to the bath. Third, insight could be gained by operating an SET far from the back action limit and monitoring the effective temperature of the resonator's mode as a function of V_{SD}, V_g, and carrier amplitude v_c, at a given bath temperature T_0.

7.3 Parting Motivation

Besides serving as a manual for myself and others, it was my hope that this text would motivate the pursuit of quantum mechanics in nanomechanical systems by demonstrating how close we are technologically to this possibility.

First, we have demonstrated that the RFSET displacement detector is a near-ideal detector, with sensitivity a factor of 4.3 from the quantum limit. It is thus a promising candidate to be used for advanced measurement techniques such as the quantum squeezing of a mechanical oscillator [29] [30]

Second, we have demonstrated that it is possible to cool and measure mechanical resonators to low thermal occupation numbers, $\langle n_{th} \rangle \sim 60$. With technical improvements and the implementation of feedback cooling [28], or by moving to higher frequency resonators, this number could be reduced toward unity where we could implement techniques to see evidence for quantized harmonic oscillator energy levels and zero-point fluctuations. Even with slight improvement, $\langle n_{th} \rangle \sim 50$, a proposal to use a Cooper-pair box to prepare a nanoresonator in a superposition of coherent position states could be implemented [25]. As well, these results open up the possibility of implementing various other proposals that could extend the study of quantum mechanics to much larger size scales [23-33].

Appendix A

Useful Mechanics Information

In this appendix, classical elasticity theory is used to model the transverse displacement of a nanomechanical beam. In the first section, I make the connection between the vibration of an elastic body and simple harmonic motion. In the second section, I calculate the spring constants for SET detection. In the third secion, I solve for the eigenfrequenices and eigenmodes of an elastic bar under tension. In section four, I discuss the case of an elastic body undergoing damped-driven motion. Finally, in the fifth section, I briefly discuss the magnetomotive detection technique.

A.1 Euler-Bernoulli Theory and The Simple Harmonic Oscillator

I start by modeling our nanomechanical resonators as prismatic bars, clamped at both ends, and composed of isotropic, linear elastic materials (Fig. A.1). If I consider small displacements from equilibrium[1] and assume the cross-sectional area of the bars remain deformationless and perpendicular to the neutral surface, the Euler-Bernoulli assumptions, I can express the equation of motion for vibration in

[1] I consider displacements sufficiently small so that the radius of curvature is large with respect to the transverse dimensions of the resonator. The resonators measured in our research easily satisfy this criteria as a typical ratio of displacement-to-length is $\sim 10^{-6}$.

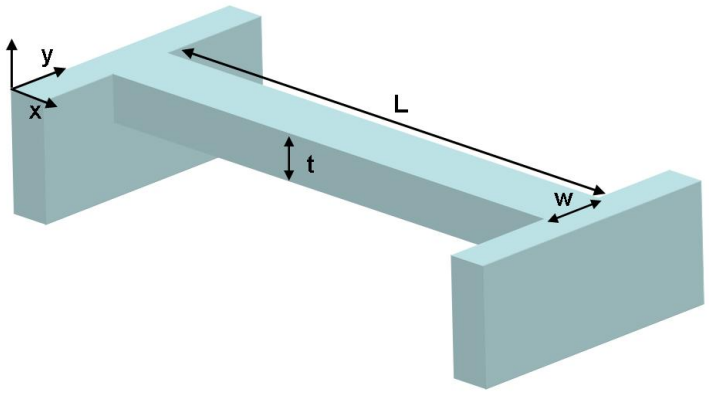

Figure A.1: A schematic of a prismatic, doubly-clamped nanoresonator.

the y-direction as [128]

$$\rho A \frac{\partial^2 y}{\partial t^2} + EI \frac{\partial^4 y}{\partial x^4} = 0. \tag{A.1}$$

Equation A.1 equates the inertial force-per-unit-length on a segment of the bar with the elastic restoring force the segment experiences when deformed. Here E is the Young's modulus of the material, and $I = w^3 t/12$ is the moment of inertia. Parameters ρ and A are the material density and the rectangular cross-sectional area respectively. For composite resonators, such as the metallized resonators in our research, EI should be replace by $E_1 I_1 + E_2 I_2$, where E_1, I_1 and E_2, I_2 are the Young's moduli and moments of inertia for the two layers, respectively. Additionally, for such a resonator, ρA should be replaced by $\rho_1 A_1 + \rho_2 A_2$, where ρ_1 and ρ_2 are the layer densities, and A_1 and A_2 are the respective layer cross-sectional areas [129].

Equation A.1 can be solved using separation of variables,

$$y(x,t) = Y(x)[C_1 \cos\omega t + C_2 \sin\omega t] \tag{A.2}$$

where C_1 and C_2 are determined from the resonator's shape and velocity at some initial time, $t = 0$.

Substituting Eq. A.2 into Eq. A.1, I eliminate the time depedence, and solve for the normal modes. Assuming clamped-clamped boundary conditions, $Y_n(0) = Y_n(L) = 0$ and $\frac{dY_n(0)}{dx} = \frac{dY_n(L)}{dx} = 0$, the normal modes are found to be [128]

$$\begin{aligned} Y_n(x) &= C_n\Big[(\sin k_n x - \sinh k_n x) - \\ &\quad - \left(\frac{\sin k_n L - \sinh k_n L}{\cos k_n L - \cosh k_n L}\right)(\cos k_n x - \cosh k_n x)\Big], \end{aligned} \tag{A.3}$$

where the constants C_n, Table A.1, are determined by normalizing the neutral surface displacement of the mode of interest to unity at maximum displacement. The choice of normalization is arbitrary. I have chosen this particular normalization convention so that, for the fundamental mode, the equations of motion represent the motion of the resonator's mid-point (mid-point with respect to resonator length). Also note that for this normalization convention the mode functions $Y_n(x)$ are dimensionless. The first four modes are plotted in Fig. A.2.

The normal mode frequencies, ω_n, are found from

$${\omega_n}^2 = \frac{EIk_n^4}{\rho A}, \tag{A.4}$$

with k_n determined by the roots of the eigenvalue equation

$$\cos k_n L \cosh k_n L = 1. \tag{A.5}$$

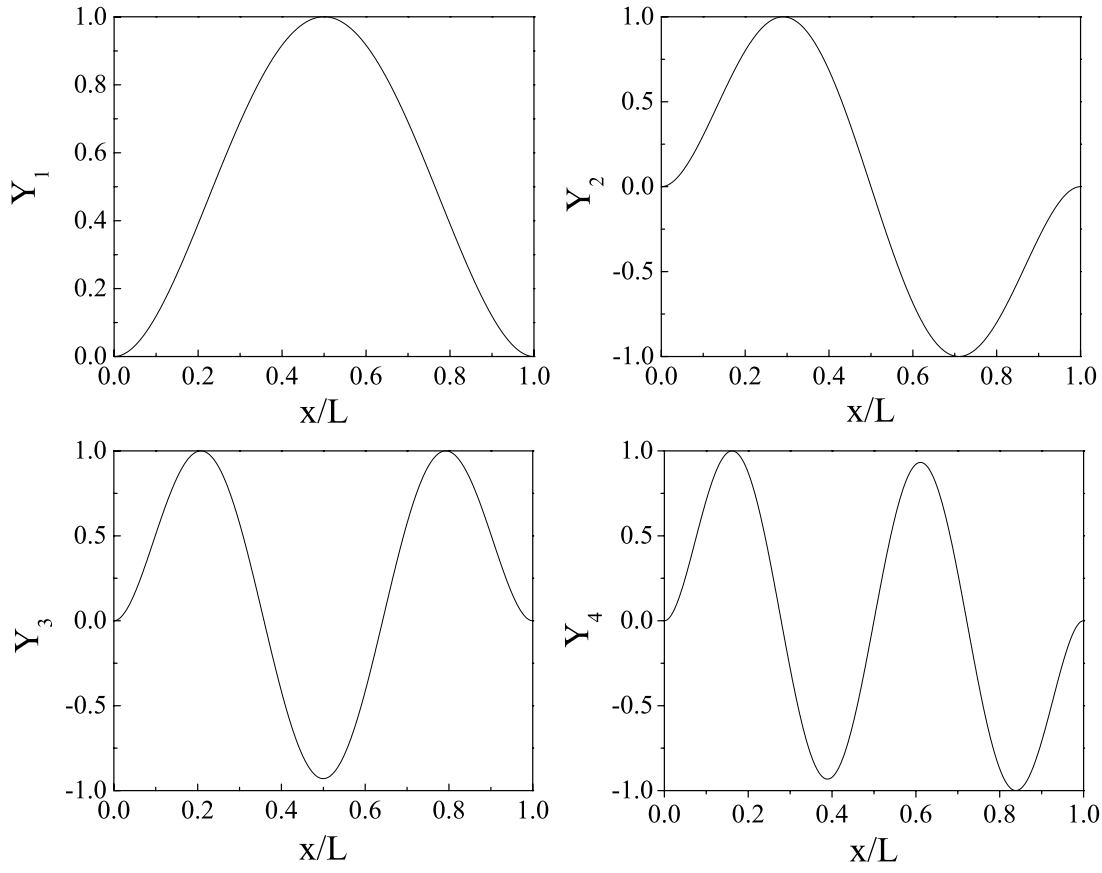

Figure A.2: The functions $Y_n(x)$ for the first four modes of a doubly-clamped resonator. The x-axis has been normalized by the resonator length in each plot.

Table A.1: Geometric Constants: Modes 1-5.

n	k_n	C_n	α_n	δ_n
1	4.730	.619	.397	.295
2	7.853	.663	.439	.145
3	10.996	.661	.437	.081
4	14.137	.661	.437	.052
5	17.279	.661	.437	.036
6	20.420	.661	.437	.026

The eigenvalue equation can be solved graphically or numerically. Table A.1 lists k_n for the first six modes.

In our research, we were typically concerned with resonator motion of purely one mode. Using Eqs. A.2 and A.3, the solution for a given mode, n is simply

$$y_n(x,t) = Y_n(x)\left[C_{n,1}\cos\omega t + C_{n,2}\sin\omega t\right]. \tag{A.6}$$

I now make the connection between the dynamics of a particular mode and the simple harmonic oscillator. To calculate the bending energy E_n of the mode, I consider the average work done in deforming the bar into the mode shape $Y_n(x)$:

$$E_n = \frac{1}{2}\int \langle d\theta_n M_n \rangle, \tag{A.7}$$

where, $M_n = EI\partial^2 y_n(x,t)/\partial x^2$ is the mode's bending moment, and $\theta_n = \partial y_n(x,t)/\partial x$ is the slope of the bar's deformation.

Plugging the expressions for M_n and θ_n into Eq. A.7, I find

$$\langle E_n \rangle \equiv \frac{EI}{2} \int_0^L \langle (\frac{\partial^2 y_n(x,t)}{\partial x^2})^2 \rangle dx = \frac{{\omega_n}^2 A\rho}{2} \int_0^L \langle y_n^2(x,t) \rangle dx$$

$$E_n = \frac{\alpha_n}{2} \rho A L {\omega_n}^2 \langle y_n^2(t) \rangle = \frac{1}{2} K_n \langle y_n^2(t) \rangle. \tag{A.8}$$

It is apparent that this is just the potential energy of an object undergoing simple harmonic motion, with effective spring constant, $K_n = m_{eff,n}\omega_n^2$, and effective mass, $m_{eff,n} = \alpha_n \rho A L$. Here α_n are dependent on mode shape, and are listed in Table (A.1) for the first 6 modes. For the fundamental mode, the paramater $\langle y_1^2(t) \rangle$ is the mean square amplitude of the resonator's mid-point (length-wise), with magnitude determined by initial conditions.

Finally, using the definitions of K_n and $m_{eff,n}$, I multiply Eq. A.1 by $Y_n(x)$ and integrate over x to recover the simple relation

$$m_{eff,n} \frac{\partial^2 y_n(t)}{\partial t^2} = -K_n y_n(t). \tag{A.9}$$

For the fundamental mode, this is simply the expression for the harmonic oscillation of the mid-point of the resonator.

A.2 Spring Constants for SET Detection

While Eq. A.8 expresses the potential energy of a particular resonator in terms of the motion of the resonator's midpoint, in practice, the SET detector is sensitive to the average displacement of the resonator over the length of the SET island. It would be nice, then, to recast Eq. A.8 in terms of this quantity so that I am

able to easily calculate the potential energy of the mode from the observed motion. For example, for a resonator undergoing brownian motion, knowing the relation between the measured displacement and the potential energy of the mode, and using the equipartition theorem, I could calculate the mechcanical mode temperature. Alternatively, knowing the temperature of the mechanical mode, I could calculate the displacement signal I should expect to measure with the detector. Essentially, then, what I want to know is the spring constant $K_{n,m}$ for the mean motion of the resonator over the length of the SET island. I can calculate $K_{n,m}$ from Eq. A.8. To do this, I need to determine the relationship between the mean displacement over the length of the SET and the displacement of the mid-point of the resonator:

$$y_{n,m}(t) = a_n y_n(t), \tag{A.10}$$

where

$$a_n = \frac{1}{L_2 - L_1} \int_{L_1}^{L_2} dx Y_n(x), \tag{A.11}$$

and L_1 and L_2 define the section of the resonator which corresponds to the length of the SET island. I assume that the SET island is centered about the mid-point of the resonator.

I solve Eq. A.11 numerically for the fundamental mode of Devices 1 - 4 (Table A.3). For each sample, the length of the SET island was approximately 5 μm. The length of the respective resonators is listed in Table A.2. For the first mode, Eq. A.8 becomes

$$E_1 = \frac{\alpha_1}{2a_1^2} \rho A L {\omega_1}^2 \langle y_{1,m}^2(t) \rangle = \frac{1}{2} K_{1,m} \langle y_{1,m}^2(t) \rangle, \tag{A.12}$$

where $K_{1,m}$=$M_{1,m}\omega_1^2$, and $M_{1,m}$=$\alpha_1/a_1^2 \rho A L$ are the effective spring constant and

effective mass for the motion of the fundamental mode of the resonator averaged over the 5 μm length of the SET. As I am only concerned with the fundamental mode frequency, the superscript "1" is dropped from $K_{1,m}$ and $M_{1,m}$ for the remainder of the section and througout the text.

To calculate K_m for each device, I need to know both M_m and ω_1. To estimate M_m, I use values of $A = wt$ and L obtained from scanning electron micrograph (SEM) images and knowledge of the etch rates in the processing of the resonator; I assume typical densities of Au and SiN to be 19.3 x 10^3 kg/m^3 and 3000 kg/m^3 respectively [130]. The raw mass $m_r = \rho ALt$ is calculated by including both the Au and SiN layers (Table A.2). To estimate ω_1 (Table A.3), I use either Eqs. A.15 and A.16 or Eq. A.17. The additional parameters required for this calculation are the Young moduli E_{Au} and E_{SiN}, which I assume to be approximately 50 GPa [131] and 250 GPa [75] respectively. I have assumed $\pm$ 50 GPa uncertainty in the value of the Young's modulus for SiN to reflect the spread in values found in the literature (see [76]) and neglected the uncertainty in Young's modulus for the Au layer (50 - 90 GPa reported in Reference [131] depending on grain size and thickness) as its contribution to the total error should be a factor of 5 - 10 times smaller than the contribution from the uncertainty in E_{SiN} (a consequence of $t_{Au} \approx 0.2 t_{SiN}$ for our samples after etching).

Table A.2: Geometry and raw mass, m_r, of Devices 1-4. The error in the length and width of the resonator comes from 10% quoted error in the SEM calibration. The error of 30% in the thickness of the Au layer on the resonator comes from the spread in etch rates over time, and is a very rough estimate.

Device	$w(nm)$	$L(\mu m)$	$t_{Au}(nm)$	$t_{SiN}(nm)$	m_r (pg)
1	300 ±30	10 ±1	30 ±20	100 ±2	2.6 ±1.2
2	200 ±20	8 ±.8	30 ±20	100 ±2	1.4 ±.7
3	200 ±20	15 ±1.5	30 ±20	100 ±2	2.6 ±1.2
4	225 ±23	18 ±1.8	30 ±20	100 ±2	3.2 ±1.5

Table A.3: Effective masses, M_m, and spring constants of Devices 1-4. "a" corresponds to frequency calculated using either Eqs. A.15 and A.16 or Eq. A.17. "b" corresponds to the frequency measured using SET detection at a temperature of 100 mK.

Device	a_1	$M_m(pg)$	$\omega_1/2\pi(MHz)^a$	$K_m^a(N/m)$	$\omega_1/2\pi^b$	K_m^b
1	.838	1.5 ±.7	17 ±5	17 ±8	17.976648(3)	19 ±9
2	.760	.96 ±.45	18 ±6	12 ±6	19.654505(7)	15 ±7
3	.941	1.2 ±.54	6 ±1.8	1.5 ±.7	9.37163340(2)	4 ±2
4	.947	1.4 ±.66	4 ±1	.9 ±.4	4.8976624(2)	1.4 ±.6

A.3 Corrections to Frequency Due to Tension

The nanomechanical resonators used in our research are made from amorphous silicon nitride, which has been deposited using low pressure chemical vapor deposition (LPCVD). The resulting intrinsic stress σ_{int} in the silicon nitride films is on the order of MPa's [132], and is largely tensile. We can model the effect of the stress by including an effective tension $T = \sigma_{int}$ A in the equation of motion (Eq. A.1): [133]

$$\rho A \frac{\partial^2 y}{\partial t^2} + EI \frac{\partial^4 y}{\partial x^4} - T \frac{\partial^2 y}{\partial x^2} = 0. \tag{A.13}$$

Using dimensional-analysis, I can estimate the order of magnitude of the contribution of the tension to the restoring force. From Eq. (A.13), the ratio of tensile-to-bending force is TL^2/EI. For $TL^2/EI \ll 1$, we can expect the bending moment to dominate, and the dynamics to be governed by the results of the previous section. For $TL^2/EI \gg 1$, the tenisle force will dominate, and the dynamics will be similiar to the case of a tensioned string. For silicon nitride nanoresonators, however, the dimensionless ratio can range from $TL^2/EI \ll 1$ to $TL^2/EI \sim 1$. For this range, it would be helpful then to calculate the corrections to normal mode shape and frequency .

Equation (A.13) can be solved exactly using separation of variables, yielding:

$$\begin{aligned} Y_n(x) &= C_n \Bigg[\left(\sin \lambda_n x - \frac{\lambda_n}{\mu_n} \sinh \mu_n x \right) - \\ &\quad - \left(\frac{\sin \lambda_n L - \frac{\lambda_n}{\mu_n} \sinh \mu_n L}{\cos \lambda_n L - \cosh \mu_n L} \right) (\cos \lambda_n x - \cosh \mu_n x) \Bigg], \end{aligned} \tag{A.14}$$

where

$$\lambda_n L = k_n L\left[(a^2+1)^{\frac{1}{2}} - a\right]^{\frac{1}{2}}, \mu_n L = k_n L\left[(a^2+1)^{\frac{1}{2}} + a\right]^{\frac{1}{2}},$$

and

$$a = \frac{T}{2EIk^2},$$

with

$$k_n^4 = \frac{\rho A \omega_n^2}{EI}. \tag{A.15}$$

The values of k are found numerically from the characteristic equation:

$$\cos(\lambda_n L)\cosh(\mu_n L) - \frac{1}{2}(\frac{\mu_n}{\lambda_n} - \frac{\lambda_n}{\mu_n})\sinh(\mu_n L)\sin(\lambda_n L) = 1. \tag{A.16}$$

It is straight-forward to verify that, as $T \to 0$, these expressions reduce to the corresponding expressions in Section A.1.

Figure A.3 demonstrates the effect of tension on the frequency of the normal modes of a doubly-clamped silicon-nitride resonator. In the Fig. A.3(a), the ratio of frequency calculated with tension, $\omega_n(T)$, to frequency calculated without tension, $\omega_n(0)$, is plotted versus the dimensionless correction factor, $TL^2/12EI$, for the first six normal modes of a resonator with a fundamental frequency of 13.037 MHz and length of 10 μm. A bi-morph resonator with cross-sectional area A = 0.0375 μm^2, width w = 250 nm, and a 50 nm thick layer of gold as the conducting layer are assumed. Young's moduli and densities of 300 GPa and 3000 $Kg/m^3$and 50 GPa and 19.3 x 10^3 Kg/m^3 are assumed for the silicon nitride and gold respectively.

It is apparent that for $TL^2/12EI < 0.01$, tension increases the resonant frequency of the first six modes by less than 0.1%. For the fundamental mode, this corresponds to a frequency shift of $\sim$ 10 kHz.

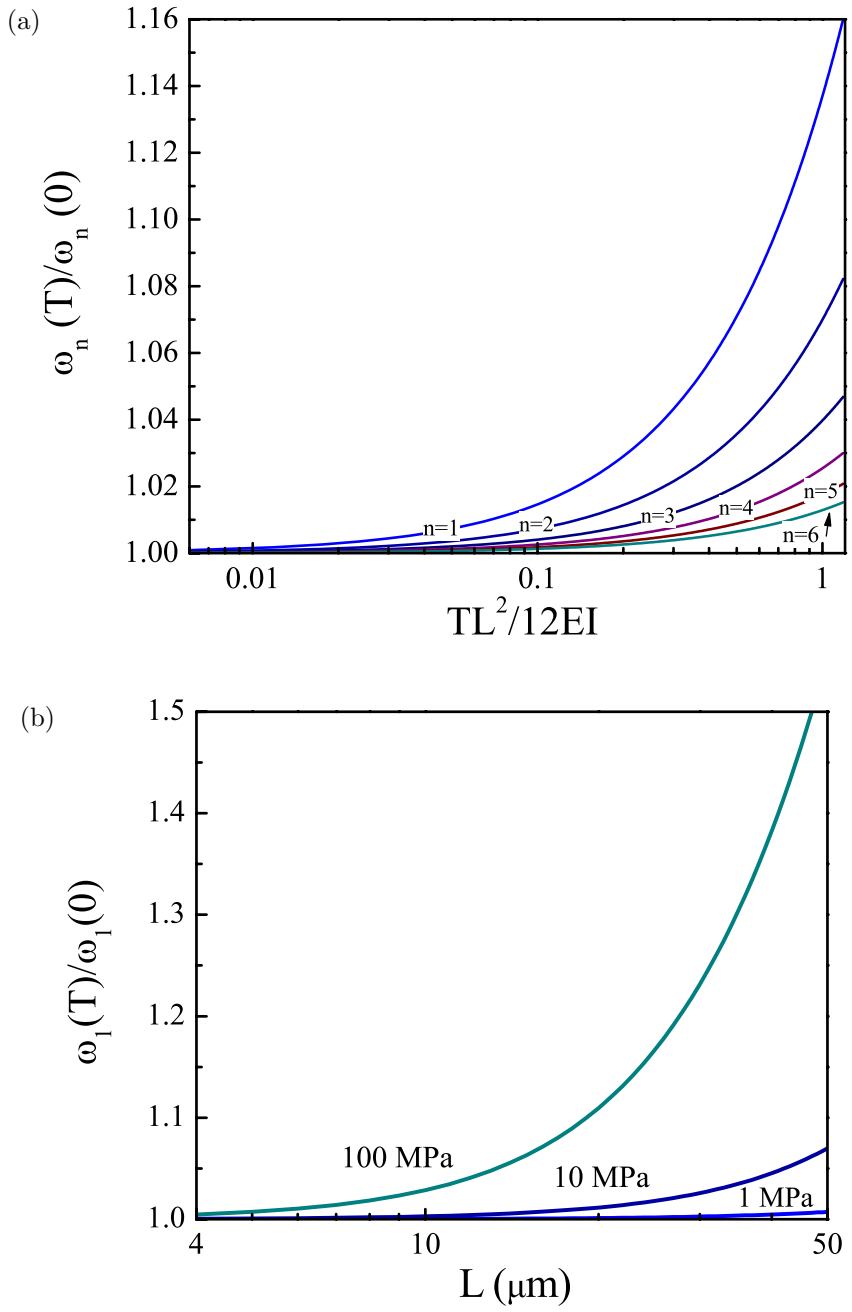

Figure A.3: (a) The normalized mode frequency is plotted versus $TL^2/12EI$, for the first six modes of a doubly-clamped resonator with fundamental frequency of 13.037 MHz and a length of 10 μm. (b) The normalized fundmental mode frequency is plotted versus resonator length for intrinsic stress values of 1, 10, and 100 MPa's.

As the tension is increased to $TL^2/12EI \sim 1$, the shift in resonant frequency for the fundamental mode grows to $\sim 15\%$. The shift in the higher order modes is smaller as they are effectively stiffer than the fundamental mode, and ranges from $\sim 1\%$ to $\sim 8\%$.

Figure A.3(b) demonstrates the shift in frequency of the fundamental mode of a doubly-clamped resonator as a function of the resonator's length for $\sigma_{int} = 1$, 10, and 100 MPa. For each curve, the tension is held constant, and the length of the resonator is increased. Here, I used the same values of EI, ρ, and cross-section as were used in Fig. A.3(a). It is evident, that for silicon nitride resonators with lengths less than 10 μm, the shift in frequency due to tension can be expected to be less than 10% for the fundamental mode - while not shown, the shift in the higher-order mode frequencies is even smaller.

An alternative to solving Eq. A.13 exactly is to use a pertubative technique in which it is assumed that the effect of tension on the mode shape is negligible, the so-called Rayleigh Method [46]. Starting with Eq. A.13, I separate variables and solve for ω_n:

$$\omega_n(T) = \omega_n(0)\left(1 + \delta_n \frac{TL^2}{12EI}\right)^{\frac{1}{2}}, \tag{A.17}$$

with

$$\omega_n(0) = \frac{\beta_n}{L^2}\left(\frac{EI}{\rho A}\right)^{\frac{1}{2}},$$

and

$$\delta_n = \frac{12}{L^2}\frac{\int_0^L dx(\partial Y_n(x)/\partial x)^2}{\int_0^L dx\,(\partial^2 Y_n(x)/\partial x^2)^2},$$

where

$$\beta_n = L^2 \left(\frac{\int_0^L dx \left(\partial^2 Y_n(x)/\partial x^2\right)^2}{\int_0^L dx Y_n^2(x)} \right).$$

I then make the approximation that $Y_n(x)$ are unaltered by the tension and given by Equation A.3. For this case, β_n are found to be equal to k_n determined from Eq. A.5. The first ten δ_n are listed in Table A.1.

For $TL^2/12EI \leq 1$, I have found that the agreement between Eq. A.17 and the exact resonant frequency calculated by solving for the roots of Eq. A.16 is better than .01%. This implies that the approximation that the $Y_n(x)$ are left unaffected by tension T is a good one, and, thus, throughout the report, I simply use the mode-shapes given by Eq. A.3.

A.4 The Driven-Damped Harmonic Oscillator

I can append Eq. A.1 to account for external non-dissipative forces by simply adding in a term $F(x,t)$ (in dimensions of Force/Length). I can account for damping by also inserting a phenomenological term proportional to the resonator's transverse velocity. Dissipation in nanomechanical resonators is not well understood [121], and several mechanisms including thermoelastic loss [134], attachment loss [135] [136], and loss due to the measurement process itself [55] [137] have been proposed. Some authors account for damping effects by defining a complex Young's modulus where dissipation is incorporated in the imaginary component (see [134] [138]). For the purpose of this appendix, however, it is sufficient to account for the damping by

inserting a velocity-dependent term, as it captures the general physics. Thus,

$$\rho A\frac{\partial^2 y(x,t)}{\partial t^2} + EI\frac{\partial^4 y(x,t)}{\partial x^4} + \mu\frac{\partial y(x,t)}{\partial t} = F(x,t), \tag{A.18}$$

Following the approach of Reference [139], I assume that the damping and driving force have a negligible effect on the mode shapes $Y_n(x)$. I then substitute solutions of the form

$$y_n(x,t) = Y_n(x)y_n(t), \tag{A.19}$$

into Eq. A.18, multiply by $Y_n(x)$, and integrate over the length of the resonator, obtaining the equation of motion for a mode, n,:

$$m_{eff,n}\frac{\partial^2 y_n(t)}{\partial t^2} + K_n y_n(t) + \gamma_n\frac{\partial y_n(t)}{\partial t} = f_n(t), \tag{A.20}$$

where

$$\gamma_n = \int_0^L dx Y_n^2(x)\mu \tag{A.21}$$

and

$$f_n(t) = \int_0^L dx F(x,t)Y_n(x). \tag{A.22}$$

Equation A.20 is the familiar damped-driven harmonic oscillator equation of motion. A simple case to treat, and one which will be important for Section A.5, is when $F(x,t)$ is spatially invariant and has an harmonic time-dependence:

$$F(x,t) = \frac{F_o}{L}e^{j\omega t}, \tag{A.23}$$

where F_o is the magnitude of the force.

In this case, $f_n(t) = \eta_n F_o e^{j\omega t}$, where η_n is the average of $\mathrm{Y}_n(x)$ over the length of the resonator,

$$\eta_n = \frac{1}{L}\int_0^L dx Y_n(x), \tag{A.24}$$

and determines the projection of the force on a given mode (Table A.1). The steady-state solutions, found for $t/\tau \gg 1$, where $\tau = m_{eff,n}/\gamma_n$, are then given by:

$$y_n(t) = A_n e^{j\omega t}, \tag{A.25}$$

where

$$A_n = \frac{\eta_n F_o}{m_{eff,n}\left(({\omega_n}^2 - \omega^2) + j\left(\omega_n\omega/Q_e\right)\right)}. \tag{A.26}$$

For a general force F(x,t), Eq. A.26 is replaced by

$$A_n = \frac{\int_0^L dx Y_n(x) F(x)}{m_{eff,n}\left(({\omega_n}^2 - \omega^2) + j\left(\omega_n\omega/Q_e\right)\right)}. \tag{A.27}$$

The resonant frequencies, ω_n, are given by Eq. A.4. The effective quality factor, Q_e is defined as $Q_e = \omega_n m_{eff,n}/\gamma_n$, and sets the width of the resonator's frequency response. I assume that it could be a result of dissipation from coupling to both the measurement environment and a thermal reservoir. Finally, I define the phase difference, ϕ_n, between drive signal and resonator response

$$\phi_n = \arctan\left(\frac{\omega_n\omega/Q_e}{{\omega_n}^2 - \omega^2}\right). \tag{A.28}$$

A.5 The Magnetomotive Technique

For the past decade, researchers have used various forms of magnetomotive detection to study the properties of nanomechanical resonators [140] [141] [142]

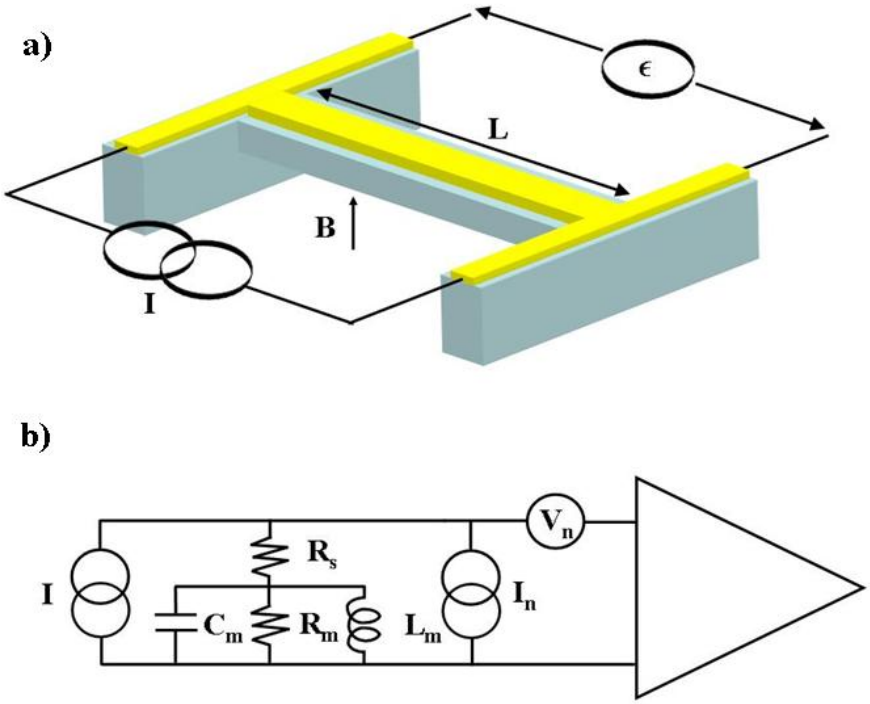

Figure A.4: a). Schematic of Magnetomotive technique. b). Circuit diagram displaying electromechanical impedance, Z_m, current drive, I, and voltage amplifier - assumed to have infinite input impedance.

[36]. In its simplest realization (Fig. A.4(a)), ac current I is applied, length-wise, through a metallized resonator; in the presence of a transverse magnetic field B the resonator is driven by the Lorentz force $F = IBL$ and an EMF $\epsilon_n = BLv_n$, develops across it's length L. Here,

$$v_n = \frac{\partial y_n(t)}{\partial t}\frac{1}{L}\int_o^L dx Y_n(x) = \eta_n \frac{\partial y_n(t)}{\partial t} \tag{A.29}$$

is resonator's mode-dependent velocity. From Eqs. A.25 and A.26, the electromotive response takes the form:

$$\epsilon_n = \frac{j\eta_n^2 B^2 L^2 \omega}{m_{eff,n}\left({\omega_n}^2 - \omega^2 + j\omega_n\omega/Q_{eff}\right)} I. \tag{A.30}$$

The response of the resonator is measured by sweeping the frequency of the applied current through the mechanical resonance, and simultaneously measuring the induced EMF. The magnetomotive measurement is thus an impedance measurement. In fact, it is apparent that the response function is equivalent to a parallel RLC circuit (Fig. A.4(b)) with an electromechanical impedance defined as [137]

$$\frac{1}{Z_m} = \frac{Q_e}{j\omega_n\omega R_n}\left(\omega_n^2 - \omega^2 + j\omega_n\omega/Q_e\right), \tag{A.31}$$

where

$$R_n = \eta_n^2 \frac{Q_e B^2 L^2}{m_{eff,n}\omega_n}, \tag{A.32}$$

and $\omega_n^2 = (L_n C_n)^{-1}$, with $L_n = \eta L^2 B^2 / m_{eff,n}\omega_n^2$, and $C_n = m_{eff,n}/\eta_n L^2 B^2$.

Figure A.5 demonstrates the magnetomotive measurement of the fundamental mode resonance of device 1. A 200 μV_{rms} voltage signal was applied through a 10 kΩ resistance to provide the current I. The data was taken at a mixing chamber

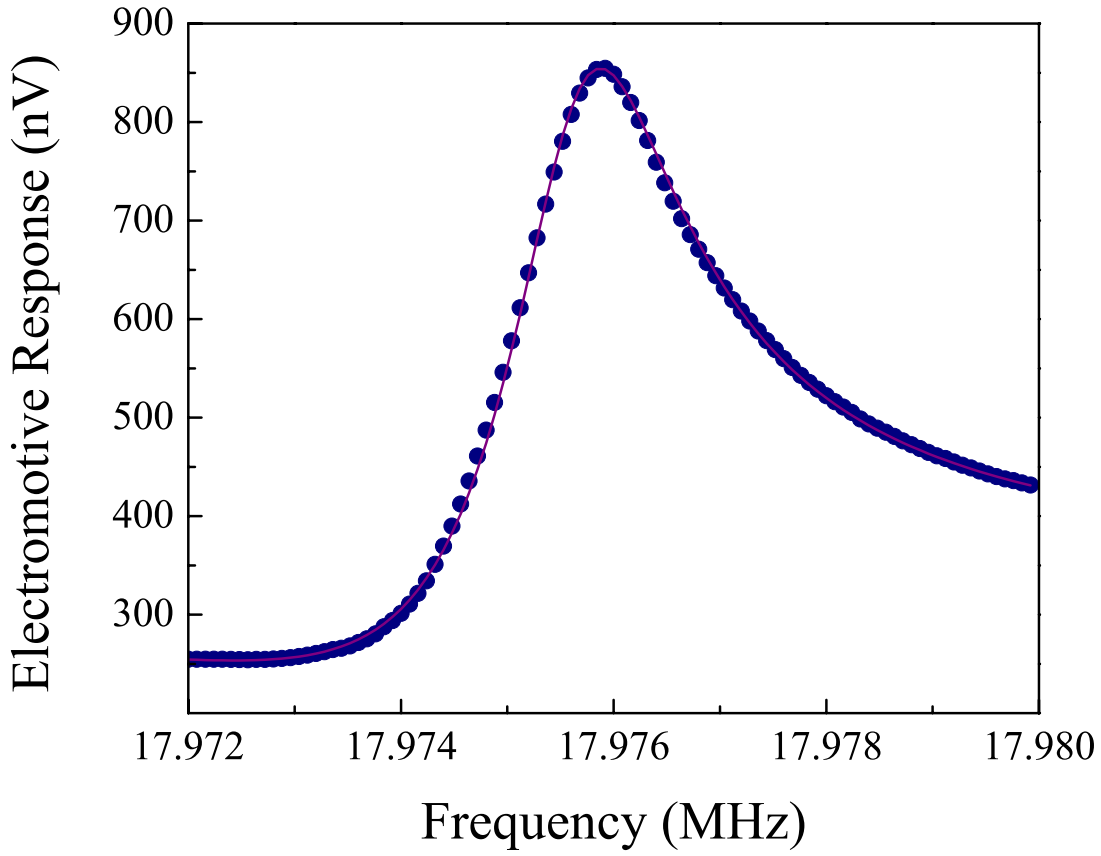

Figure A.5: Plot of the response of the fundamental mode resonance of Device 1, measured using magnetomotive detection. A lock-in was used to measure the quadrature components of the resonator response. The response (solid line) was fit to a driven-damped harmonic oscillator response. The data (circles) were taken at a mixing chamber temperature of 15 mK and magnetic field B = 6 T. A drive current of I $\sim$ 10 nA was used. The quality factor, resonant frequency, and amplitude were determined to be 10881(3), 17.9756642(3)MHz, and 601.1(1) nV respectively.

temperature of 15 mK and a magnetic field of 6 T. A lock-in was used to measure the quadrature components of the resonator's response. These were then fit to a driven-damped harmonic oscillator response. In the plot, the circles are the amplitude of the response from the measured quadratures, and the line is the amplitude of the least-squares fits to the individual quadratures. The resonant frequency and quality factor were extracted from the fit and determined to be $f_1 = 19.976$ MHz and $Q_e = 10.9 \times 10^3$. While the resonant frequency agrees very well with results of the SET displacement detection technique, the quality factor is substantially lower. This is a result of the loading from the capacitance of the co-axial cable and the 50 Ω amplifier impedance, which is much greater than the loading from SET detection. For more details on the loading effect and the magnetomotive measurement in general, please see reference [137].

Appendix B

Useful SET and RFSET Information

Knowledge of the SET and measurement circuit parameters is essential for both the determination of the operating points of the RF-SET displacement detection scheme and for the characterization of its performance. In this appendix, using the normal state and superconducting state current-voltage (IV) characteristics, I first demonstrate how to extract the coupling-capacitance C_{NR}, the gate capacitance C_g, the junction capacitances C_j, the SET junction resistances R_j, and the superconducting gap energy Δ. I then discuss a technique to evaluate the frequency response of the measurement circuit. Finally, I summarize a method that allows for the calibration of the charge sensitivity.

B.1 SET Parameters

IV Map Measurement

To determine the SET parameters, four DC measurements of the SET source-drain current, I_{SD}, were made (Fig. B.1): in the normal state, I_{SD} as a function of the source-drain bias V_{SD} and the resonator bias V_{NR}; in the normal state, I_{SD} as a function of V_{SD} and the gate bias V_g; in the superconducting state (SSET), I_{SD} as a function of V_{SD} and V_{NR}[1]; in the superconducting state, I_{SD} as a function of V_{SD}

[1]Both of the leads and the island are superconducting so the SET is in fact an (SSS) SET.

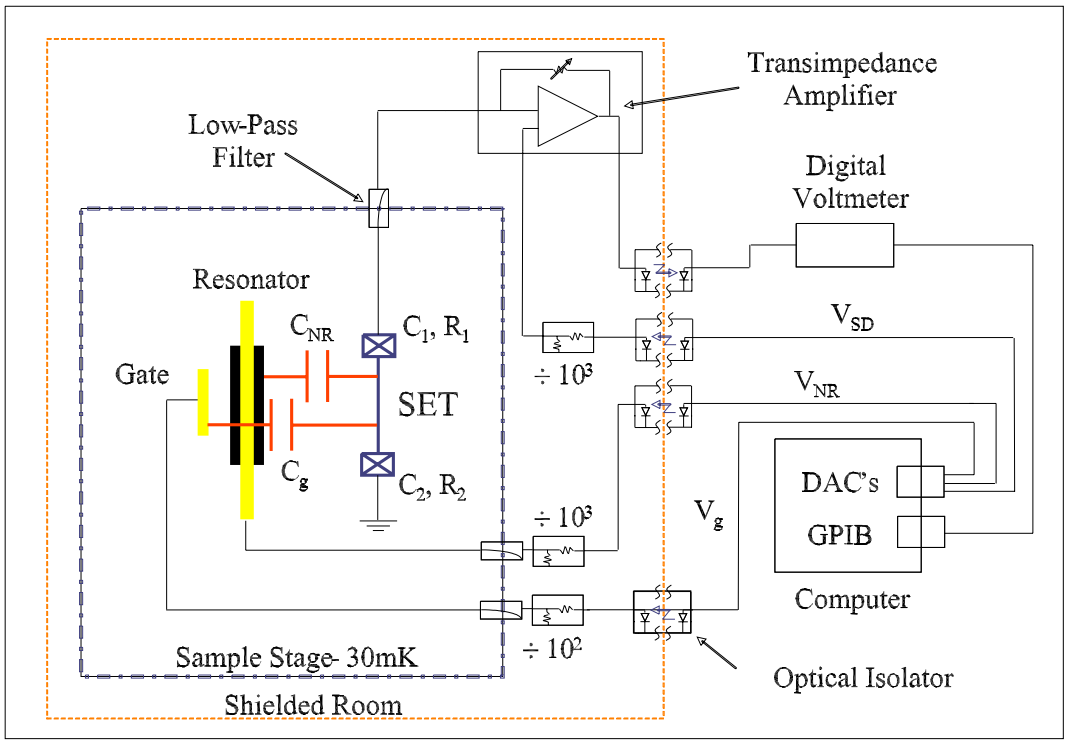

Figure B.1: Circuit diagram for IV map measurement .

and V_g. The voltages are set and swept by a computer-controlled digital-to-analog card. For each increment of the voltages, the current is sensed by a transimpedance amplifier, and the output is measured by a digital voltmeter and recorded by the computer through GPIB. A 1 Tesla magnetic field is applied to operate the SET in the normal state.

The Normal-State Characteristics: The Orthodox Theory and Capacitance Calculations

Figure B.2 demonstrates a typical result of a normal-state IV map measurement. Coulomb-blockade suppresses I_{SD} for V_{SD} below a threshold voltage V_t, which

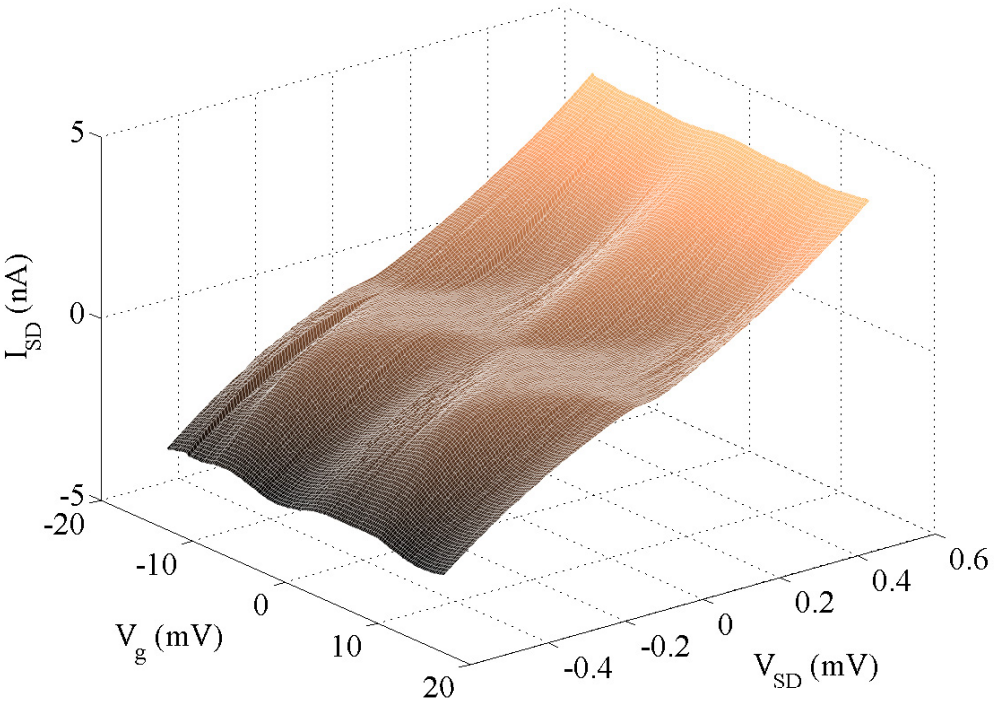

Figure B.2: Normal state IV map Device 2.

is periodic in $V_{NR}(V_g)$ with period e. Above V_t, I_{SD} asymptotes to a linear dependence on V_{SD}. The value and periodicity of V_t are sensitive functions of C_j and $C_{NR}(C_g)$, and the asymptotic behavior of I_{SD} at large V_{SD} is a function of the series combination of the R_j's. Both limits, the onset of current and large V_{SD}, are described by the orthodox theory of single-electron tunneling [68], and can, in principle, be used to extract the corresponding parameters [143] [144] [145].

In the orthodox theory, it is assumed that the charge state of the SET island evolves stochastically through single-electron tunneling events, yielding, at any instant of time, a value of n electrons with steady-state probability $P(n)$ [68].

The tunneling events occur through either of the SET junctions, i, and in either direction, on (+) or off of (-) the SET island. They are characterized by the tunneling rates $\Gamma_i^{\pm}$ [68].

The net charge transfer or current through each junction is determined by performing a weighted sum over all charge states, n, of the difference between the (+) and (-) tunneling rates [68]:

$$I_1 = -e \sum_{n=0}^{\infty} P(n) \left(\Gamma_1^+ - \Gamma_1^- \right)$$

$$I_2 = -e \sum_{n=0}^{\infty} P(n) \left(\Gamma_2^- - \Gamma_2^+ \right).$$

As $P(n)$ is assumed to be stationary in time, charge accumulation on the SET island does not occur, and the current through each junction must be equal, yielding [68]

$$I_{SD} = I_1 = I_2. \tag{B.1}$$

The assumption that $P(n)$ be stationary, also leads to the condition of detailed balance [68],

$$P(n+1)\Gamma^{-}(n+1) = P(n)\Gamma^{+}(n), \tag{B.2}$$

where

$$\Gamma^{-}(n+1) = \Gamma_1^{-}(n+1) + \Gamma_2^{-}(n+1)$$

and

$$\Gamma^{+}(n) = \Gamma_1^{+}(n) + \Gamma_2^{+}(n).$$

The tunneling rates $\Gamma_i^{\pm}$ are calculated using Fermi's golden rule [50]:

$$\Gamma_i^{\pm}(n) = \frac{\Delta F_i^{\pm}(n)}{e^2 R_i} \frac{1}{e^{\beta \Delta F_i^{\pm}(n)} - 1}, \tag{B.3}$$

where $\beta = \mathrm{k}_B T$ and $\Delta \mathrm{F}_i^{\pm}(n)$ is the change in system free-energy accompanying a particular tunneling event, and given, for the case of an asymmetrically biased SET, by

$$\begin{aligned} \Delta F_1^{\pm}(n) = \pm E_c \Big[2\left(n - \frac{C_{NR}V_{NR}}{e} - \frac{C_g V_g}{e} \right) \pm 1 + \\ + \frac{2(C_2 + C_{NR} + C_g)V_{SD}}{e} \Big] \end{aligned} \tag{B.4}$$

and

$$\Delta F_2^{\pm}(n) = \pm E_c \left[2\left(n - \frac{C_{NR}V_{NR}}{e} - \frac{C_g V_g}{e} \right) \pm 1 - \frac{2C_1 V_{SD}}{e} \right]. \tag{B.5}$$

where $E_c = e^2/2C_\Sigma$ is the charging energy or electrostatic cost for the tunneling of a single electron, and $C_\Sigma = C_1 + C_2 + C_{NR} + C_g$.

Knowing $\Gamma_i^{\pm}$, $P(n)$ and I_{SD} can be calculated using Eqs. B.2 and B.1.

I can obtain a quantitative understanding of the Coulomb-blockade regime without explicitly solving for $P(n)$. For simplicity's sake, I first set $n = 0$, $V_{NR} = 0$, and $V_g = 0$ in Eqs. B.4 and B.5). For small $|V_{SD}|$, $\Delta F_i^{\pm}(n) > 0$, and the work done by the bias V_{SD} is not enough to overcome the charging energy E_c. Consequently all four transisitions ($\pm$, junctions 1 and 2) are exponentially suppressed through Eq. B.3, and no current is observed.

As V_{SD} is increased from zero bias, eventually one of the transitions becomes energetically favorable. That is, either $\Delta F_2^+(0) = 0$ or $\Delta F_1^-(0) = 0$, depending on which threshold is smaller, $V_T^{+,2}(0) = e/2C_1$ or $V_T^{-,1}(0) = e/(2(C_2 + C_{NR} + C_g))$. If $C_1 > (C_2 + C_{NR} + C_g)$, then an electron tunnels onto the island. As a result, $n = 1$, and the corresponding discharging step, $\Delta F_1^-(1)$, becomes energetically favorable, and an electron tunnels off through junction 1. After the discharge, $n = 0$, and the charging step through junction 2 again becomes favorable, and so on. On the other hand, if $C_1 < (C_2 + C_{NR} + C_g)$, then $V_t^{-,1}(0) < V_t^{+,2}(0)$, and the onset of current begins with an electron tunneling off through junction 1,[2] at which point $\Delta F_2^+(-1)$ < 0, and an electron tunnels on through junction 2, and so on. Similiar processes are observed if V_{SD} is decreased from zero bias, as one can verify from Eqs. B.4 and B.5.

Returning to Eqs. B.4 and B.5, it is apparent that the threshold voltage can be tuned by adjusting V_{NR} or V_g. Leaving $V_g = 0$, increasing $|V_{NR}|$ lowers the

[2]In practice there is an unknown background charge on the SET island which should be included into Eqs. B.4 and (B.5). The designation of the SET island charge state as n thus refers to n electrons induced above or below the background.

electrostatic tunneling cost and reduces $|V_t|$. At $C_{NR}|V_{NR}|$ = e/2, the barrier is completely removed, and current flows for infinitesimal $|V_t|$. At this bias point, the charge configurations $n = 0$ and $n = \pm 1$ are equally probable ($n = 1$ if V_{NR} is positive and n = -1 if V_{NR} is negative). As $|V_{NR}|$ is increased further, the $n = \pm 1$ state becomes more favorable than the $n = 0$ state. $|V_t|$ thus increases, and eventually returns to the maximum, $V_t = e/2C_1$ or $V_t = e/2(C_2 + C_{NR} + C_g)$ at $C_{NR}V_{NR} = \pm e$. This process is repeated for higher n states as V_{NR} is further increased. I have thus found that the threshold for tunneling is periodic in $C_{NR}V_{NR}$ with a period of one electron. The same is found to be true for tuning of V_g with $V_{NR} = 0$.

Turning back to Fig. B.2, the Coulomb-blockade regions are now understood to be a result of $\Delta F_i^{\pm}(n) > 0$ for all four transisitions ($\pm$, junctions 1 and 2) and all n. From Eqs. B.4 and B.5, the width of the blockade in V_{SD} is seen to be periodic in $C_{NR}V_{NR}$ with a period of e: minimized when $C_{NR}V_{NR} = en/2$; and maximized when $C_{NR}V_{NR} = 0$ or a multiple of ne. Knowing the blockade to have period e, I can calculate C_{NR} from the relation

$$C_{NR}\Delta V_{NR} = e, \tag{B.6}$$

where ΔV_{NR} is the corresponding periodicity in mV (Fig. B.3). Similarly, I can calculate C_g, from the normal-state IV map with $V_{NR} = 0$ (not shown),

$$C_g\Delta V_g = e. \tag{B.7}$$

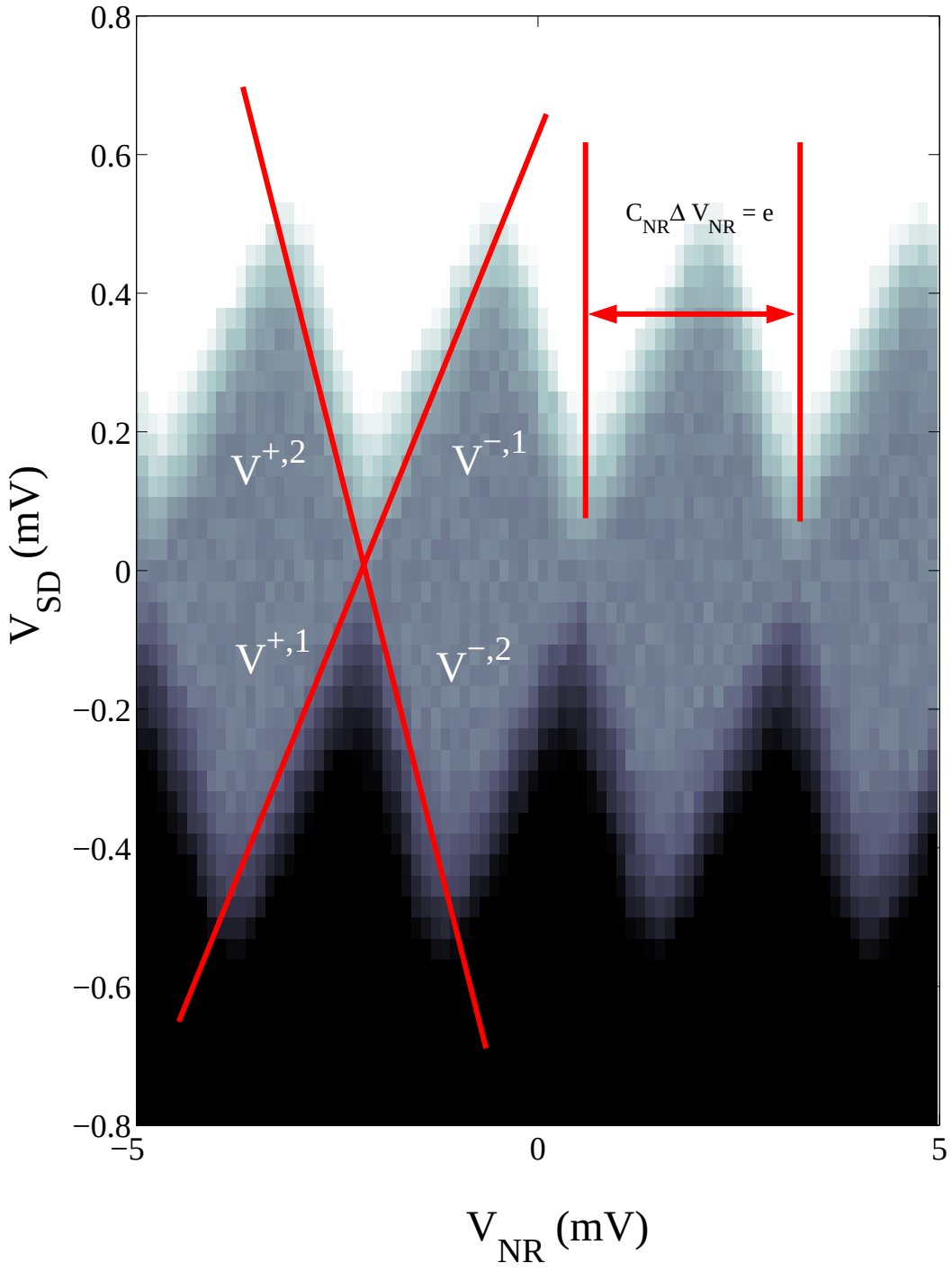

Figure B.3: Extracting capacitances from normal-state IV Device 2.

An expression for the edge of the blockade V_t can be derived by noting that the onset of tunneling occurs when at least one of $\Delta F_i^{\pm}$ satisfies $\Delta F_i^{\pm} = 0$:

$$V_t^{\pm,1} = \frac{C_{NR}V_{NR} + C_g V_g}{(C_{NR} + C_g + C_2)} \mp \frac{e(1 \pm 2n)}{2(C_{NR} + C_g + C_2)} \tag{B.8}$$

and

$$V_t^{\pm,2} = -\frac{C_{NR}V_{NR} + C_g V_g}{C_1} + \frac{e(2n \pm 1)}{2C_1}. \tag{B.9}$$

With the knowledge of C_{NR} and C_g, the junction capacitances C_1 and C_2 can be extracted by equating the slopes of the experimental tunneling onset (Fig. B.3) with the pre-factor of V_{NR} in Eqs. B.8 and B.9.

Normal-State Characteristics: Junction Resistances

I cannot simply extract R_Σ from electrostatic considerations, and must solve for I_{SD} using the detailed balance condition (Eq. B.2) and the definitions of $\Gamma_i^{\pm}$. For $V_{SD} \gg 2E_c/e$, it is necessary to compute P(n) for several thousand n. I solve Eq. B.2 numerically, and find that the slope of I_{SD} vs. V_{SD} asymptotes to R_Σ^{-1}. The serial resistance, R_Σ is thus extracted from the normal-state IV map by a linear fit of I_{SD} at large V_{SD} (Fig. B.4).

With the knowledge of the junction capacitances C_1 and C_2 and the serial resistance R_Σ, a rough estimate of the individual junction resistances R_1 and R_2 can be made [145] (Table B.1). Assuming that the thicknesses of the two junctions are equal (both junctions are grown at the same time under similiar conditions of pressure and temperature, see Chapter 3) and that $C_i \propto A_i$ and $R_i \propto 1/A_i$, where

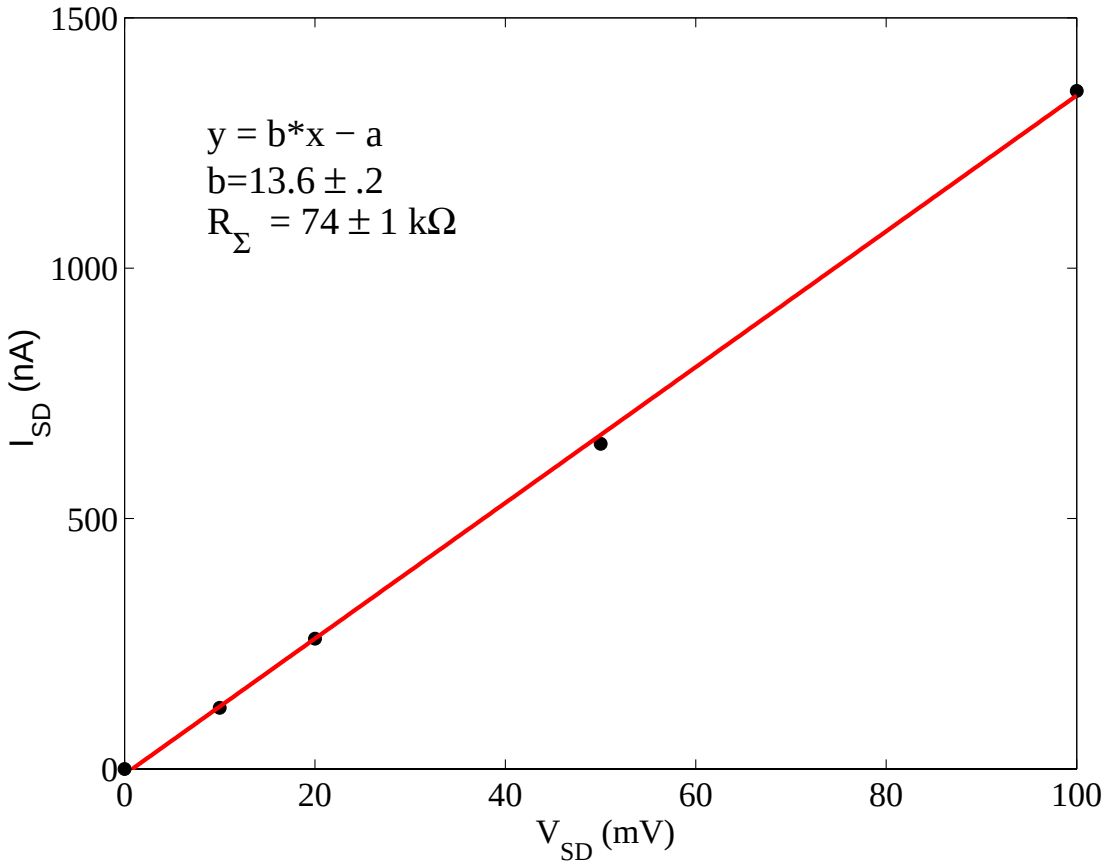

Figure B.4: Extraction of junction resistance Device 2

A_i is the cross-sectional area of junction-i, the individual junction resistances can be expressed as

$$R_1 = \frac{C_2}{C_1 + C_2} R_\Sigma \tag{B.10}$$

$$R_2 = \frac{C_1}{C_1 + C_2} R_\Sigma. \tag{B.11}$$

Failure of Normal-State Extraction Method

Two effects combine to make the extraction of the junction capacitances from the normal-state IV map unreliable: self heating of the SET island and quantum charge fluctuations (co-tunneling).

Self-heating of the SET island results from the combination of dissipation in the SET island and poor thermal coupling between the electron gas and phonon bath [152]. Using the standard model for electron-phonon coupling [123] [124], and assuming that $\sim 50\%$ of the total power dissipated in the SET is dissipated in the SET island, with the SET leads thermalized at the temperature of the phonon bath, the SET-island electron-bath temperature T_{island} at the onset of tunneling can be estimated [152]:

$$T_{island} = \left(\frac{P_{island}}{\Sigma \Omega} \right)^{\frac{1}{5}}, \tag{B.12}$$

where $\Sigma = 0.2\ nW/\mu m^3 K^5$ [152] is the electron-phonon coupling for aluminum and $\Omega = 0.05\ \mu m^2$ is the total volume of the SET island. I have assumed that the phonon-bath temperature, $T_b \ll T_{island}$. If $P_{island} \approx I_{SD} V_{SD}/2$, with $V_{SD} = e/C_\Sigma$ and $I_{SD} \approx e/4R_j C_\Sigma$ from Eqs. B.3, B.4, and B.5, then

$$T_{island} \approx \left(\frac{e^2}{8 R_j C_\Sigma^2 \Omega \Sigma} \right)^{\frac{1}{5}} \approx 350 - 400 mK \tag{B.13}$$

for parameters $C_\Sigma = 1$ fF and $R_j = 50$ kΩ. This estimate does not take into account cooling of the island due to the tunneling of electrons to and from the lower-temperature SET leads and should thus be considered as an upper-bound [152].

Nonetheless, the tunneling threshold is broadened, leaving the onset of current V_t indistinct [151]. This is modeled with the orthodox theory. Figures B.4(a) and B.4(b) shows two simulations of the onset of tunneling of a normal-state SET with charging energy $E_C/k_B = 1.5$ K and $C_1 = C_2 \gg C_g = 10$ aF, and $C_\Sigma = 590$ aF. In Fig. B.4(a), $T_{island} = 10$ mK, and the onset of tunneling is very clear and readily fit, yielding onset contour slopes of 0.033 and thus $E_C = 1.5$ K through Eqs. B.8 and B.9. In Fig. B.4(b), $T_{island} = 300$ mK, the onset of tunneling is unclear, and different slopes are obtained depending on the contour chosen.

In addition to self-heating, quantum charge fluctuations, or co-tunneling, can round the onset of current [69]. In general, co-tunneling is the process of charge transfer through the SET via an energetically unfavorable intermediate virtual state, and is the dominant charge transfer mechanism within the coulomb-blockade regime [69]. From the energy-time uncertainty relation, for example, an electron may tunnel through one junction to a forbidden island state, and dwell there for time $\Delta t = \hbar/\Delta E$, where $\Delta E \sim E_C$ is the energy required to make the transition. During Δt, it is energetically favorable for an electron to tunnel off the island through the second junction, resulting in a finite probability for the net transfer of one electron across the SET.

The transition probability rate for the net process, and thus the contribution

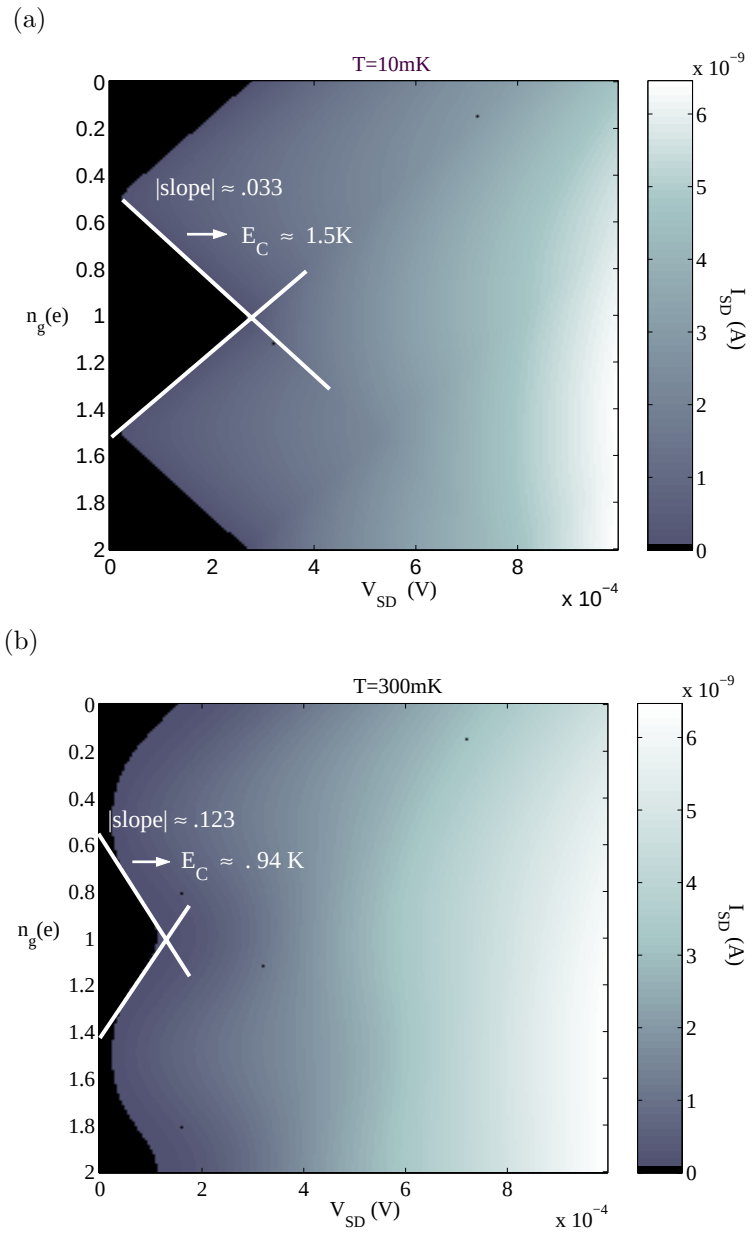

Figure B.5: Normal-state IV simulation for (a) T = 10 mK and (b) T = 300 mK.

of co-tunneling to I_{SD}, can be estimated by multiplying the transition probability rate for the forbidden transisition, $\Gamma_1 \sim 1/R_\Sigma C_{Sigma}$, by the probability for the energetically favorable tunneling event $\Gamma_1 \Delta t$:

$$\Gamma_{co-tunneling} \sim \Gamma_1 \frac{R_Q}{R_\Sigma}, \tag{B.14}$$

where $R_Q = h/e^2$ is the quantum of resistance. The contribution of co-tunneling is thus found to be a fraction R_Q/R_Σ of the sequential-tunneling current. For our devices, $\frac{R_Q}{R_\Sigma} \sim .2 - .8$. This is expected to result in the renormalization of the charging energy by the same order of magnitude [150]:

$$E_C' \approx E_C(1 - 4\frac{R_Q}{\pi^2 R_\Sigma}). \tag{B.15}$$

By not accounting for the effect of co-tunneling in the normal-state IV characteristics, I thus expect to err by as much as 30% in the determination of the junction capacitances. While modeling of the SET self-heating is straight-forward, accounting for the co-tunneling processes would require calculating 2nd-order (and higher, depending on the precision desired) transition matrices for the tunneling rates and could become both tedious and difficult. Rather than going to all that trouble, a simpler method is to use the features of the superconducting IV curve.

Superconducting IV Characteristics

Figure B.6 demonstrates a typical result of the superconducting IV map measurement $I_{SD}V_{SD}Vg$. The complexity of the map reflects the large variety of tunneling processes that can occur in an SSET due to the combination of Coulomb

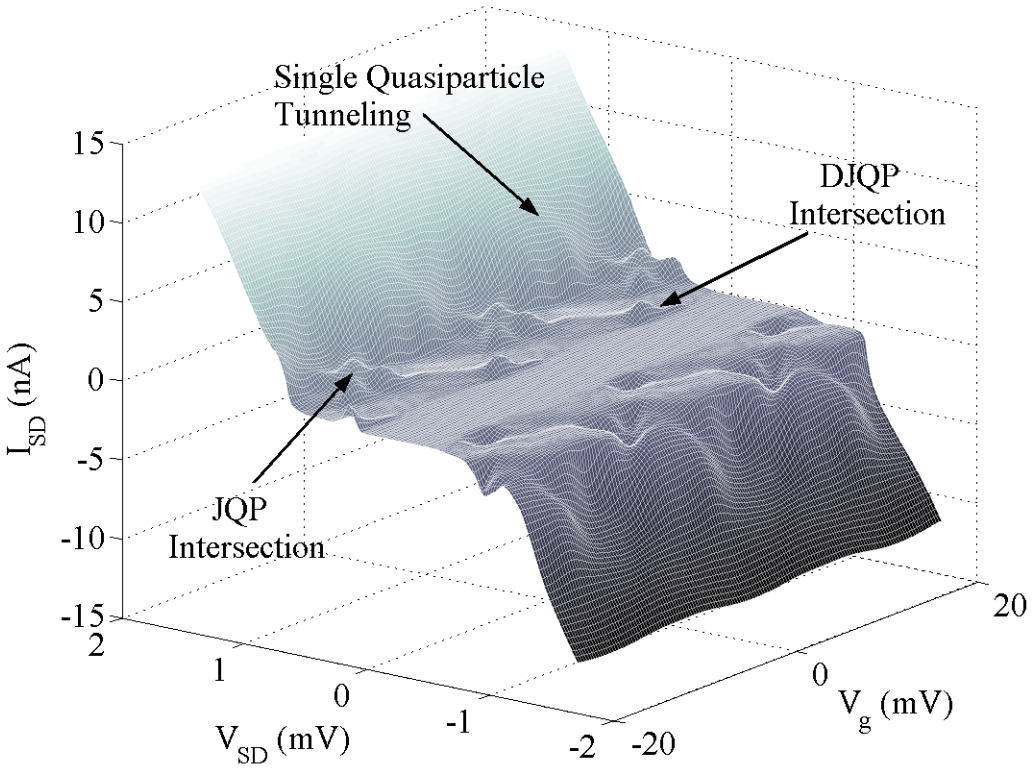

Figure B.6: Supreconducting IV map Device 2.

blockade, Josephson tunneling effects, and the superconducting gap energy [148] [149]. Most prominent here are three distinct processes: the double Josephson-quasiparticle resonance (DJQP) [146], the Josephson-quasiparticle resonance (JQP) [147], and single quasiparticle tunneling. All three processes have been studied extensively, and consideration of the respective dynamics can be used to infer the junction capacitances and the superconducting gap energy, Δ.

Figure B.7 is a color contour plot of the superconducting IV map in Fig. (B.6. The threshold for single quasiparticle tunneling defines the width of the IV plateau. This threshold corresponds to the energy required for a quasiparticle to overcome both the superconducting gap energy and the Coulomb charging barrier, and is seen from simple electrostatic considerations to vary between 4Δ and $4\Delta + e/C_{\Sigma}$. The minimum width of the plateau is thus 8Δ.

Knowing Δ, I can determine the Josephson coupling E_j of each junction - I assume Δ is equal for the leads and the island, which should be the case considering that they have similiar cross-sections and composition - using the Ambegaokar/Baratoff relation [144]:

$$E_{j,i} = \frac{\hbar\pi\Delta}{4e^2 R_i}. \tag{B.16}$$

Within the plateau, current ridges are evident. Along these ridges, the bias voltage is sufficient for the resonant tunneling of Cooper-pairs, followed by the tunneling of single quasiparticles [146] [147]. As the processes are initiated with the tunneling of a Cooper-pair, the thresholds for the processes can be determined using electrostatic arguments similiar to the case of normal-state tunneling processes

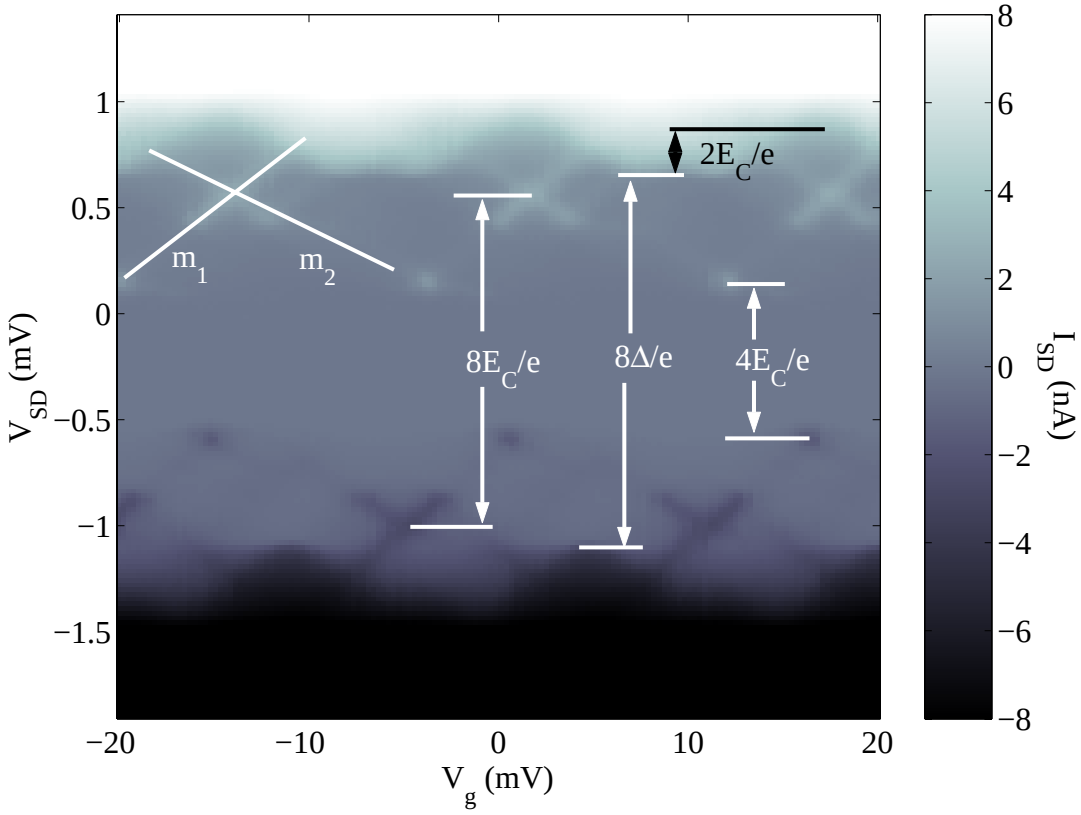

Figure B.7: Extracting junction capacitances from superconducting IV map Device 2.

(previous section). From these thresholds, the slope of ridges can be determined:

$$m_1 = \frac{C_g}{C_2 + C_{NR} + C_g} \tag{B.17}$$

$$m_2 = -\frac{C_g}{C_1}. \tag{B.18}$$

Having already determined C_{NR} and C_g, I can use m_1 and m_2 to determine the individual junction capacitances, Table B.1.

The intersection of the ridges at $V_{SD} = e/C_\Sigma$ and $V_{SD} = 2e/C_\Sigma$ are known as the DJQP and JQP resonance peaks respectively. In the case of the JQP resonance, it is energetically favorable for a Cooper-pair tunneling event to occur through either of the two junctions, followed by two sequential quasiparticle tunneling events through the opposite junction (for example, the charge state of the island, n, goes from $0 \rightarrow 2 \rightarrow 1 \rightarrow 0$ and so on). In the case of the DJQP resonance, the Cooper-pair tunneling event is followed, first, by a single quasiparticle, then the tunneling of a Cooper-pair, and finally the tunneling of a single quasiparticle ($0 \rightarrow 2 \rightarrow 1 \rightarrow$ -1 $\rightarrow 0$ and so on). For all four transitions in the DJQP cycle to be energetically favorable, it is necessary for $E_c > 2\Delta/3$. The locations of the JQP and DJQP intersections in terms of V_{SD} give independent determinations of C_Σ (Table B.2).

For Devices 1, 2, 3, I find that C_Σ's calculated from the slope of the current ridges and the C_Σ's calculated from the JQP and the DJQP process agree to within 15%. Comparison of C_Σ calculated using the JQP and DJQP process shows agreement within 7%. For Device 4, the DJQP peak was absent and the ridges of the JQP were very indistinct. The only available calculation of C_Σ was from the location of the JQP peaks. From the symmetry in the normal-state IV map with respect to V_g

Table B.1: Junction capacitances and resistances of Devices 1-4.

Device	$C_1(aF)$	$R_1(k\Omega)$	$C_2(aF)$	$R_2(k\Omega)$	$C_g(aF)$	$C_{NR}(aF)$
1	81	61	84	59	14	61
2	250	21	100	53	10	26
3	173	47	341	24	14	64
4	~ 600	~ 15	~ 600	~ 15	19	63

Table B.2: Total capacitance, charging energy, gap energy and Josephson energies Devices 1 - 4. (a) Total capacitance found by summing C_i, C_g , C_{NR}. (b) Total capacitance found from position of JQP peak. (c) Total capacitance found from position of DJQP peak.

Device	$C_\Sigma^a(aF)$	$C_\Sigma^b(aF)$	$C_\Sigma^c(aF)$	$\frac{E_c}{e}(\mu V)$	$\frac{\Delta}{e}(\mu V)$	$\frac{E_{j,i}}{e}(\mu V)$
1	241	-	279	287	220	12, 12
2	386	410	435	184	220	37, 14
3	592	577	540	148	200	15, 21
4	-	1310	-	61	180	~ 40, 40

for Device 4, we assume that $C_1 \sim C_2$ and $R_1 \sim R_2$.

For Devices 1, 2, 3, I find that $E_C/e > 2\Delta/3e$, consistent with the observation of the presence of the DJQP resonance in the superconducting IV maps for these devices. For Device 4, $E_C/e \approx \Delta/3$, consistent with the absence of the DJQP resonance in the superconducting IV map.

For Devices 1, 2, 3, I see that $E_C/e > E_j/e$. This is consistent with the absence of a supercurrent in the superconducting IV map for these devices. For Device 4, $E_C/e \approx E_j/e$. This is consistent with the presence of a supercurrent modulated with V_g in the superconducting IV map of Device 4.

The reason for the chronologically increasing junction capacitances (decreasing charging energy) is not known, but is consistent with the observed line-widths of the SET leads and islands becoming progressively larger for each successive device (see Chapter 3). As well, it is consistent with the general trend of decreasing R_Σ and charge sensitivity.

B.2 Measurement Circuit Parameters

The measurement circuit parameters, including the RF tank circuit, were determined by applying a large dc bias ($V_{SD} \gg V_t$) across the SET source-drain, and recording shot noise ring-up of the tank circuit with a spectrum analyzer [63] (Fig. B.8).

For $V_{SD} > V_t$ and time-scales slow with respect to the SET tunneling time, $\sim R_\Sigma C_\Sigma \sim 0.1$ GHz^{-1}, the spectral density of the SET shot noise is white and given

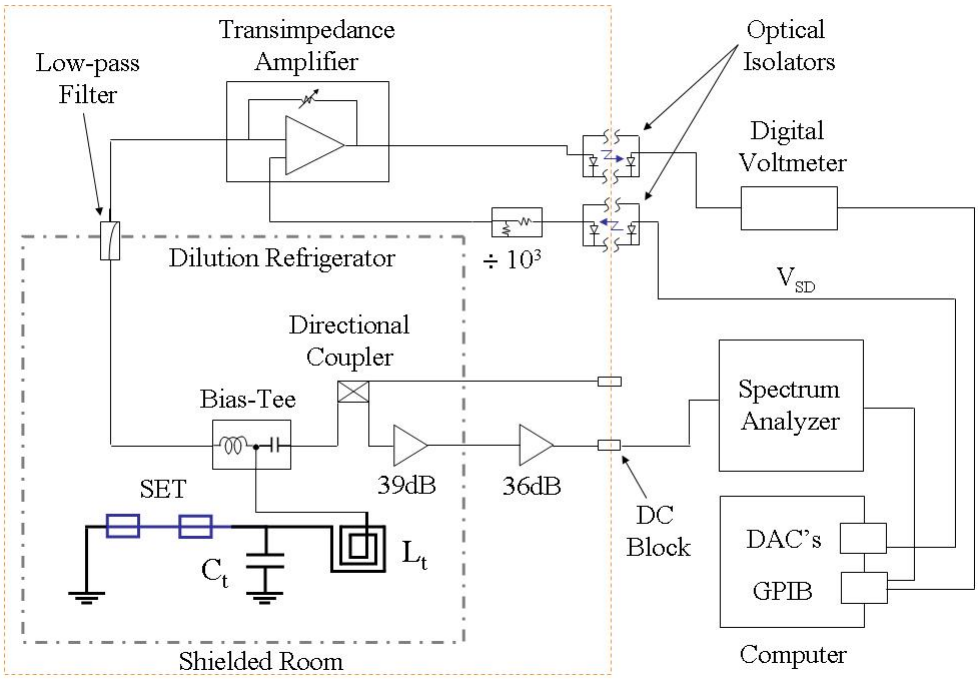

Figure B.8: Circuit schematic for the measurement of the shot noise ring-up of the tank circuit.

by $S_{II} = eI_{SD}$ [43]. As the center frequency of the tank circuit was designed to be ~ 1 GHz $< 1/R_{\Sigma}C_{\Sigma}$, the shot noise served as a calibrated white noise source with which we could probe the measurement circuit's frequency response.

The resulting noise power density measured at the input of the spectrum analyzer (Fig. B.9) takes the form:

$$P_{in} \simeq GeI_{SD}Z_o \frac{f_o^4}{\left(f_T^2 - f^2\right)^2 + \left(f f_T/Q\right)^2}. \tag{B.19}$$

Here,

$$Q = \left(\frac{Z_{LC}}{R_{\Sigma}} + \frac{Z_o}{Z_{LC}}\right)^{-1} = Z_{LC}\Big(Z_{LCR} + Z_o\Big)^{-1} \tag{B.20}$$

is the loaded quality factor of the tank resonance, Z_o is the 50 Ω transmission line impedance, $Z_{LC} = \sqrt{L_T/C_T}$ is the tank circuit characteristic impedance, Z_{LCR} $=L_T/(R_{\Sigma}C_T)$ is the transformed-SET impedance on resonance, and G is the power gain of the measurement circuit.

Because the LC circuit was superconducting at the measurement temperature, $T \sim 50$ mK, and because the length of the circuit was at most $0.1\lambda_{1GHz}$, I have assumed that the tank circuit was a dissipation-less, lumped-element LC component. Additionally, I have neglected the effect of loading on the resonant frequency, $f_o = 1/(2\pi\sqrt{L_T C_T})$, as it was of the order $Z_o/R_{\Sigma} \sim 0.001$.

Including the noise of the measurement circuit, on resonance, the noise power at the input of the spectrum analyzer thus takes the form:

$$P \simeq GB\left(eI_{SD}Q^2Z_o + k_B T_n^{det}\right), \tag{B.21}$$

where T_n^{det}, and B are measurement circuit noise temperature, and bandwidth respectively. I have assumed that T_n^{det} is independent of the SET bias point, at large

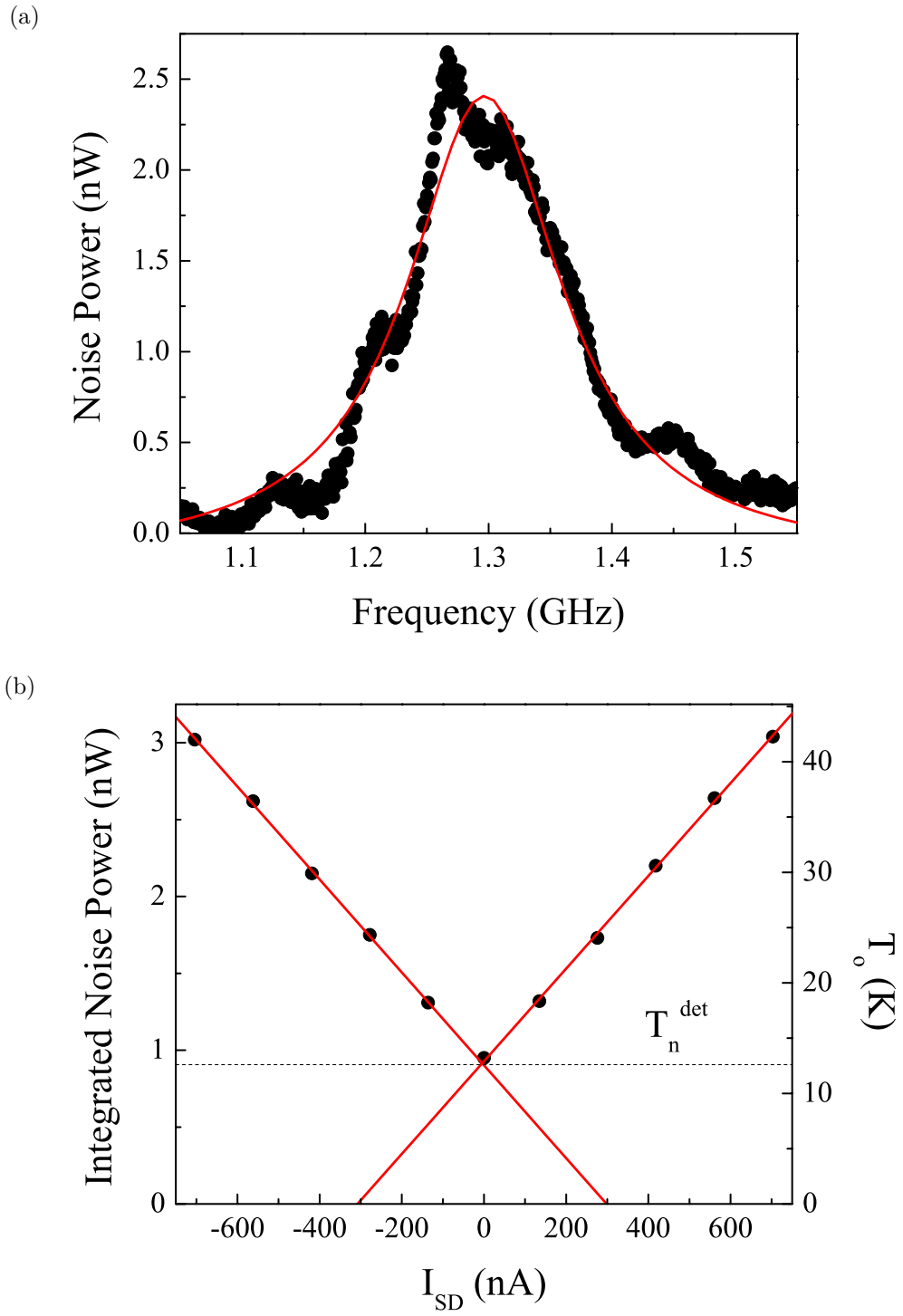

Figure B.9: Tank circuit response Device 3. (a) A lorentzian fit (red line) of the noise power versus frequency for $I_{SD} = 120$ nA (black circles). (b) A linear fit (red line) of the integrated noise power versus I_{SD} (black circles).

Table B.3: Measurement circuit matching, gain, and noise temperature Devices 1-4. T_{SET} measured at $I_{SD} \sim 120$nA.

Device	$Z_{LCR}(\Omega)$	Γ_{max}	$M(dB)$	$T_n^{det}(K)$	$G(dB)$	$T_{SET}(K)$
1	-	-	-	-	-	-
2	2.2-3.4	.87-.92	.72-1.2	20.2-31.7	62-64	4.3-6.6
3	2.5	.90	.82	12.6	67	5.8
4	5.6	.8	2.0	13.4	66.5	3.8

V_{ds} [116]. The equivalent noise temperature of the detection scheme T_o is then defined by dividing Eq. B.21 by 'GBk_B':

$$T_o = \frac{eI_{SD}Q^2Z_o}{k_B} + T_n^{det}. \tag{B.22}$$

Figure B.9 displays a typical result of the shot noise measurement. Figure B.9(a) is a plot of the noise spectrum as was measured using the spectrum analyzer. From a fit to Eq. B.19, I can extract the width Δf and center frequency f_T of the resonance. From the width, I estimate the quality factor $Q = f_T/\Delta f$, and the detection bandwidth $\Delta F = \Delta f/2$. From the definitions of f_T and Q, I calculate L_T, C_T, Z_{LC}, and the impedance of the LRC on resonance Z_{LCR} (Tables 3.1 and B.3).

Figure B.9(b) displays the integrated noise power and total noise temperature of the detection scheme T_o as a function of I_{SD}. The integration was done over a 1 MHz band about the center frequency. As expected, the noise power increased linearly with I_{SD}. Fitting Eq. B.21 to the data, I estimate G and T_n^{det} from the

slope and y-intercept respectively (Table B.3).

For Devices 2, 3, and 4, T_n^{det} = 20.2 K, 12.6 K, 13.4 K respectively. The decrease of $\sim$ 40% between Device 2 and Devices 3 and 4 is believed to have been due mainly to the factor of $\sim$ 2 improvement in gain of the measurement scheme for the measurement of Devices 3 and 4. For Devices 3 and 4, the calculated gain, G, was $\sim$ 2 dB less than the gain measured from room temperature transmission measurements (see Chapter (4)). For Device 2, G is $\sim$ 5 dB less than expected.

Finally, the contribution of the SET shot noise T_{SET} to the overall detection noise can be estimated by subtracting T_n^{det} from T_o at a particular V_{SD}. At $\sim$ 120 nA, the smallest I_{SD} at which we measured the output shot noise power, T_{SET} ranged from $\sim$ 3.8 K - 5.8 K, or $\sim$ 20% - 50% of the total noise.

B.3 Calibration of Charge Sensitivity

The charge sensitivity of the detection scheme was measured using amplitude-modulated (AM) reflectometry (Chapter 5). Microwaves resonant with the LC circuit were applied to the SET drain, and the reflected signal was recorded. Simultaneously, a 1 MHz sine wave bias of charge amplitude ΔQ_g (in units of electrons) was applied to the gate of the SET, modulating the amplitude of the reflected carrier signal, and producing sidebands at $f_o \pm \mathrm{n}f$, where $f = 1$ MHz . The sidebands were recovered using homodyne detection, mixing the reflected signal with the carrier, and measured with a spectrum analyzer. The charge sensitivity was then calculated from the ratio of the background noise power level $P_{Background}$ to the power in the

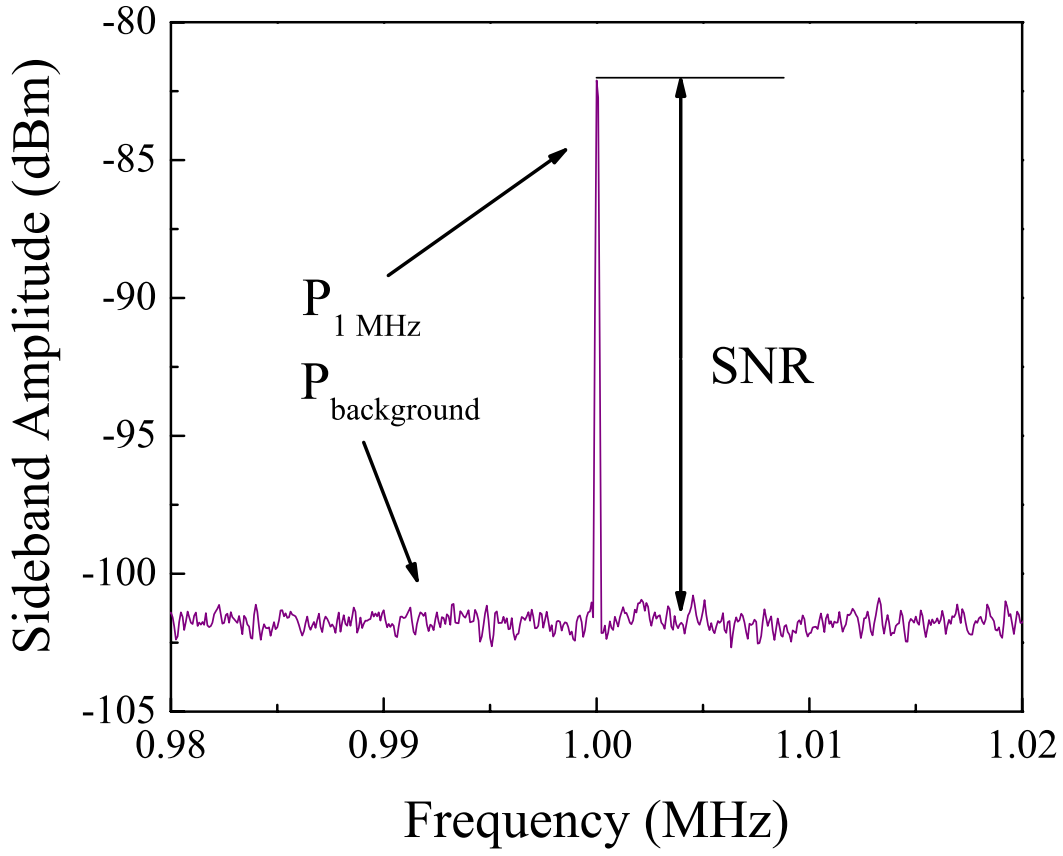

Figure B.10: Illustration of the experimental determination of the charge sensitivity from amplitude-modulated reflectometry. The plot shows a 1 MHz sideband of the measured reflected signal after recovery with homodyne mixing at the carrier frequency.

1MHz sideband P_{1MHz} (Fig. B.10):

$$\sqrt{S_Q} = \frac{\Delta Q_g}{\sqrt{B}} 10^{-\mathrm{SNR}/10}, \tag{B.23}$$

where SNR = $P_{1MHz}(dBM)$ - $P_{Background}(dBm)$ is the signal-to-noise ratio and B is the resolution bandwidth of the spectrum analyzer.

In practice, due to losses in the sample lead and losses in the cabling and filters inside the dilution refrigerator, the amplitude of the charge signal applied to the SET gate at 1MHz was not known. However, from the dependence of the reflected signal's sideband amplitude on the amplitude of the 1 MHz modulation, I can calculate the losses in the circuit and calibrate the charge sensitivity.

For a dc gate bias, $V_g \approx 0$, the sideband power response can be approximated by [153]

$$P = P_o \sin(2\pi \Delta Q_g \sin 2\pi f t), \tag{B.24}$$

where f=1MHz. This can be expanded in terms of the Bessel functions $J_n(2\pi\Delta Q_g)$ [153]:

$$P = 2P_o \sum_{n=0}^{\infty} J_{2n+1}(2\pi \Delta Q_g) \sin\left((2n+1)\omega t\right). \tag{B.25}$$

Using lock-in detection, we measured the amplitude of the fundamental of the response, n = 0, as a function of the amplitude ΔV_g of the 1 MHz modulation at the output of the waveform generator (Fig. B.11). I assume that the relationship between the voltage modulation at the generator and the charge modulation at the device is given by $\Delta Q_g = A\Delta V_g/e$. Fitting the response to $J_1(A\Delta V_g)$, and knowing that the first zero of $J_1(x)$ occurs at $x = 3.832$, I extract A and determine the ratio $\Delta Q_g/\Delta V_g$ in electrons/volt. From the value of ΔV_g, I calculate ΔQ_g, and, using Eq.

B.23, I calculate the charge sensitivity at the operating points of the the Devices 1 - 4 (Table B.5).

For Devices 3 and 4, using the Bessel function fit, I find 5 - 7 dB attenuation in the gate line. This is consistent with room temperature transmission measurements of the same line (see Chapter 4). For Devices 1 and 2, we were not aware of the Bessel function calibration technique. Thus the reported values of $\sqrt{S_Q}$ are estimated using a value of 6 dB attenuation in the gate line.

Finally, the uncoupled energy sensitivity of the total detection scheme, SET shot noise plus measurement circuit noise, is defined as [116]

$$\delta\epsilon = \frac{S_Q}{2C_\Sigma}. \tag{B.26}$$

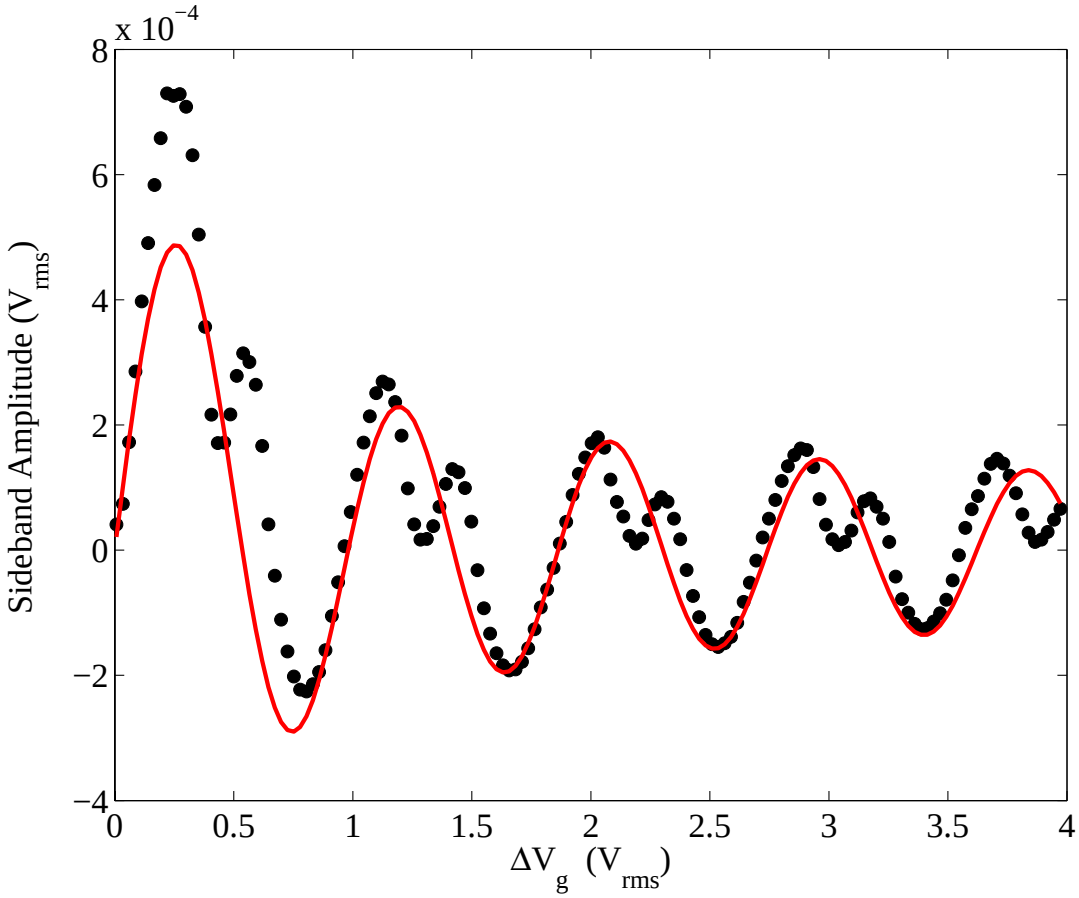

Figure B.11: Bessel function fit to sideband response Device 3.

Table B.4: Charge modulation calibration Devices 1 - 4. Note that the attenuation listed is the attenuation of the gate line. This does not include an additional 60 dB of attenuation due to attenuators put in place at the top of the fridge.

Device	A ($\frac{e_{rms}}{V}$)	$\Delta V_g(V_{rms})$	$\Delta Q_g(e_{rms})$	Attenuation (dB)
1	-	0.50	$\sim$ .015	$\sim$ 6
2	-	0.50	$\sim$ .015	$\sim$ 6
3	.036	1.0	.036	7
4	.062	1.0	.062	5

Table B.5: Charge sensitivity Devices 1 - 4. (a) Measured charge sensitivity. (b) Calculated charge sensitivity from curvature of $I_{SD}V_{SD}V_g$ map. Both at 1 MHz

Device	SNR (dB)	$\sqrt{S_Q}^a(\mu e_{rms}/\sqrt{Hz})$	$\sqrt{S_Q}^b$	$\delta\epsilon(J/Hz)$	$\delta\epsilon_{SET}(J/Hz)$
1	56	20	30	85$\hbar$	-
2	58	30	20	50$\hbar$	10$\hbar$
3	52	90	70	1300$\hbar$	600$\hbar$
4	50	200	150	3750$\hbar$	1100$\hbar$

BIBLIOGRAPHY

[1] W. Heisenberg. "Ueber den anschaulichen Inhalt der quantentheoretischen Kinematik and Mechanik," *Zeitschrift für Physik* **43** (1927), 172-198.

[2] C. M. Caves, K. S. Thorne, R. W. P. Drever, V. D. Sandberg, and M. Zimmerman. "On the Measurement of a Weak Classical Force Coupled to a Quantum-Mechanical Oscillator. I. Issues of Principle," *Review of Modern Physics* **52**, no. 2 (1980), 341-392.

[3] C. M. Caves."Quantum Limits on Noise in Linear Amplifiers," *Physical Review D* **26**, no. 8 (1982), 1817-1839.

[4] V. B. Braginsky and F. Y. Khalili. *Quantum Measurement*. Cambridge: Cambridge University Press, 1995.

[5] H. P. Yuen. "Contractive States and the Standard Quantum Limit for Monitoring Free-Mass Positions," *Physical Review Letters* **51**, no. 9 (1983), 719-722.

[6] M. F. Bocko and R. Onofrio. "On the Measurement of a Weak Classical Force Coupled to a Harmonic Oscillator: Experimental Progress," *Review of Modern Physics* **68**, no.3 (1996), 755-799.

[7] Y. Hadjar, P. F. Cohadon, C. G. Aminoff, M. Pinard, A. Heidmann. "High-Sensitivity Optical Measurement of Mechanical Brownian Motion," *Europhysics Letters* **47**, no. 5 (1999), 545-551.

[8] G. M. Harry, I. Jin, H. J. Paik, T. R. Stevenson, and F. C. Wellstood. "Two-Stage Superconducting-Quantum-Interference-Device Amplifier in a High-Q Gravitational Wave Transducer," *Applied Physics Letters***76**, no. 11 (2000), 1446-1448.

[9] P. Falferi et al. "Noise Sources and Dissipation Mechanisms of a 120 $\hbar$ SQUID Amplifier," *Applied Physics Letters* **82**, no. 6 (2003), 931-933.

[10] A. Buonanno and Y. Chen. "Optical Noise Correlations and Beating the Standard Quantum Limit in Advanced Gravitational-Wave Detectors," *Classical and Quantum Gravity* **18**, no. 15 (2001), L95-L101.

[11] B. Abbott et al. "Limits on Gravitational-Wave Emission from Selected Pulsars Using LIGO Data," *Physical Review Letters* **94** (2005), 181103/1-6.

[12] M. P. Blencowe and M. N. Wybourne. "Sensitivity of a Micromechanical Displacement Detector Based on the Radio-Frequency Single-Electron Transistor," *Applied Physics Letters* **77**, no. 23 (2000), 3845-3847.

[13] Y. Zhang and M. P. Blencowe. "Intrinsic Noise of a Micromechanical Displacement Detector Based on the Radio-Frequency Single-Electron Transistor," *Journal of Applied Physics* **91**, no. 7 (2002), 4249-4255.

[14] R. G. Knobel and A. N. Cleland. "Nanometre-Scale Displacement Sensing Using a Single Electron Transistor," *Nature* **424** (2003), 291-293.

[15] M. D. LaHaye, O. Buu, B. Camarota, and K. C. Schwab. "Approaching the Quantum Limit of a Nanomechanical Resonator," *Science* **304** (2004), 74-77.

[16] A. A. Clerk. "Quantum-Limited Position Detection and Amplification: A Linear Response Perspective," *Physical Review B* **70**, no. 24 (2004), 245306/1-9.

[17] V. Giovannetti, S. Lloyd, L. Maccone. "Quantum-Enhanced Measurements: Beating the Standard Quantum Limit," *Science* **306** (2004), 1330-1336.

[18] K. S. Thorne, "Gravitational Radiation," in *Three Hundred Years of Gravitation*, ed. S. W. Hawking and W. Israel (Cambridge: Cambridge University Press, 1987), 330-458.

[19] H. J. Paik. "Superconducting Tunable-Diaphragm Transducer For Sensitive Acceleration Measurements," *Journal of Applied Physics* **47**, no. 3 (1976), 1168-78.

[20] J. A. Sidles et al. "Magnetic Resonance Force Microscopy," *Reviews of Modern Physics* **67**, no. 1 (1995), 249-265.

[21] D. Rugar, R. Budaklan, H. J. Mamin, and B. W. Chul. "Single Spin Detection by Magnetic Resonance Force Microscopy," *Nature* **430**, no. 6997 (2004), 329-332.

[22] K. L. Ekinci, Y. T. Yang, and M. L. Roukes. "Ultimate Limits to Inertial Mass Sensing Based Upon Nanoelectromechanical Systems," *Journal of Applied Phyiscs* **95**, no. 5 (2004), 2682-2689.

[23] A. N. Cleland and M. R. Geller. "Superconducting Qubit Storage and Entanglement with Nanomechanical Resonators," *Physical Review Letters* **93**, no. 7 (2004), 070501/1-4.

[24] M. R. Geller and A. N. Cleland. "Superconducting Qubits Coupled to Nanoelectromechanical Resonator: An Architecture for Solid-State Quantum Information Processing," *Physical Review A* **71** (2005), 032311/1-17.

[25] A. D. Armour, M.P. Blencowe, and K.C. Schwab. "Entanglement and Decoherence of a Micromechanical Resonator Via Coupling to a Cooper-Pair Box," *Physical Review Letters* **88**, no. 14 (2002), 148301/1-4

[26] E. K. Irish and K. C. Schwab. "Quantum Measurement of a Coupled Nanomechanical Resonator-Cooper-Pair Box System," *Physical Review B* **68** (2003), 155311/1-7.

[27] M. L. Roukes. "Nanoelectromechanical Systems Face the Future," *Physics World* **14** (2001), 25-28.

[28] A. Hopkins, K. Jacobs, S. Habib, and K. C. Schwab. "Feedback cooling of a nanomechanical resonator," *Physical Review B* **68**, no. 23 (2003), 235328/1-10.

[29] R. Ruskov, A. N. Korotkov, and K. C. Schwab. "Quantum Nondemolition Squeezing of a Nanomechanical Resonator," *IEEE Transactions on Nanotechnology* **4**, no. 1 (2005), 132-140.

[30] M. P. Blencowe and M. N. Wybourne. "Quantum Squeezing of Mechanical Motion For Micron-Sized Cantilevers," *Physica B* **280** (200), 555-556.

[31] M. P. Blencowe. "Quantum Electromechanical Systems," *Physics Reports* **395** (2004), 159-222.

[32] D. H. Santamore, A. C. Doherty, and M. C. Cross. "Quantum Nondemolition Measurement of Fock States of Mesoscopic Mechanical Oscillators," *Physical Review B* **70** (2004), 144301/1-16.

[33] I. Wilson-Rae, P. Zoller, and A. Imamoglu. "Laser Cooling of a Nanomechanical Resonator Mode to its Ground State," *Physical Review Letters* **92**, no. 7 (2004), 075507/1-4.

[34] M. L. Roukes et al. "Zeptogram Mass Detection-Weighing Molecules," Physics News Updates. *The AIP Bulletin of Physics News* no. 725 (2005).

[35] Kittel, C. and H. Kroemer, *Thermal Physics*. 2nd ed. New York: Freeman, 1980.

[36] X. M. H. Huang, C.A. Zorman, M. Mehregany, and M.L. Roukes. "Nanodevice Motion at Microwave Frequencies," *Nature* **421** (2003), 496.

[37] K. Schwab, E. A. Henriksen, J. M. Worlock, and M. L. Roukes. "Measurement of the Quantum of Thermal Conductance," *Nature* **404**, no. 6781 (2000), 974-977.

[38] D. M. Meekhof, C. Monroe, B. E. King, W. M. Itano, and D. J. Wineland. "Generation of Nonclassical Motional States of a Trapped Atom," *Physical Review Letters* **76** (1996), 17961799.

[39] H. Park et al. "Nanomechanical Oscillations in a Single-C_{60} Transistor," *Nature* **407** (2000), 57-60.

[40] K. Hornberger et al. "Collisional Decoherence Observed in Matter Wave Interferometry," *Physical Review Letters* **90**, no. 16 (2003), 160401/1-4.

[41] R. J. Schoelkopf, P. Wahlgren, A. A. Kozhevnikov, P. Delsing, and D. E. Prober. "The Radio-Frequency Single-Electron Transistor: A Fast and Ultrasensitive Electrometer," *Science* **280** (1998), 1238-1242.

[42] M. H. Devoret and R. J. Schoelkopf. "Amplifying Quantum Signals With the Single-Electron Transistor," *Nature* **406** (200), 1039-1046.

[43] A. N. Korotkov. "Intrinsic Noise of the Single-Electron Transistor," *Physical Review B* **49**, no. 15 (1994), 10381-10392.

[44] N. W. Ashcroft and N. D. Mermin. *Solid State Physics*. Orlando: Saunders College Publishing, 1976.

[45] A. N. Cleland *Foundations of Nanomechanics*. New York: Springer, 2003.

[46] H. A. C. Tilmans, M. Elwenspoek, and J. H. J. Fluitman. "Microresonant Force Gauges," *Sensors and Actuators A* **30**, no. 1-2 (1992), 35-53.

[47] W. H. Zurek, S. Habib, J. P. Paz. "Coherent States Via Decoherence," *Physical Review Letters* **70**, no. 9 (1993), 1187-1190.

[48] M. D. LaHaye, O. Buu, B. Camarota, K. C. Schwab, Unpublished.

[49] R. K. Pathria. *Statistical Mechanics*. 2nd ed. Oxford: Butterworth-Heinemann, 1996.

[50] J. S. Townsend. *A Modern Approach to Quantum Mechanics*. New York: McGraw-Hill, 1992.

[51] J. J. Sakurai. *Modern Quantum Mechanics*. Revised ed. New York: Addison-Wesley, 1994.

[52] R. J. Glauber. "Coherent and Incoherent States of the Radiation Field," *Physical Review* **131** (1963), 2766-2788.

[53] R. Kubo. "The Fluctuation-Dissipation Theorem," *Reports on Progress in Physics* **29** (1966), 255-284.

[54] R. J. Schoelkopf, A. A. Clerk, S. M. Girvin, K. W. Lehnert, and M. H. Devoret. "Qubits As Spectrometers of Quantum Noise." *Quantum Noise In Mesoscopic Physics*. Proceedings of the NATO Advance Research Workshop. Dordrecht, Netherlands: Kluwer Academic Publishers, 2003. p. 175-203.

[55] A. D. Armour, M. P. Blencowe, and Y. Zhang. "Classical Dynamics of a Nanomechanical Resonator Coupled to a Single-Electron Transistor," *Physical Review B* **69**, no. 12 (2004), 125313/1-15.

[56] D. Mozyrsky and I. Martin. "Quantum-Classical Transition Induced by Electrical Measurement," *Physical Review Letters* **89**, no. 1 (2002), 018301/1-4.

[57] A. Y. Smirnov, L. G. Mourokh, and N. J. M. Horing. "Nonequilibrium Fluctuations and Decoherence in Nanomechanical Devices Coupled to the Tunnel Junction," *Physical Review B* **67**, no. 11 (2003), 115312/1-9.

[58] A. A. Clerk, S. M. Girvin, A. K. Nguyen, and A. D. Stone. "Resonant Cooper-Pair Tunneling: Quantum Noise and Measurement Characteristics," *Physical Review Letters* **89**, no. 17 (2002), 176804/1-4.

[59] A. A. Clerk. Unpublished Notes (2004).

[60] M. P. Blencowe. Unpublished Notes (2005).

[61] A. A. Clerk, S. M. Girvin, and A. D. Stone. "Quantum-Limited Measurement and Information in Mesoscopic Detectors," *Physical Review B* **67**, no. 16 (2003), 165324/1-12.

[62] A. Aassime, G. Johansson, G. Wendin, R. J. Schoelkopf, and P. Delsing. "Radio-Frequency Single-Electron Transistor as Readout Device For Qubits: Charge Sensitivity and Backaction," *Physical Review Letters* **86**, no. 15 (2001), 3376-3379.

[63] A. Aassime, D. Gunnarsson, K. Bladh, P. Delsing, and R. Schoelkopf. "Radio-Frequency Single-Electron Transistor: Toward the Shot-Noise Limit," *Applied Physics Letters* **79**, no. 24 (2001), 4031-4033.

[64] A. Shnirman and G. Schon. "Quantum Measurements Performed With a Single-Electron Transistor," *Physical Review B* **57**, no. 15 (1997), 15400/1-7.

[65] FastCap UNIX version by RLE Computational Prototyping Group, Massachusetts Institute of Technology Cambridge, MA 02139, see www.fastfieldsolvers.com/links.

[66] V. O. Turin and A. N. Korotkov. "Numerical Analysis of Radio-Frequency Single-Electron Transistor Operation," *Physical Review B* **69**, no. 19 (2004), 195310/1-13.

[67] A. N. Korotkov and M. A. Paalanen. "Charge Sensitivity of Radio-Frequency Single-Electron Transistor," *Applied Physics Letters* **74**, no. 26 (1999), 4052-4054.

[68] D. V. Averin and K.K Likharev. "Coulomb Blockade of Single-electron Tunneling, and Coherent Oscillations In Small Tunnel Junctions." *Journal of Low Temperature Physics* 62, no. 3-4 (1986): 345-373.

[69] D. V. Averin and Y. Nazarov, "Macroscopic Quantum Tunneling of Charge and Co-Tunneling." *Single Charge Tunneling.* Eds M. H. Devoret and H. Grabert. New York: Plenum, 1992.

[70] D. Song, A. Amar, C. J. Lobb, and F. C. Wellstood. "Advantages of Superconducting Coulomb Blockade Electrometers," *IEEE Transactions on Applied Superconductivity* **5**, no. 2 (1995), 3085-3089.

[71] A. N. Korotkov. "Charge Sensitivity Of Superconducting Single-Electron Transistor". *Applied Physics Letters* 69, no. 17 (1996): 2593-2595.

[72] M. S. Choi, F. Plastina, and R. Fazio. "Shot Noise for Resonant Cooper Pair Tunneling," *Physical Review Letters* **87**, no. 11 (2001), 116601/1-4.

[73] O. Buu, M. D. LaHaye, A. Naik, A. D. Armour, A. A. Clerk, K. C. Schwab, unpublished.

[74] MEMS and Nanotechnology Exchange, Reston, VA 20191, Tel. (703) 262-5368.

[75] C. M. Hernandez, T. W. Murray, S. Krishnaswamy ."Photoacoustic Characterization of the Mechanical Properties of Thin Flms," *Applied Physics Letters* **80**, no. 4 (2002): 691693.

[76] D. M. Profunser, J. Vollmann, and J. Dual. "Determination of the Material Properties of Microstructures by Laser Based Ultrasound," *Ultrasonics* **42** (2004): 641-646.

[77] Futurrex Inc., Franklin, NJ 07416, Tel. (973) 209-1563.

[78] Alfa Aesar, Ward Hill, MA 01835, Tel. (978) 521-6300.

[79] Madou, Marc. *Fundamentals of Microfabrication*. Boca Raton: CRC Press, 1997.

[80] The recipe for the tri-layer was provided to us by Pierre Echternach.

[81] JEOL USA, Inc., Peabody, MA 01960, Tel. (978) 535-5900.

[82] Upperspace Co., Pryor, OK 74361, Tel. (918) 825-4844.

[83] JC Nabity Lithography Systems, Bozeman, MT 59717, Tel. (406) 587-0848.

[84] MicroChem Co., Newton MA 02464, Tel. (617) 965-5511.

[85] J. G. Lu, J. M. Hergenrother, and M. Tinkham. "Effect of Island Length on the Coulomb Modulation in Single-Electron Transistors," *Physical Review B* **57**, no. 8 (1998): 4591-4598.

[86] T. A. Fulton and G. J. Dolan. "Observation of Single-Electron Charging Effects in Small Tunnel Junctions," *Physical Review Letters* **59**, no. 1 (1987), 109-12.

[87] Arch Chemicals, Inc., Norwalk, CT 06856, Tel.(203) 229-2900

[88] Atomergic Chemetals Co., Farmingdale, NY 11735, Tel. (631) 694-9000.

[89] R.D. Mathis Company, Long Beach, CA 90809, Tel. (562) 426-7049.

[90] Sierra Proto Express, Sunnyvale, CA 94086, Tel. (408) 735-7137.

[91] Technic, Cranston, RI 02910, Tel. (401) 781-6100.

[92] Sigma Aldrich Chemicals, St. Louis, MO 63178, Tel. (800) 588-9160.

[93] TVZ 0001, GE varnish by Oxford Instruments, Concord, MA 01742, Tel. (978) 369-9933.

[94] ISO 100CP by Burr Brown Co., Tuscon, AZ 85734, Tel. (520) 746-1111.

[95] DC block 8039 by Inmet, Ann Arbor, MI 48103, Tel. (888) 244-6638.

[96] SLP and VLP series by Mini-Circuits, Brooklyn, NY 11235, Tel., (718) 934-4500.

[97] J. M. Martinis, M.H. Devoret, and J. Clarke. "Experimental Tests For the Quantum Behavior of a Macroscopic Degree of Freedom: The Phase Difference Across a Josephson Junction," *Physical Review B* **35** (1987), 4682-4698.

[98] Pi filters 1293-001 and 1250-059 by Spectrum Control, Columbia, MD 21045 Tel. (866) 281-0989.

[99] 28% part B of A Stycast 1266 by Lake Shore Cryotronics, Inc., Westerville OH 43082 Tel. (614) 891-2244.

[100] SHP series by Mini-Circuits, Brooklyn, NY 11235, Tel., (718) 934-4500.

[101] BW-S40 series by Mini-Circuits, Brooklyn, NY 11235, Tel., (718) 934-4500.

[102] cc-ss-500 braided stainless steel coax by Lake Shore Cryotronics, Inc., Westerville OH 43082 Tel. (614) 891-2244.

[103] SC-033/50-CN-CN CuNi-CuNi Coax, 0.33 mm outer diameter by Alahlam Limited,3-25-4-101 Matsushiro Tsukuba-shi Ibaraki, 305-0035 Japan.

[104] C3203-20 by MAC Technology, Klamath Falls, OR97603, Tel., (800) 428-0341.

[105] ZFBT-4R2GW by Mini-Circuits, Brooklyn, NY 11235, Tel., (718) 934-4500.

[106] Nb-Nb 0.085 in. OD Coax, PTFE dielectric by KeyCom U.S.A. Co., Valley Stream, NY 11581 USA, Tel. (516) 825-1835.

[107] L1.5-30H by Berkshire Technologies, Oakland, CA 94609, Tel. (510) 655-1986.

[108] model number 15542 by Mini-Circuits, Brooklyn, NY 11235, Tel., (718) 934-4500.

[109] RX-102a-br by Lake Shore Cryotronics, Inc., Westerville OH 43082 Tel. (614) 891-2244.

[110] AVS-47 resistance bridge by RV Elektronikka Oy Veromiehentie(Picowatt) 14 FIN-01510 VANTAA Finland, Tel. 358-9-822087.

[111] Pobell, F. *Matter and Methods at Low Temperatures*. 2nd ed. Berlin: Springer, 1996.

[112] Nuclear Orientation Kit by Oxford Instruments, Concord, MA 01742, Tel. (978) 369-9933.

[113] Lusher, C.P., J. Li, V.A. Maidanov, M.E. Digby, H. Dyball, A. Casey, J. Nyeki, V.V. Dmitiev, B.P. Cowan, J. Saunders. "Current Sensing Noise Thermometry Using A Low T_C DC SQUID Preamplifier." *Measurement Science and Technology* 12, (2001): 1-15.

[114] Model 550 SQUID system by Quantum Design San Diego, CA 92121 Tel.(858) 481-4400.

[115] ZFM-2000 Frequency Mixer by Mini-Circuits, Brooklyn, NY 11235, Tel., (718) 934-4500.

[116] L. Roschier, P. Hakonen, K. Bladh, P. Delsing, K. W. Lehnert, L. Spietz, and R. J. Schoelkopf. "Noise Performance of the Radio-Frequency Single-Electron Transistor," *Journal of Applied Physics* **95**, no. 3 (2004), 1274-1286.

[117] W. H. Press, S.A. Teukolsky, W. T. Vetterling, B. P. Flannery. *Numerical Recipes in C*. 2nd ed. New York: Cambridge University Press, 1992.

[118] E. Fukushima. *Experimental Pulse NMR: a Nuts and Bolts Approach*. Reading: Addison-Wesley, 1981.

[119] M. Mück, J. B. Kycia, and J. Clarke. "Superconducting Quantum Interference Device as a Near-Quantum Limited Amplifier at .5 GHz," *Applied Physics Letters* **78**, no. 7 (2001), 967-969.

[120] M. Mück. "Increasing the Dynamic Range of a SQUID Amplifier by Negative Feedback," **368** (2002),141-145.

[121] A. B. Hutchinson, P. A. Truitt, K. C. Schwab, L. Sekaric, J. M. Parpia, H. G. Craighead, J. E. Butler. "Dissipation in Nanocrystalline-Diamond Nanomechanical Resonators," *Applied Physics Letters* **84**, no. 6 (2004), 972-974.

[122] J. P. Holman. *Heat Transfer*. 6th ed. New York: McGraw-Hill, 1986.

[123] M. L. Roukes, M. R. Freeman, R. S. Germain, R. C. Richardson, and M. B. Ketchen. "Hot Electrons and Energy Transport In Metals at MilliKelvin Temperatures," *Physical Review Letters* **55**, no. 4 (1985), 422-425.

[124] F. C. Wellstood, C. Urbina, and J. Clarke. "Hot-Electron Effects In Metals," *Physical Review B* **49**, no. 9 (1994), 5942-5955.

[125] M. M. Levio and J. P. Pekola. "Thermal Characteristics of Silicon Nitride Membranes at Sub-Kelvin Temperatures," *Applied Physics Letters* **72** (1998), 1305-1307.

[126] B. A. Glavin. "Low-Temperature Heat Transfer in Nanowires," *Physical Review Letters* **86**, no. 19 (2001), 4318-4321.

[127] R. Lifshitz and M. C. Cross. "Elastic Wave Transmission At an Abrupt Junction In a Thin Plate With Application to Heat Transport and Vibrations in Mesoscopic Systems," *Physical Review B* **64**, no. 8 (2001), 085324/1-22.

[128] L. D. Landau and E. M. Lifshitz. *Theory Of Elasticity*. 3rd ed. Oxford: Butterworth-Heinemann, 1986.

[129] Y. T. Yang, K. L. Ekinci, X. M. H. Huang, L. M. Schiavone, M. L. Roukes, C. A. Zorman and M. Mehregany. "Monocrystalline silicon carbide nanoelectromechanical systems," *Applied Physics Letters* **78**, no. 2 (2001), 162-164.

[130] see http://www.memsnet.org/material/

[131] M. A. Haque and M. T. A. Saif. "Deformation Mechanisms in Free-Standing Nanoscale Thin Films: A Quantitative in situ Transmission Electron Microscope Study," *Proceedings of the National Academy of Sciences of the United States of America* **101**, no. 17 (2004), 6335-6340.

[132] C. A. Zorman and M. Mehregany, "Materials for Microelectromechanical Systems," *The MEMS Handbook*. Ed. M. Gad-El-Hak. Boca Raton: CRC Press, 2001.

[133] S. Timoshenko and D. H. Young. *Vibration Problems in Engineering*. chapter 5, 3rd Ed. New York: D. Van Nostrand Company, 1955.

[134] R. Lifshitz and M. L. Roukes. "Thermoelastic Damping In Micro- and Nanomechanical Systems," *Physical Review B* **61**, no. 8 (2000), 5600-5609.

[135] D. M. Photiadis and J. A. Judge. "Attachment Losses of High Q Oscillators," *Applied Physics Letters* **85**, no. 3 (2004), 482-484.

[136] Y. Jimbo and K. Itao. "Attachment Loss of a Vibrating Cantilever," *Journal of Horological Instruments Japan* **47**, no. 1 (1968), 1-12.

[137] A. N. Cleland and M. L. Roukes. "External Control of Dissipation In a Nanometer-Scale Radiofrequency Mechanical Resonator," *Sensors and Actuators A* **72**, no. 3 (1999), 256-261.

[138] S. Rast, C. Wattinger, U. Gysin, and E. Meyer. "Dynamics of Damped Cantilevers," *Review of Scientific Instruments* **71**, no. 7 (2000), 2772-2775.

[139] B. Yurke, D. S. Greywall, A. N. Pargellis, and P. A. Busch. "Theory of Amplifier-Noise Evasion In an Oscillator Employing a Nonlinear Resonator," *Physical Review A* **51**, no. 5 (1995), 4211-4229.

[140] D. S. Greywall, B. Yurke, P. A. Busch, A. N. Pargellis, R. L. Willett. "Evading Amplifier Noise in Nonlinear Oscillators," *Physical Review Letters* **72**, no. 19 (1994), 2992-2995.

[141] A. N. Cleland and M. L. Roukes. "Fabrication of High Frequency Nanometer Scale Mechanical Resonators From Bulk Si Crystals," *Applied Physics Letters* **69**, no. 18 (1996), 2653-2655.

[142] K. L. Ekinci, Y. T. Yang, X. M. H. Huang, and M. L. Roukes. "Balanced Electronic Detection of Displacement In Nanoelectromechanical Systems," *Applied Physics. Letters* **81**, no. 12 (2002), 2253-2255.

[143] J. G. Liu. "Even-Odd Electron Number Effect in Small Superconducting Islands." Ph.D. dissertation, Harvard University 1997.

[144] M. Tinkham. *Introduction to Superconductivity.* 2nd Ed. New York: Dover, 1996.

[145] D. Song. "Properties of Coulomb-Blockade Electrometers in the Superconducting State." Ph.D. dissertation, University of Maryland at College Park, 1997.

[146] A. M. Van den Brink, G. Schön, and L. J. Geerligs. "Combined Single-Electron and Coherent-Cooper-Pair Tunneling In Voltage-Biased Josephson Junctions," *Physical Review Letters* **67**, no. 21 (1991), 3030-3033.

[147] T. A. Fulton, P. L. Gammel, D. J. Bishop, and L. N. Dunkelberger. "Observation of Combined Josephson and Charging Effects In Small Tunnel Junction Circuits," *Physical Review Letters* **63**, no. 12 (1989), 1307-1310.

[148] P. Hadley, E. Delvigne, E. H. Visscher, S. Lähteenmäki, and J. E. Mooij. "3e Tunneling Processes In a Superconducting Single-Electron Tunneling Transistor," *Physical Review B* **58**, no. 23 (1998), 15317-15320.

[149] R. J. Fitzgerald, S. L. Pohlen, and M. Tinkham. "Observation of Andreev Reflection In All-Superconducting Single-Electron Transistors," *Physical Review B* **57**, no. 18 (1998), 11073-11076.

[150] M. Thalakulam, Z. Ji, and A.J. Rimberg. "Sensitivity and linearity of Superconducting Radio-Frequency Single-Electron Transistors: Effects of Quantum Charge Fluctuations," *Physical Review Letters* **93**, no. 6 (2004), 066804/1-4.

[151] I would like to thank Rob Schoelkopf and Per Delsing for bringing this fact to our attention.

[152] R. L. Kautz, G. Zimmerli, and J.M. Martinis. "Self-Heating In the Coulomb-Blockade Electrometer," *Journal of Applied Physics* **73**, no. 5 (1993), 2386-2396.

[153] Wahlgren, P. "The Radio Frequency Single-Electron Transistor and the Horizon Picture for Tunneling." Ph.D. dissertation, Chalmers University of Technology, G*ö*teborg University, 1998.